

**TSUNAMIS: FORCES ON A VERTICAL WALL CAUSED BY
LONG WAVES, BORES, AND SURGES ON A DRY BED**

Thesis by
Jerald Day Ramsden

In Partial Fulfillment of the Requirements
for the Degree of
Doctor of Philosophy

California Institute of Technology
Pasadena, California

1993

(Submitted November 18, 1992)

© 1993

Jerald Day Ramsden

All Rights Reserved

ACKNOWLEDGMENTS

I would like to thank my advisor, Fredric Raichlen, for suggesting this research topic and arranging my financial support while at Caltech. I appreciated his assistance during this investigation, and enjoyed his company and good humor over the past few years.

I appreciate the time and helpful suggestions of the members of my thesis committee: Professors Norman Brooks, John Hall, John List, and Ted Wu. I would also like to thank Jack Nath for introducing me to experimental research.

I will certainly miss the fine people at the W. M. Keck Laboratory without whose help this research would have been next to impossible. I would like to thank Joe Fontana, Rich Eastvedt, Hai Vu, and John Lee for their knowledgeable assistance with the design and construction of the equipment used during this study. The smiling faces of Rayma Harrison, Gunilla Hastrup, and Susan Leising were always a welcome sight in the Keck library. The drafting assistance of Nancy Tomer and Cecilia Lin was very helpful. Fran Matzen, Karen Hodge, Jennifer Packman, Evelina Cui, and Joan Mathews were always available to help and spread good cheer. I enjoyed my discussions with Vito Vanoni and Bob Koh as well as the great times and camaraderie I have shared with many fellow graduate students here. I would like to thank Russell Mau for the scepter which I enthusiastically pass to Catherine Petroff whose stamina and determination never fail to amaze me.

I would like to thank my family and friends for their generous support and encouragement, and my wife, Denise, not only for typing and formatting this thesis but for making me laugh when I needed it most.

This research was sponsored by the National Science Foundation, Grant No. CES-8719931. The high speed motion picture camera was purchased with funds provided by the Miriam G. and Omar J. Lillevang Fund at Caltech.

To My Best Friend,

Denise

ABSTRACT

The major objective of this study has been to investigate experimentally the forces and overturning moments produced by tsunamis on vertical walls. The experimental results are compared with several analytical and numerical models. Several types of waves were used in a horizontal tank including solitary waves, undular bores, turbulent bores, and surges on a dry bed. Bores produced from breaking solitary waves in a tilting wave tank were also investigated. Various measurements were made, including the incident wave celerity, the wave profile, the runup, force, overturning moment, and pressure time histories. The impact process of the bores in the tilting wave tank were recorded with high-speed movies.

The wave profiles in the horizontal tank were defined using a laser induced-fluorescence system (LIF) which allows the free surface on a two-dimensional plane in the center of the wave tank to be recorded. This method was developed to measure accurately the surface elevation profile of turbulent high-speed flows which is difficult to measure reliably either with conventional flow visualization techniques or intrusive devices such as wave gages. The LIF method was also used to determine the runup on the wall.

Strong vertical accelerations were shown to occur during the reflection of bores and steep solitary waves at a vertical wall. These reduced the force on the wall relative to a hydrostatic force computed from the maximum runup height on the wall. The accelerations also cause the maximum force to occur before and after the maximum runup for steep solitary waves and bores, respectively. For these cases, the maximum measured force and overturning moment were always less than computed from the maximum measured runup on the wall using hydrostatic considerations. The maximum

force due to surges on a dry bed was also less than the hydrostatic force calculated from the maximum runup height on the wall. For all the dry bed cases studied, the maximum runup height on the wall was between 1.46 and 1.62 times the velocity head computed from the celerity of the incident surge. For the entire range of wave conditions of this study, the maximum relative runup occurred for a bore with a relative wave height of 1.23, and produced a runup equal to 3.8 times the velocity head computed from the wave celerity.

The maximum measured water surface slopes along the front of long waves, bores, and dry bed surges were computed from the measured wave profiles. At the transition from undular bores to turbulent bores, there was a discontinuity in the maximum water surface slope where the slope increased by a factor of 2.5 to three for turbulent bores. This discontinuity corresponded with a rapid increase in the measured runup, force, and moment on the wall.

The properly normalized force on a vertical wall due to the impingement of a bore on a mildly sloping beach is shown to be equivalent to the force produced by a bore of constant volume on a horizontal bed. This implies the results from the horizontal wave tank experiments can be used to estimate the loads expected from bores propagating on mild beaches with slopes ranging up to 0.02m/m.

Two numerical models were compared with the experimental results. A boundary integral element model, which solves the potential flow problem subject to the full nonlinear free surface boundary conditions, predicted the loads imposed on the wall due to steep solitary waves quite well. A finite difference model of the Navier-Stokes equations was also used to simulate the reflection of solitary waves and mild turbulent bores at a vertical wall. This finite difference model predicted the solitary wave loads

quite well; however, it over-predicted the steepness of the incident bore profiles and produced a force-time history with a high amplitude and short-duration peak, which was not observed in the measurements. Except for this sharp peak, the agreement of the finite difference model with the experimental results was quite reasonable.

TABLE OF CONTENTS

| <u>Chapter</u> | <u>Page</u> |
|---------------------------------------------------------------------------|-------------|
| Acknowledgments | i |
| Abstract | iii |
| Table of Contents | vii |
| List of Figures | x |
| List of Tables..... | xx |
| List of Symbols | xxi |
| 1. INTRODUCTION..... | 1 |
| 1.1 Objectives and Scope | 3 |
| 2. LITERATURE REVIEW..... | 6 |
| 2.1 Dam Break Flows | 6 |
| 2.2 Hydrodynamic Loading on a Vertical Wall due to Tsunami Impact..... | 8 |
| 3. THEORETICAL MODELING | 18 |
| 3.1 Boundary Integral Element Model..... | 18 |
| 3.2 Finite Difference Volume of Fluid Model | 30 |
| 4. EQUIPMENT AND PROCEDURES..... | 36 |
| 4.1 Tilting Wave Tank Study | 36 |
| 4.1.1 Tank and Wave Generator..... | 36 |
| 4.1.2 Vertical Wall..... | 40 |
| 4.1.3 Wave Gages | 52 |
| 4.1.4 Flow Visualization Equipment..... | 57 |

| <u>Chapter</u> | | <u>Page</u> |
|----------------|--------------------------------------------------------|-------------|
| 4. | 4.1.5 Data Acquisition | 59 |
| | 4.1.6 Procedures | 59 |
| 4.2 | Horizontal Wave Tank Experiments | 64 |
| | 4.2.1 Tank and Wave Generator..... | 64 |
| | 4.2.2 Vertical Wall..... | 67 |
| | 4.2.3 Pressure Transducer | 75 |
| | 4.2.4 Dam-Break Gate | 85 |
| | 4.2.5 Laser-Induced Fluorescence System..... | 90 |
| | 4.2.6 Celerity Gage..... | 96 |
| | 4.2.7 Procedures | 97 |
| | 4.2.7.1 Solitary Waves | 97 |
| | 4.2.7.2 Bores and Dry Bed Surges..... | 100 |
| 5. | RESULTS AND DISCUSSION..... | 103 |
| 5.1 | Tilting Wave Tank Study | 103 |
| | 5.1.1 Amplitude and Celerity Considerations | 103 |
| | 5.1.2 Force Considerations..... | 115 |
| 5.2 | Solitary Waves | 129 |
| | 5.2.1 Amplitude and Celerity Considerations | 129 |
| | 5.2.2 Pressure, Force, and Moment Considerations | 137 |
| 5.3 | Bores..... | 146 |
| | 5.3.1 Amplitude and Celerity Considerations | 147 |
| | 5.3.2 Pressure and Force Considerations | 155 |

| <u>Chapter</u> | <u>Page</u> |
|---------------------------------------------------------------------|-------------|
| 5. | |
| 5.3.3 Comparison Between Theoretical and Experimental Results | 162 |
| 5.3.4 Comparison Between Bores on Different Bottom Slopes | 165 |
| 5.4 Surges on a Dry Bed..... | 167 |
| 5.4.1 Celerity Considerations | 168 |
| 5.4.2 Amplitude Considerations | 170 |
| 5.4.3 Runup, Force, and Pressure Considerations..... | 180 |
| 5.4.4 Comparison Between a Bore and a Dry Bed Surge..... | 186 |
| 5.5 Summary..... | 189 |
| 5.6 Application to the 1960 Chilean Tsunami at Hilo, Hawaii | 207 |
| 6. | |
| CONCLUSIONS..... | 212 |
| References | 219 |
| Appendix A | 231 |
| Appendix B | 236 |
| Appendix C | 247 |

LIST OF FIGURES

| <u>Number</u> | <u>Description</u> | <u>Page</u> |
|---------------|----------------------------------------------------------------------------------------------------------------------------------------------------------------|-------------|
| 3.1.1 | Definition sketch of the boundary integral problem. | 19 |
| 3.1.2 | Transformation from physical space, \mathbf{x} , to the mapped space, ζ . | 26 |
| 3.2.1 | Definition sketch of a stationary hydraulic jump. | 32 |
| 3.2.2 | Creation of a bore using the "SOLA-VOF" model. | 34 |
| 3.2.3 | Propagation of the bore into the wall using the "SOLA-VOF" model. | 34 |
| 4.1.1 | Schematic of the tilting wave tank (after Skjelbreia (1987)). | 37 |
| 4.1.2 | Photograph of the wave generator in the tilting wave tank (after Skjelbreia (1987)). | 39 |
| 4.1.3 | Schematic of the wave generator and control equipment. | 39 |
| 4.1.4 | Wave tank cross section showing the location of the false walls and the instrumented wall ($\delta_1 = 0.13$ mm to 0.24 mm, $\delta_2 = 0.13$ mm to 0.18 mm). | 41 |
| 4.1.5 | Photo showing the instrumented wall to the left of the "s" shaped force transducers which are mounted to the steel T section. | 41 |
| 4.1.6 | Schematic of the instrumented wall used for the tilting wave tank experiments. | 42 |
| 4.1.7 | Schematic of the welded steel frame and T sections used to support the force transducers (all dimensions are in cm except where specified otherwise). | 43 |
| 4.1.8 | Schematic of the connection between the steel frame and the tilting wave tank (all dimensions are in cm except where specified otherwise). | 45 |
| 4.1.9 | Circuit diagram of the force transducer amplifier. | 46 |

| <u>Number</u> | <u>Description</u> | <u>Page</u> |
|---------------|---------------------------------------------------------------------------------------------------------------------------------------------------------------------------------------------|-------------|
| 4.1.10 | Schematic of the supporting structure for the false walls (all dimensions are in cm). | 48 |
| 4.1.11 | Calibration of the force transducer connected to channel 1. | 49 |
| 4.1.12 | Device used to calibrate the instrumented wall where the load, P, caused an applied force, F, on the wall. | 49 |
| 4.1.13 | Response of the instrumented wall due to point loads applied with the device shown in Figure 4.11. | 50 |
| 4.1.14 | (a) Schematic of a typical wave gage (after Raichlen (1965)) (b) circuit diagram of the bridge for the wave gage. | 53 |
| 4.1.15 | Calibrations of a wave gage spaced one hour apart. | 54 |
| 4.1.16 | Calibration of the wave gage by displacing the gage relative to the water and by changing the water level on the gage. | 55 |
| 4.1.17 | Second-order least square approximation of each calibration method. | 56 |
| 4.1.18 | Schematic of the high-speed camera and lighting location while recording the bore profiles; a) as seen from the wave generator and b) from above the tank. | 58 |
| 4.1.19 | Schematic of the high-speed camera and lighting location while recording the runup on the instrumented wall. | 58 |
| 4.1.20 | Definition sketch showing solitary wave generation in a tilting wave tank which caused the wave to break and propagate to the vertical wall as a turbulent bore. | 60 |
| 4.1.21 | (a) Measured force due to an incident wave, $H_0/h_0 = 0.288$, with $h_0 = 42.78$ cm; (b) signal after applying a numerical low-pass filter at 55 Hz. | 63 |
| 4.1.22 | Normalized energy spectrum from (a) force record before impact shown in Figure 4.1.21; (b) expanded frequency scale (total energy in force record, E_t was $1.221 \text{ N}^2\text{s}$). | 63 |
| 4.2.1 | Schematic drawing of a typical section of the horizontal wave tank (after French (1969)). | 65 |

| <u>Number</u> | <u>Description</u> | <u>Page</u> |
|---------------|-------------------------------------------------------------------------------------------------------------------------------------------------------------------------|-------------|
| 4.2.2 | Photo of the wave generator in the horizontal wave tank (after Goring (1979)). | 66 |
| 4.2.3 | Schematic drawing of the instrumented wall used in the horizontal wave tank experiments (all dimensions are in cm). | 68 |
| 4.2.4 | Schematic drawing of the supporting structure for the instrumented wall shown in Figure 4.2.3 (all dimensions are in cm). | 69 |
| 4.2.5 | Schematic drawing of the supporting structure for the false walls in the horizontal wave tank (all dimensions are in cm). | 70 |
| 4.2.6 | Response of the wall due to a hydrostatic load and a point load. | 71 |
| 4.2.7 | Output of each force transducer due to an impulsive load applied to the wall. | 72 |
| 4.2.8 | (a) Spectra of the response in each force transducer (shown in Figure 4.2.7) due to an impulsive load; (b) spectrum of the force due to the free vibration of the wall. | 73 |
| 4.2.9 | Response of the wall due to an applied moment. | 74 |
| 4.2.10 | Schematic drawing of the brass and plastic (Delrin) housings used to isolate the pressure transducer. | 76 |
| 4.2.11 | Photo showing the pressure transducer mounted in the plastic housing. | 77 |
| 4.2.12 | Circuit diagram of the pressure cell amplifier. | 78 |
| 4.2.13 | Photo of the apparatus used to calibrate the pressure cell while it was mounted in the instrumented wall. | 80 |
| 4.2.14 | A typical calibration curve obtained from the pressure transducer. | 81 |
| 4.2.15 | Effect of the housing material on the thermal response of the pressure transducer with a 15 v excitation. | 82 |
| 4.2.16 | Thermal offset of the pressure transducer due to solitary wave and bore reflection from the wall. | 83 |

| <u>Number</u> | <u>Description</u> | <u>Page</u> |
|---------------|-----------------------------------------------------------------------------------------------------------------------------------------------------------------------------------------------------------------------------------------------------------------------------------------------------------|-------------|
| 4.2.17 | Photo of the lucite tube used to test the natural frequency of the pressure transducer with various water depths. | 84 |
| 4.2.18 | Response of the pressure cell due to an impulsive load applied to a water column. | 85 |
| 4.2.19 | Photo of the dam break gate and the apparatus used to produce and control the motion of the gate. | 86 |
| 4.2.20 | Schematic drawing of (a) the brass insert built into the side of the wave tank to provide a slot for the gate shown in Figure 4.2.19; (b) the windshield wiper blade which is mounted along each side of the gate; (c) the rubber H section used along the bottom of the gate (all dimensions are in cm). | 87 |
| 4.2.21 | Schematic of the dam-break gate and control equipment. | 88 |
| 4.2.22 | Displacement of the gate during the generation of a dry bed surge. | 90 |
| 4.2.23 | Definition sketch showing the advantage of a laser-induced fluorescence (LIF) flow visualization system relative to a conventional system for the measurement of turbulent bore profiles. | 91 |
| 4.2.24 | Schematic of the optical components used in the laser induced fluorescence system. | 93 |
| 4.2.25 | Photo of the carriage used to support the LIF transmitting optics. | 94 |
| 4.2.26 | Definition sketch of the solitary wave experiments in the horizontal tank. | 97 |
| 4.2.27 | Definition sketch of the bore and dry-bed surge experiments in the horizontal tank using the dam-break method of wave generation. | 100 |
| 5.1.1 | Schematic drawing of the tilting wave tank experiment where (a) a solitary wave was produced on a sloping beach, broke as a plunging breaker and arrived at the vertical wall as a turbulent bore; (b) and (c) show details near the wall. | 104 |

| <u>Number</u> | <u>Description</u> | <u>Page</u> |
|---------------|-------------------------------------------------------------------------------------------------------------------------------------------------------------------------------------------------------------------------------------------------------------------------------------------------------------------------------------------------------------------|-------------|
| 5.1.2 | (a) Profile of a bore with a wave height of 4.59 cm which has just reached the vertical wall; (b) a subsequent bore profile during runup on the wall; (c) composite bore profile from the profiles shown in (a) and (b) (run no. TB109). | 107 |
| 5.1.3 | Relative celerity of the bores normalized using (a) the depth at the wall, h_w , (b) the effective depth, h , three horizontal length scales behind the tip of the bore (run no.'s TB108 through TB119). | 109 |
| 5.1.4 | (a) through (f) measured and average bore profiles at the instant the bore tip meets the vertical wall; (g) averaged bore profiles from (a) through (f) (run no.'s TB108 through TB119). | 111 |
| 5.1.5 | Relative horizontal water particle velocity along the bore surface at the moment the bore tip reaches the wall (run no.'s TB108 through TB119). The half filled symbols show measurements obtained after the bore reached the wall. | 112 |
| 5.1.6 | Impact of a bore on the vertical wall due to an incident solitary wave with $H_0/h_0 = 0.044$, as recorded with the movie camera; the maximum runup and force occurred at $t - t_i = 0.241$ sec and 0.322 sec, respectively (run no. TB119). | 114 |
| 5.1.7 | Effect of the gap width along the bottom of the instrumented wall on the measured force. | 115 |
| 5.1.8 | Relative force and water surface profiles at selected non-dimensional times for a 2.2 cm high bore generated from a solitary wave with $H_0/h_0 = 0.044$ (run no. TB119). | 116 |
| 5.1.9 | Relative force and water surface profiles at selected non-dimensional times for a 4.71 cm high bore generated from a solitary wave with $H_0/h_0 = 0.288$ (run no. TB108). | 118 |
| 5.1.10 | Non-dimensional plots comparing the measured force (F) to (a) the hydrostatic force (F_R) computed from the runup height on the vertical wall; (b) with expanded time scale (run no.'s TB94, TB96, TB98, TB100, TB102, and TB104); (c) normalized theoretical force from Equation 5.1.4 and 2.4 (run no.'s TB109, TB111, TB112, TB114, TB116, and TB119). | 120 |

| <u>Number</u> | <u>Description</u> | <u>Page</u> |
|---------------|------------------------------------------------------------------------------------------------------------------------------------------------------------------------------------------------------------------------------------------------------------------------------------------------------------------------------------------------------------------------------------------------------------|-------------|
| 5.1.11 | The (o) measured runup, R , and fourth order polynomial curves fitted to data points near (—) maximum runup and (----) maximum measured force (run no.'s TB94, TB96, TB98, TB100, TB102, and TB104). | 123 |
| 5.1.12 | Variation with respect to the relative incident bore height of (a) the maximum measured wave slope; the maximum measured runup normalized by (b) twice the incident wave height and (c) the velocity head computed from the bore celerity; and the maximum measured force normalized by (d) the linear force scale, F_l ; (e) the hydrostatic force computed from the maximum runup on the wall, F_R . | 127 |
| 5.2.1 | Times of solitary wave arrival at the celerity probes for a solitary wave of $H/h = 0.504$ which was propagating on a depth of $h = 17.74$ cm (run no. HW37). | 130 |
| 5.2.2 | Relative celerity of solitary waves near the wave generator ($x/h = 107.6$) and near the vertical wall ($x/h = 12.5$). | 131 |
| 5.2.3 | Comparison of theoretical and experimental solitary wave profiles for waves traveling on depths, h , of (a) 17.74 cm (run no. HW36) and (b) 17.71 cm (run no. HW42). | 133 |
| 5.2.4 | A comparison of water surface time histories at $x/h = 1.37$ using the LIF system and a wave gage for two identical experiments (a) (run no. HW45) and (b) (run no. HW46) with $H/h = 0.42$; both LIF time histories from (a) and (b) are shown in (c). | 135 |
| 5.2.5 | Profiles of a solitary wave with $H/h = 0.504$ running up the vertical wall as obtained from the laser induced fluorescence system (run no. HW37). | 136 |
| 5.2.6 | Plot of the measured runup time histories caused by solitary waves for various relative wave heights (run no.'s HW36, HW37, HW40, HW42, and HW44). | 137 |

| <u>Number</u> | <u>Description</u> | <u>Page</u> |
|---------------|----------------------------------------------------------------------------------------------------------------------------------------------------------------------------------------------------------------------------|-------------|
| 5.2.7 | Comparison of experimental and theoretical water surface time histories 12.4 water depths in front of the vertical wall due to a solitary wave with $H/h = 0.504$ (run no. HW37). | 138 |
| 5.2.8 | Comparison of experimental and theoretical time histories of the (a) runup; (b) force; (c) moment; and (d) pressure due to a solitary wave with $H/h = 0.504$ (run no. HW37). | 139 |
| 5.2.9 | Comparison of the maximum experimental and theoretical (a) forces and (b) moments on a vertical wall due to the reflection of solitary waves. | 144 |
| 5.2.10 | The forces on a vertical wall calculated using the BEM for a solitary wave with $H/h = 0.504$. | 145 |
| 5.3.1 | Experimental and theoretical celerity of the undular and turbulent bores as a function of the relative wave heights. | 147 |
| 5.3.2 | Photo taken from the video image of a turbulent bore with a relative wave height of $H/h = 0.81$ and an ambient depth, h , of 10.26 cm (run no. HB66). | 149 |
| 5.3.3 | Experimental profiles of a bore ($H/h = 6.23$, $h = 1.43$ cm) at several times before and during reflection on the vertical wall (run no. HB64). | 150 |
| 5.3.4 | (a) Composite wave profile which includes the profiles shown in Figure 5.3.3; (b) the averaged profile. | 152 |
| 5.3.5 | Several composite wave profiles showing the variation of the maximum wave slope as a function of the relative wave height (run no.'s HB68, HB84, HB83, HB79, and HB72). | 154 |
| 5.3.6 | Experimental force time histories measured during the impact of the bores shown in Figure 5.3.5. | 156 |
| 5.3.7 | (a) Incident bore profile where $H/h = 7.9$ and $h = 1.1$ cm; (b) the pressure and runup time histories; (c) experimental and theoretical force time histories; (d) the pressure on an expanded time scale (run no. HB91). | 160 |

| <u>Number</u> | <u>Description</u> | <u>Page</u> |
|---------------|------------------------------------------------------------------------------------------------------------------------------------------------------------------------------------------------------------------------------------------------------|-------------|
| 5.3.8 | Comparison of experimental and theoretical (a) bore profiles and (b) force time histories for a bore with $H/h = 0.64$ and $h = 11.94$ cm (run no. HB67). | 162 |
| 5.3.9 | Comparison of experimental and theoretical (a) bore profiles and (b) force time histories for a bore with $H/h = 0.81$ and $h = 10.26$ cm (run no. HB66). | 165 |
| 5.3.10 | Comparison between bores with $H/h = 2.65$ in the horizontal tank (run no. HB63) and the tilting tank for (a) the incident bore profiles (run no. TB111); (b) the runup (run no. TB96); and (c) force time histories (run no. TB111). | 166 |
| 5.4.1 | Comparison between experimental and theoretical propagation of a dry-bed surge for various reservoir depths, h_r ; (a) $h_r = 15.28$ cm; (b) $h_r = 30.17$ cm; (c) $h_r = 50.20$ cm; and (d) definition sketch (run no.'s HS86, HS102, and HS103). | 169 |
| 5.4.2 | Definition sketch of the control volume for the tip of the surge. | 172 |
| 5.4.3 | Theoretical and experimental surge profiles for various reservoir depths, h_r ; (a) $h_r = 15.28$ cm; (b) $h_r = 30.17$ cm; and (c) $h_r = 50.20$ cm (run no.'s HS86, HS102, and HS103). | 175 |
| 5.4.4 | Experimental and theoretical (a) surge profile and (b) wave propagation down the tank where the friction term yielding the best fit to the experimental profile was used for a reservoir depth of $h_r = 15.28$ cm (run no. HS102). | 177 |
| 5.4.5 | Experimental and theoretical (a) surge profile and (b) wave propagation down the tank where the friction term yielding the best fit to the experimental profile was used for a reservoir depth of $h_r = 30.17$ cm (run no. HS103). | 178 |
| 5.4.6 | Experimental and theoretical (a) surge profile and (b) wave propagation down the tank where the friction term yielding the best fit to the experimental profile was used for a reservoir depth of $h_r = 50.20$ cm (run no. HS86). | 179 |

| <u>Number</u> | <u>Description</u> | <u>Page</u> |
|---------------|---------------------------------------------------------------------------------------------------------------------------------------------------------------------------------------------------------------------------------------|-------------|
| 5.4.7 | Experimental and theoretical surge profiles for reservoir depths of $h_r = 15.28$ cm, $h_r = 30.17$ cm, and $h_r = 50.20$ cm (run no.'s HS86, HS102, and HS103). | 180 |
| 5.4.8 | (a) Experimental pressure and runup time histories; (b) experimental and theoretical force time histories for a surge created with a 15.28 cm reservoir depth (run no. HS102). | 181 |
| 5.4.9 | Experimental and theoretical force time histories for a surge created with a 30.17 cm reservoir depth (run no. HS103). | 182 |
| 5.4.10 | (a) Experimental pressure and runup time histories; (b) experimental and theoretical force time histories; (c) experimental runup time history on a reduced abscissa caused by a surge from a 50.20 cm deep reservoir (run no. HS86). | 183 |
| 5.4.11 | Comparison of the experimental (a) wave profile; (b) runup; (c) pressure head; and (d) force due to a strong turbulent bore and a dry bed surge with approximately the same celerity (run no.'s HS86 and HB87). | 187 |
| 5.5.1 | Experimental and theoretical wave celerities for all the experiments conducted during this study. | 190 |
| 5.5.2 | Experimental and theoretical (a) maximum water surface slopes; (b) runup normalized by twice the incident wave height; and (c) runup normalized by twice the velocity head due to the wave celerity. | 196 |
| 5.5.3 | Maximum experimental pressures as a function of the relative vertical position on the wall for various relative wave heights. | 199 |
| 5.5.4 | Experimental and theoretical maximum force on the wall normalized by (a) the hydrostatic force due to a runup equal to twice the incident wave height; (b) the hydrostatic force due to the maximum runup. | 203 |
| 5.5.5 | Experimental and theoretical maximum moment on the wall normalized by (a) the hydrostatic moment due to a runup equal to twice the incident wave height; (b) the hydrostatic moment due to the maximum runup. | 206 |

| <u>Number</u> | <u>Description</u> | <u>Page</u> |
|---------------|--------------------------------------------------------------------------------------------------------------------------------------------------------------|-------------|
| 5.6.1 | Schematic drawing for the impact of the 1960 Chilean tsunami on a vertical wall at Hilo, Hawaii. | 208 |
| B.1 | Distorted view of the control points in the wave tank as seen with the video camera. | 237 |
| B.2 | Definition sketch of the image plane in the video camera and the plane in the center of the wave tank where the air-water surface is located. | 238 |
| B.3 | Schematic of the camera orientation as seen from above the wave tank. | 239 |
| B.4 | Definition sketch showing the relationship between distances in the video image and the plane in the wave tank for an oblique camera orientation. | 240 |
| B.5 | Comparison of control point locations in the wave tank with locations computed from the video image (as seen in Figure B.1) using a cubic calibration model. | 244 |
| B.6 | Image of the still water surface computed from the video image using a (a) linear, (b) parabolic, and (c) cubic two-dimensional polynomial approximation. | 245 |
| C.1 | Photo of the device used to measure the air-water surface tension. | 249 |
| C.2 | Schematic of the surface tension meter. | 249 |

LIST OF TABLES

| <u>Number</u> | <u>Description</u> | <u>Page</u> |
|---------------|--------------------------------------------------------------------------------------------------------------------------------------------------------------------------------------|-------------|
| 4.1 | Measured characteristics of the force transducers. | 52 |
| 4.2 | Measured and calculated (using a least squares analysis) vertical locations of the force transducers above the bottom of the tank. | 75 |
| 5.1.1 | Variation of the relative acceleration of the water surface at wall (computed from the polynomial curves shown in Figure 5.1.11) with the relative incident wave height, H_o/h_o . | 124 |
| 5.5.1 | Maximum measured pressure heads obtained during this study which were greater than the runup height on-the wall. | 199 |

LIST OF SYMBOLS

| | |
|-------|-----------------------------------------------------------------------------------------------------------------------------------|
| A | volume of fluid function |
| b | effective width of instrumented wall [$b=4.97$ cm] (tilting tank experiments); [$b=6.04$ cm] (horizontal wave tank experiments) |
| C_F | theoretical force coefficient |
| C_f | coefficient of skin-friction drag force along one side of a flat plate |
| c | bore celerity |
| d | distance behind the tip of a dry-bed surge |
| E | spectral energy of the measured force |
| E_t | total spectral energy of the measured force |
| F | force on the wall |
| F_l | linear force scale $\left[F_l = \frac{1}{2} \gamma b (2H + h_w)^2 \right]$ |
| F_R | runup force scale $\left[F_R = \frac{1}{2} \gamma b (R + h_w)^2 \right]$ |
| f | friction factor |
| G | two-dimensional Green's function |
| g | acceleration due to gravity |
| H | wave height |
| H_o | initial wave height (tilting wave tank experiments) |
| H_b | breaking wave height (tilting wave tank experiments) |
| h | water depth in front of the instrumented wall (horizontal wave tank experiments), effective depth (tilting wave tank experiments) |

| | |
|-------------|-----------------------------------------------------------------------------------------------------------------------------------------------|
| h_b | water depth at the wave breaking location (tilting wave tank experiments) |
| h_{mk} | product of the shape function $N_m(\zeta)$ and the Jacobian $J_k(\zeta)$ |
| h_r | reservoir depth (horizontal wave tank; dam-break experiments) |
| h_o | water depth at location of initial wave height measurement [$h_o=42.8$ cm] |
| h_w | water depth in front of the instrumented wall [$h_w=0.5$ cm] (tilting wave tank experiments); [$h_w=h$] (horizontal wave tank experiments) |
| I_{ijk}^d | boundary integral term involving $\phi \frac{\partial G}{\partial n}$ |
| I_{ijk}^n | boundary integral term involving $\frac{\partial \phi}{\partial n} G$ |
| K_{jm}^d | matrix representing the integrals of $\phi \frac{\partial G}{\partial n}$ along boundaries with known ϕ |
| K_{jm}^n | matrix representing the integrals of $G \frac{\partial \phi}{\partial n}$ along boundaries with known $\nabla \phi \cdot \mathbf{n}$ |
| l | horizontal length scale $\left[l = \frac{H}{\ d\eta/dx\ } \right]$ |
| M | moment on the wall |
| M_d | number of nodes at which ϕ is known (Dirichlet boundary condition) |
| M_l | linear moment scale $\left[M_l = \frac{1}{6} \gamma b (2H + h_w)^3 \right]$ |
| M_n | number of nodes where $\nabla \phi \cdot \mathbf{n}$ is known (Neuman boundary condition) |
| M_R | runup moment scale $\left[M_R = \frac{1}{6} \gamma b (R + h_w)^3 \right]$ |
| N | shape function |

| | |
|-----------|--------------------------------------------------------------------------------------------------------------------------------|
| n | unit vector normal to a boundary surface |
| p | pressure |
| p_a | atmospheric pressure |
| R | runup on the wall |
| r | position vector of a free surface fluid particle |
| S | beach slope |
| S_p | stroke of the piston wave maker |
| s | arc length along the free surface |
| s | unit vector tangential to the free surface |
| t | time |
| t_H | time of last video image or high-speed movie frame before the wave causes a change in the water depth at the instrumented wall |
| $t_{H/2}$ | time when the position of a wave, corresponding to $\eta = H/2$, would reach the wall if the wall were not there |
| t_i | time when the front of a bore or a dry-bed surge reaches the wall |
| t_s | time when the crest of a solitary wave would be at the wall if the wall were not present (horizontal wave tank experiments) |
| U | velocity of a boundary such as a wave generator |
| u | horizontal water particle velocity |
| u_1 | horizontal water particle velocity at the shallow side of a stationary hydraulic jump |
| u_2 | horizontal water particle velocity at the deep side of a stationary hydraulic jump |
| u_η | horizontal water particle velocity at the water surface |

| | |
|---------------|--------------------------------------------------------------------------------------------------------------|
| w | vertical water particle velocity |
| x | horizontal Cartesian coordinate coincident with the longitudinal axis of the wave tank |
| x_b | horizontal position where wave breaking occurs (tilting wave tank experiments) |
| x_g | location of pneumatic gate for bore experiments (horizontal wave tank experiments) |
| x_H | horizontal position where $\eta = H / 2$ at time, t_H |
| x_p | location of the piston wave generator prior to wave generation |
| x_v | horizontal Cartesian coordinate in the video image |
| x_w | location of the instrumented wall [$x_w=25.0$ cm] (tilting wave tank experiments) |
| y | horizontal Cartesian coordinate in the transverse direction of the wave tank |
| z | vertical Cartesian coordinate |
| z_p | elevation of the pressure transducer above the still water level (or the tank bottom for the dry-bed surges) |
| z_v | vertical Cartesian coordinate in the video image |
| α | the interior angle μ divided by 2π (i.e., $\mu/2\pi$) |
| β | counter clockwise angle from the x axis to the s axis |
| δ_1 | gap between the instrumented wall and the false walls |
| δ_2 | gap between the instrumented wall and the tank bottom |
| δ_{ij} | Kronecker delta function |
| ϕ | velocity potential |

| | |
|-------------|-------------------------------------------------------------------------------------------------------|
| Γ_b | bottom boundary |
| Γ_d | boundary along which ϕ is specified |
| Γ_l | left lateral boundary |
| Γ_n | boundary along which $\nabla\phi \cdot \mathbf{n}$ is specified |
| Γ_r | right lateral boundary |
| γ | weight of water per unit volume |
| η | height of free surface above the still water level |
| Λ | diagonal matrix where $\Lambda_{ij} = \alpha(\mathbf{x}_i)$ |
| μ | interior angle along the perimeter of Θ |
| ρ | mass of water per unit volume |
| $\Theta(t)$ | two-dimensional fluid domain |
| θ | angle between the tangent to the free surface and the x axis |
| τ | shear stress |
| ν | kinematic viscosity of the fluid |
| ξ | coordinate along the free surface which increases by a value of one, from one nodal point to the next |
| ζ | shape function coordinate |

Operators

| | |
|----------|---------------------------------------------------|
| $ $ | magnitude of a vector (i.e., $r = \mathbf{r} $) |
| $\ \ $ | denotes maximum value |
| ∇ | gradient vector operator |

$\partial(\)/\partial t,$ denotes partial differentiation with respect to the indicated independent
 $\partial(\)/\partial x$ variable

$D(\)/Dt$ total derivative $\left(\frac{\partial(\)}{\partial t} + u \frac{\partial(\)}{\partial x} + w \frac{\partial(\)}{\partial z} \right)$ in two dimensions

$J(\)$ Jacobian operator

1. INTRODUCTION

Tsunamis are waves produced by motions of the earth's crust. This motion may be caused by underwater landslides, volcanic activity such as an explosion, or more commonly an earthquake. Tsunamis have a long history of causing tremendous damage and loss of life along low-lying coastal areas around the world. One of the most destructive tsunamis in relation to loss of life was generated by the eruption of volcano Karakatoa in Indonesia on August 27, 1883. A 30 m high tsunami was generated which killed approximately 36,000 people.

Tsunami activity in the Pacific basin is particularly severe due to numerous subduction zones located around its rim. Japan suffered the loss of over 27,000 people and the destruction of more than 10,000 buildings due to a tsunami along the Sanriku coast on June 15, 1896. The tsunami generated by the 1964 Alaskan earthquake on March 28 caused a total of 119 deaths and \$110,000,000 in damage along the Alaskan coast, the Hawaiian coast, and the western coast of the United States. Most recently, in September 1992, a near shore earthquake of magnitude 7.0 offshore of Nicaragua generated a tsunami that inundated large areas causing significant loss of life and property. One of the most dramatic documented cases of tsunami runup occurred in Lituya Bay, Alaska in 1958 where a landslide-generated tsunami leveled trees up to 525 m above the original water level and produced a 50 m high wave in the bay.

When earthquakes produce vertical motions of the earth's crust under the ocean a tsunami is produced from the resulting localized rise or depression in the water surface which then radiates from the source region in all directions. Although the amplitude of a tsunami tends to be very small in the ocean (less than one meter), it can have a large volume of fluid in motion due to its long wavelength (on the order of one hundred to

several hundred kilometers). When a tsunami propagates from the open ocean toward the shoreline its wavelength decreases due to shoaling leading to an increase in the wave height. In some cases very large breaking waves (on the order of 10 m to 30 m) may develop which propagate toward the shoreline as a strong turbulent bore. There are numerous eye-witness accounts and photographic records indicating tsunami waves can reach the shore as strong turbulent bores. These bores can pass the shoreline and continue onshore as high speed surges propagating over a dry bed with a celerity of the order of tens of meters per second and a wave height of the order of several meters. A tsunami may also inundate a coastal area as a relatively mild flood wave without the generation of high velocity flows. The type of wave obtained at the shoreline is a function of the incident tsunami as well as the local bathymetry and the tidal level. Local bathymetry can cause effects such as wave resonance in near shore regions or harbors, and wave focusing on headlands and in gradually narrowing estuaries with steep sidewalls.

The evidence for high speed onshore flows due to tsunami waves can be found in several documented structural failures, eyewitness accounts, and photographic records. For some of these structural failures, the evidence suggests the damage was caused by the force of the flow itself as opposed to the impact of floating debris. Matlock, Reese, and Matlock (1962) reported 14 such cases of structural failures in Hilo, Hawaii due to the tsunami caused by the 1960 Chilean earthquake. Based on the strength of the structural members and an assumption that the loading on the structure was equivalent to a hydrodynamic drag force, they were able to estimate the fluid velocities needed to produce such failures. Their estimated velocities ranged up to a maximum value of 16 m/sec. This can be compared with the observations of Eaton, Richter, and Ault (1961) where they reported the bore traveled from the breakwater to the shore of Hilo (about 2,100 m) within 2.5 to 3 minutes. The speed of the bore between the breakwater and the

shoreline would have been between 12 m/s and 14 m/s which agrees quite well with the highest velocity estimates of 16 m/sec obtained by Matlock, Reese, and Matlock(1962). In Seward, Alaska, an isolated 115 ton locomotive resting on tracks 5.8 meters above mean lower low-water was overturned and displaced several tens of meters shoreward due to the passage of a tsunami wave caused by the 1964 Alaskan earthquake. Wilson and Torum (1968) provide an analysis where they calculated the speed of the fluid to have been at least 8 m/sec to capsized the locomotive. They assumed the wave was 1.8 meters higher than the tracks, which corresponded to maximum measured runup heights shoreward of this region.

There have been numerous studies of the generation and propagation of tsunamis across the ocean. Likewise, there have been a considerable number of laboratory experiments and analytical models developed to simulate the behavior of tsunami waves as they inundate the shoreline. The study of terminal effects of tsunamis have been primarily limited to the observation of tsunami damage to coastal areas including structural damage, high water marks in the region, scour, and deposition of both sediments and floating debris. There have been few laboratory and theoretical studies of the hydrodynamic loads imposed on structures by the impact of tsunamis. In this study, several questions about the structural loading due to the impact of tsunamis are addressed.

1.1 Objectives and Scope

The objective of this study was to investigate experimentally and theoretically the interaction of long waves, bores, and surges on a dry bed with a vertical wall. This study is focused on the impact of translatory waves with a vertical wall in contrast with the large body of literature concerning breaking wave pressures on walls. Several different

types of waves were used in this study, including waves generated in a tilting tank and a horizontal fixed bed tank.

Most of the experiments were performed in a horizontal tank where solitary waves, bores, and surges on a dry bed were produced. For all of the experiments in the horizontal tank, the incident wave profile, the celerity, and the force, moment, and runup histories on the wall were measured along with pressures at selected elevations.

The impact of a turbulent bore on a wall was also investigated in a tilting wave tank with a bottom slope of 0.02 m/m. The bores were produced by shoaling a solitary wave which produced a plunging breaker. This broken wave propagated toward the shoreline as a turbulent bore and was reflected by a vertical wall which was located slightly offshore. The experiments in the tilting wave tank were performed to determine if bores traveling over mild slopes produce the same loading on a vertical wall as a bore of equal relative wave height traveling over a horizontal bottom. This appears to be the first study to investigate the impact on a vertical wall of well developed bores that were generated from breaking solitary waves.

Two theoretical models were used to simulate the impact process. The first model was based on the boundary integral element method (BIEM) where the Euler Equations and the full nonlinear free surface boundary conditions were used following the work of Grilli, Skourup, and Svendsen (1989). This model assumes irrotational flow with a simply-connected fluid domain. The second model solves the Navier-Stokes Equations with a finite-difference algorithm where the free surface is modeled with the volume of fluid algorithm (VOF) which will be described in Chapter 3. Previous investigators (Nichols, Hirt, and Hotchkiss (1980)) have shown that this approach can produce bore profiles which agree qualitatively with experimental bore profiles. This

approach provides a more physically realistic theory than has previously been used to model the impact of bores on a wall, since it accounts for vertical variations in the flow quantities. This finite-difference method not only provides a reasonable bore shape but also includes the strong local vertical accelerations along the wall which are shown to be important during the reflection process.

2. LITERATURE REVIEW

The subject of this work is the terminal effects of tsunamis on structures and in particular, the impact of wave forms on a vertical wall. Thus, attention in this literature review will be focused on the impact and reflection of bores, solitary waves, and surges on a dry bed at a vertical wall. There is a considerable volume of literature concerning the propagation of these three types of waves. To present a comprehensive literature survey of all relevant works in these three areas of wave propagation would be impractical. Therefore, only selected works directly related to this study will be mentioned in this review. For more detailed literature reviews on the subject of solitary waves, breaking waves, surf-zone dynamics, and wave runup consult Miles (1980), Peregrine (1983), Battjes (1988), and Zelt (1991).

Likewise, there is a large body of literature on wave impacts on structures where the wave develops a very steep face just prior to impact. These studies include many types of incident waves and structures along with a corresponding number of proposed models. This work will not be reviewed here. For reviews on this subject consult Wiegel (1964), Silvester (1974), Horikawa (1978), and the Shore Protection Manual (1984). The direction of more recent work in the area of breaking waves on structures can be found in the field work of Blackmore and Hewson (1984), the experimental work of Chan and Melville (1988), and the theoretical work of Cooker and Peregrine (1990). For information on tsunami wave generation, propagation, runup, and damage see the reviews by Wiegel(1970), Wilson and Torum (1972) and Camfield (1980).

2.1 Dam-Break Flows

A theoretical description of the two-dimensional dam break problem for an inviscid fluid was originally obtained by Ritter (1892) for a dry bed. The resulting water

surface profile is parabolic and concave upward. A negative wave propagates upstream into the reservoir with the shallow water wave celerity $c = \sqrt{gh_r}$ where c is the wave celerity, g is the gravitational acceleration, and h_r is the reservoir depth. The tip travels downstream across the dry bed with $c = 2\sqrt{gh_r}$. Dressler (1952) and Whitham (1955) independently developed an analysis to obtain the first order correction to the tip speed due to the effect of bottom friction. Whitham (1955) compared the tip speed from both theories showing they both approach the Ritter solution for small non-dimensional times. Both theories agreed within 12% over the entire range of non-dimensional times shown. Whitham argued that near the tip of the surge where the water surface slope is steep and the depth becomes small, the friction term and the pressure gradient terms in the horizontal momentum equation should be approximately equal. The pressure gradient term is proportional to the slope of the water surface profile, while the friction term is inversely proportional to the local water depth. Noting that the acceleration terms would remain finite, Whitham (1955) reasoned that the friction and the pressure gradient terms must balance each other as they become large near the tip of the surge. Neglecting the acceleration terms in the equation of motion, while using a friction model which is quadratic in the flow velocity results in a parabolic water surface profile for the surge tip which is concave downward. This profile asymptotically approaches a vertical face near the tip of the surge and tends to a very mild slope far behind the front of the surge.

Cross (1967) included the effects of local acceleration, the bottom slope, the pressure gradient, and the friction loss along the bed to obtain an expression for the profile of a surge tip. In the case where the terms corresponding to the local acceleration and bottom slope either cancel or are both zero, his solution reduces to the parabolic profile presented by Whitham (1955). Wang and Ansari (1986) presented a model for the flow in a surge where the velocity field was approximated with a power law. They computed the pressure field with a finite element solution of Poisson's equation where an

eddy viscosity turbulence model and an experimentally determined head loss distribution along the water surface were used to obtain a closed solution. Their model indicated the pressure distribution in the tip region was less than hydrostatic. The computed surge profiles agreed quite well with both the height and shape of the experimentally obtained profiles behind the tip region. However, there were significant discrepancies between the model and the experiments with respect to both the location of the surge tip and the shape of the profile in the region very close to the tip. Fujima and Shuto (1990) investigated the velocity field in a stationary surge front produced using a flume with a bottom composed of an inclined moving belt. A laser Doppler velocimeter was used to measure the mean velocity field and the Reynolds stresses. For a belt velocity of 184 cm/sec, their results indicated the boundary layer was turbulent for distances greater than 4 cm behind the surge tip. They concluded that the friction law for uniform flow over a flat plate (Schlichting (1979)) can be used to model the energy loss in the boundary layer near the tip of a surge on a dry bed. A more detailed review can be found in the report of Wang and Ansari (1986).

2.2 Hydrodynamic Loading on a Vertical Wall Due to Tsunami Impact

Cumberbatch (1960) presented a similarity solution for the impact of a two-dimensional fluid wedge on a flat impermeable surface. The incident wedge is oriented with its axis perpendicular to the wall. He assumed a constant wedge angle before impact, an inviscid fluid, and irrotational flow where the velocities throughout the wedge before impact are equal to the constant approach velocity. He used a no-flux boundary condition at the wall and the full nonlinear free surface boundary conditions. Since gravity was neglected in the problem formulation, Cumberbatch indicated the theory was intended to model the dynamics soon after impact, before the gravitational acceleration begins affecting the flow along the wall. Water surface profiles and pressure distributions along the wall were presented for wedge angles of 22.2 degrees and 45

degrees. Cumberbatch defined a force coefficient which relates the force on the wall to the momentum flux which would occur at the wall location if the wall were not present, as follows:

$$F = C_F \rho b \eta c^2, \quad (2.1)$$

where C_F is the force coefficient which was shown to be a function only of the incident wedge angle, θ , ρ is the density of the fluid, b is the width of the wall, η is the water surface profile at the wall location, and c is the celerity of the incident fluid wedge which is equal to the fluid particle velocity throughout the flow. For wedge angles of 22.5 degrees and 45 degrees, Cumberbatch found C_F to be 1.6 and 2.4, respectively.

Fukui, Nakamura, Shiraishi, and Sasaki (1963) measured the pressures generated on walls due to the reflection of bores. The bores were generated by suddenly releasing a reservoir of water using the dam-break method. The incident bore profile, the bore celerity, the pressures at three vertical stations along the wall, and the runup height were measured. They varied the slope of the wall from 34° to 90° and the incident bores ranged in relative wave height from $H/h \cong 0.5$ to $H/h \cong 3.0$, where H is the wave height of the incident bore above the still water surface and h is the still water depth. They used ambient depth ranging from $h=5$ cm to $h=20$ cm and obtained bores with celerities ranging from 120 cm/sec to 220 cm/sec. They also performed a limited number of tests in a large scale tank where they obtained bores with celerities ranging from 2.20 m/sec to 3.50 m/sec.

Fukui et al. (1963) differentiated between what they called the "impulsive" pressure which is obtained soon after the bore strikes the wall and the "continuous" pressure which corresponds to the hydrostatic pressure at the wall once the reflected bore

has propagated away from the wall. They proposed that the impulsive pressure scales as the fourth power of the incident wave celerity. This conclusion was reached by fitting a line through the impulsive pressure data which were plotted against the bore celerity. However, the impulsive pressure measurements varied in some cases by $\pm 70\%$ relative to the median value at a given wave celerity. Their expression for the maximum impulsive pressure, p , was;

$$p = K_o \frac{c^2}{gh} \rho c^2, \quad (2.2)$$

where K_o is an experimentally determined constant which was equal to 0.5 for their vertical wall experiments. They also proposed a linear relationship between the impulsive pressures and the depth along the wall. From the experimental results they concluded the maximum runup height was equal to 3.3 times the velocity head computed from the incident bore celerity.

Cross (1966, 1967) investigated the properties of incident surges propagating over smooth and roughened bottoms and the forces caused by their impact on a vertical wall. He generated bores using the dam-break method in a tank which had a negative slope of 0.002 in the direction of wave propagation. Expressions were derived for the surface height and slope of the surge, while the similarity solution of Cumberbatch was applied to calculate the forces on the wall. Cross (1967) included the force due to the hydrostatic pressure from the surge depth at the wall. He proposed the following expression for the force time history, $F(t)$, on the wall:

$$F(t) = \frac{1}{2} \gamma b \eta(t)^2 + \rho C_F(t) b \eta(t) c^2, \quad (2.3)$$

where γ is the weight of water per unit volume, $\eta(t)$ = the water surface time history which would occur at the wall if the wall were not there, c = the surge celerity, and b = the width of the wall. Cross (1967) computed the force coefficient, C_F , numerically using the analysis of Cumberbatch (1960) for wedge angles, θ , between 0° and 72° and found the following relation agreed with his results:

$$C_F = 1 + (\tan \theta)^{1.2}. \quad (2.4)$$

Cross (1967) proposed using the surge profile near the wall while assuming it would pass the wall with a nearly steady shape when viewed from a frame of reference moving with the surge tip. With this assumption both the water surface slope and the force coefficient in Equation 2.4 are functions of time at the wall location. Combining the result of Equation 2.4 with the water surface profile at the wall, η , and the celerity of the surge, c , the force time history in Equation 2.3 can be computed.

The experimental results of Cross (1967) exhibit a sharp peak in the force coinciding with the occurrence of the maximum force. Based on experimental observations, Cross (1967) suggested that this peak occurred when the runup tongue collapsed onto the incoming surge forming the reflected bore. In addition, he found that early in the impact process, the forces computed from Equation 2.3 while using the measured incident surge profile and bore celerity predicted the measured forces quite well. However, as time progressed, the predicted forces tended to be less than the measured forces for the rough bottom cases and greater than the measured forces for the smooth bottom cases. Indeed, when the maximum measured force occurred for some cases (Cross (1966)), the measured force was up to 60% greater than that predicted. In

addition, Cross (1967) noted that the maximum run-up height on the wall varied from 1.3 to 2.2 times the velocity head computed from the incident surge speed.

Nakamura and Tsuchiya (1973) studied the pressures on composite structures caused by the impact of surges propagating over a horizontal bed. The surges were generated by the dam-break method with initial reservoir depths of 30 cm, 40 cm, and 50 cm. They measured large pressure heads of relatively short duration just after impact, followed by relatively constant pressures due to the nearly hydrostatic condition once the bore propagated away from the wall. The maximum measured pressure head they reported was 46 cm with a rise time of 50 msec which was obtained from a pressure cell located 2.5 cm off the bottom of the tank. This maximum pressure was only 50% larger than the maximum hydrostatic pressure developed on the wall (31 cm) which occurred approximately five seconds after the surge initially struck the wall. They reported velocity measurements significantly larger than the theoretical predictions of Whitham (1955) and Dressler (1952); in some cases the theory was only 30% of the measured value. The pressure-time histories measured just after impact were compared to the theory of Cumberbatch (1960), but the maximum measured pressures were up to 30% greater than those predicted.

Togashi (1986) investigated the runup of solitary waves on a mildly sloping composite beach and the impact and over-topping at a vertical wall located a large distance beyond the shoreline. The main focus of the study was the determination of conditions which produce over-topping of a vertical barrier of finite height and the hydrodynamic load produced on the barrier. Togashi (1986) proposed a method based on the time rate of change of momentum within a control volume to predict the resulting force on the barrier. This method qualitatively agreed with the experimental results for

the two cases shown. However, the experimental pressure measurements contained a noise level equal to approximately $\pm 50\%$ of the maximum "averaged" pressure.

There are numerous models for wave propagation and runup in which the vertical variation of the flow quantities is either approximated or averaged and the pressure distribution is assumed hydrostatic (see Zelt (1991) for a review). Since 1976, numerous models which make no approximations in the vertical variation of the flow quantities have been proposed. Longuet-Higgins and Cokelet (1976) developed a numerical boundary integral element algorithm to solve for the two-dimensional potential flow, subject to the full nonlinear free surface boundary conditions. A Lagrangian description of the free surface was used to advance the solution in time. They computed the overturning and jet formation in a periodic breaking wave on deep water. By making no approximations in the vertical variation of flow quantities (such as made in developing the depth-averaged equations), they were able to carry the simulation well beyond the development of a vertical face on the front of the wave. Unlike Longuet-Higgins and Cokelet (1976) whose model was formulated in a conformally-mapped domain, Vinje and Brevig (1981) presented a model in the physical domain where waves on a finite depth could be simulated. By formulating the problem in the physical domain, the model could accommodate non-periodic waves as well as structures placed in the flow field. Dold and Peregrine (1984) presented an accurate time-stepping method based on a Taylor expansion of the free surface boundary conditions with respect to time. The method is explicit and its accuracy allows much larger time steps than preceding methods. This dramatically reduces the computation time for a given simulation. Since the computational effort is primarily a function of the number of times the integrals around the boundary must be computed, the computation time decreases as the time step increases. Grilli, Skourup, and Svendsen (1989) presented a boundary element model which is formulated in the physical space and uses the time stepping algorithm of Dold

and Peregrine (1984). In a later work, Grilli and Svendsen (1991) applied this method to the reflection of steep solitary waves at a vertical wall, among numerous other examples. Fenton and Rienecker (1982) presented a Fourier series solution of the equations of motion. They applied their model to the reflection of solitary waves on a vertical wall and presented maximum forces and overturning moments. Grilli and Svendsen (1991) applied the third order solitary wave collision model of Su and Mirie (1980) to calculate the maximum force and overturning moment due to the reflection of a solitary wave at a vertical wall. They showed excellent agreement between the results from their boundary element model, the results of Fenton and Rienecker (1982), and the results from Su and Mirie (1980). For more detailed reviews on numerical methods applied to the simulation of highly nonlinear waves see Yeung (1982), Liggett and Liu (1984), and Grilli, Skourup, and Svendsen (1989).

In this work, a boundary element model similar to that reported in Grilli, Skourup, and Svendsen (1989) was developed. This model is experimentally verified for the reflection of steep solitary waves at a vertical wall where the pressure, force, moment, and runup on the wall, as well as the water surface profile in front of the wall were measured.

One limitation with the boundary integral element methods is the inability of the algorithms to handle fluid re-entry which produces multiple free surfaces or the generation of turbulence, both of which are inherent in the wave-breaking process. There are several early works where the nonlinear shallow-water equations were used to investigate the problem of bore propagation on slopes (Whitham (1958) and Keller et al. (1960)), and the resulting runup (Ho and Meyer (1962), Shen and Meyer (1963 a, b)). These models assume the bore is a discontinuity (shock) in the water surface profile and cannot be used to obtain any information on the water surface profile or velocity field

across the jump. Madsen and Svendsen (1983) and Svendsen and Madsen (1984) presented analyses where the turbulence production and dissipation across the bore were used to augment the shallow water equations for horizontal and sloping bottoms, respectively. During the impact of bores on a vertical wall, vertical accelerations along the wall were shown by Ramsden and Raichlen (1990) to significantly alter the resulting force-time history on the wall relative to a hydrostatic condition. Therefore, to accurately model the physics of bore impact on a vertical wall, a theory is needed which can model both the shear layer at the still water surface caused by a passing bore, and accounts for the shape and velocity field across the bore, as well as the vertical distribution of the flow variables during the impact process.

There have been several models for fluid flow where the Navier-Stokes equations are solved in Eulerian coordinates with finite-differences used to approximate the governing equations. In these models only the characteristic length scales of the flow on the order of the mesh spacing or larger are resolved. Harlow and Welsh (1965) developed the Marker-and-Cell method where marker particles distributed throughout the fluid were used to define the two-dimensional fluid region. The pressure and velocity components were used as the independent variables. The method was successfully applied to a variety of free surface flow problems. Chan and Street (1970) improved the treatment of the free surface pressure condition by applying it at the actual position of the free surface, as opposed to the center of the nearest cell as in the model of Harlow and Welsh (1965). They showed reasonable agreement between their model and experimentally determined runup heights of steep solitary waves on a vertical wall. Nichols, Hirt, and Hotchkiss (1980) presented a model, "SOLA-VOF," where the free surface of the fluid is modeled with a fractional volume of fluid (VOF) algorithm. In this method, a variable is defined which is equal to unity in a filled computational cell, zero in an empty cell, and lies between zero and unity for a partially full cell. They

demonstrated the use of the model to simulate numerous flow problems including the development of a turbulent bore. Torrey, et al. (1985) improved the model to more accurately treat surface tension and wall adhesion effects for the simulation of fluid reorientation problems in liquid fuel tanks. Heinrich (1992) applied the model of Torrey et al. (1985) to the generation and propagation of laboratory simulations of landslide generated waves. In some cases the initial wave motion in the laboratory resulted in wave breaking which was also predicted by the theoretical model. The theoretical model was able to continue the simulation past the time of breaking to model the propagation of the waves out of the generation region. For more detailed reviews see the series of reports by Hirt, Nichols, and Romero (1975), Nichols, Hirt, and Hotchkiss (1980), and Torrey et al. (1985). In this study the experimental results for bores are compared with the model reported in Nichols, Hirt, and Hotchkiss (1980).

This study addresses several issues which are not resolved in the current literature concerning the loading imposed on vertical walls due to the impact of tsunami waves. There is no indication of the forces one should expect on a vertical wall due to the impact of bores as a function of the incident bore strength. Although the work of Fukui et al. (1963) contains pressure measurements for a significant range of incident bore strengths, neither the number of pressure cells used nor the way in which the results were presented allow an accurate determination of the forces and overturning moments to be expected for the impact of a turbulent bore of a given strength. In this study, experimentally determined pressures, forces, moments, and runup histories on a vertical wall for a wide range of incident bore conditions are presented. There also seem to be no physical measurements indicating the effect of a small bottom slope on the hydrodynamic loads imposed on a vertical wall due to the impact of a turbulent bore. In this study the force and runup history on a vertical wall are presented for bores with equal relative wave heights propagating over a horizontal slope and a mild slope of 0.02 m/m. This appears

to be the first study where experimentally determined pressure, force, moment, and runup histories have been used to verify the finite difference hydrodynamic model of Nichols, Hirt, and Hotchkiss (1980) for the impact of bores on a vertical wall, and a boundary integral element model similar to that of Grilli and Svendsen (1989) for the reflection of solitary waves (propagating on a horizontal bottom) from a vertical wall.

3. THEORETICAL MODELING

In this chapter, the two numerical models which were compared with the experimental results of this study are discussed. In Section 3.1, a boundary integral element method similar to that presented in Grilli et al. (1989) will be discussed. This numerical approach solves the potential flow problem in two dimensions subject to the full nonlinear free surface boundary conditions. The application of this theory to the reflection of solitary waves by a vertical wall will also be discussed. In Section 3.2, the finite difference model, "SOLA-VOF," of Nichols, Hirt, and Hotchkiss (1980) is briefly described along with the methods used to compare this model to the experimental results of this study.

3.1 Boundary Integral Element Model

To simulate highly nonlinear wave reflections on structures, a numerical boundary integral element model (BIEM) following the approach of Grilli et al. (1989) was developed. This model solves the two-dimensional potential flow problem subject to the full nonlinear kinematic and dynamic free surface boundary conditions.

The following development is brief and basically follows that of Grilli et al. (1989). For inviscid-irrotational flow in two dimensions a velocity potential, ϕ , can be defined as $\mathbf{u} = \nabla\phi(\mathbf{x}, t)$, where ∇ is the gradient operator, while $\mathbf{u} = (u, w)$ and $\mathbf{x} = (x, z)$ are defined in Figure 3.1.1.

Since irrotational flow is assumed and continuity in ϕ will be imposed, the appropriate field equation for ϕ is Laplace's equation:

$$\nabla^2\phi = 0 \tag{3.1}$$

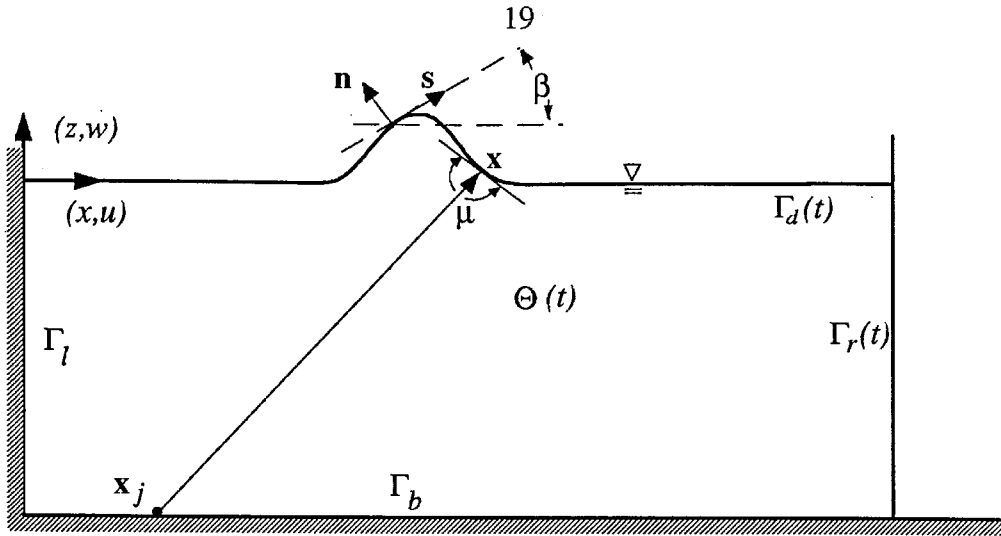


Figure 3.1.1 Definition sketch of the boundary integral problem.

which must be satisfied throughout the fluid domain, $\Theta(t)$. On the free surface, $\Gamma_d(t)$, the following dynamic:

$$\frac{D\phi}{Dt} = \frac{1}{2} |\nabla\phi|^2 - gz - \frac{p_a}{\rho} \quad (3.2)$$

and kinematic:

$$\frac{D\mathbf{r}}{Dt} = \nabla\phi \quad (3.3)$$

boundary conditions must be satisfied, where D/Dt is the total derivative, $(\partial/\partial t + \nabla\phi \cdot \nabla)$; g is the acceleration due to gravity; p_a is the atmospheric pressure, which for this work will be set to zero; ρ is the mass of the fluid per unit volume; and $\mathbf{r}(t)$ is the position vector of a free surface fluid particle. The free slip, no flux boundary condition is applied along the bottom, Γ_b , the right lateral boundary, $\Gamma_r(t)$, and the left lateral boundary, Γ_l :

$$\nabla\phi \cdot \mathbf{n} = \frac{\partial\phi}{\partial n} = \mathbf{U} \cdot \mathbf{n}, \quad (3.4)$$

where \mathbf{n} is the unit normal vector of the fluid surface which points away from the domain, and $\mathbf{U}(\mathbf{x}, t)$ is the velocity of the boundary. In this development, $\mathbf{U} \cdot \mathbf{n} = 0$ along the bottom and the left lateral boundary, while a wave plate velocity is applied at the right lateral boundary for wave generation.

To generate a solitary wave in the numerical wave tank as the sketch in Figure 3.1.1 shows, the method developed by Goring (1979) is used to calculate the required displacement time history of the right lateral boundary. Goring's method is applicable for long waves which propagate with a permanent shape such as solitary and cnoidal waves. He calculated the required trajectory by propagating an existing wave away from the wave generator. The trajectory of the piston was determined to give the desired wave plate velocity at the particular location for that instant of time. The water particle velocity was assumed constant over the depth which allows it to be easily related to the wave celerity using the continuity equation. The celerity of the solitary wave was estimated as $c = \sqrt{g(H + h)}$. With the model of Goring (1979), the piston (or lateral boundary) motion can be specified which determines the required Neuman boundary data, $\partial\phi/\partial n$.

Introducing the two-dimensional Green's function, $G(\mathbf{x}, \mathbf{x}_j)$, which represents a continuous distribution of source strength around the fluid boundary, one can invoke Green's identity along with Laplace's equation to derive the following integral equation for the velocity potential:

$$\alpha(\mathbf{x}_j)\phi(\mathbf{x}_j) = \oint \left[\frac{\partial \phi}{\partial n} G(\mathbf{x}, \mathbf{x}_j) - \phi \frac{\partial G(\mathbf{x}, \mathbf{x}_j)}{\partial n} \right] d\Gamma, \quad (3.5)$$

where $\alpha(\mathbf{x}_j) = \mu(\mathbf{x}_j)/2\pi$, $\mu(\mathbf{x}_j)$ is the interior angle, \mathbf{x}_j is the collocation point, and \mathbf{x} is the variable of integration as shown in Figure 3.1.1. In two dimensions the Green's function is:

$$G = -\frac{1}{2\pi} \ln r \quad (3.6)$$

and its partial derivative with respect to the normal to the boundary is:

$$\frac{\partial G}{\partial n} = -\frac{1}{2\pi} \frac{\mathbf{r} \cdot \mathbf{n}}{r^2}, \quad (3.7)$$

where $r = |\mathbf{r}|$ and $\mathbf{r} = \mathbf{x} - \mathbf{x}_j$ are the distance between, and the vector from the collocation point to the integration point, respectively.

A second order Taylor expansion in time is used to integrate the two free surface boundary conditions. This is a Lagrangian method which computes the location of the new value of ϕ at the next time step, $t + \Delta t$. This method was developed by Dold and Peregrine (1984). The free surface location and the velocity potential are computed from:

$$\mathbf{r}(t + \Delta t) = \mathbf{r}(t) + \Delta t \frac{D\mathbf{r}(t)}{Dt} + \frac{(\Delta t)^2}{2} \frac{D^2\mathbf{r}(t)}{Dt^2} + O[(\Delta t)^3] \quad (3.8)$$

and:

$$\phi(\mathbf{r}(t+\Delta t), t+\Delta t) = \phi(\mathbf{r}(t), t) + \Delta t \frac{D\phi(\mathbf{r}(t), t)}{Dt} + \frac{(\Delta t)^2}{2} \frac{D^2\phi(\mathbf{r}(t), t)}{Dt^2} + O[(\Delta t)^3], \quad (3.9)$$

where Δt is the time step.

Since ϕ is a solution of Laplace's equation, then so is $\partial\phi/\partial t$. A second Laplace problem, using the partial derivatives of the boundary data in time, is used to obtain the expressions required to compute the coefficients in the Taylor expansions of Equations 3.8 and 3.9. To simplify the derivation, use the tangential and normal vectors to the fluid surface, (\mathbf{s}, \mathbf{n}) , where β is the counter clockwise angle from the x axis to the s axis as shown in Figure 3.1.1. With $\cos\beta = \partial x/\partial s$ and $\sin\beta = \partial z/\partial s$, Equation 3.3 becomes:

$$\frac{D\mathbf{r}}{Dt} = \left[\frac{\partial\phi}{\partial s} \cos\beta - \frac{\partial\phi}{\partial n} \sin\beta, \frac{\partial\phi}{\partial n} \cos\beta + \frac{\partial\phi}{\partial s} \sin\beta \right]. \quad (3.10)$$

The continuity and irrotational conditions in the new coordinates become:

$$\frac{\partial^2\phi}{\partial s^2} = -\frac{\partial^2\phi}{\partial n^2} \quad (3.11)$$

$$\frac{\partial^2\phi}{\partial n\partial s} = \frac{\partial^2\phi}{\partial s\partial n} \quad (3.12)$$

while the second derivative of Equation 3.3 can be written as:

$$\begin{aligned}
\frac{D^2 \mathbf{r}}{Dt^2} &= \left(\frac{\partial^2 \phi}{\partial t \partial s} + \frac{\partial \phi}{\partial s} \frac{\partial^2 \phi}{\partial s^2} + \frac{\partial \phi}{\partial n} \frac{\partial^2 \phi}{\partial n \partial s} \right) \cos \beta \\
&+ \left(\frac{\partial \phi}{\partial n} \frac{\partial^2 \phi}{\partial s^2} - \frac{\partial \phi}{\partial s} \frac{\partial^2 \phi}{\partial n \partial s} - \frac{\partial^2 \phi}{\partial t \partial n} - \frac{\partial \beta}{\partial s} |\nabla \phi|^2 \right) \sin \beta, \\
&\left(\frac{\partial^2 \phi}{\partial t \partial n} - \frac{\partial \phi}{\partial s} \frac{\partial^2 \phi}{\partial s^2} + \frac{\partial \phi}{\partial s} \frac{\partial^2 \phi}{\partial n \partial s} + \frac{\partial \beta}{\partial s} |\nabla \phi|^2 \right) \cos \beta \\
&+ \left(\frac{\partial^2 \phi}{\partial t \partial s} + \frac{\partial \phi}{\partial s} \frac{\partial^2 \phi}{\partial s^2} + \frac{\partial \phi}{\partial n} \frac{\partial^2 \phi}{\partial n \partial s} \right) \sin \beta. \tag{3.13}
\end{aligned}$$

From Equation 3.2, the second derivative of ϕ can be written as:

$$\begin{aligned}
\frac{D^2 \phi}{Dt^2} &= \frac{\partial \phi}{\partial s} \frac{\partial^2 \phi}{\partial t \partial s} + \frac{\partial \phi}{\partial n} \frac{\partial^2 \phi}{\partial t \partial n} + \frac{\partial \phi}{\partial s} \left(\frac{\partial \phi}{\partial s} \frac{\partial^2 \phi}{\partial s^2} + \frac{\partial \phi}{\partial n} \frac{\partial^2 \phi}{\partial n \partial s} \right) \\
&- \frac{\partial \phi}{\partial n} \left(\frac{\partial \phi}{\partial n} \frac{\partial^2 \phi}{\partial s^2} - \frac{\partial \phi}{\partial s} \frac{\partial^2 \phi}{\partial n \partial s} \right) + \frac{\partial \phi}{\partial n} |\nabla \phi|^2 \frac{\partial \beta}{\partial s} \\
&- g \left(\frac{\partial \phi}{\partial n} \cos \beta + \frac{\partial \phi}{\partial s} \sin \beta \right) - \frac{1}{\rho} \frac{Dp_a}{Dt}. \tag{3.14}
\end{aligned}$$

The use of a second-order time stepping scheme includes terms such as $\partial^2 \phi / \partial t \partial n$ along the free surface. The solution to the first Laplace problem will determine $\partial \phi / \partial n$ along the free surface and ϕ along the rigid boundaries. The second Laplace problem is solved using the $\partial / \partial t$ derivatives of the boundary data from the first Laplace problem. From this second Laplace problem, $\partial^2 \phi / \partial t \partial n$ will be determined along the free surface. This second Laplace problem requires $\partial \phi / \partial t$ along the free surface which is calculated from Equation 3.2, while $\partial^2 \phi / \partial t \partial n$ is required along the rigid boundaries. At each time step

the new values of r and ϕ calculated from Equations 3.8 and 3.9 give the new water surface position and the potential on the free surface.

The boundary is discretized into elements which connect each nodal point around the perimeter of the computational domain, $\Theta(t)$. All quantities are calculated at the nodal locations. Shape functions are used to allow interpolation and differentiation of the variable of interest anywhere along the boundary from the known values at the nodal locations.

The free surface location is defined by two functions, $x(\xi)$ and $z(\xi)$, where ξ is the independent variable which increases by a value of one between each free surface node. From the known free surface nodal locations, a Hermite cubic spline (De Boor (1978)) is calculated along the free surface which allows interpolation between nodal points. The linear system of equations, which must be solved for the slope at each nodal point along the entire free surface is completed by specifying the slope at the two end points. Symmetry across Γ_l requires a zero flow slope (since surface tension is neglected), while the slope at Γ_r is computed from a cubic polynomial through the last four nodal points along Γ_d . This approach is known to preserve the accuracy of the Hermite cubic spline method in the absence of a known end slope condition (De Boor (1978)). By using $x(\xi)$ and $z(\xi)$, overturning surfaces such as breaking waves can be calculated, which would produce a multi-valued free surface coordinate, η , based on the vertical distance above the still water line.

The interpolation of ϕ , $\partial\phi/\partial n$, $\partial\phi/\partial t$, $\partial^2\phi/\partial n\partial t$, and the boundary positions along Γ_r , Γ_b , and Γ_l , are performed with linear shape functions. The $\partial/\partial s$ and $\partial^2/\partial s^2$ derivatives along Γ_d are computed with fourth order shape functions, while $\partial\phi/\partial s$ along

Γ_l (which is needed to compute the force and moment) is computed from second-order shape functions.

Interpolation of a variable, a , using polynomial (Figure 3.1.2) shape functions, is computed by:

$$a(\zeta) = N_l(\zeta)a_l, \quad l = 1, \dots, m, \quad (3.15)$$

where a_l is the value of the variable at the l^{th} nodal location, the summation convention for repeated subscripts is in effect, $-1 \leq \zeta \leq 1$, the order of the shape function is $m-1$, and $N_l(\zeta)$ is the shape function which for linear interpolation is $N_1(\zeta) = (1-\zeta)/2$ and $N_2(\zeta) = (\zeta+1)/2$. Notice that the interpolation takes the nodal value of the function at a particular node. This property of shape functions, in conjunction with following relations:

$$N_i(\zeta_l) = \delta_{il}, \zeta_l = (2l-m-1)/(m-1) \\ i, l = 1, \dots, m \quad (3.16)$$

are used to derive them. In Equation 3.16, δ is the Kronecker delta function, where $\delta_{ij} = 1$ when $i = j$, and $\delta_{ij} = 0$ when $i \neq j$. Letting $s(\zeta)$ denote the arc length of the boundary in physical space, the Jacobian $J_m(\zeta)$ of the transformation between $s(\zeta)$ and ζ is:

$$J_k(\zeta) = \frac{\partial s(\zeta)}{\partial \zeta} = \left[\left(\frac{dN_i(\zeta)}{d\zeta} x_i \right)^2 + \left(\frac{dN_i(\zeta)}{d\zeta} z_i \right)^2 \right]^{1/2} \\ i = 1, \dots, m; \quad k = 1, \dots, N_\Gamma, \quad (3.17)$$

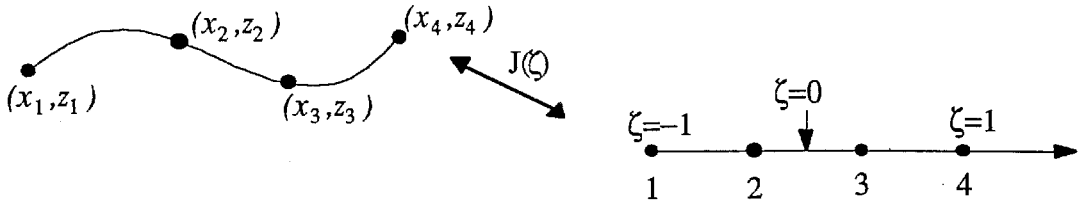


Figure 3.1.2 Transformation from physical space, \mathbf{x} , to the mapped space, ζ .

where k indicates a specific boundary element of which there are N_Γ . The normal vector to the boundary surface is computed as follows:

$$\mathbf{n}(\zeta) = (-\sin \beta, \cos \beta) = \frac{1}{J_k(\zeta)} \left[-\frac{dN_i(\zeta)}{d\zeta} z_i, \frac{dN_i(\zeta)}{d\zeta} x_i \right]. \quad (3.18)$$

The derivatives with respect to arc length along the boundary are computed by:

$$\frac{\partial a}{\partial s} = \frac{1}{J_k(\zeta)} \frac{dN_i(\zeta)}{d\zeta} a_i \quad (3.19)$$

$$\frac{\partial^2 a}{\partial s^2} = \frac{1}{(J_k(\zeta))^2} \left[\frac{d^2 N_i(\zeta)}{d\zeta^2} - \frac{1}{J_k(\zeta)} \frac{dN_i(\zeta)}{d\zeta} \frac{d^2 N_i(\zeta)}{d\zeta^2} (\cos \beta x_i + \sin \beta z_i) \right] a_i, \quad (3.20)$$

where a denotes the variable to be differentiated and:

$$\frac{\partial \beta}{\partial s} = \frac{1}{(J_k(\zeta))^2} \frac{d^2 N_i(\zeta)}{d\zeta^2} (\cos \beta z_i + \sin \beta x_i). \quad (3.21)$$

Since the distribution of ϕ , $\partial\phi/\partial n$, and their $\partial/\partial t$ derivatives are interpolated linearly, Equation 3.5 yields a linear algebraic system of equations in the unknown ϕ and $\partial\phi/\partial n$ values for the first Laplace problem, and the time derivatives of these in the second Laplace problem. For either Laplace problem, Equation 3.5 can be written:

$$\begin{aligned} \alpha(\mathbf{x}_j)a(\mathbf{x}_j) + \int a(\mathbf{x}) \frac{\partial G(\mathbf{x}, \mathbf{x}_j)}{\partial n} d\Gamma_n - \int \frac{\partial a(\mathbf{x})}{\partial n} G(\mathbf{x}, \mathbf{x}_j) d\Gamma_d = \\ \int \frac{\partial \bar{a}(\mathbf{x})}{\partial n} G(\mathbf{x}, \mathbf{x}_j) d\Gamma_d - \int \bar{a}(\mathbf{x}) \frac{\partial G(\mathbf{x}, \mathbf{x}_j)}{\partial n} d\Gamma_n, \end{aligned} \quad (3.22)$$

where a denotes the unknown ϕ or $\partial\phi/\partial t$, \bar{a} is the known ϕ or $\partial\phi/\partial t$, Γ_n is that portion of the boundary with Neuman boundary data (known $\partial\phi/\partial n$) which has M_n nodal points, and Γ_d is the surface over which Dirichlet boundary data (ϕ) is specified and which includes M_d nodes. Equation 3.22 can be written:

$$\left[\Lambda_{ji} + K_{ji}^d \right] a_i - K_{ji}^n \frac{\partial a_i}{\partial n} = K_{ji}^n \frac{\partial \bar{a}_i}{\partial n} - \left[\Lambda_{jl} + K_{jl}^d \right] \bar{a}_l, \quad (3.23)$$

where the K are defined as:

$$\begin{aligned} K_{jm}^d &= \sum_{k=1}^{N_\Gamma} \int N_m(\zeta) \frac{\partial G(\mathbf{x}(\zeta), \mathbf{x}_j)}{\partial n} J_k(\zeta) d\zeta = \sum_{k=1}^{N_\Gamma} I_{jmk}^d \\ K_{jm}^n &= \sum_{k=1}^{N_\Gamma} \int N_m(\zeta) G(\mathbf{x}(\zeta), \mathbf{x}_j) J_k(\zeta) d\zeta = \sum_{k=1}^{N_\Gamma} I_{jmk}^n \\ j, m &= 1, \dots, M_d + M_n; i = 1, \dots, M_d; \\ l &= M_d + 1, \dots, M_d + M_n; k = 1, \dots, N_\Gamma, \end{aligned} \quad (3.24)$$

where m has replaced i and l from Equation 3.23 in Equation 3.24. Equation 3.23 was solved using an International Math and Science Library (IMSL) subroutine.

The matrix, Λ , is diagonal with $\Lambda_{jj} = \alpha(\mathbf{x}_j)$. Instead of calculating the angle, $\theta(\mathbf{x}_j)$, from the geometry near \mathbf{x}_j , a Dirichlet problem (with $\phi = b$ around the entire boundary where b is any non-zero constant) is solved (Brebbia (1978)). The velocity normal to the surface must vanish everywhere, and Equation 3.24 becomes:

$$[\Lambda_{ji} + K_{ji}^d] \bar{a}_i = 0; \quad \bar{a}_i = \text{constant} \neq 0 \quad (3.25)$$

which can be written:

$$\Lambda_{ii} + K_{ii}^d = -\sum_{l \neq i} K_{il}^d \quad i, l = 1, \dots, M_d + M_n \quad (3.26)$$

and determines the $\alpha(\mathbf{x}_j)$ such that continuity is satisfied. Grilli et al. (1989) found that this method reduced the condition number of their system by an order of magnitude relative to numerically computing $\alpha(\mathbf{x}_j)$ from the geometry at \mathbf{x}_j .

Since Hermite cubic splines are used to interpolate the free surface coordinates, the integrals in Equation 3.24 cannot be integrated analytically. Thus, a ten-point Gauss quadrature integration scheme (Abramowitz and Stegun (1970)) is used when the collocation node, \mathbf{x}_j , does not occur in the integrated element. When \mathbf{x}_j does lie on the integrated element, a special technique of integration has been developed (Grilli et al. (1989)) to treat the singularity which develops in $\ln r$ as r tends to zero. When \mathbf{x}_j lies on the integrated element, $\ln|\zeta - \zeta_j|$ is added and subtracted from:

$$I_{jmk}^n = \int G(\zeta, \mathbf{x}_j) h_{mk}(\zeta) d\zeta, \quad (3.27)$$

where $h_{mk}(\zeta) = N_m(\zeta)J_k(\zeta)$. For the Hermite cubic spline approximation of the free surface and linear interpolation of the gradient of the velocity potential, the following can be derived from Equation 3.27:

$$\begin{aligned} I_{jmk}^n &= -\frac{1}{2\pi} \int_{-1}^1 \ln \frac{2r_j(\zeta)}{|\zeta - \zeta_j|} h_{mk}(\zeta) d\zeta \\ &+ \frac{1}{\pi} \int_0^1 \left[\zeta_{-1} h_{mk}(\zeta_j - 2\zeta_{-1}\zeta) + \zeta_1 h_{mk}(\zeta_j + 2\zeta_1\zeta) \right] \ln \frac{1}{\zeta} d\zeta, \end{aligned} \quad (3.28)$$

where ζ_j is the coordinate of the collocation node, $\zeta_{-1} = (\zeta_j + 1)/2$ and $\zeta_1 = (1 - \zeta_j)/2$.

The first integral in Equation 3.28 is not singular and is integrated using Gauss quadrature integration while the second is singular and is computed with Berthod-Zaborowsky quadrature integration (Stroud and Secret (1966)).

The corners where two intersecting boundaries meet needs special treatment to properly account for the physics of the problem. Across any corner, ϕ must be continuous. However, $\partial\phi/\partial n$ is generally discontinuous in corners as it would be, for example, where a piston wave maker intersects a horizontal bottom. The discontinuity in $\partial\phi/\partial n$ occurs since each side of the corner node is associated with a different boundary element which can have different normal velocities. Thus, at each corner, two nodal points are assigned the same location. The value of ϕ for each are the same, while different values are used for $\partial\phi/\partial n$ which are equal to the normal velocity of the respective boundary element. At the intersection of a rigid wall with the free surface, ϕ

and $\partial\phi/\partial n$ along the rigid boundary are known while the only unknown is $\partial\phi/\partial n$ along the free surface. At the intersection of the two rigid boundaries, $\partial\phi/\partial n$ along both edges are known and the value of ϕ , which is the same for both nodes, must be determined. Therefore, only one equation is generated in the linear system at each corner although two nodal points reside there.

3.2 Finite Difference Volume of Fluid Model

In this section, a brief description of the model "SOLA-VOF" (Nichols, Hirt, and Hotchkiss (1980)) and its application to the experimental conditions of this study will be given. For a more detailed discussion, refer to the original report of Nichols et al. (1980). The "SOLA-VOF" method was applied to solitary waves and turbulent bores. This method was not applied to surges on a dry bed.

The model solves the Navier-Stokes equations in an Eulerian mesh of rectangular cells which can have variable spacing in the x and z directions. The Navier-Stokes equations in two dimensions, are:

$$\frac{\partial u}{\partial t} + u \frac{\partial u}{\partial x} + w \frac{\partial u}{\partial z} = -\frac{1}{\rho} \frac{\partial p}{\partial x} + g_x + \nu \left[\frac{\partial^2 u}{\partial x^2} + \frac{\partial^2 u}{\partial y^2} \right] \quad (3.29)$$

and:

$$\frac{\partial w}{\partial t} + u \frac{\partial w}{\partial x} + w \frac{\partial w}{\partial z} = -\frac{1}{\rho} \frac{\partial p}{\partial y} + g_z + \nu \left[\frac{\partial^2 v}{\partial x^2} + \frac{\partial^2 v}{\partial y^2} \right], \quad (3.30)$$

where u , w , and g_x , g_z are the water particle velocities and the gravitational acceleration components in the x , z directions, respectively. In Equations 3.31 and 3.32, the pressure is expressed as p , ρ is the fluid density, ν is the kinematic viscosity of the fluid, and t is time. For an incompressible fluid, the conservation of mass can be expressed as:

$$\frac{\partial u}{\partial x} + \frac{\partial w}{\partial z} = 0. \quad (3.31)$$

The function, $A(x, z, t)$, is used to monitor the position of the fluid in the domain and has a particular value between one and zero at every computational cell. The value of A corresponds to the fraction of the cell area occupied by fluid. The time dependence of A is described by the equation:

$$\frac{\partial A}{\partial t} + u \frac{\partial A}{\partial x} + w \frac{\partial A}{\partial z} = 0. \quad (3.32)$$

Equations 3.29 through 3.32 are sufficient to solve for the unknowns u , w , p , and A at each new time step. At the beginning of a new time step, explicit expressions derived from Equations 3.29 and 3.30 are used to obtain a first estimate of the new velocity field. With the new estimate of the velocity field, the continuity condition (Equation 3.31) is applied throughout the entire domain using an iterative over-relaxation process. An iterative process is required since the application of the continuity condition at one cell affects the fluid velocities in all neighboring cells due to the elliptic nature of the problem. Once the incompressibility condition is satisfied, the volume of fluid function, A , in each cell is determined using Equation 3.32 to calculate the evolution of A . Along all boundaries, the known boundary conditions are imposed during all calculations at a given time step. For more details regarding the finite differences used to

approximate Equations 3.29 through 3.32, stability issues, and the methods used to solve the resulting system of equations, see the report by Nichols, Hirt, and Hotchkiss (1980).

The following method was used to numerically generate a bore which allowed the use of a fairly short numerical wave tank (approximately 1 m). This approach was used since it would be impractical to numerically simulate the 28 m length of the wave tank while retaining a reasonable grid resolution. The experimental measurements of the arrival times of the bore along the wave tank has shown that the celerity of the bore was nearly constant with only a slight deceleration as it approaches the wall for the conditions explored. Therefore, the bore can be modeled approximately as a steady bore when viewed in a reference frame moving with the bore. The measured ambient water depth at the wall and the measured bore celerity are then sufficient to specify a numerically equivalent bore.

For the stationary hydraulic jump shown in Figure 3.2.1, the conservation of horizontal momentum and mass across the jump can be used to derive the following expression (Stoker (1957)) for the velocity of the flow entering the jump, u_1 :

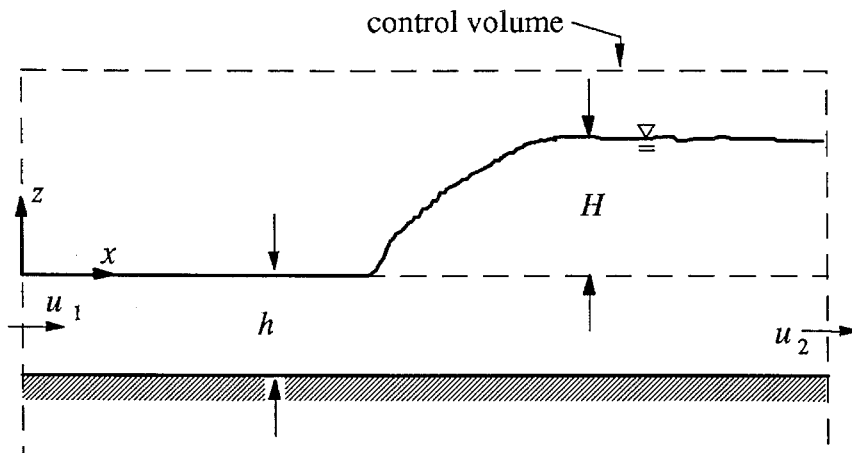


Figure 3.2.1 Definition sketch of a stationary hydraulic jump.

$$\frac{u_1}{\sqrt{gh}} = \sqrt{\left[\left(2 \left(\frac{H+h}{h} \right) + 1 \right)^2 - 1 \right] \frac{1}{8}} \quad (3.33)$$

and:

$$u_2 = u_1 \left(\frac{h}{H+h} \right), \quad (3.34)$$

where u_1 , u_2 , h , and H are defined in Figure 3.2.1. Equation 3.34 is simply the continuity equation applied across the jump.

To produce a bore in the numerical tank using the "SOLA-VOF" model, the program is started with initial conditions as shown in Figure 3.2.2, where the water surface is shown with the solid line. The depth, h , in the numerical wave tank is set to the measured depth from the experimental wave tank. The experimentally determined bore celerity, c , in a moving hydraulic jump is equal to the inflow velocity, u_1 , in a stationary hydraulic jump. With Equation 3.33, the velocity, u_1 , and h , can be used to calculate H . These three variables are then used in Equation 3.34 to calculate u_2 . The initial fluid in the numerical wave tank was then given the speed, $u = u_1 - u_2$, and a free flow boundary condition at the left side allows water of depth, h , and speed, $u_1 - u_2$, to continuously enter. Referring to Figure 3.2.1, if the control volume is moved to the right with speed, u_2 , then the water will enter the left control volume boundary with speed, $u_1 - u_2$, and a no flux condition will prevail at the right boundary. A no flux boundary condition is imposed on the right lateral boundary of the numerical wave tank as shown

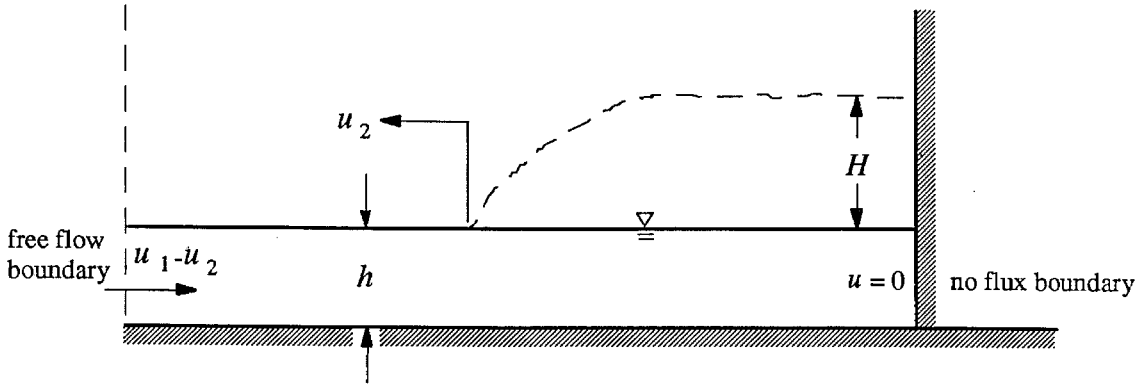


Figure 3.2.2 Creation of a bore using the "SOLA-VOF" model.

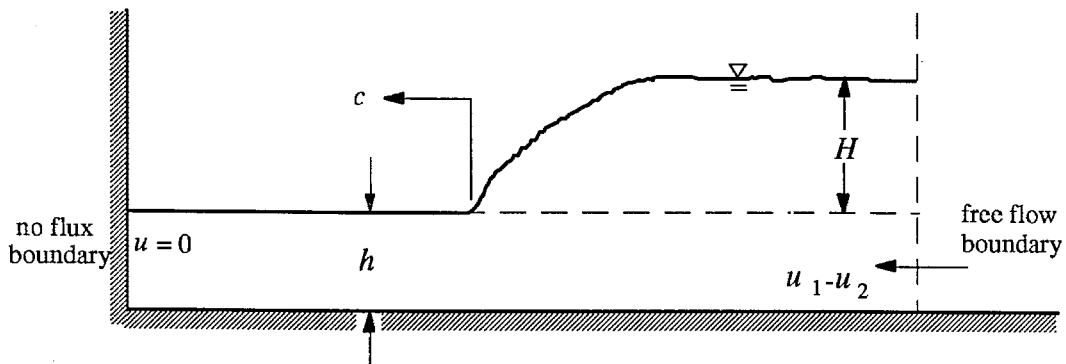


Figure 3.2.3 Propagation of the bore into the wall using the "SOLA-VOF" model.

in Figure 3.2.2. This no flux boundary forces the flow to create a bore which then propagates with height, H , and celerity, u_2 , toward the left boundary as shown in Figure 3.2.2. When the bore is approximately halfway between each lateral boundary, the simulation is stopped. The velocity, $u_1 - u_2$, is then subtracted from the flow field. The code is started again with a no flux left lateral boundary and a free flow boundary at the right side where the flow of depth $H + h$ is allowed to enter with fluid velocity, $u_1 - u_2$. This produces the conditions shown in Figure 3.2.3 where a bore with celerity, c , propagating on a still water depth of h will eventually strike the impermeable wall. The celerity of the bore, c , is equal to the water particle velocity, u_1 , in Equation 3.33.

The "SOLA-VOF" model was also used to generate solitary waves which propagated along the numerical wave tank and were reflected at a vertical wall. Whereas the lateral boundary in the BIEM model was moved as a piston wave generator, a horizontal water particle velocity corresponding to a solitary wave was specified at the stationary boundary in the "SOLA-VOF" model. In both models the velocity of a solitary wave due to Boussinesq (1872):

$$c = \sqrt{g(H + h)} \quad (3.35)$$

was used, along with the following continuity equation relating the horizontal water particle velocity to the celerity of the wave:

$$u = c \frac{\eta}{\eta + h}, \quad (3.36)$$

where the water particle velocity is assumed uniform over the depth. The following expression for the solitary wave profile was used:

$$\eta = H \operatorname{sech}^2 \sqrt{\frac{3}{4} \frac{H}{h^3}} (x - ct), \quad (3.37)$$

where H is the wave height of the solitary wave.

4. EQUIPMENT AND PROCEDURES

The impact of waves on a vertical wall was investigated in two separate wave tanks. The forces associated with strong turbulent bores generated from broken solitary waves were investigated in a tilting wave tank. The remainder of the experimental program, which included the impact of bores, solitary waves, and surges over a dry bed, was conducted in a horizontal wave tank. The equipment and procedures used in the tilting wave tank are discussed in Section 4.1, while those used in the horizontal tank are described in Section 4.2. The two different tanks were used since mild slopes are most easily produced in the tilting tank, while the gate arrangement used to generate the bores was easier to construct in the relatively narrow horizontal tank.

4.1 Tilting Wave Tank Study

4.1.1 Tank and Wave Generator

The experiments were conducted in a tilting tank that is 40 m long, 110 cm wide, and 61 cm deep (Figure 4.1.1). The side walls are composed of 1.28 cm thick tempered glass windows which are each 63.5 cm high and 1.52 m long. The bottom is constructed of stainless steel plates that are plane to within approximately ± 2.5 mm. The tank can be tilted from horizontal to a maximum slope of 1 vertical on 50 horizontal. The joints along the edges of the glass and the bottom are sealed with silicone caulking to eliminate leakage. Stainless steel rails 3.81 cm in diameter are mounted on studs along the top edge of the wave tank and are level to within ± 0.3 mm. A steel measuring tape is located along the top edge of the tank to allow accurate determination of location along the tank.

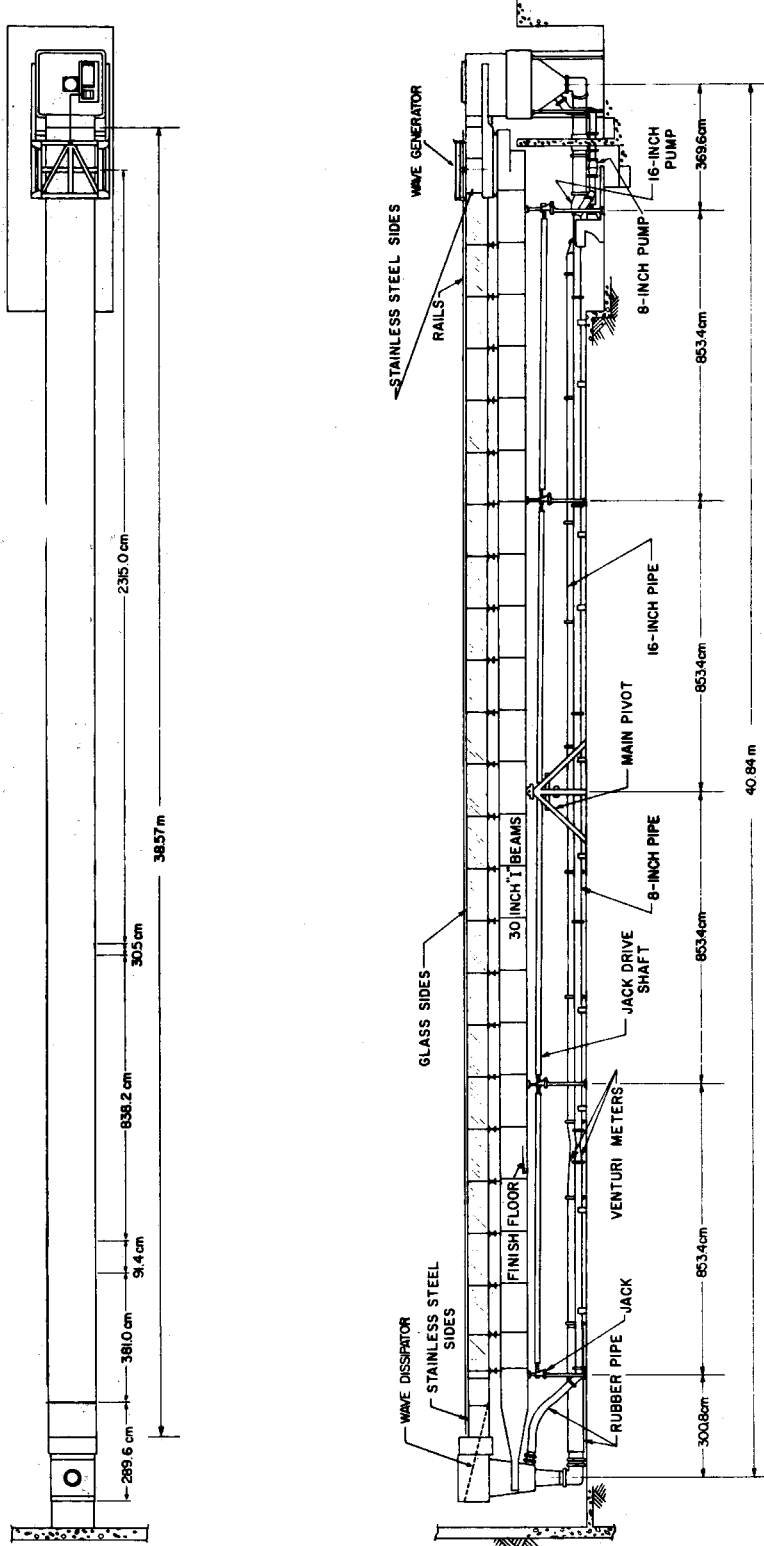


Figure 4.1.1 Schematic of the tilting wave tank (after Skjelbreia (1987)).

The programmable hydraulic-powered piston-type wave machine shown in Figure 4.1.2 produced the solitary waves used in these experiments. Since the wave machine is supported on the tank substructure, it tilts with the tank, allowing a simple means of producing breaking waves. The 6.4 mm thick aluminum wave plate and its supporting frame are mounted to a carriage which moves along the stainless steel rails on open pillow block ball bushings (Thompson Model SPB-16-OPN). The size of this aluminum plate is slightly less than the dimensions of the wave tank. This allowed the installation of rubber windshield wiper blades along the edges of the plate to minimize flow around the sides and under the bottom of the plate during wave generation.

The hydraulic actuator (Miller Model DR-77B), which produces motion of the wave plate carriage, is controlled by a servo-valve (Moog Model 72-103). This arrangement is shown schematically in Figure 4.1.3. The bore of the actuator is 8.25 cm and the rod diameter is 3.49 cm which gives an effective bearing area of 43.9 cm² for the hydraulic fluid. The normal hydraulic seals in the cylinder were removed and replaced with step seals (Shamban Model S32573-126) to reduce the friction forces acting on the piston rod. Such forces affect the movement of the piston near its zero velocity position. The servo-valve is powered by a hydraulic power supply composed of a variable displacement pump rated at a discharge of 0.00252 m³s⁻¹ with a pressure of 17,000 KNm⁻². This pump is powered by a 56 KW, 1800 rpm electric motor and draws oil from a 0.681 m³ reservoir. A Moog valve (Model 72-103), rated at 0.0037 m³s⁻¹ for a 40 mA current applied to the valve, controls flow to each side of the actuator. The direction and rate of flow to the actuator is determined by the applied current to the valve, which is supplied by the servo controller (Moog Model 82D300). The displacement of the wave generator is monitored with a linear variable differential transformer (LVDT) (Collins Model LMT-811T41). Ting (1989) provides additional details about the hydraulic supply system.

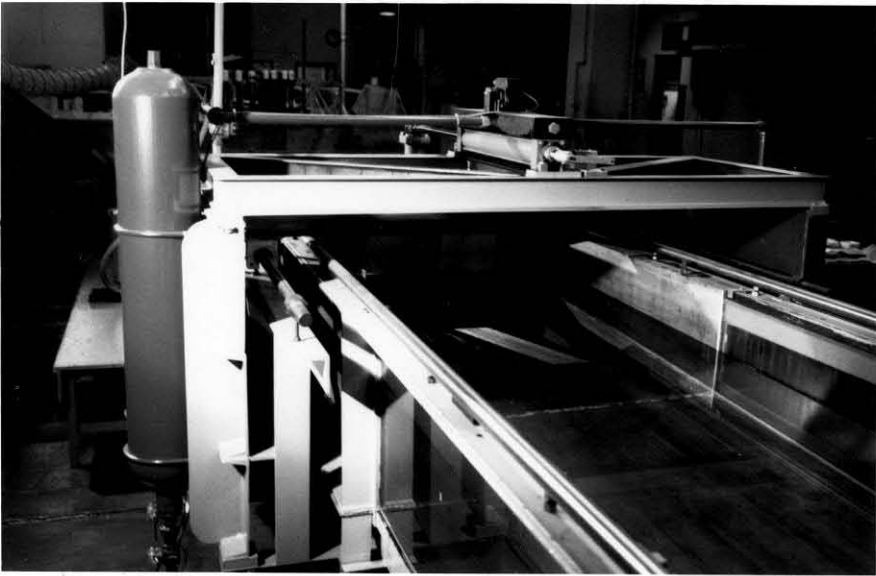


Figure 4.1.2 Photograph of the wave generator in the tilting wave tank (after Skjelbreia (1987)).

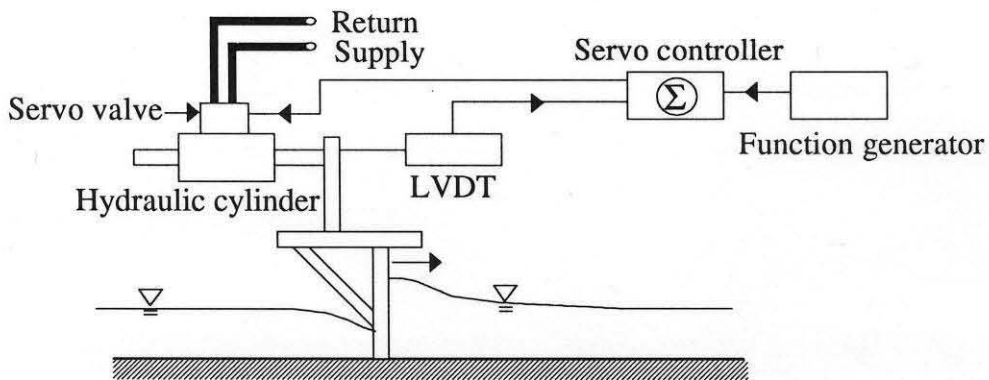


Figure 4.1.3 Schematic of the wave generator and control equipment.

The signal used in the feedback system which controls the Moog valve is the difference between the desired trajectory of the wave plate and the actual trajectory measured with the LVDT. The subtraction of these signals to produce the feedback control is performed

in analog circuits within the servo-controller. The desired trajectory was determined on a minicomputer (Digital Equipment Corporation Model LSI-11/23). This signal was transferred to a microprocessor controlled function generator which was built and discussed in detail by Skjelbreia (1987). The output from the function generator was supplied to the servo-controller.

4.1.2 Vertical Wall

The vertical wall that extended the entire width of the tank was composed of false walls on either side of an instrumented section located at the centerline of the tank as shown in Figure 4.1.4. The instrumented section, which is 59.06 cm high and 4.95 cm wide, was constructed of a 1.27 cm thick aluminum plate and mounted to three force transducers (Interface Model SSM-250) as shown in Figure 4.1.5. A detailed drawing of the instrumented wall is shown in Figure 4.1.6. The total mass of the wall system supported by the three force transducers was 846.6 g. This included the mass of nine bolts and three 1.27 cm square aluminum rods used to connect the force transducers to the wall, which can be seen in Figure 4.1.5. The centerline of two transducers was located 3.83 cm above the bottom of the wall while the centerline of the third transducer was mounted 30.48 cm above those two.

A portion of the steel structure to which the other end of the force cells was connected is shown in Figure 4.1.5. The force cells were bolted to the top of a three inch structural tee section (WT 3"×8(lb/ft)) (American Institute of Steel Construction (1980) designation) as shown in Figure 4.1.5. The top of the tee section was bolted to a welded steel frame composed of five channel sections which were three inches wide (C 3"×6(lb/ft)) and two steel I beams which were also three inches wide (W 3"×7.5(lb/ft)). The bottom of the tee section was connected to the other side of the frame with two channels (C 3"×6(lb/ft)) as shown in Figure 4.1.7. The steel frame was connected to

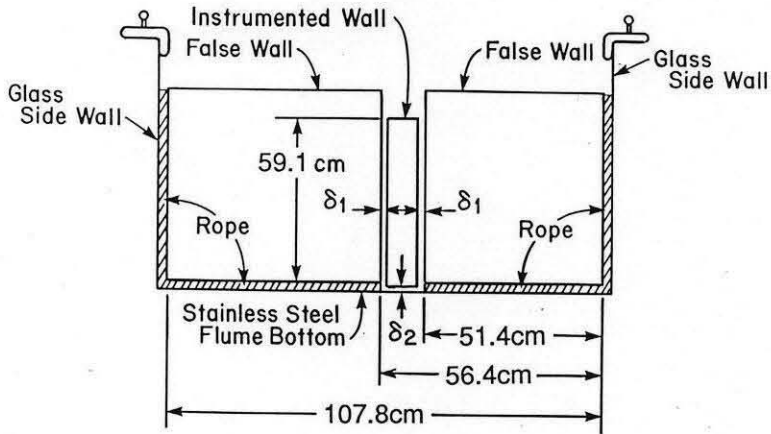


Figure 4.1.4 Wave tank cross section showing the location of the false walls and the instrumented wall ($\delta_1 = 0.13$ mm to 0.24 mm, $\delta_2 = 0.13$ mm to 0.18 mm).

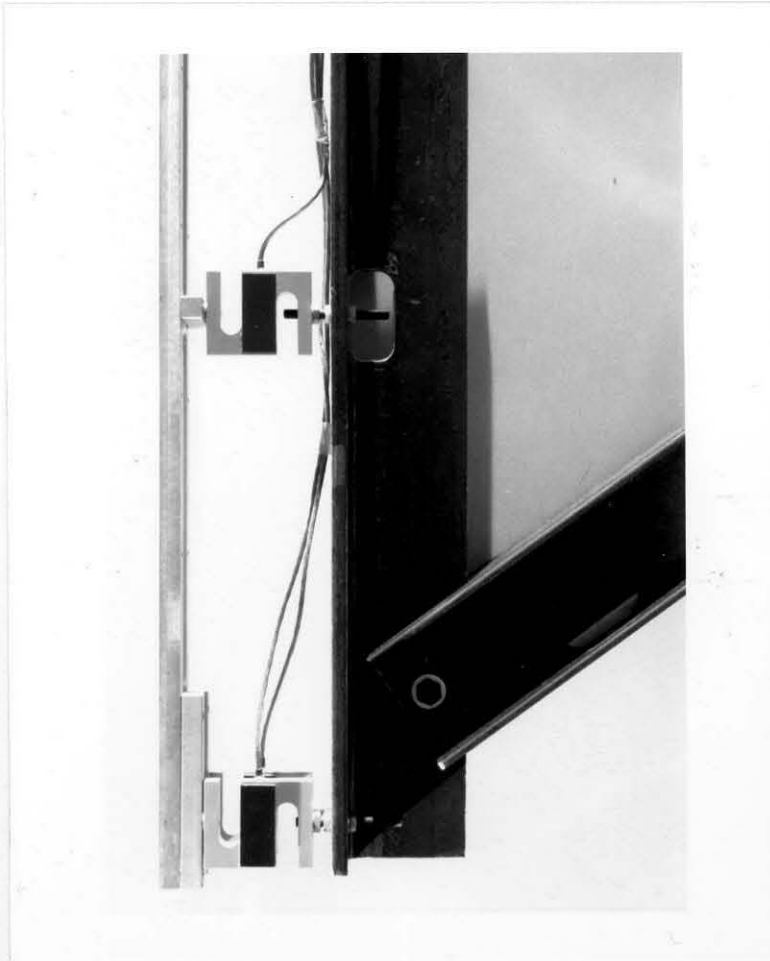
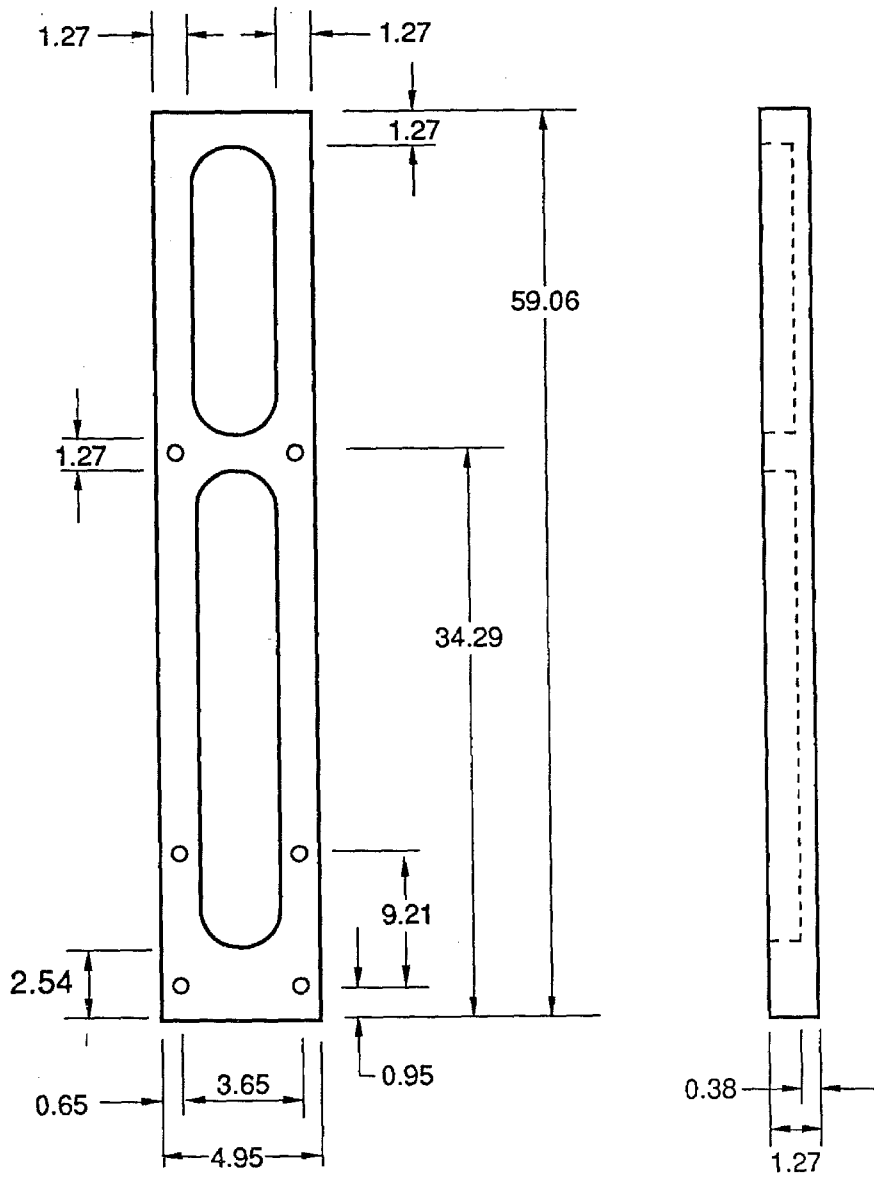


Figure 4.1.5 Photo showing the instrumented wall to the left of the "s" shaped force transducers which are mounted to the steel T section.



(a) BACK VIEW

(b) SIDE VIEW

Figure 4.1.6 Schematic of the instrumented wall used for the tilting wave tank experiments.

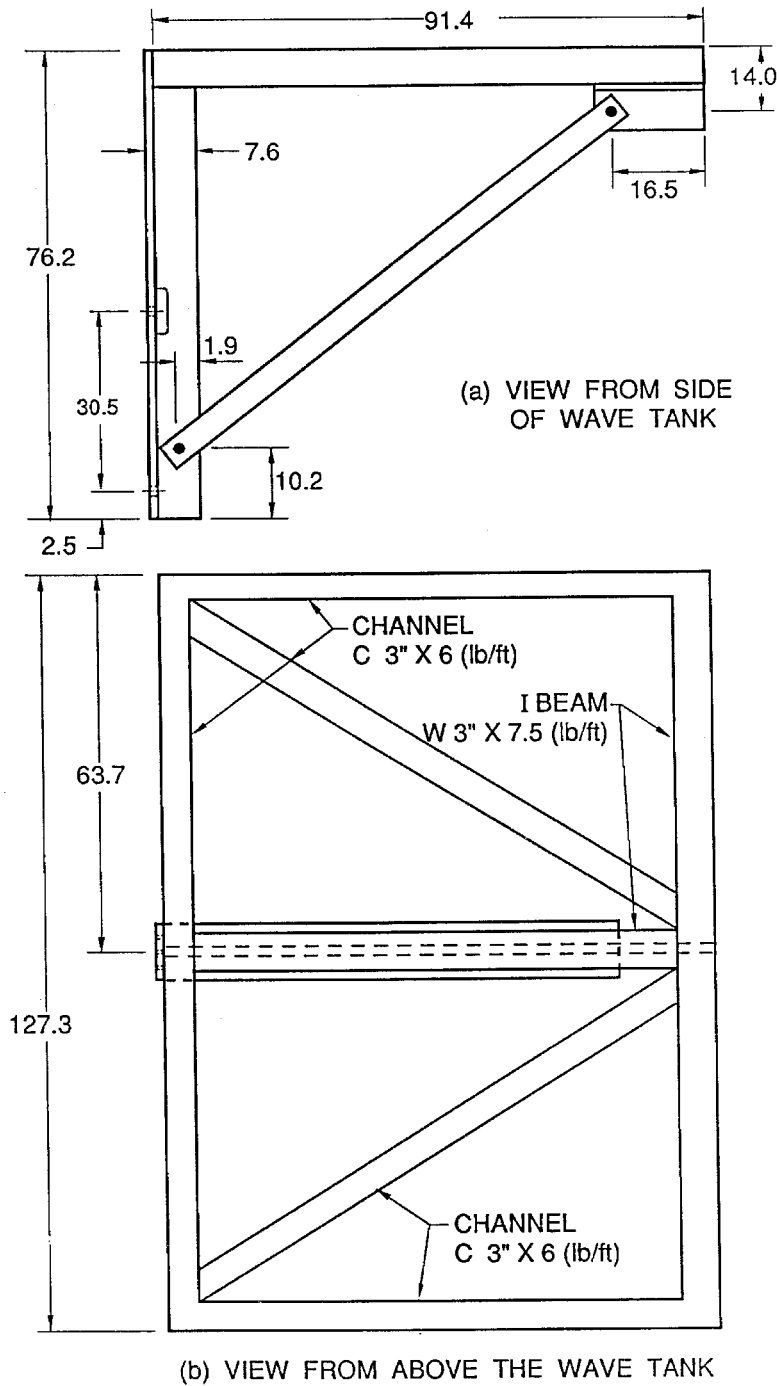
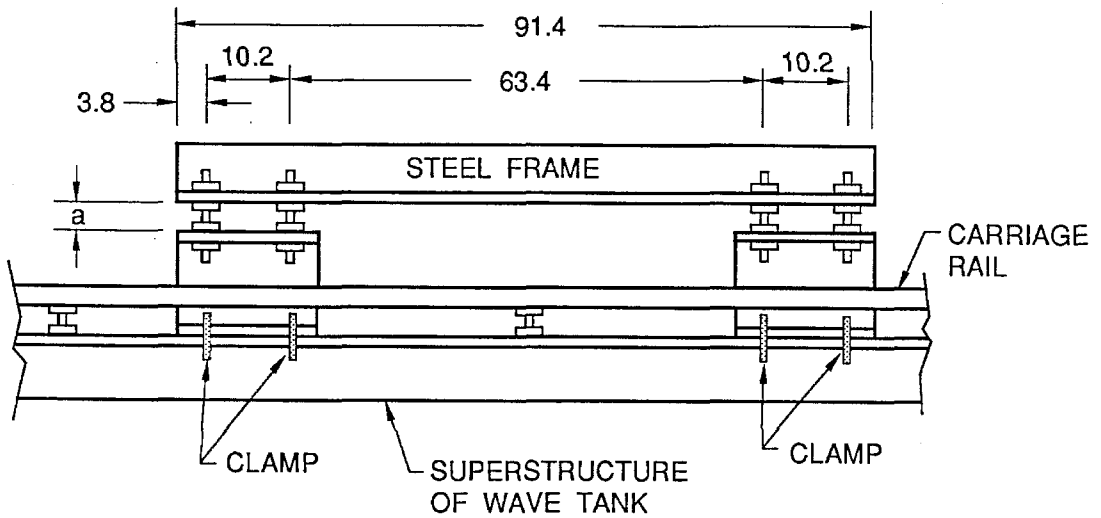


Figure 4.1.7 Schematic of the welded steel frame and T sections used to support the force transducers (all dimensions are in cm except where specified otherwise).

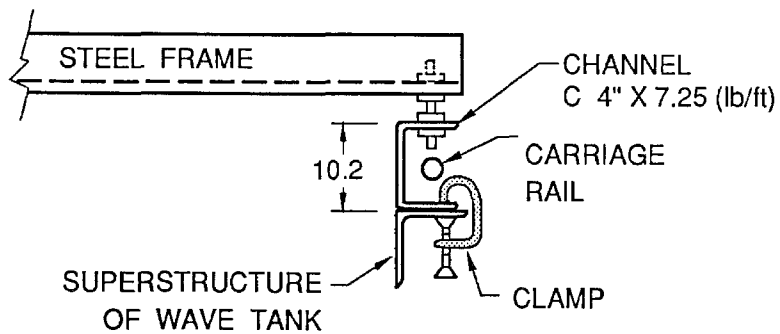
each side of the wave tank using two 15.2 cm long, four inch wide channel sections (C 4"×7.25(lb/ft)) as shown in Figure 4.1.8. The steel frame was connected to the four inch channels with eight 3/8 inch diameter threaded brass studs. The four inch channel sections were rigidly clamped to the top angle of the wave tank, which allowed precision adjustment of the dimension a shown in Figure 4.1.8(a).

Due to the large stiffness of the force transducers relative to the anticipated loads and the resultant deflection, a low-noise amplifier was necessary. A schematic of this amplifier is shown in Figure 4.1.9; amplification factors from 10 to 18,480 can be achieved with this circuit. At an amplification of 18,480, the standard deviation of the background noise levels in the force transducers was between 0.051 N and 0.058 N. Small but finite stresses were imposed on the force transducers when the instrumented wall was mounted to the support structure. Since these stresses in the force cell produce a finite voltage, an offset capability was built into the amplifier. Each force transducer was rated at 1112 N full scale which produced about 31 mV of response before amplification for the recommended 10 V excitation. During the experiments in the tilting wave tank, the force transducer amplifiers were powered by a 60 Hz AC supply.

To obtain a smooth surface, the false walls, composed of 1.90 cm thick plywood, were faced with formica on the side exposed to waves. The support structure for the false walls was isolated from the support structure for the instrumented wall. The false walls were connected to three inch channel sections (C 3"×6(lb/ft)) which were rigidly clamped to the steel angles along the top of the wave tank as shown in Figure 4.1.10. The gaps between the false walls and the tank walls were sealed with closed-cell foam rope to prevent leakage as shown in Figure 4.1.4.



(a) VIEW FROM SIDE OF WAVE TANK



(b) VIEW LOOKING ALONG THE WAVE TANK

Figure 4.1.8 Schematic of the connection between the steel frame and the tilting wave tank.

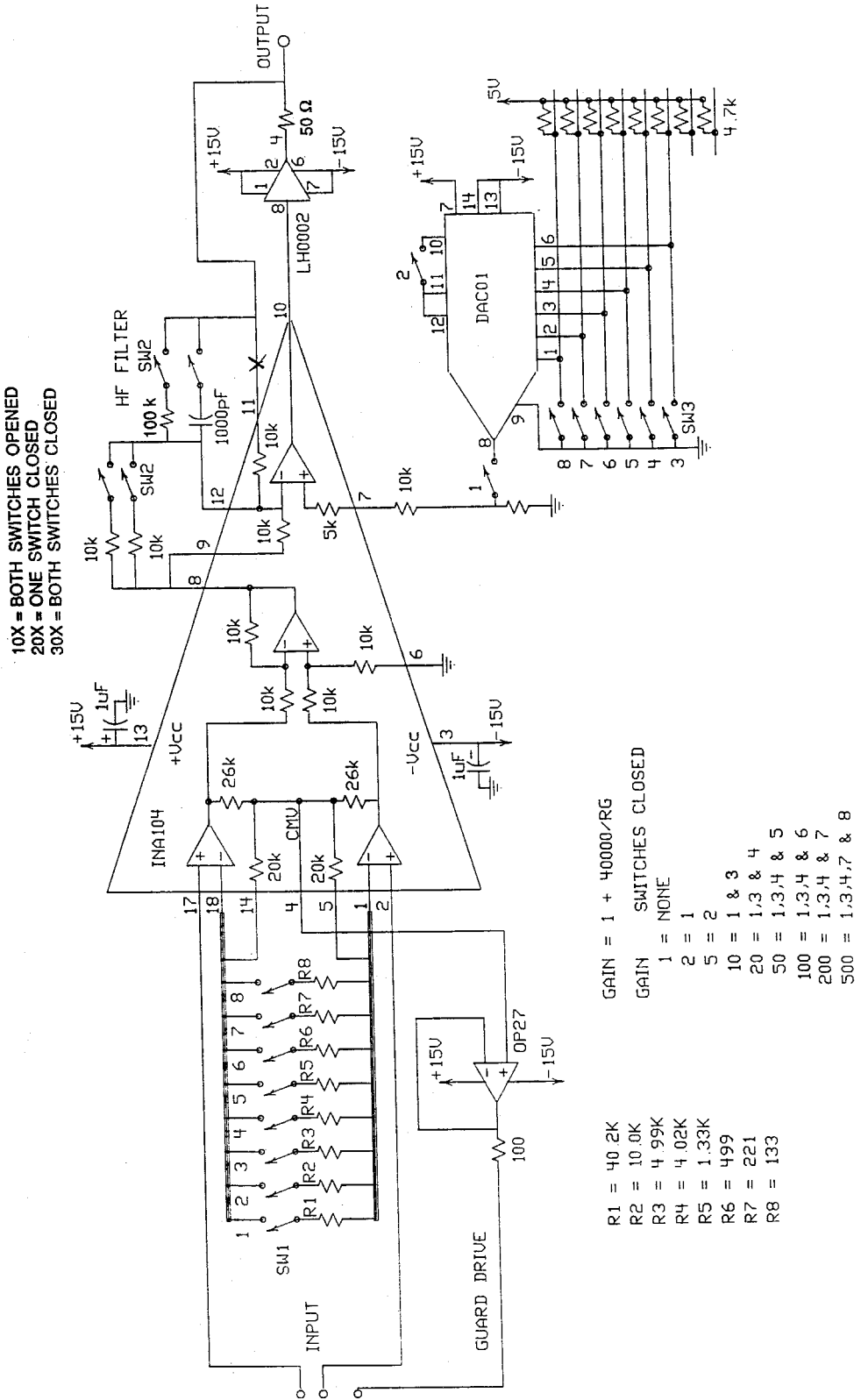


Figure 4.1.9 Circuit diagram of the force transducer amplifier.

Since the force cells produce a voltage signal proportional to their displacement, it was necessary to isolate the instrumented section of the wall. In this way, the transducers would indicate only the loads imposed on the instrumented wall. To ensure it was not touching the tank bottom or the false walls, gaps varying from 0.13 mm to 0.24 mm were left between the instrumented section and the false walls, and somewhat smaller gaps (0.13 mm to 0.18 mm) were left between the instrumented wall and the bottom. These gaps along the sides and bottom are shown in Figure 4.1.4, and denoted as δ_1 and δ_2 , respectively. Although water will pass through the gaps around the instrumented wall, the aspect ratio of the gap (at least 50) and its narrow width will produce shear losses along the walls due to the flow through the gap. Thus, a portion of the flow losses through the gaps will be recorded by the transducers as shear forces along the instrumented wall. The results of experiments to determine the effect of the gap width along the bottom on the measured force will be discussed in Section 5.1 (see Figure 5.1.7).

Figure 4.1.11 shows the calibration results for one of the force transducers before it was mounted to the wall. The force transducer alone was loaded with weights to provide this calibration. The abscissa is the applied force and the ordinate is the output voltage. Since the response is linear, the slope of the line from a linear fit of the data is used as the calibration constant.

After calibrating the individual transducers, they were connected to the wall. The calibration device shown in Figure 4.1.12 was used to check the response of the wall by applying a point force perpendicular to the wall at predetermined locations. The apparatus shown in Figure 4.1.12, consists of a triangular aluminum plate, which is free to rotate about point c. It was important that shear forces did not develop between the

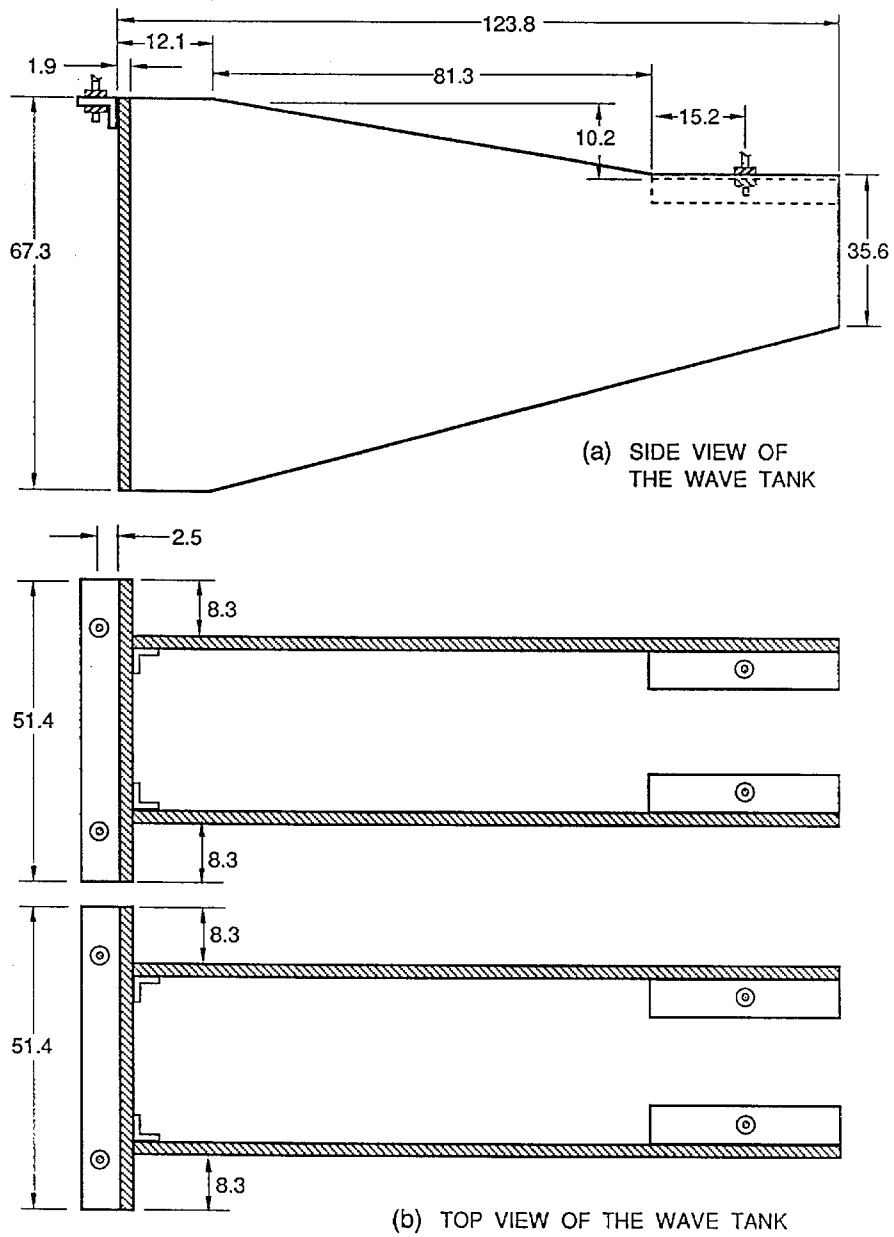


Figure 4.1.10 Schematic of the supporting structure for the false walls (all dimensions are in cm).

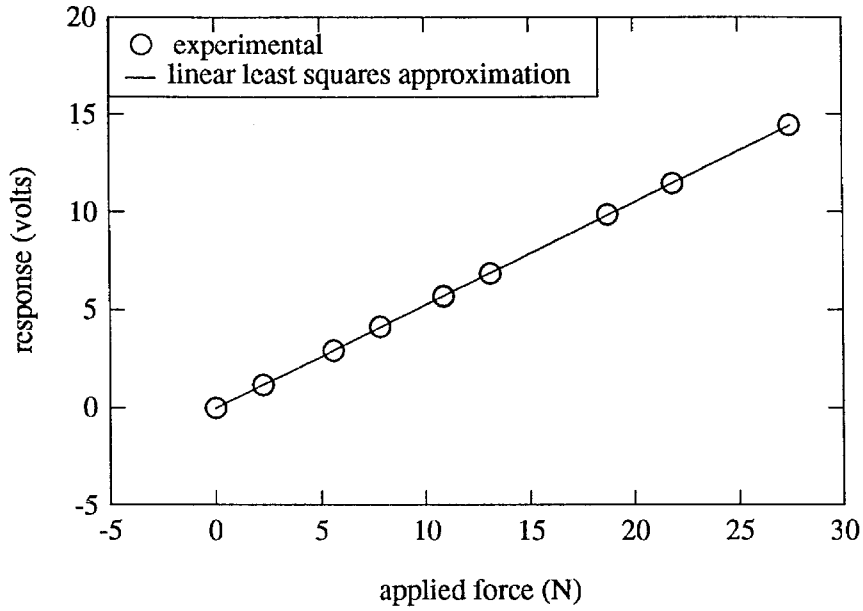


Figure 4.1.11 Calibration of the force transducer connected to channel 1.

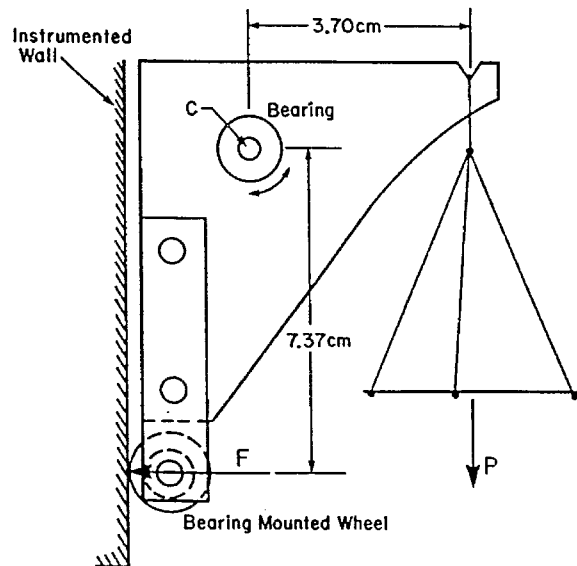


Figure 4.1.12 Device used to calibrate the instrumented wall where the load, P , caused an applied force, F , on the wall.

calibration device and the wall, which were minimized by the bearing mounted wheel. A load, P , placed in the weight pan produces the force, F , on the wall. The output voltage from each transducer was converted to a force using the calibration constant from the linear fit shown in Figure 4.1.11. These forces were added to give the force response

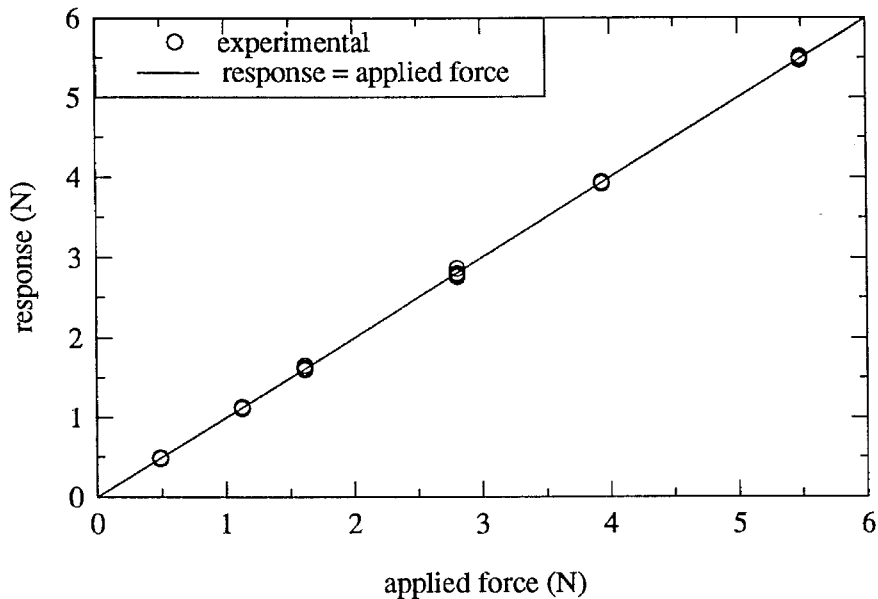


Figure 4.1.13 Response of the instrumented wall due to point loads applied with the device shown in Figure 4.11.

shown as the ordinate in Figure 4.1.13. If the system is responding properly, the force response determined in this manner should equal the applied force which is shown by the solid line in Figure 4.1.13. The agreement between the applied force and the response was always within $\pm 2\%$.

Each force cell was tested separately to determine its spring constant and effective mass in the following manner: the force transducer was bolted to a 1.27 cm thick aluminum plate which was placed on the floor, this plate was loaded with four 12 kg lead bricks to obtain a fixed support for the transducer, then the force cell was tapped lightly with the end of a screwdriver to produce oscillations at its natural frequency. The experiment was repeated with a mass of 159.8 g bolted to the free end of the force cell, which produced oscillations at a lower frequency. The damping ratio (i.e., the measured damping normalized by critical damping) of the loaded force transducer connected to channel 4 was 0.8%. This was computed from the measured response using the logarithmic decrement method over 23 cycles of oscillation. The natural frequency of an oscillator with such a small damping ratio agrees with the undamped natural frequency to within 4 decimal places. Therefore, there should be little error in determining the effective mass and the spring constant assuming the system is undamped. Defining m_e to be the effective mass of the unloaded force transducer and m the mass of the load applied to the force transducer, the undamped natural frequency of the unloaded and loaded force cells can be expressed as $\omega_u = \sqrt{k/m_e}$ and $\omega_l = \sqrt{k/(m_e+m)}$, respectively, where k is the unknown spring constant, ω_u is the unloaded natural frequency, and ω_l is the loaded natural frequency. After the frequencies of the oscillation for the unloaded and the loaded transducers are measured, the two relations for the natural frequency can be solved to determine the effective mass, m_e , and the spring constant, k . The results for each of the force transducers are compiled in Table 4.1.

The natural frequencies of the instrumented wall as mounted in the wave tank were determined experimentally. Two modes were identified which had natural frequencies of 970 Hz and 113 Hz. The 970 Hz mode was excited by tapping the wall with a 0.79 cm allen wrench near the bottom, in front of the two force cells. The lowest mode was excited by plucking the wall at the top edge. Since the heights of the incident

| Transducer serial number | Channel number | Calibration coefficient (N/Volt) | Effective mass m_e (g) | Spring constant k (KN/mm) | f_N (Hz) |
|--------------------------|----------------|----------------------------------|--------------------------|-----------------------------|------------|
| B34106 | 1 | 1.906 | 21.3 | 5.54 | 2570 |
| B30750 | 2 | 1.893 | 21.3 | 5.52 | 2560 |
| B30774 | 3 | 1.881 | 20.6 | 5.49 | 2600 |
| B30769 | 4 | 1.933 | 22.0 | 5.85 | 2600 |

Table 4.1.1 Measured characteristics of the force transducers.

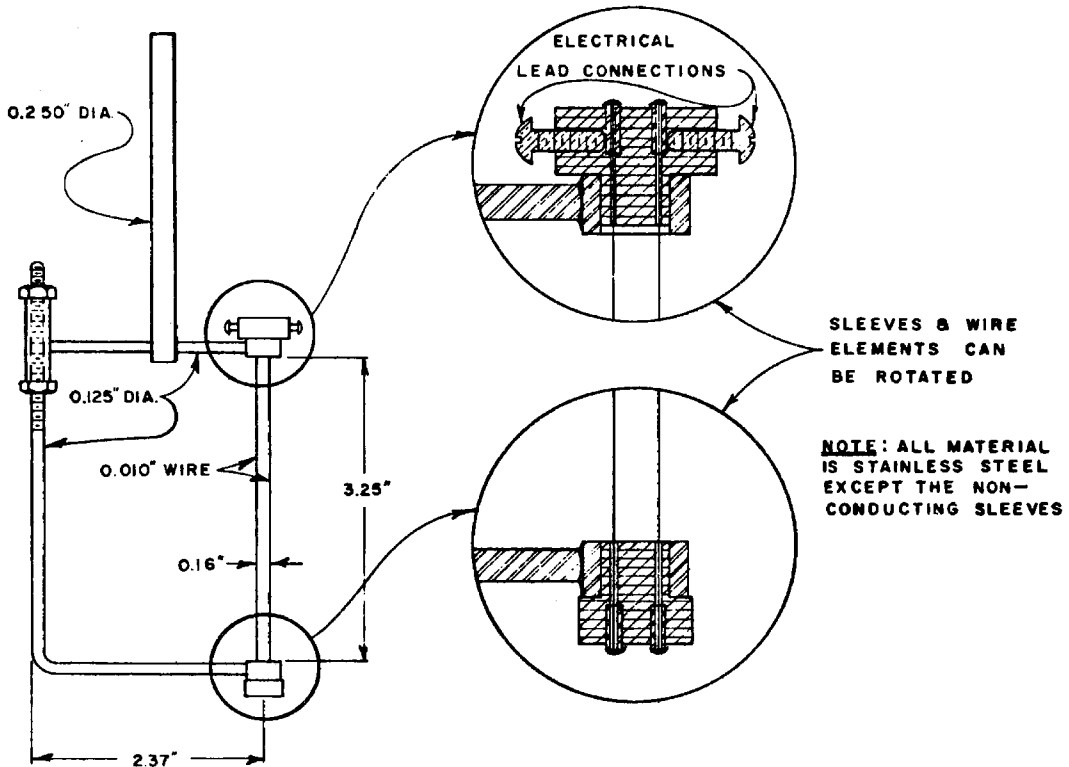
bores (presented in Section 5.1) are on the order of a few centimeters, the hydrodynamic force primarily acts near the bottom of the wall where the 970 Hz mode was produced. Therefore, the 970 Hz mode should dominate the dynamic response of the wall during the initial stages of the bore impact. The transducers should measure the force amplitude accurately for frequency components up to approximately 200 Hz.

4.1.3 Wave Gages

The water surface time histories were measured using resistance-type wave gages similar to that shown in Figure 4.1.14(a). The wave gage is composed of two 0.23 mm diameter stainless steel wires which are mounted parallel to each other with a separation of 3.2 mm. These parallel wires are electrically isolated at the top and bottom of the gage. The sensitive wires on the wave gages used in this study were 33.2 cm long and were located 10.5 cm from the 0.125 inch diameter supporting rod. The gage is used as one arm of a Wheatstone bridge as shown in Figure 4.1.14(b). The bridge is connected to a carrier preamplifier (Hewlett Packard Model 8848A) which provides the excitation voltage, the signal conditioning, and display.

The two wires of the wave gage produce an electrical field in the water and the air. Since air acts as an insulator between the two wires while water is an efficient conductor, the resistance experienced by the current across the electrical field varies with

a)



b)

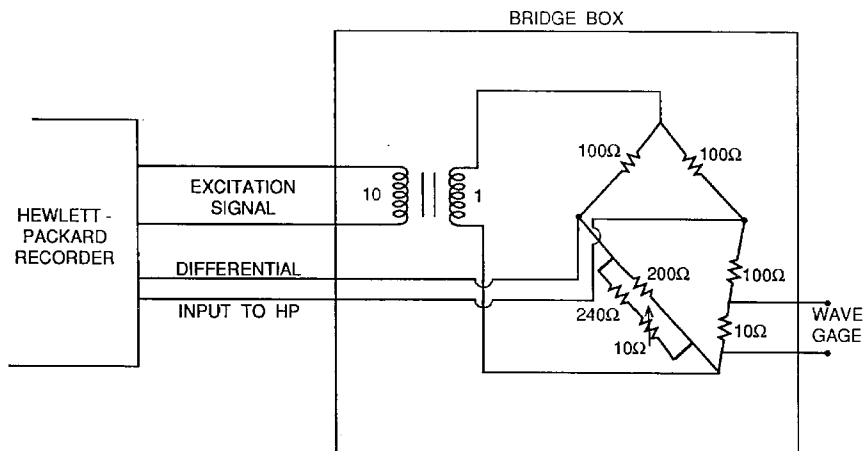


Figure 4.1.14 (a) Schematic of a typical wave gage (after Raichlen (1965)); (b) Circuit diagram of the bridge for the wave gage.

the water level. The wave gage is normally calibrated by changing its vertical position relative to the water and recording its output. A typical calibration is shown in Figure 4.1.15 where the experimental data have been approximated by a second-order polynomial, whose coefficients are determined by the least squared error method. This second-order approximation is then used to calculate the water surface displacement from the measured voltage. Figure 4.1.15 also shows a calibration one hour after the first calibration indicating the need to periodically recalibrate such gages.

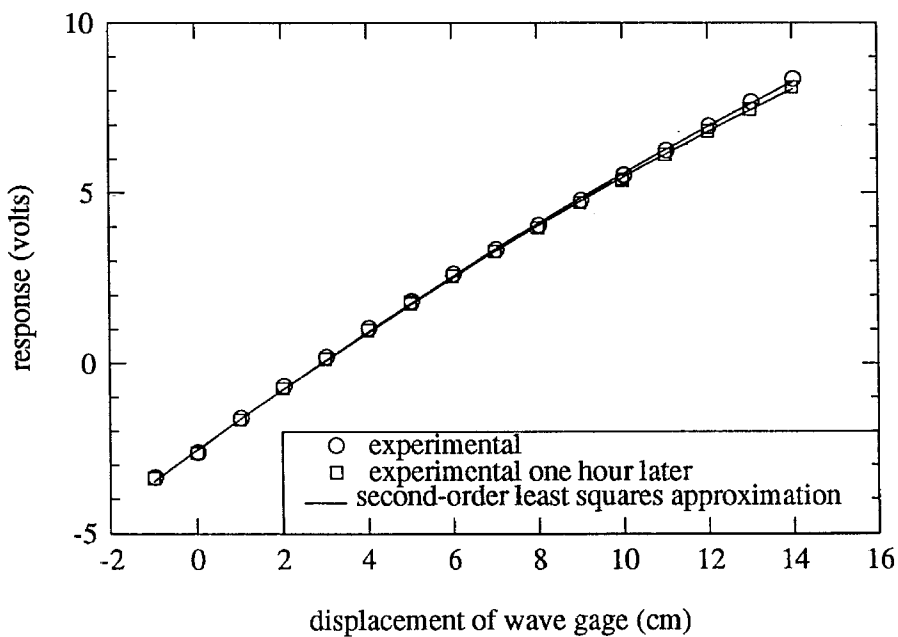


Figure 4.1.15 Calibrations of a wave gage spaced one hour apart.

Both Wiegel (1955) and Dean and Ursell (1959) have dynamically tested resistance wave gages over a wide range of frequencies and amplitudes. They both found the errors in amplitude were within $\pm 5\%$ of the wave height for frequencies in the range of small scale laboratory water waves. In Section 5.2 (see Figure 5.2.4), a comparison between measurements obtained with a wave gage and a laser induced fluorescence (LIF) system is presented. This comparison shows the wave gage completely resolved the water surface profile relative to the results obtained with the LIF system. Therefore, the

wave gage appears to have an adequate frequency response to resolve the solitary waves used in this study.

When calibrating for the measurement of large waves, depending on the depth, the bottom of the wave gage may approach the wave tank bottom. Since the electrical field around the bottom of the wave gage is affected by the position of the wave gage relative to the steel tank bottom, one would expect this effect to increase as the separation

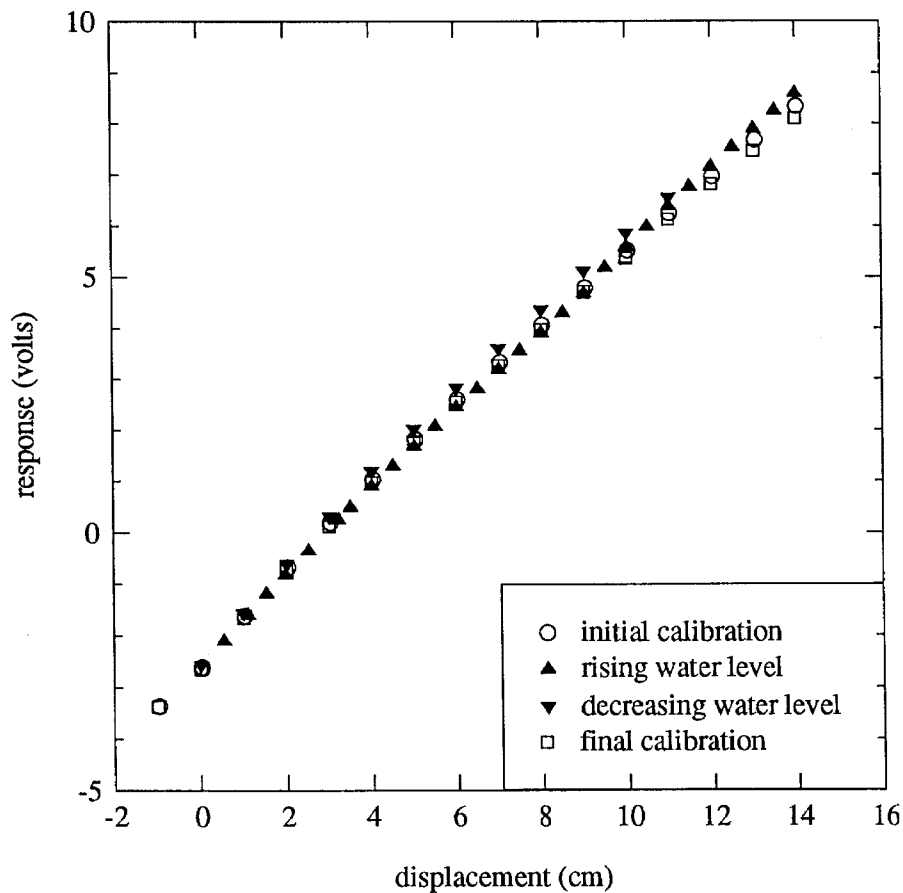


Figure 4.1.16 Calibration of the wave gage by displacing the gage relative to the water and by changing the water level on the gage.

between the bottom of the wave gage and the tank decrease. This effect is important because it may affect the calibration but not the measurement of the wave, since for the

latter, the bottom of the gage is relatively far from the bottom. To determine the size of the error introduced by this proximity effect, a wave gage was calibrated in the normal way and compared with a calibration performed by varying the water level in the tank with the gage a significant distance from the bottom. The results are shown in Figure 4.1.16. For this test, the at-rest position of the bottom of the wave gage was about 14.3 cm above the bottom of the tank with a water depth of 17.61 cm. The wave gage was lowered during the normal calibration until the base of the gage came to rest on the bottom of the tank. During the second calibration, the gage was returned to its at-rest position and the water level was raised until the submergence of the gage was equal to the amount the gage had been lowered during the normal calibration. Although the two calibrations agree for small displacements, the response produced by the variable water level method is larger for large displacements which can be seen more easily in Figure 4.1.17, where the least square error approximations to the data have been plotted. It is seen that using the results of a calibration with a variable wave gage position, as opposed

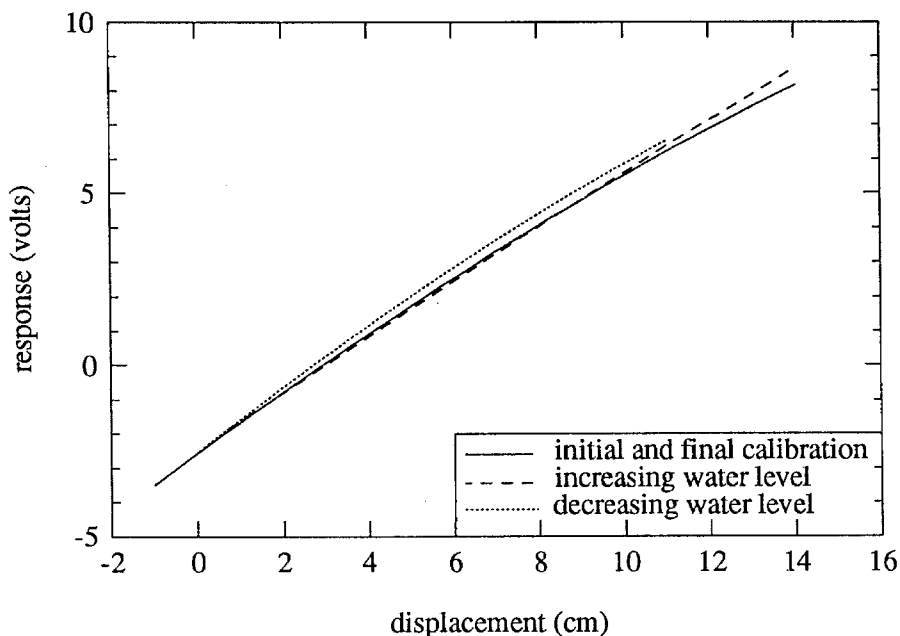


Figure 4.1.17 Second-order least square approximation of each calibration method.

to a variable water level, over-estimates the actual water surface elevation near the crest of large waves. The amount of the error is a function of the initial position of the wave gage with respect to the bottom of the tank, the initial water depth, and the resulting water levels due to the passage of the waves. For the solitary wave experiments reported in Section 5.2, the maximum error due to this effect would be less than 2% for a 10.6 cm wave in a water depth of 17.7 cm.

4.1.4 Flow Visualization Equipment

The location of wave breaking and the wave height at breaking were recorded with a Magnavox (Model VR9244/46AV) video camera which records 30 frames/sec. A shutter speed of 1/1,000 sec was used for all experiments in the tilting wave tank and the horizontal wave tank.

The kinematics of the bore and the run-up on the wall in the tilting wave tank experiments were recorded with a Redlake Corp. (Model 51-0003) high-speed movie camera, operating at 300 frames per second with a shutter speed of 1/1,000 sec and the f-stop set at 2.6. Figure 4.1.18 shows the camera located outside the tank and a mirror mounted inside the tank. This provides a split-frame where a side and a top view of the advancing bore can be viewed simultaneously. The mirror was 101.5 cm long and 16.0 cm wide. Surface velocities were obtained from the film using black buoyant foam disks. The disks were 1 cm in diameter and about 1.5 mm thick. In addition to the views from the side, the run-up on the instrumented wall was obtained with movies from the high-speed camera, mounted about 2 m in front of the wall as seen in Figure 4.1.19.

With this arrangement, three-dimensional aspects of the run-up process could be observed from this view. The runup and the location of the front of the bore were

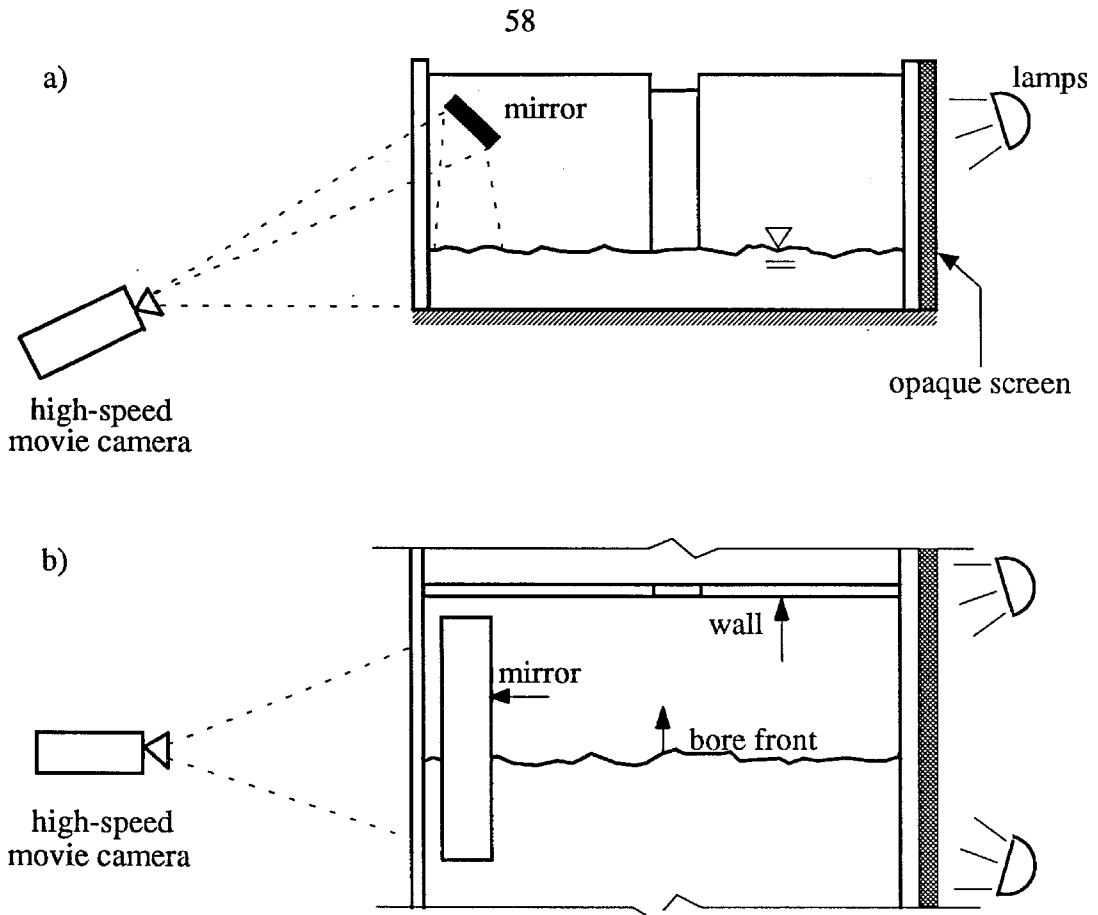


Figure 4.1.18 Schematic of the high-speed camera and lighting location while recording the bore profiles; a) as seen from the wave generator and b) from above the tank as tracers.

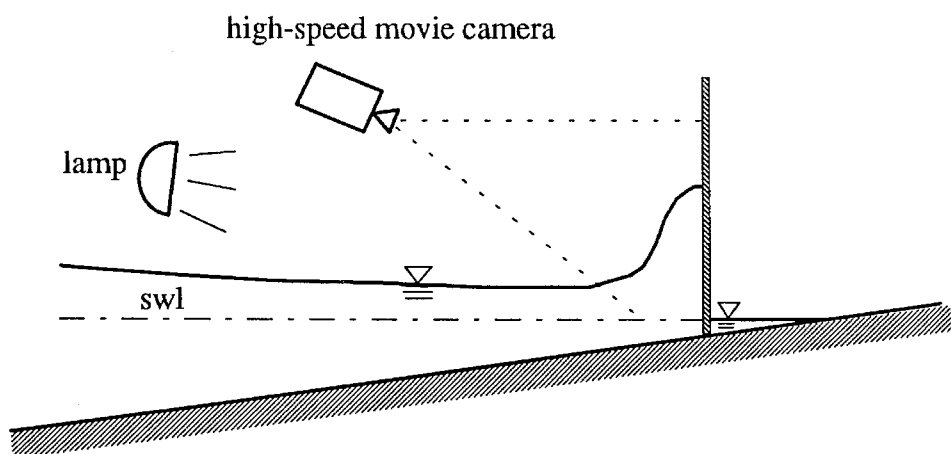


Figure 4.1.19 Schematic of the high-speed camera and lighting location while recording the runup on the instrumented wall.

determined from the spatial average of the surface across the wall and mirror, respectively. The movies of the bore profile and the runup on the wall were obtained during different runs where the same wave generation conditions were used.

4.1.5 Data Acquisition

The voltage signals from the force transducers, the resistance wave gages, and the displacement of the wave board were recorded with a personal computer (IBM AT compatible). This computer is equipped with a 12 bit resolution analog-to-digital data-acquisition card (RC card) (RC Electronics Model ISC-16) that can sample up to 16 channels at approximately 62.5 KHz each, or one channel at a maximum rate of 1 MHz. The RC card only has 128 Kbytes of RAM which limits the signal length for high data acquisition rates. The force data and the high-speed movies were referenced to the same time using a digital clock in the movie frame that displayed the time in milliseconds. An electronic signal started the data acquisition system at the instant the clock was started.

A test of this system showed that the clock and the force record began within one millisecond of each other.

4.1.6 Procedures

The numerical model developed by Goring (1979), as described in Section 3.1, was used to compute the trajectories used to drive the wave plate.

A definition sketch for the experiments is shown in Figure 4.1.20. The origin of the coordinate system is at the shoreline, with the x-axis directed toward the wave generator along the still water surface and the z-axis directed upward. The slope of the bottom, S , for all experiments in the tilting tank, was 0.02 m/m, while the depth at the wall, h , was 5 mm for all runs. The vertical wall was located 25 cm from the shoreline at $x = x_w$. The at-rest position of the wave board was $x = 24.02$ m. The initial relative

wave height, H_0 / h_0 , was determined using a resistance wave gage located at $x = 21.39$ m, where $h_0 = 42.8$ cm. The wave height at breaking, H_b , and the breaking location, x_b , were recorded with the Magnavox video camera. Once the solitary wave shoaled, it propagated as a turbulent bore and has a maximum wave height of H at the instant its tip strikes the wall. The profile of the incident bore and its celerity, the runup history on the vertical wall, and the water particle velocities along the free surface of the bore were recorded with the high-speed movie camera.

A minimum of six experiments were conducted for each wave condition. The profile of the initial wave and the breaking wave were determined using a resistance wave gage and

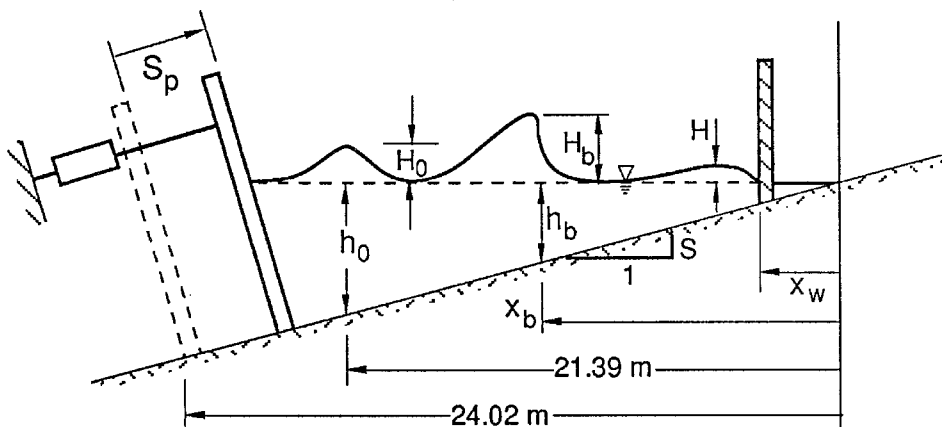


Figure 4.1.20 Definition sketch showing solitary wave generation in a tilting wave tank which caused the wave to break and propagate to the vertical wall as a turbulent bore.

a video camera. The trajectory of the wave generator was also recorded during these runs. The force on the wall was recorded simultaneously with the high-speed movies of the impact process, but without wave gage records for four runs. This was necessary because at the rate the force data were collected (1 KHz), the computer memory was insufficient to record the wave data and wave board trajectory at the same time. This was not considered a problem, since it has been found that the initial wave can be

generated with a repeatability in amplitude of less than 1%. In addition, the forces were to be related to the wave-generated bore, whose characteristics were recorded along with the force time history.

The first two runs were used to establish the incident and breaking wave conditions. The approximate location where wave breaking occurred was observed during the first run while recording the incident wave profile (with the wave gage) and the wave plate trajectory. A 2 cm square grid drawn on a transparency was attached to the glass side wall to cover the region where the inception of wave breaking occurred. The second run with the same initial conditions was performed and the inception of wave breaking was recorded with the video camera. The wave plate trajectory and initial wave profile were also recorded for this run to check the reproducibility of the experiment. The still water level and fiduciary marks spaced horizontally at 50 cm intervals were used to determine the location of the grid with respect to the wave tank geometry. From the video record, the inception of breaking was defined at the instant a multi-valued free surface developed. All the initial wave conditions for this portion of the study conducted in the tilting tank produced plunging, breaking waves.

The third and fourth runs were performed with the high-speed movie camera placed as shown in Figure 4.1.19. This provided a record of the run-up height on the instrumented wall which could not be obtained from the movies collected during the fifth and sixth runs. After generating the wave, the movie camera and clock were started by hand.

The fifth and sixth runs were performed with the high-speed movie camera placed as shown in Figures 4.18(a) and (b) while recording the force on the wall. This provided a record of the bore profile and a view of the three-dimensional bore front with the

mirror. Before generating the wave, about 30 of the buoyant disks (described in Section 4.1.4) were placed between 0.5 m and 2.5 m in front of the wall, under the mirror in the region of the tank within about 16 cm of the glass side-wall.

Run-up heights, velocities of the particles, and surge profiles were obtained from a frame-by-frame analysis of the high-speed movies. Errors in estimating the water surface and particle locations are about ± 2 mm and the time of each movie frame is known to within ± 0.0005 sec. Thus, the maximum error in the water surface profiles is less than 10% of the smallest incident bore height (2.4 cm), while the maximum error in the velocity measurements is less than 2% of the bore celerity for each wave condition.

A sample of the analyzed record of the force on the instrumented wall is shown in Figure 4.1.21. To resolve the force adequately, the frequency components above 55 Hz (including the 60 Hz AC noise) that are present in the signal were eliminated by using a low-pass filter. This noise is primarily caused by the amplifier used in the circuit which, after filtering, was reduced to a standard deviation expressed as a force of 0.035 N. The resulting force history is shown in Figure 4.1.21(b). The 55-Hz limit was determined by examining the spectrum for the percentage of energy in the recorded force both before and after the wave impact. The corresponding normalized energy spectra for one experiment are shown in Figures 4.1.22(a) and (b), where the latter is an expansion of Figure 4.1.22(a) below about 100 Hz. It is obvious from these spectra that a frequency cut-off of 55 Hz. will retain all of the important aspects of the signal resolved with this force cell arrangement. The evidence of electrical noise at 60 Hz is obvious in Figure 4.1.22(b) for both records.

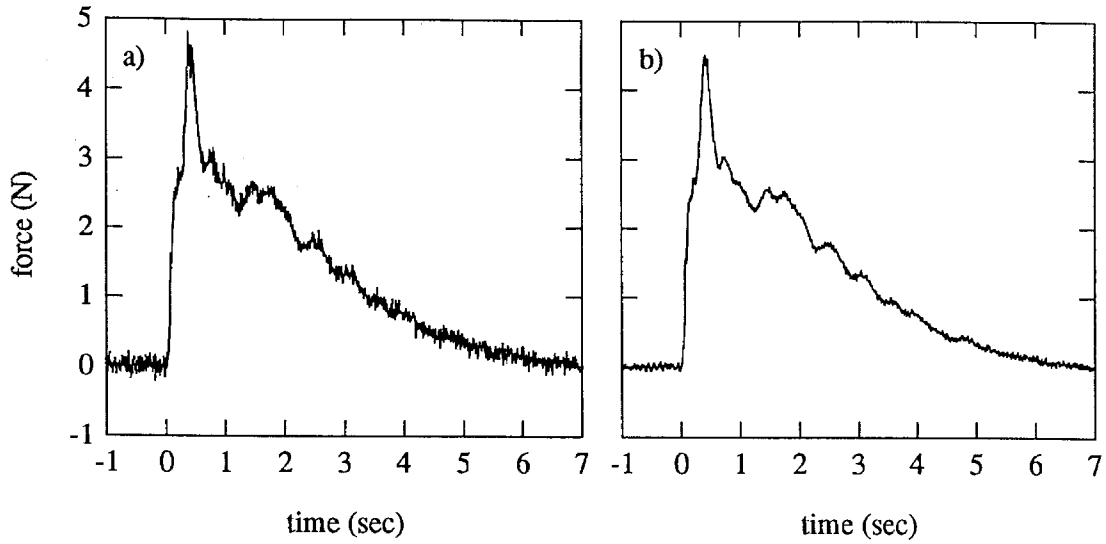


Figure 4.1.21 (a) Measured force due to an incident wave, $H_0/h_0 = 0.288$, with $h_0 = 42.78$ cm; (b) signal after applying a numerical low-pass filter at 55 Hz.

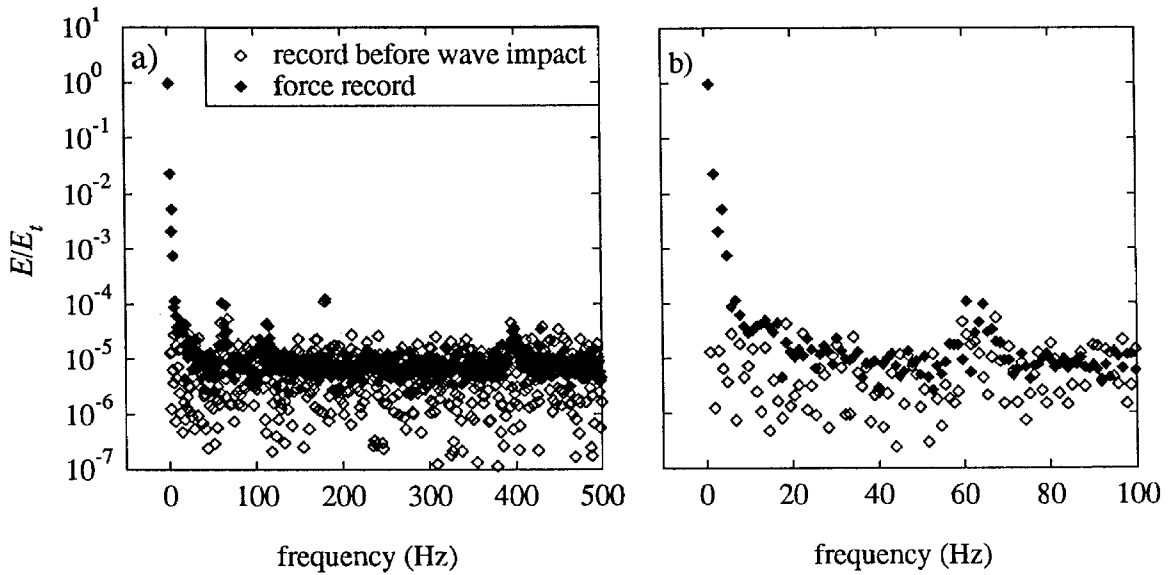


Figure 4.1.22 Normalized energy spectrum from (a) force record before impact shown in Figure 4.1.21; (b) expanded frequency scale (total energy in force record, E_t was 1.221 N^2s).

4.2 Horizontal Wave Tank Experiments

4.2.1 Tank and Wave Generator

This wave tank is composed of 12 identical modules; a drawing of one module is shown in Figure 4.2.1. Each module is 3.048 m long giving a total tank length of 36.57 m. The tank is 39.6 cm wide and 61 cm deep. The tank sidewalls are composed of 1.28 cm thick plate glass windows. The tank bottom is composed of a structural steel channel which is painted to produce a reasonably smooth bottom. There are 2.54 cm diameter stainless steel rails (as seen in Figure 4.2.1) and a steel measuring tape located along the top of the wave tank.

The wave generator is similar to the one used in the tilting tank. The wave generator in this tank is designed so that it can be powered by either of two available actuators. The actuator used for this study (Miller Model No. DH77B) has a stroke of 2.44 m, a bore diameter of 6.35 cm, and transfers its load through a 3.49 cm diameter rod. This arrangement produces a net bearing area of 22.1 cm² for the oil supply. Both actuators are mounted to a welded steel frame which is bolted into the concrete wall adjacent to the tank (see Figure 4.2.2). The hydraulic actuators draw their oil supply from the same pump and reservoir system as the actuator on the tilting tank. The actuator is controlled by the same type of valve and controller circuit described in Section 4.1.1. The motion of the wave plate is monitored with a linear displacement transducer (LDT) (MTS Corp. Model 01109050100) which has a 2.44 m stroke. The output from the LDT is compared to the desired trajectory in the feedback control system as with the wave generator used in the tilting wave tank.

The microprocessor, function generator, and minicomputer used for the tilting wave tank study to control wave generation, were replaced prior to conducting the horizontal tank experiments. A 12 bit analog-to-digital and digital-to-analog (Omega Model DAS-16F) card, resident on the motherboard of a personal computer (IBM AT

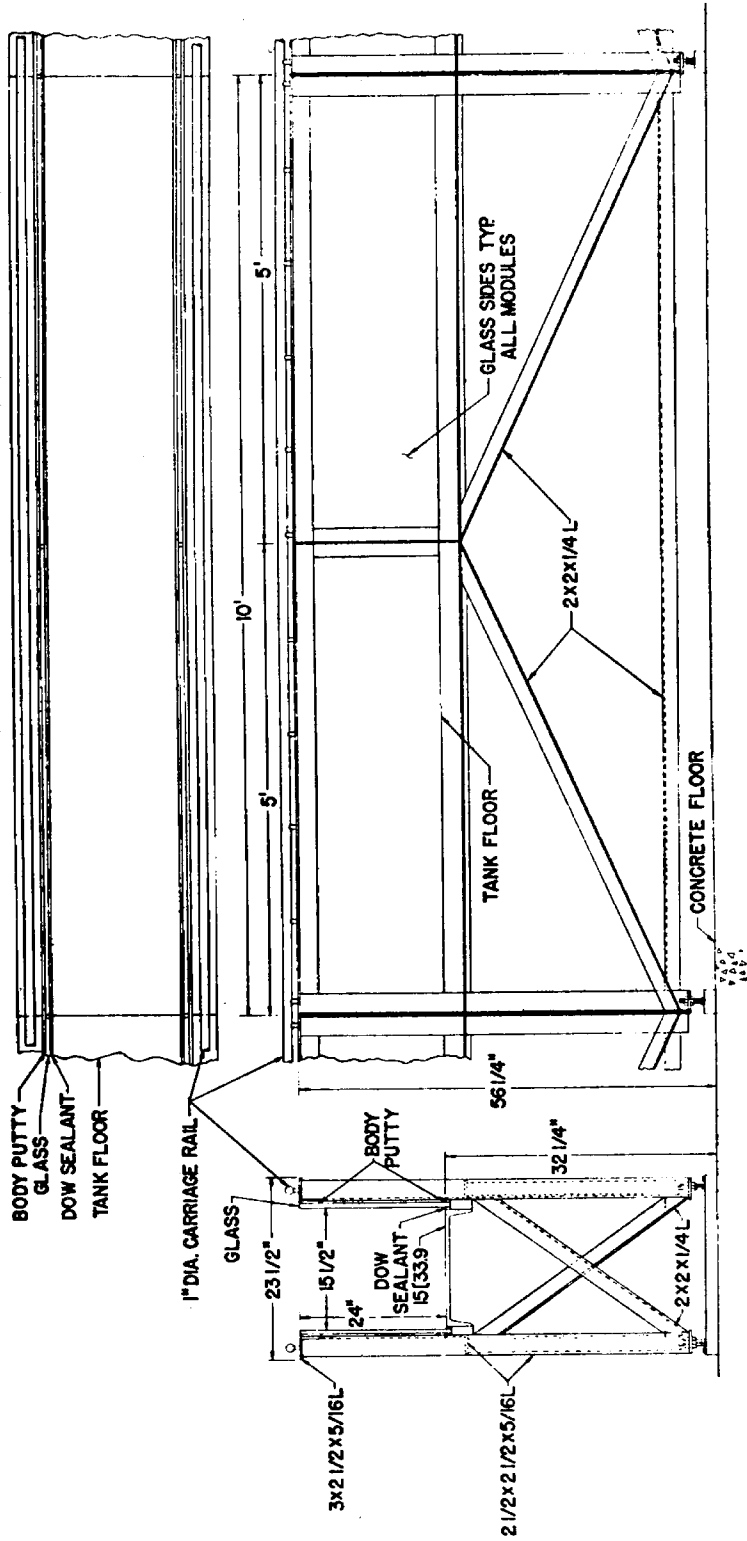


Figure 4.2.1 Schematic drawing of a typical section of the horizontal wave tank (after French (1969)).

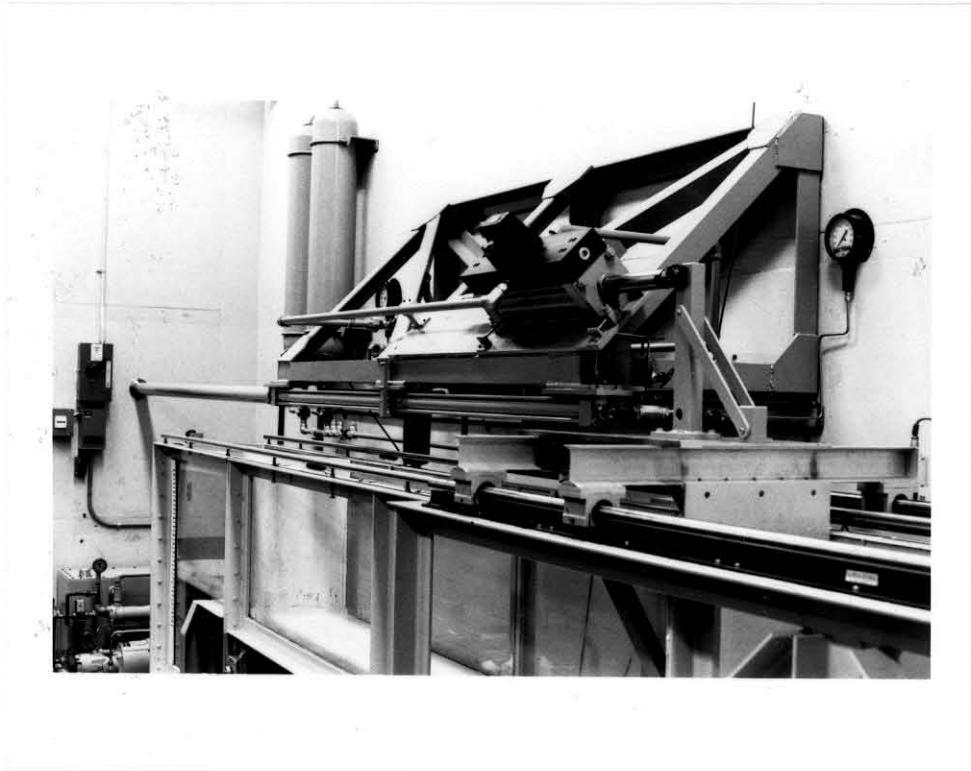


Figure 4.2.2 Photograph of the wave generator in the horizontal wave tank (after Goring (1979)).

compatible) was used to produce the signal for the servo-controller. The wave plate trajectory file is stored in the random access memory of the computer and the Omega card behaves as a function generator by producing an analog signal from the stored trajectory. The Omega card has two software selectable counters which can produce a wide range of sampling rates from one sample per hour to 100 KHz. The trajectory used to drive the wave generator was obtained using the method of Goring (1979) as described in Section 3.1.

4.2.2 Vertical Wall

The vertical wall used for this study extends the entire width of the tank and was composed of false walls to either side of an instrumented section, located on the centerline of the tank. The instrumented section, which was 60.96 cm high and 6.04 cm wide, was machined from a 1.90 cm thick aluminum plate as shown in Figure 4.2.3. Figure 4.2.4 shows the steel and aluminum structure used to support the force cells and the instrumented wall. In Figure 4.2.4, all the members except the "I" beams were aluminum, and all connections were bolted. The steel "I" beams were bolted to the steel angles which comprise the top of the wave tank. Six lead bricks with a total mass of 60 kg were used to hold the bottom of the "T" section in place. The false walls on either side of the instrumented wall were made from 1.27 cm thick aluminum plate. The false walls were supported by a structure which was independent of the support for the instrumented wall. The supporting structure for the false walls is shown in Figure 4.2.5. The instrumented wall, false walls, and all the aluminum parts of the supporting structures were anodized to minimize corrosion.

The same amplifier system used during the study in the tilting tank was used for these experiments. However, the 60 Hz AC power supply was replaced with a 12 v DC power supply obtained from two automobile batteries. This power supply reduced the background noise level in the force cells to a standard deviation expressed in units of force (at the amplification used in the force measurements), ranging from 0.035 N to 0.050 N with no filtering. The use of the DC power supply also eliminated the small peaks in the spectra of Figure 4.1.22(a) at 60 Hz, 120 Hz, and 180 Hz.

During the experimental investigation, the wall was calibrated using the device shown in Figure 4.1.12. On one occasion, it was also calibrated hydrostatically by varying the water level and comparing the measured force with the hydrostatic force

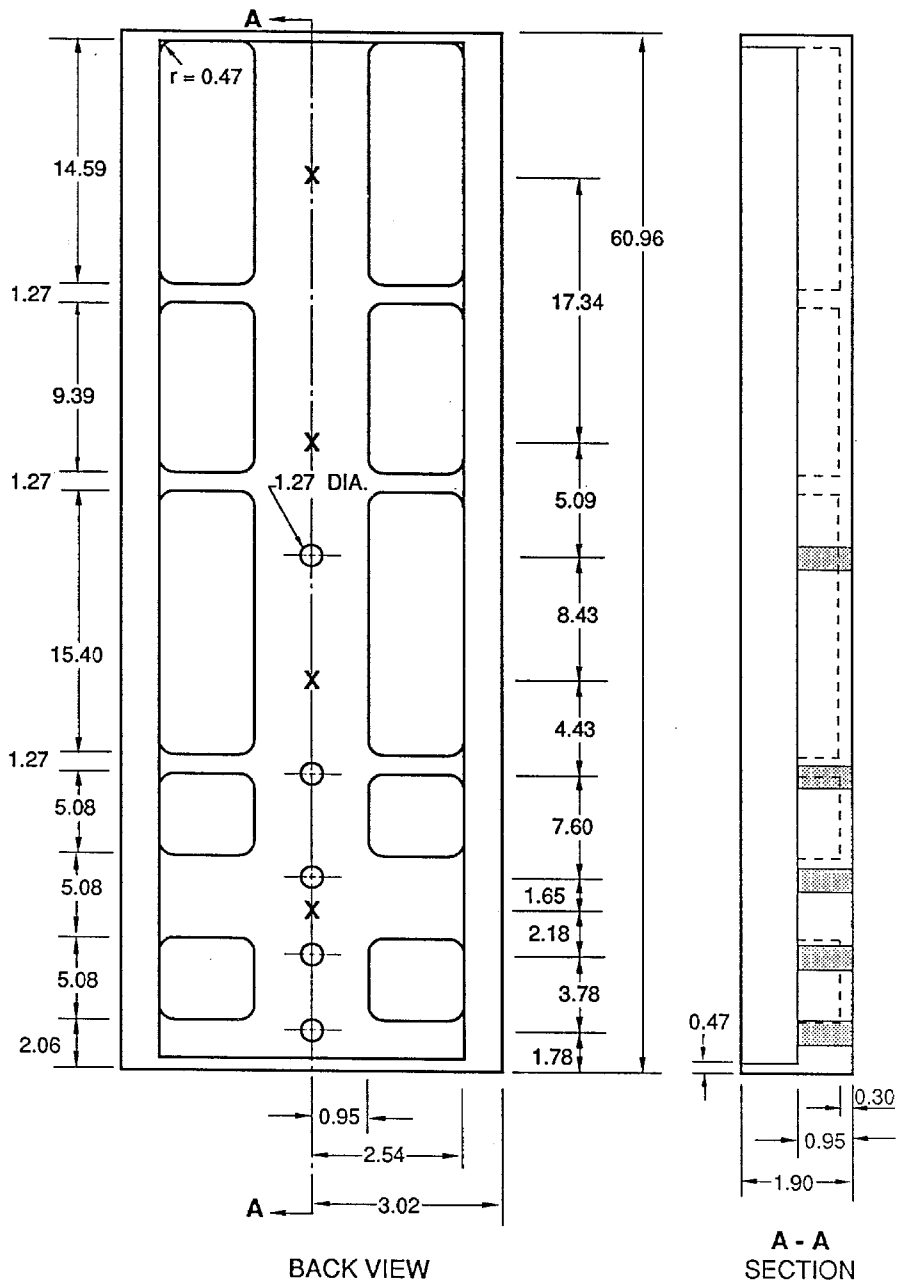
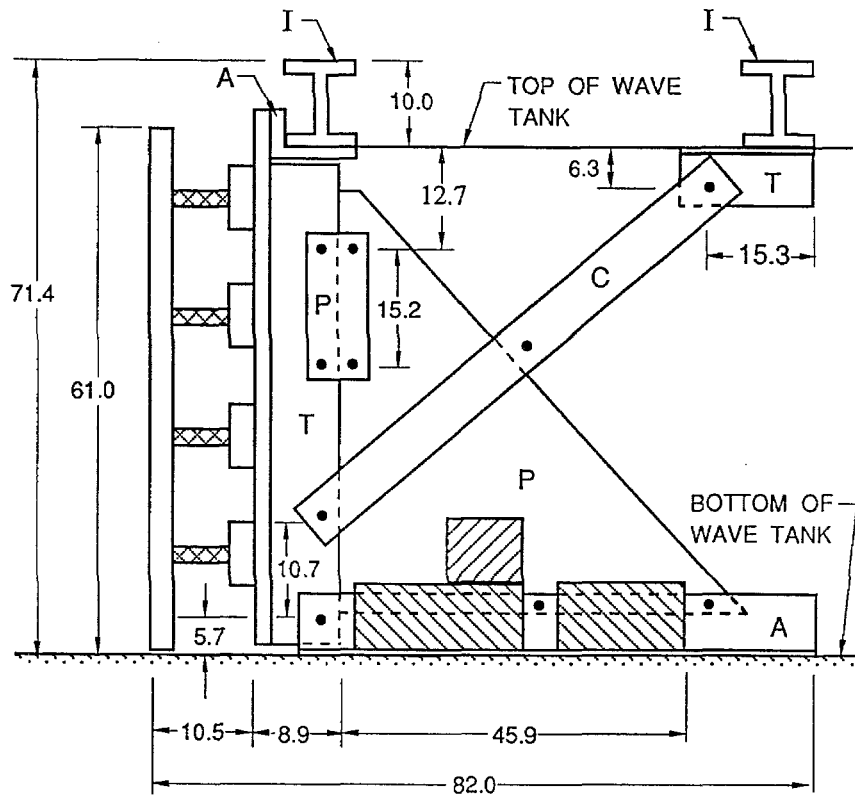


Figure 4.2.3 Schematic drawing of the instrumented wall used in the horizontal wave tank experiments (all dimensions are in cm).





-  FORCE TRANSDUCER
-  LEAD BRICK
- A ANGLES
- C CHANNEL
- I STEEL "I" BEAM
- P PLATE
- T "T" SECTION

Figure 4.2.4 Schematic drawing of the supporting structure for the instrumented wall shown in Figure 4.2.3 (all dimensions are in cm).

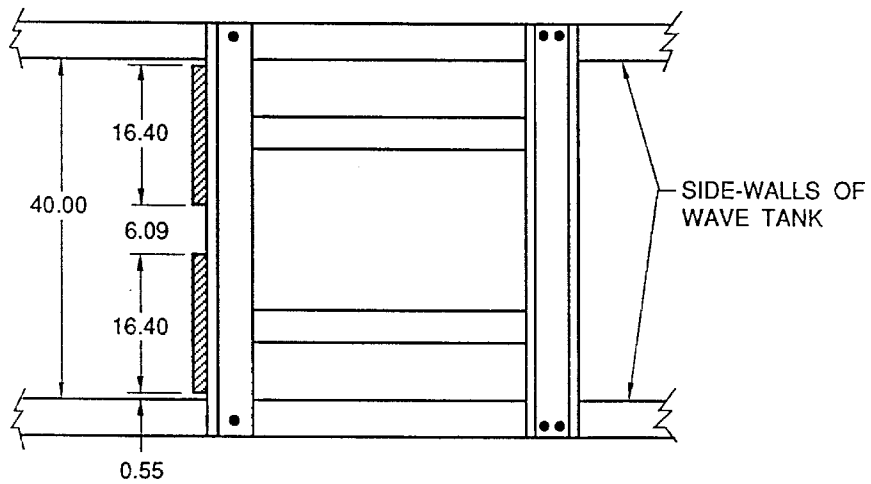
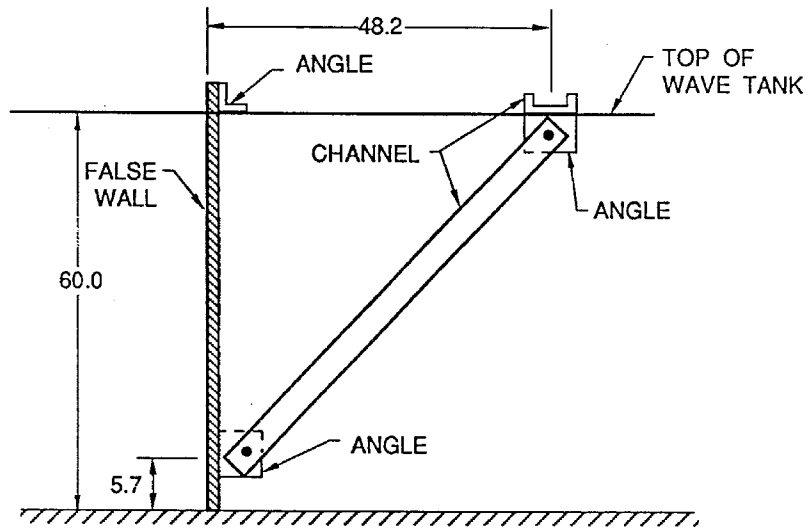


Figure 4.2.5 Schematic drawing of the supporting structure for the false walls in the horizontal wave tank (all dimensions are in cm).

computed from the difference of the measured depths on each side of the structure. The results from both of these calibration methods are shown in Figure 4.2.6. In Figure 4.2.6 the symbols are the measured data while the solid line is the relation: measured force = applied force. The agreement between the applied and measured forces are excellent for both calibration procedures. Therefore, during all the experiments conducted, the instrumented wall was calibrated using the device shown in Figure 4.1.12.

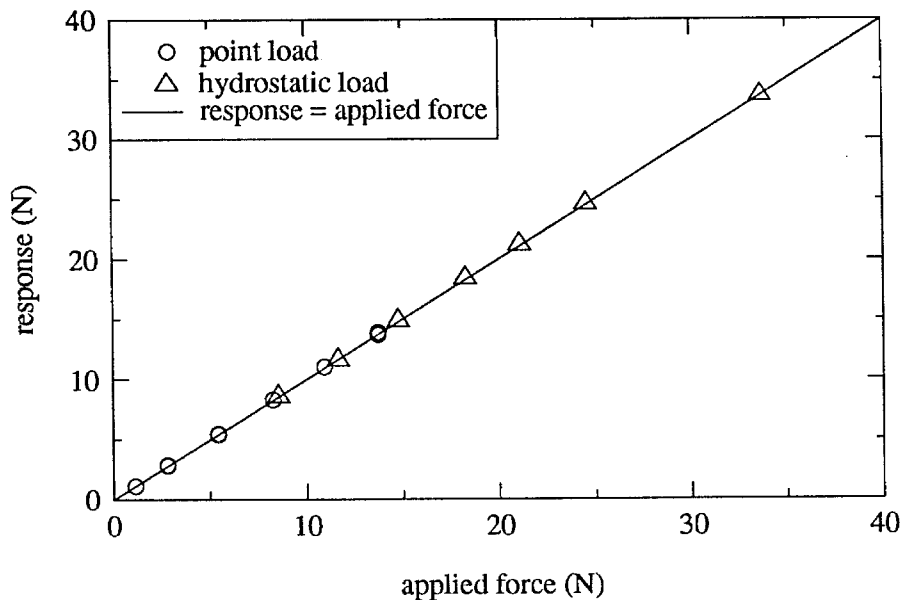


Figure 4.2.6 Response of the wall due to a hydrostatic load and a point load.

The total mass of the instrumented section of the wall and the pressure cell (see Section 4.2.3) which was supported by the force transducers, was 1.009 kg. The four force transducers were mounted with the objective to increase the lowest natural frequency of the system as much as possible. This was accomplished by attempting to equalize the amount of mass effectively supported by each transducer. The results of a test to determine the natural frequencies of the system is shown in Figure 4.2.7. An impulsive load was applied by tapping the instrumented wall with the end of a small screwdriver. The output of each of the force transducers is presented in Figure 4.2.7.

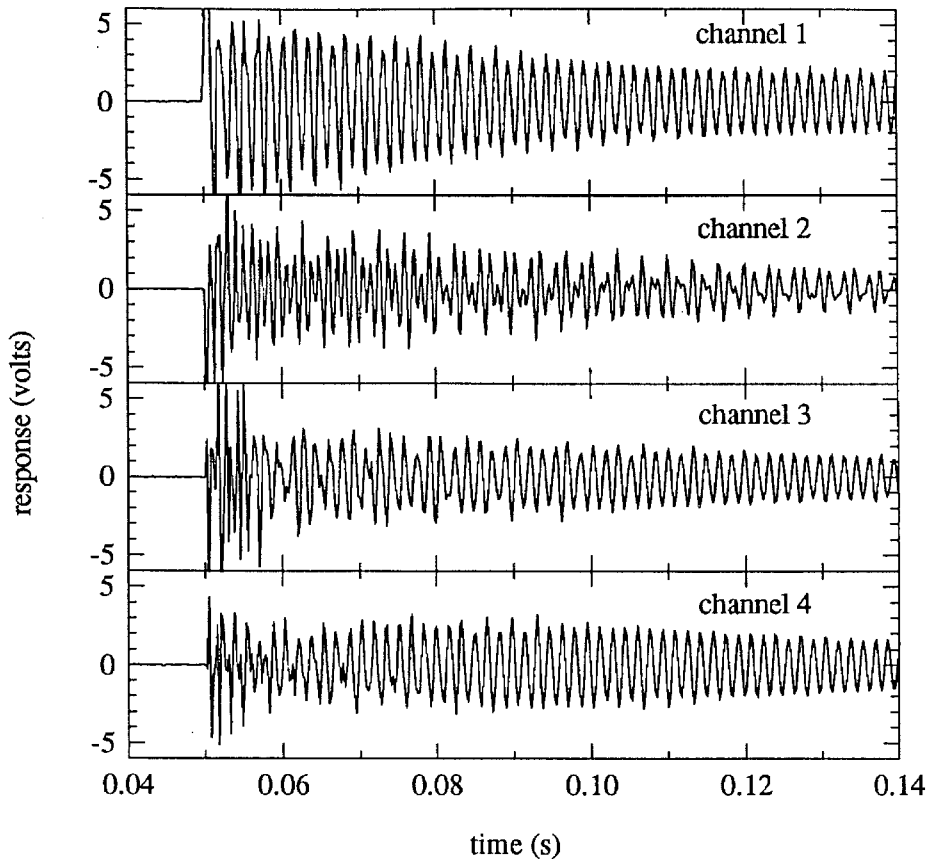


Figure 4.2.7 Output of each force transducer due to an impulsive load applied to the wall.

The spectra of these outputs were then obtained using the Fast Fourier Transform (FFT) method, and these are shown in Figure 4.2.8(a). Figure 4.2.8(b) shows the spectrum of the force time history. Two modes of oscillation of the wall can be seen at 613 Hz and 909 Hz. It is of interest to compute the frequency of the first mode of oscillation for comparison. The estimate is obtained by assuming the entire mass of the wall is oscillating on a spring with a stiffness equal to the sum of the spring constants of each of the four force transducers. Using the mass of the wall and the spring constants shown in Table 4.1, a frequency of 750 Hz is calculated. If the force cells were not arranged to equalize the mass supported by each force cell, then one would expect the frequency of the first mode of the wall to be smaller than this. This may explain the discrepancy between the 613 Hz mode and estimated frequency of 750 Hz.

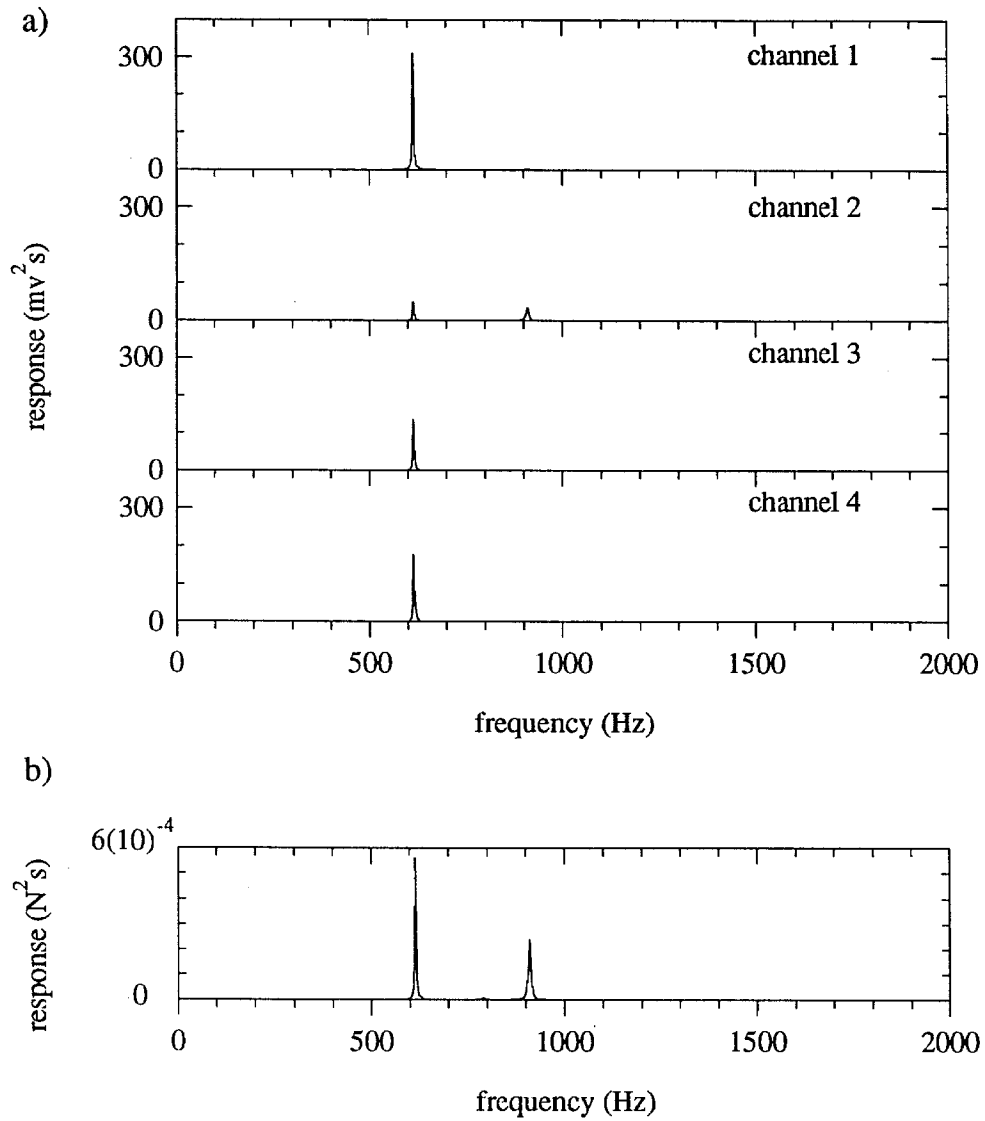


Figure 4.2.8 (a) Spectra of the response in each force transducer (shown in Figure 4.2.7) due to an impulsive load; (b) spectrum of the force due to the free vibration of the wall.

The effective moment-arms of the force cells about the bottom of the wave tank were calculated from measurements using point loads applied at eight elevations using the calibration device shown in Fig. 4.1.12. The moment-arms were then used as the unknown coefficients in a linear least squares error scheme. Table 4.2 shows the known locations of the force cells above the bottom of the tank and the effective moment-arms calculated from the least squares error analysis. Figure 4.2.9 shows the applied moment

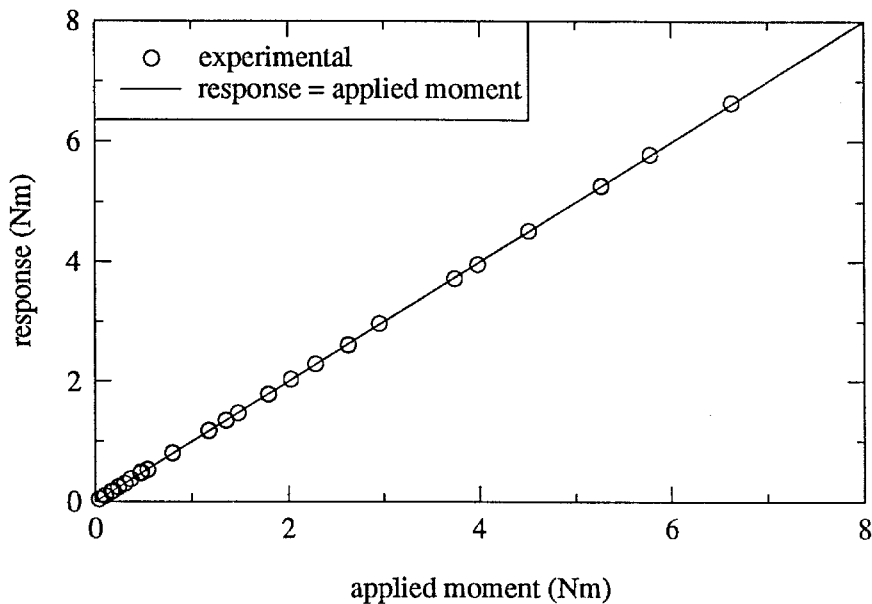


Figure 4.2.9 Response of the wall due to an applied moment.

using the calibration device as the abscissa, the ordinate, the moment calculated from the corresponding measured force, and the effective moment-arm. The agreement between the applied and measured moment is excellent, indicating this is a reasonable method of determining the effective moment arms of a structure of this type. The effective moment-arms shown in Table 4.2 were used with the measured force from each cell to calculate the moment of the hydrodynamic load about the tank bottom for all the experiments in the horizontal tank. Once the wall was installed and the effective

moment-arms were calculated for each force transducer, the instrumented wall was not removed until the experiments were completed.

| Channel number | Measured location (cm) | Calculated location (cm) |
|----------------|------------------------|--------------------------|
| 1 | 7.74 | 7.60 |
| 2 | 21.42 | 21.85 |
| 3 | 34.94 | 34.36 |
| 4 | 52.28 | 51.96 |

Table 4.2.1 Measured and calculated (using a least squares analysis) vertical locations of the force transducers above the bottom of the wave tank.

4.2.3 Pressure Transducer

The pressure transducer (Endevco Model 8510B-2) was mounted in a housing (see Figure 4.2.10) to minimize thermal effects and to protect the sensitive diaphragm against corrosion. The location of the pressure transducer in Figure 4.2.10 is shown with the dashed line. The diameter of the transducer is 0.38 cm. Figure 4.2.11 is a photo of the pressure cell mounted in the housing. The housing used in this study is similar to the stainless steel housing developed by French (1969) to minimize thermal effects in his pressure transducer. French (1969) found that when a pressure transducer is exposed to air then suddenly wetted by a water wave, there can be an appreciable portion of the response which is due to thermal effects. The thermal effect on the signal is completely different from the hydrodynamic load which is the signal of interest. Unless the time dependence of the thermal effect is known, it cannot be eliminated from the signal, thus it constitutes an error in the pressure measurement. For this study, both a brass and a plastic (Delrin) housing were constructed. The reason for this is discussed below. French (1969) also analyzed the effect of a finite transducer size on the resulting pressure measurement as compared to the actual hydrodynamic pressure distribution which acts over the sensitive surface of the transducer. A transducer of finite size integrates the

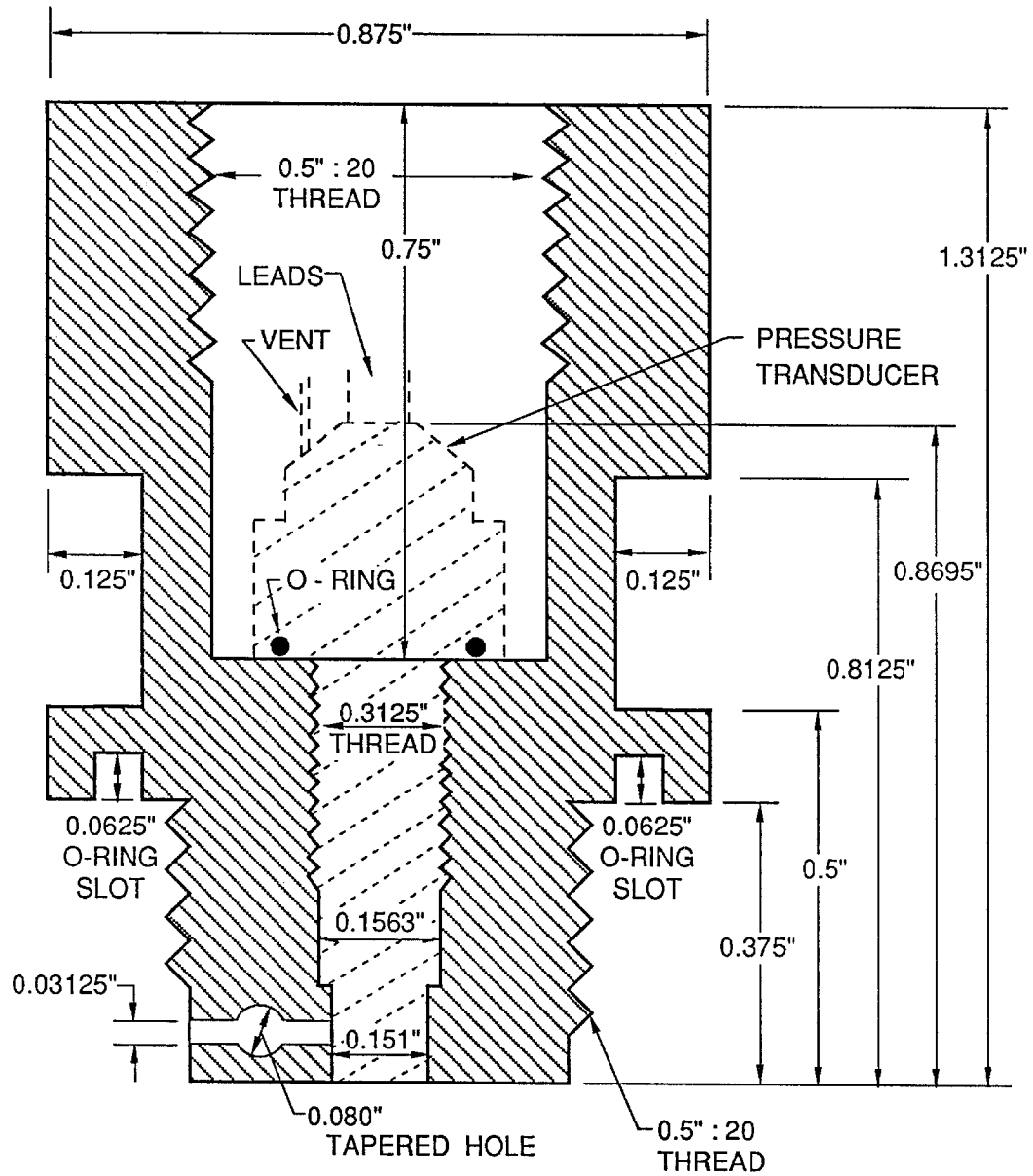


Figure 4.2.10 Schematic drawing of the brass and plastic (Delrin) housings used to isolate the pressure transducer.

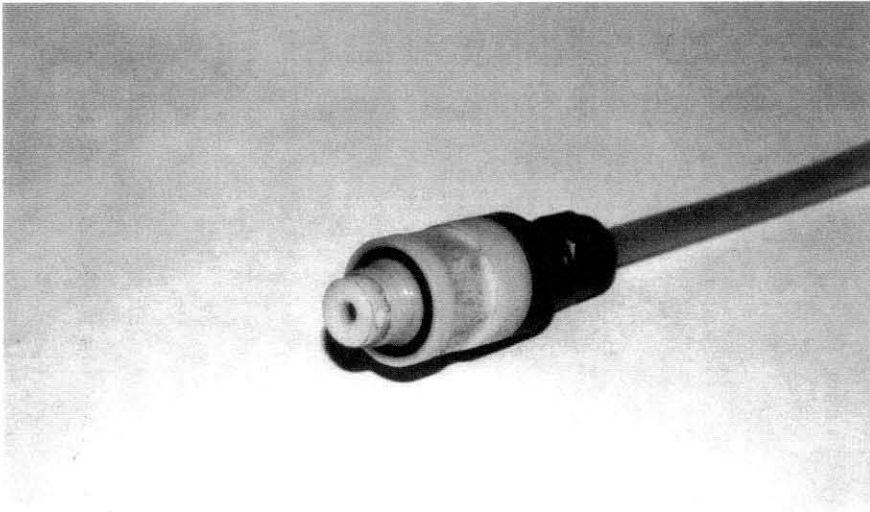
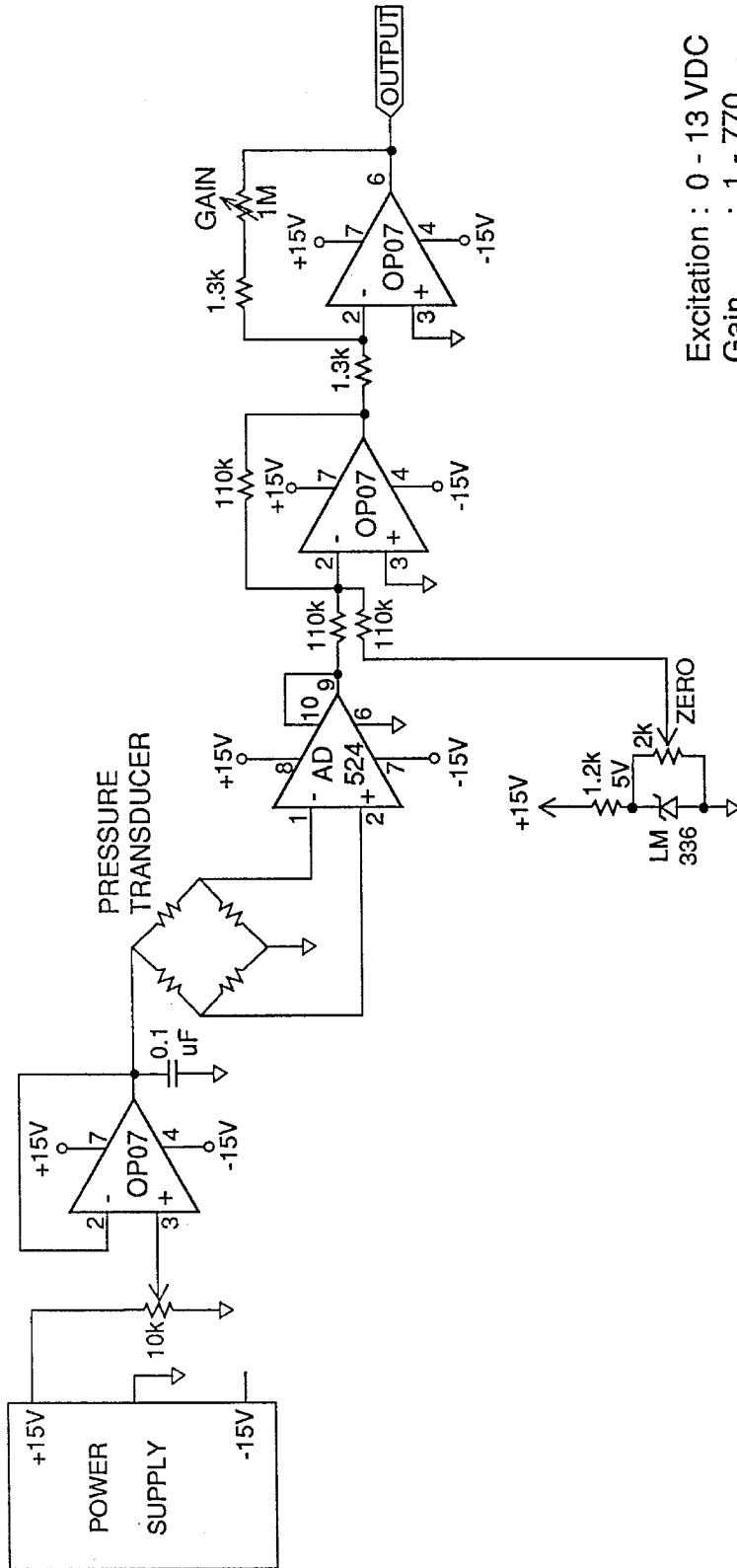


Figure 4.2.11 Photo showing the pressure transducer mounted in the plastic housing.

pressure distribution which causes small scale variations in the pressure to be averaged out. Therefore, if the largest pressures developed are associated with a very small spatial scale, then the measured pressure will record these fluctuations with a reduced amplitude. The natural frequency of the pressure transducer relative to the frequency scale of the hydrodynamic pressures can also contribute to an attenuation of the pressure signal.

A schematic for the power supply and amplifier used with the pressure cell is shown in Figure 4.2.12. The electronics allowed a variable excitation voltage, an offset capability and amplification, by factors ranging from unity to 770.

Care was taken while inserting the pressure cell in the housing to make sure no air was trapped inside the cavity formed in front of the pressure cell. The front face of the housing was cleaned and clear cellophane tape (Scotch Model 850-transparent) was

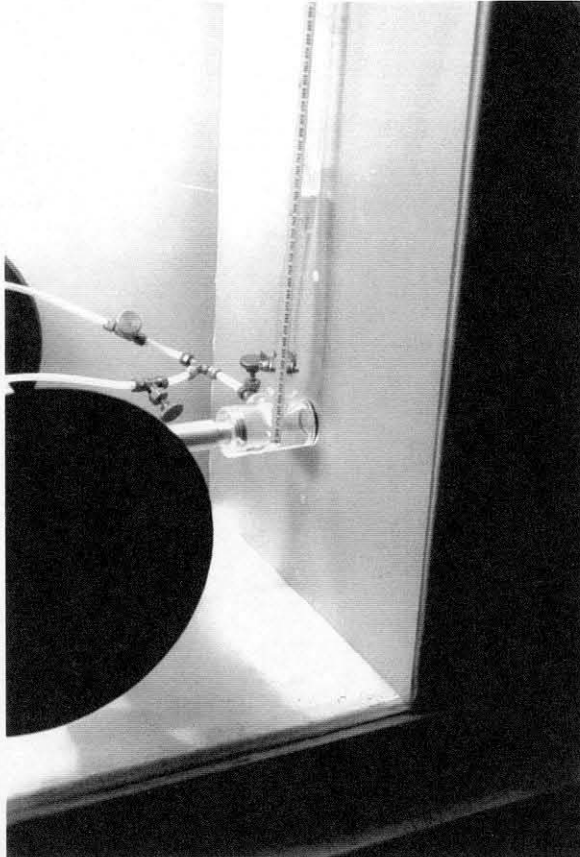


Excitation : 0 - 13 VDC
Gain : 1 - 770

Figure 4.2.12 Circuit diagram of the pressure cell amplifier.

placed over the face of the housing. A syringe was filled with about 2 cc of one centistoke silicone oil (Dow Corning 200 Fluid) from a beaker which had been deaerated using a vacuum pump for 3 hours to eliminate air bubbles. The housing was tilted to the right and held at approximately a 45 degree angle with the bleed port pointing in an upward direction. The oil was inserted at the bottom corner formed by the housing and the cellophane tape and allowed to fill the cavity and bleed port up to the level in the housing where the "O"-ring of the pressure transducer was to be seated. This "O"-ring seats against the horizontal ledge 0.75 inches below the top of the housing. Once the cavity and bleed port were full, a tapered teflon stopper was used to plug the bleed port. The configuration of the gage is such that the diaphragm is recessed about 2 mm, resulting in a "cup" with the sensitive face of the transducer forming its bottom. The pressure transducer was held with its sensitive face pointing upward and the small "cup" was filled with oil. Utilizing the effect of surface tension this region was filled with oil until a spherical dome of fluid was sitting over the top of the rim forming the "cup." The sides of the pressure transducer were also wetted with oil between the sensitive diaphragm and the "O"-ring along the threads. The pressure transducer was then rotated 180° and inserted into the housing. When the spherical dome of fluid touches the flat fluid surface in the housing, the air is squeezed out along the side of the pressure transducer. Before the "O"-ring on the pressure transducer seated itself, the housing was rotated 90° so the bleed port was pointing upward. The teflon plug was then removed and the pressure transducer screwed into the housing to seat the "O"-ring, while forcing the excess oil out the bleed port. The teflon plug was then re-inserted and trimmed flush to the side of the housing wall. The leads for the pressure transducer were threaded through a 0.63 cm diameter polyflow tube which was connected to the back of the housing with an "o-seal straight thread connector" (Swagelok Model B-400-1-OR). This allowed submergence of the pressure cell and housing in water while keeping the transducer dry and the back side of the diaphragm vented to air.

The pressure cell was calibrated while mounted in the wall, prior to a given series of experiments. The arrangement shown in Figure 4.2.13 was used where the suction



4.2.13 Photo of the apparatus used to calibrate the pressure cell while it was mounted in the instrumented wall.

cups mounted to the sidewalls of the tank transferred the reaction force taken by a channel section to the glass walls of the wave tank. A bar with a stud mounted on one end was screwed into the channel section. With this bar, a compressive force could be produced on a lucite cavity which was placed over the pressure cell. The perimeter of the cavity was sealed against the instrumented wall with an "O"-ring. A system of polyflow tubes was used to control the head on the pressure transducer. A typical

calibration is shown in Figure 4.1.14 where a linear least squares approximation shown with the solid line was fit to the data. This linear approximation was used to convert the voltage response of the pressure transducer into pressure head.

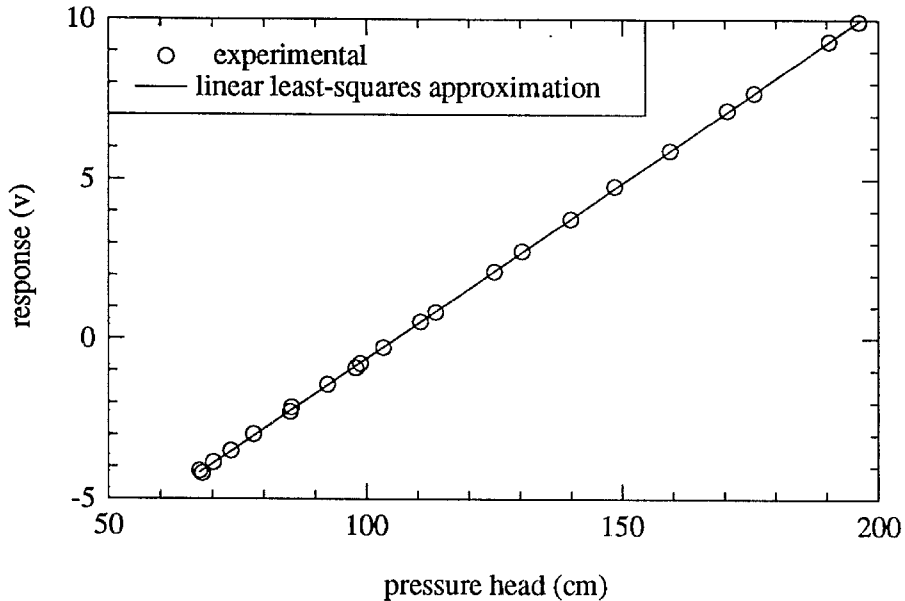


Figure 4.2.14 A typical calibration curve obtained from the pressure transducer.

Several experiments were performed to determine the temperature sensitivity of the pressure transducer when the sensitive face was suddenly wetted. The brass housing which contained the pressure transducer was mounted flush to a 5.08 cm square, 1.27 cm thick aluminum plate. This plate formed the bottom of an open aluminum box which could be mounted in a point gage to be moved up and down to immerse the transducer. The pressure cell was powered with a 15 v excitation for one half hour to allow the transducer and aluminum plate to achieve temperature equilibrium. The aluminum plate was moved into the water relatively slowly so that no hydrodynamic load was imposed on the pressure transducer. The resulting signal revealed a voltage shift due to what may be thermal effects as shown with the solid line in Figure 4.2.15. To minimize this effect, a plastic housing composed of Delrin, identical to the brass housing, was constructed.

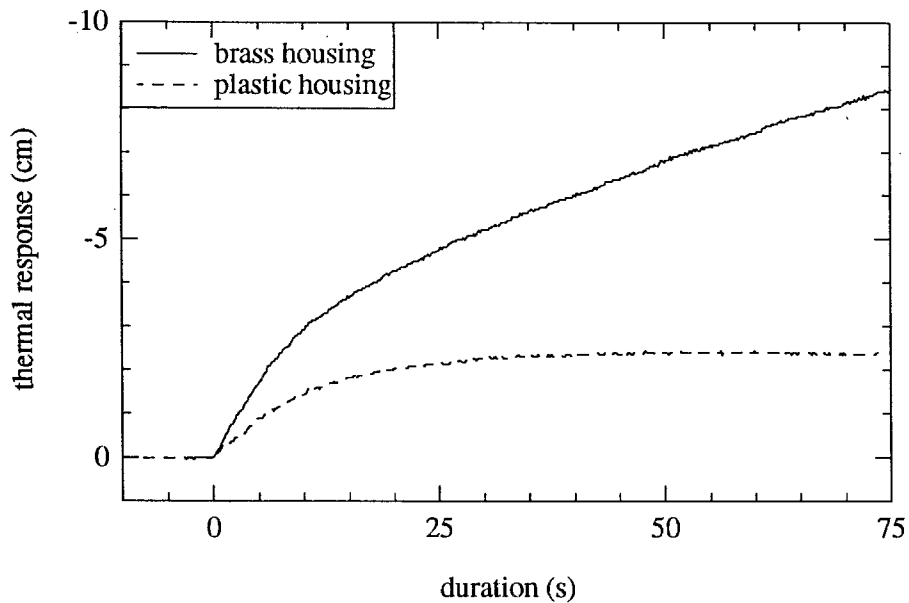


Figure 4.2.15 Effect of the housing material on the thermal response of the pressure transducer with a 15 v excitation.

The same test performed with the brass fitting was repeated with the Delrin fitting and is shown in Figure 4.2.15 with the dashed line. The thermal effect is significantly less. Thus, the transducer housing composed of Delrin was used in all of the experiments reported in Chapter 5.

The pressure transducer electronics were modified to allow a variable excitation voltage to provide a means of further reducing the difference in temperature between the transducer and the water. The pressure transducer was mounted in the instrumented wall and submerged for various amounts of time by solitary waves and undular bores. The results of these experiments, with the pressure transducer mounted in the Delrin fitting excited at 10 v, 3 v, and 2 v shown in Figure 4.2.16. The results from the brass fitting with the pressure cell which excited at 15 v, are also shown. One can see a significant decrease in the thermal offset for a given duration of submergence with the 3 v and 2 v excitation relative to the 10 v excitation used with the Delrin fitting. For all experiments

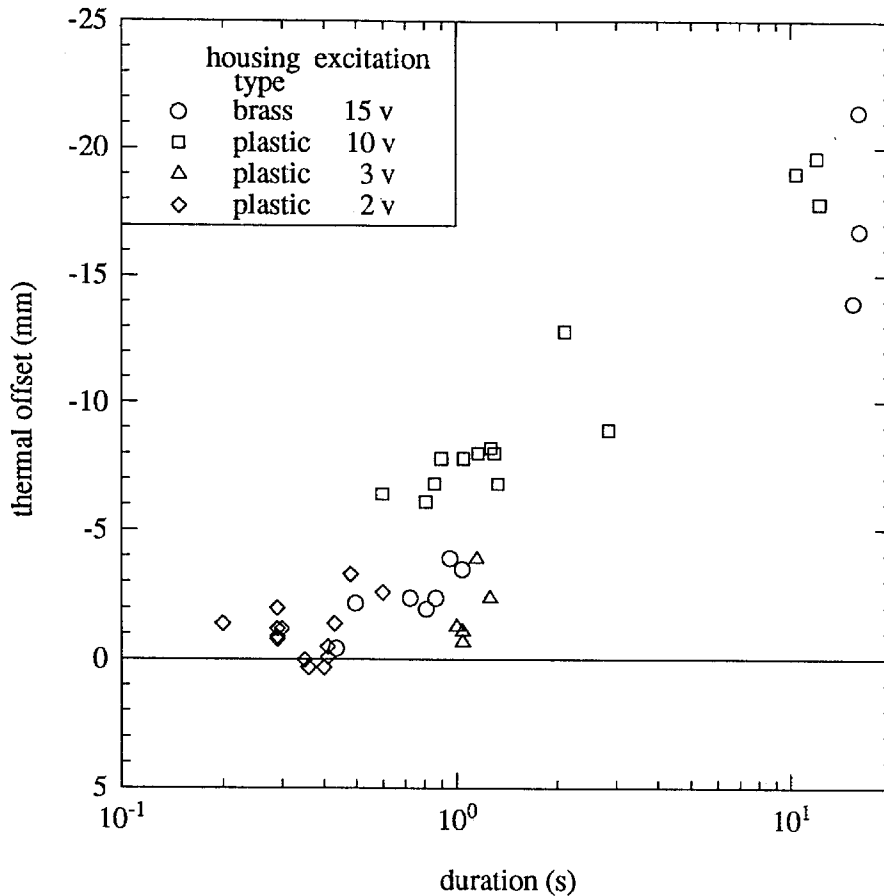


Figure 4.2.16 Thermal offset of the pressure transducer due to solitary wave and bore reflection from the wall.

with the pressure transducer, the Delrin fitting and an excitation of 2 v were used. The brass fitting with the 15 v excitation curiously produced less thermal offset than the Delrin fitting excited at 10 v. However, due to the result shown in Figure 4.2.15, the Delrin fitting was selected for the experimental program.

The pressure cell had a natural frequency in air without the housing of about 42 KHz and a natural frequency in air with the oil-filled housing of 13.0 KHz. The device shown in Figure 4.2.17 was used to determine the natural frequency of the pressure cell in the housing while submerged in various depths of water. This was done to determine if the added mass caused by the presence of water outside the oil-filled cavity decreased

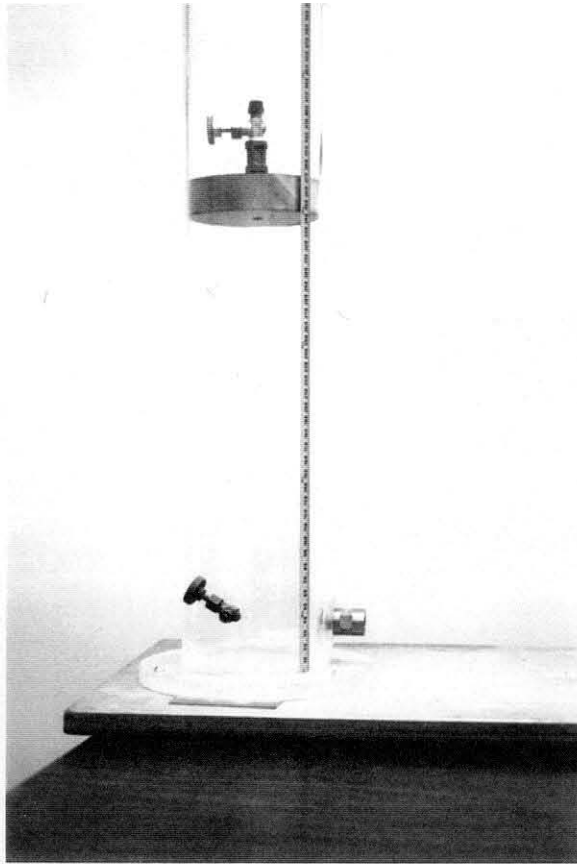


Figure 4.2.17 Photo of the lucite tube used to test the natural frequency of the pressure transducer with various water depths.

the natural frequency of the system. The cylinder shown in Figure 4.2.17 was filled with water to several depths with a wood piston floating on the water surface. The piston was tapped to provide a pressure pulse to excite the pressure cell. A typical time series of the pressure cell signal is shown in Figure 4.2.18 where the initial head on the pressure cell was 5.9 cm, plus the weight of the wood piston. There was no apparent trend in the natural frequency of the transducer for depths ranging from 5.9 cm to 38 cm. This result would be expected, since the region of fluid which contributes to the added mass is limited to an area near the transducer on the order of several diaphragm diameters. The average natural frequency computed from the measured oscillations, with four different

water depths, was 11.4 KHz. This represents a decrease in the natural frequency of 12%, relative to the value obtained in air. This implies the added mass due to the surrounding water is quite small relative to the mass of the oil and the diaphragm.

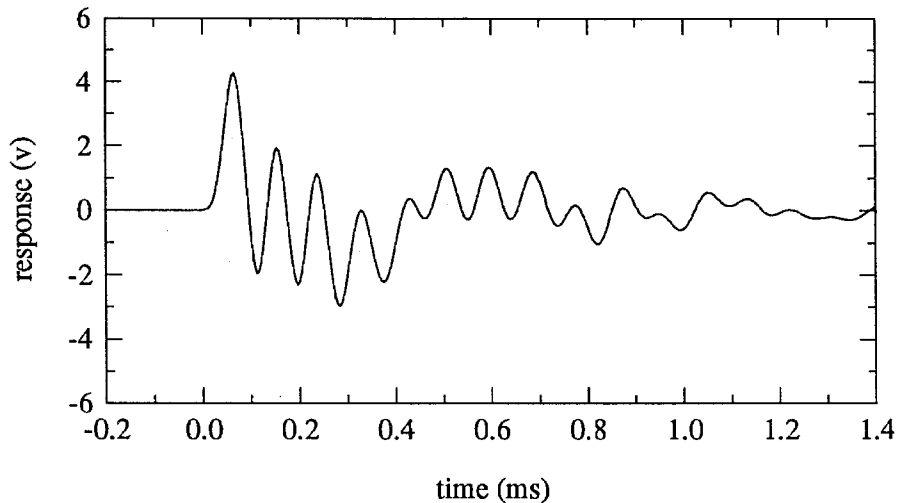


Figure 4.2.18 Response of the pressure cell due to an impulsive load applied to a water column.

4.2.4 Dam Break Gate

A gate was used to create bores and surges on a dry bed by releasing a volume of water in a reservoir. This method was selected since relatively large bores and high speed surges could be produced relative to what could be obtained using broken waves or waves which run up a beach and then advance across a dry bed. Thus, using the gate allowed the experiments to be carried out on a larger scale which decrease scale effects. The gate shown in the photo of Figure 4.2.19, was designed to minimize leakage while allowing it to be quickly lifted to simulate an instantaneous release of the fluid in the reservoir. The gate is powered by a 3.17 cm diameter bore air cylinder made by Modesto. The cylinder has a 50.8 cm stroke and a rear cushion which prevents the piston from slamming into the end of the cylinder when the maximum stroke is exceeded. Nitrogen gas at 1030 KNm^{-2} is used to power the cylinder. The cylinder is mounted to

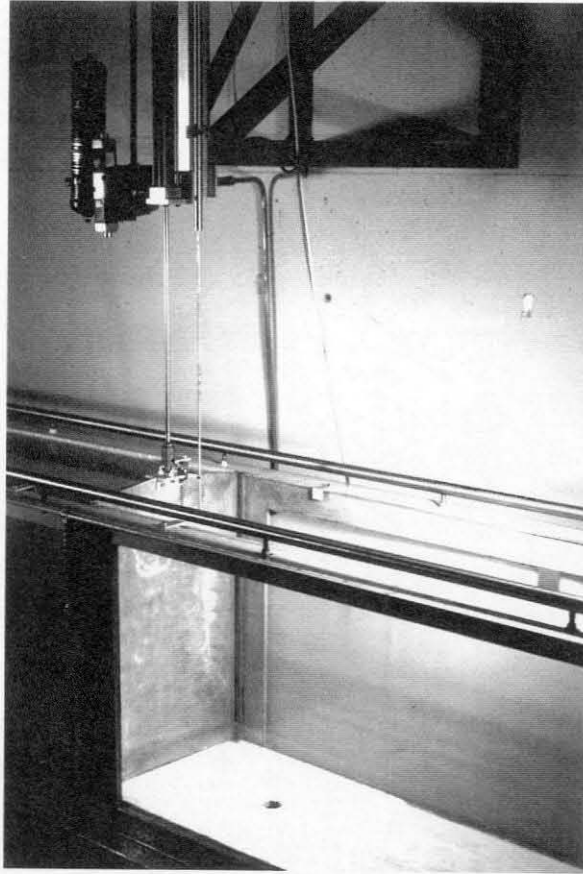
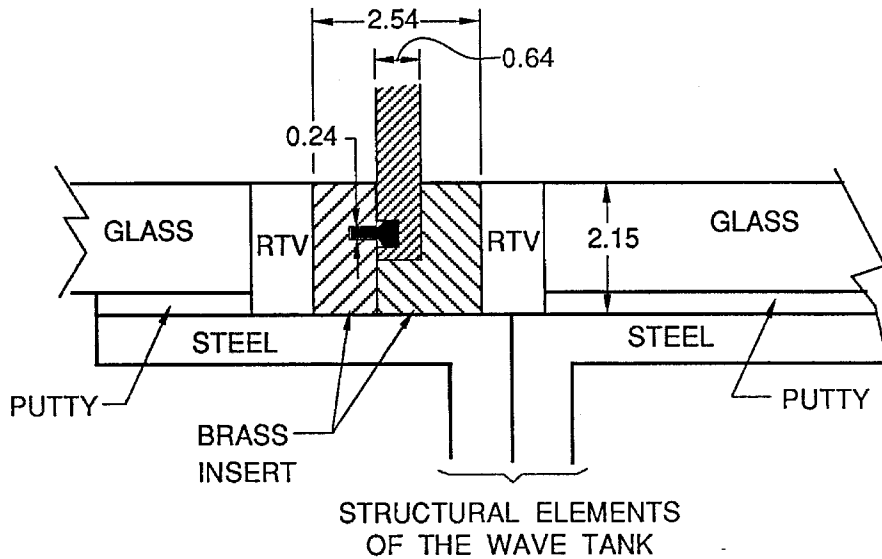


Figure 4.2.19 Photo of the dam break gate and the apparatus used to produce and control the motion of the gate.

an aluminum plate which is bolted to a welded steel frame. This frame was then bolted into the concrete wall adjacent to the tank. The gate is a 0.63 cm thick stainless steel plate which had slots machined into each side and the bottom to allow installation of windshield wiper blades as shown in Figure 4.2.20, and which minimize leakage of the reservoir fluid past the gate. To minimize the generation of waves in the flow due to the supporting structure for the gate, the recessed slot shown in Figure 4.2.20(a) was machined from brass and placed in the tank flush with the glass sidewalls. Silicone grease was placed along the sides of the gate which slide inside the brass slot on either



(a)

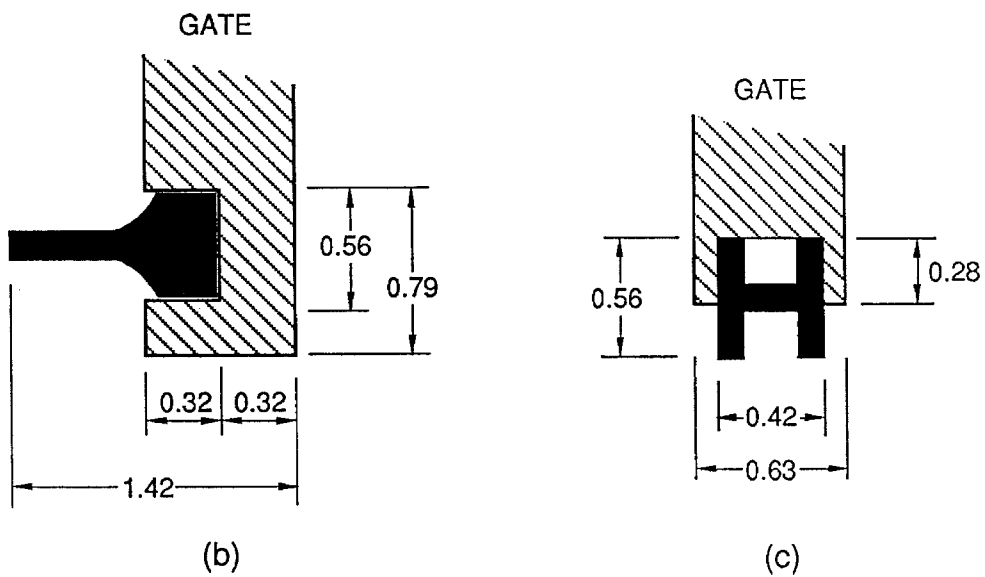


Figure 4.2.20 Schematic drawing of (a) the brass insert built into the side of the wave tank to provide a slot for the gate shown in Figure 4.2.19; (b) the windshield wiper blade which is mounted along each side of the gate; (c) the rubber H section used along the bottom of the gate (all dimensions are in cm).

side of the tank. When the gate clears the free surface, the flow only experiences a small recess in the sidewall of the tank where the brass slots for the gate are located.

A schematic of the control system for the cylinder is shown in Figure 4.2.21. A four way air valve (Numatics Replacement number 081SS600b032R) rated at

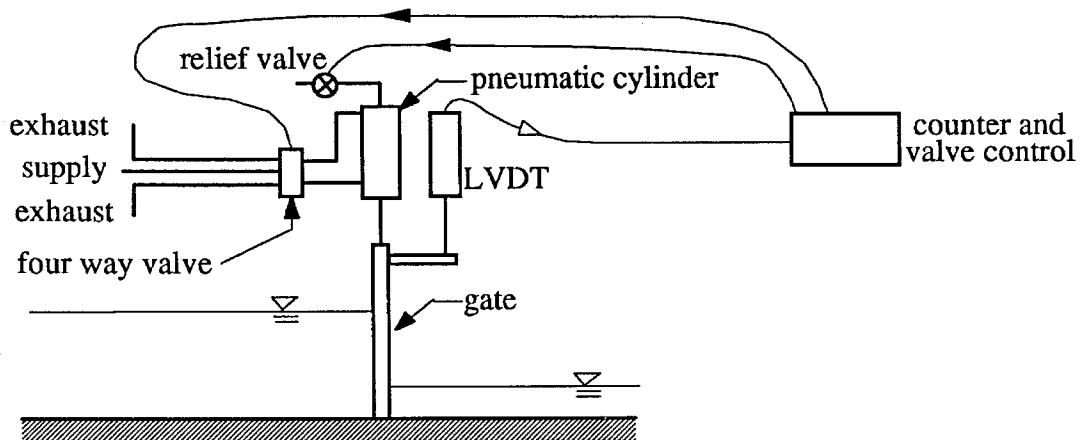


Figure 4.2.21 Schematic of the dam-break gate and control equipment.

1030 KNm^{-2} was used to apply a pressure difference across the piston inside the cylinder. To allow a rapid rise of the gate without slamming the cylinder into the end of its stroke, the control system shown in Figure 4.2.21 was developed. The small relief valve (Skinner Model B2RX127) rated at 1202 KNm^{-2} releases the pressure on top of the cylinder for the amount of time specified on the counter (1.5 sec for all experiments). This decreases the amount of time it takes the gate to clear a previously specified vertical position since the low pressure side of the piston starts at nearly atmospheric pressure, as opposed to 1030 KNm^{-2} . Once the counter registers 1.5 sec, the four-way valve is opened which accelerates the gate. An LVDT (Collins Model LMT-711P39) is used to monitor the trajectory of the gate. When the gate reaches a specified displacement above

the bottom of the tank, the four-way valve is turned off which prevents the piston from exceeding the stroke of the cylinder.

The location of the gate, which determines the proportion of reservoir length to wave propagation distance, was planned to allow at least five seconds between the time the wave impacts the instrumented wall and the arrival of the negative wave reflected from the end of the reservoir. The arrival of the negative wave can be determined by calculating the propagation of the leading characteristic of the negative wave in the reservoir. Hammack (1972) provides an analysis of the wave propagation in a two-dimensional tank caused by the dam break method using the method of characteristics. This leading characteristic will propagate through the reservoir, reflect off the wall, and propagate toward the front of the bore and will eventually overtake it, given a sufficient length of time. The ratio of reservoir length to downstream distance was designed so the leading characteristic of the negative wave would arrive at least 5 sec after the tip of the bore reached the wall. These calculations were performed using the characteristic solutions of the nonlinear shallow-water equations (Stoker (1957)).

A typical gate displacement time history measured with the LVDT is shown in Figure 4.2.22. For a dry bed surge, the depth of the fluid at the gate once it is opened can be calculated from nonlinear shallow water theory (Stoker (1957)). Once the gate is fully open, the depth at the gate will be $4/9$ of the original depth in the reservoir and the speed of the bore front will be approximately $2\sqrt{gh_r}$; where g is the gravitational acceleration and h_r is the reservoir depth. Figure 4.2.22 shows that it takes the gate 0.185 sec to reach an elevation of 22 cm, which is $4/9$ of the 50 cm reservoir depth. From the relation for the surge front speed, one can see that for a 50 cm reservoir depth the bore front would be 82 cm in front of the gate before the tip of the gate reached 22 cm. Thus, an instantaneous release cannot be achieved with this arrangement. The gate

has risen sufficiently to clear the free surface of the water when the surge has propagated less than 6% of the 15.08 m distance from the gate to the wall.

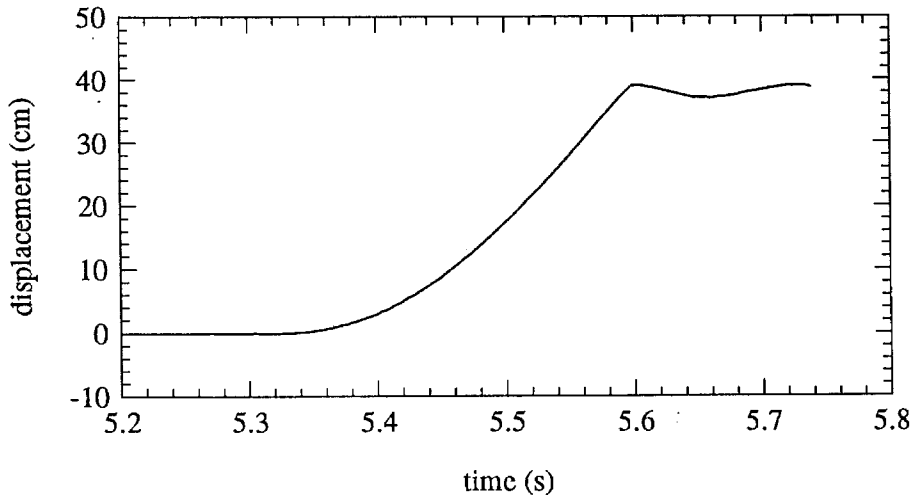


Figure 4.2.22 Displacement of the gate during the generation of a dry bed surge.

4.2.5 Laser-Induced Fluorescence System

The laser induced fluorescence system was developed to record accurate two-dimensional profiles of the incident wave. A two-dimensional sheet of laser light is produced in the wave tank which causes dye in the water to fluoresce along the free surface. The accurate measurement of the wave profile is important for this study since the shape of the wave front determines the behavior of the initial loading on the wall. The flow visualization system used is similar to that described by Yeh, Ghazali, and Marton (1989).

There are several advantages of this system relative to conventional photographic techniques and water surface measurements using intrusive devices such as wave gages. The main advantage of the laser induced fluorescent (LIF) system is the ability to illuminate a specific two-dimensional plane in the experiment which, for example, can be located along the centerline of the wave tank. Conventional photographic techniques

(like those used for the tilting tank study) record the location of the meniscus along a transparent sidewall of the wave tank. Thus, the results contain sidewall effects which are not present in the center of the tank where the forces and pressures were measured during this study. Another problem avoided with the LIF system is the disappearance of the meniscus for certain motions of the free surface, which result in incomplete records of the water surface profile. Both methods of flow visualization are depicted in Figure 4.2.23. For strong bores it is very difficult to determine the free surface intersection with

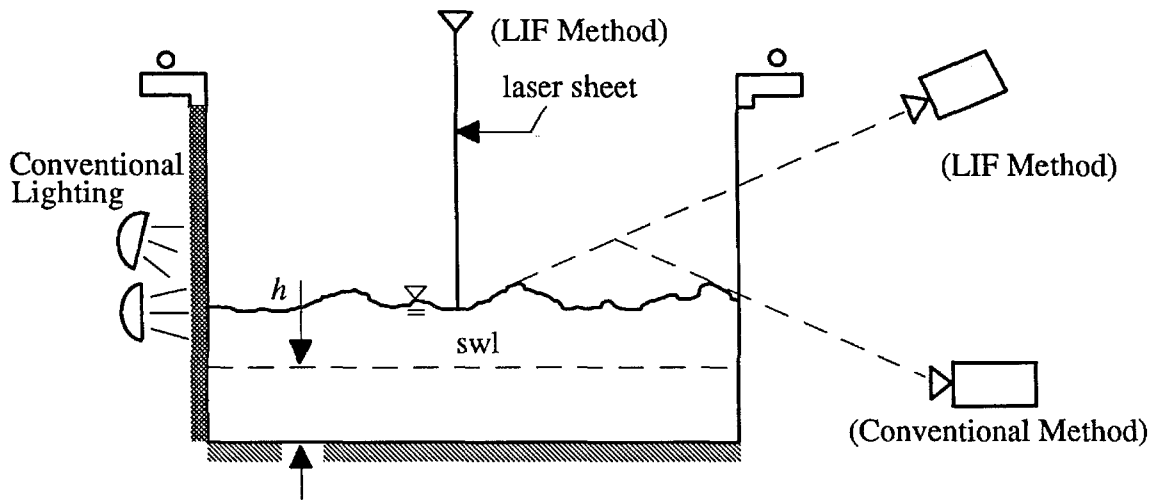


Figure 4.2.23 Definition sketch showing the advantage of a laser-induced fluorescence flow visualization system relative to a conventional system for the measurement of turbulent bore profiles.

the sidewall if the elevation of the camera is above the advancing wave. This difficulty is primarily caused by the turbulent bubbly flow near the front of the bore. Thus, the camera is usually positioned as shown in Figure 4.2.23, where the vertical location of the camera is below the elevation of the free surface to be measured. If the meniscus on the side wall cannot be identified precisely, the water surface at some location inside the tank may be mistaken for the meniscus location as shown in Figure 4.2.23. If this occurs at several points along the wave profile the results are biased and a true two-dimensional

wave profile may not be obtained. The LIF method avoids this difficulty by illuminating only a thin line of the water surface in the plane coincident with the laser light. Flow visualization methods are superior to intrusive devices for high speed flows with very small depths, like surges on a dry bed and very strong bores. This is because the high-speed flow will cause runup on the front of any device placed in the flow and a corresponding draw-down on the downstream side. Another advantage of optical methods is that they produce spatial information each time an exposure is obtained.

The intent was to measure the incident wave profiles in a plane coincident with the pressure transducer and the centerline of the wall instrumented with the force transducers. Thus, for all the experiments in the horizontal tank, the laser light sheet was aligned in a vertical plane parallel to the longitudinal axis of the wave tank which intersected the centerline of the instrumented wall.

A schematic of the laser optics is shown in Figure 4.2.24. The light from a 200 mW argon ion laser (Lexel Model 75) was transmitted through a 10 m long multimode fiber optic cable (Newport Model FC-MSD-50). The laser light first was focused on the end of the fiber optic cable with a microscope objective (Newport Model M-20X) which was mounted in a fiber optic coupler (Newport Model F-91-C1-T). The fiber optic coupler allowed the cleaved end of the fiber optic cable to be placed perpendicular to the laser beam at the location where the beam was focused. Each end of the fiber optic cable was cleaved in the factory and mounted in a connectorized end which was mounted in a chuck (Newport Model FPH-CA). The chuck was placed in the fiber-optic coupler. The light emitted from the end of a multimode fiber optic cable acts as a point source. As shown in Figure 4.2.24, this produced a cone of light with a spreading angle, θ_l . This cone of light was focused at the bottom of the wave tank with a plano-convex lens (Newport Model KPX076) which has a focal length of 25.4 mm. A few centimeters

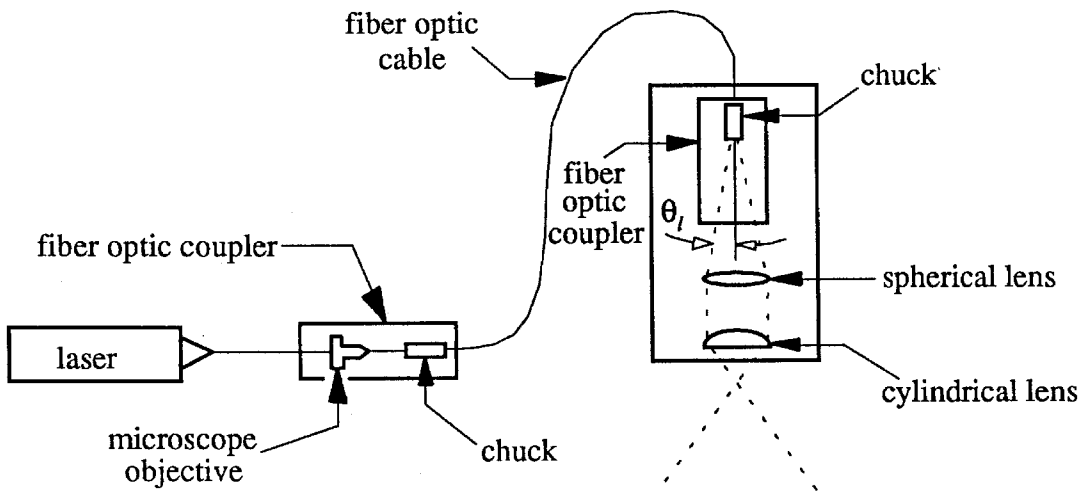


Figure 4.2.24 Schematic of the optical components used in the laser-induced fluorescence system.

beyond the focusing lens, a cylindrical plano-convex lens (Newport Model CKX012) with a focal length of 12.7 mm was placed in the beam. The cylindrical lens spread the beam in one direction producing a 1.5 mm thick sheet of light which illuminated a 90 cm long test section located 1.73 m below the elevation of the lens. Figure 4.2.25 is a photo of the carriage used to support the transmitting optics. The transmitting optics were mounted on an aluminum plate which was enclosed in a box. This box was supported by a camera-tripod connector, which allows three rotational degrees of freedom. This connector was supported on the carriage in a way which allowed three translational degrees of freedom.

The laser produced several wavelengths (lines) of light. The 200 mW rating of the laser includes the power in all four of the significant lines. When the Rhodamine 6-G dye in the water is exposed to light within a range of wavelengths between approximately 470 and 550 nm (Green (1990)), it will fluoresce and give off light at approximately 570

nm. The two dominant lines of the laser (514 nm and 488 nm) lie in the middle of this range. Therefore, all the lines of laser light were used to obtain as much light intensity as possible at the test section.

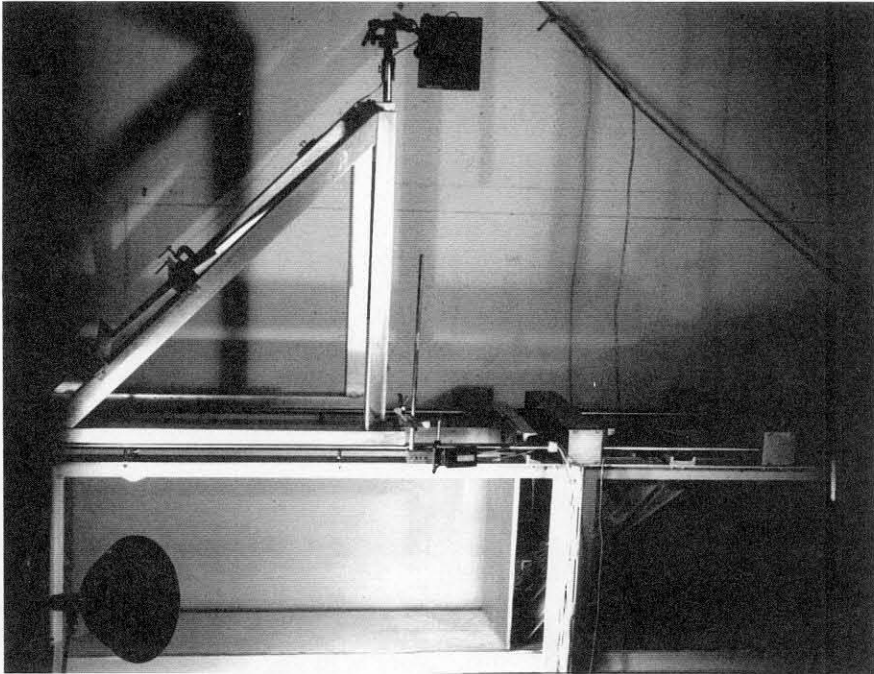


Figure 4.2.25 Photo of the carriage used to support the LIF transmitting optics.

The image recorded by the video camera is a two-dimensional array of light intensity. Thus, the information consists of a value of the light intensity recorded by each pixel location in the video camera. The pixel image obtained with the video camera is transformed into an electrical signal which consists of 480 lines of analog information. This information representing the light intensity is stored on a magnetic super-VHS tape. The video information stored on tape was viewed with a super-VHS editor (Panasonic Model AG-7500), which can produce a still frame on a monitor. Each still frame was digitized with a frame grabber (Imaging Technology Inc. Model PCVISION plus) which was mounted on the motherboard of an IBM AT compatible computer. The frame grabber automatically digitizes a 512 square pixel frame for each image selected. The

operation of the frame grabber as well as data file manipulations were accomplished with the image analysis software, denoted VICAR, which was developed at the Caltech Jet Propulsion Laboratory in Pasadena , CA.

To calibrate the video camera images of the wave profiles with respect to the physical locations in the wave tank, a 101.5 cm by 53.5 cm rectangular sheet of lucite was bolted onto an aluminum frame, painted white, and covered with black grid lines spaced 4 cm apart in each direction. This lucite board was placed on the centerline of the wave tank and recorded using the video camera. Three adjustable length studs were placed on the back of the lucite board. The length of these were adjusted so they rested on the back wall of the tank when the face of the board was at the centerline of the tank and coincident with the vertical plane. The video image shows the two-dimensional array of control points in the wave tank which covered the region in which the wave profiles were to be recorded. The location of these control points within the wave tank were known. The video image shows these control points at a particular location in the video image. A calibration procedure was developed to determine where a particular location in the video image is located in the wave tank. A two-dimensional least squares error scheme was used to calculate the coefficients in equations which relate the pixel space locations to physical locations in the wave tank. The coefficients were determined by minimizing the errors between the calculated control point positions and the known location of the control points on the lucite plate. The details of this calibration procedure and its use to calculate the physical location of the water surface in the wave tank from the video image are presented in Appendix B.

The runup on the wall during the impact of bores and surges was recorded with a super-VHS video camera (Mitsubishi Model HS-C30U). This camera was mounted on the carriage which supported the transmitting optics of the laser beam. In some cases,

drops of water and spray were thrown quite high after the impact of bores and surges. Some of this fluid which lies in the laser light is located in front of the instrumented wall and is not in contact with it. The method used to observe the runup could distinguish between fluid in front of the wall and the location where the air-water interface met the wall. To accomplish this, the camera was offset relative to the centerline of the instrumented wall. From the calibration of the video image relative to the physical locations in the wave tank, the centerline of the instrumented wall in the video image could be identified. Any fluid surface in the laser sheet which lies in front of the instrumented wall would be displaced to one side of the known location of the wall centerline in the video image. With this method, the free surface location on the wall could be identified even in the presence of drops and spray, provided the line of sight was not obstructed by fluid (which rarely occurred).

For all the video recordings during the impact of bores and surges, 49 mm diameter filters (Tiffen Model 21 orange) were used to attenuate the laser light scattered off the tank bottom and reflected off the water surface. These filters transmit about 90 percent of the light at the dye fluorescence wavelength and only a small percentage of the incident laser light. This is important for strong turbulent bores since a direct reflection of the laser light into the video camera will saturate the signal, making it difficult to determine the free surface location using numerical image processing.

4.2.6 Celerity Gage

A series of five contact probes were placed along the tank for the experiments in the horizontal tank. These probes were made from a 0.165 cm diameter, 21 cm long stainless steel rod soldered into the end of a 0.63 cm diameter, 13 cm long brass rod. The top 1.5 cm of the brass rod was milled to a slightly smaller diameter and placed in a short piece of polyflow tube which provided electrical insulation from the wave tank.

This polyflow covered end was held in a point gage which allowed accurate vertical placement of the tip of the probe with respect to the still water surface. Each probe was connected to an electrical circuit which is closed when the water touches the probe. The five probes were connected to an analog summing device which produced an electrical DC signal and decreased in voltage each time a successive probe was submerged in the wave. These data were modeled with a least squares approximation which was used to compute the wave celerity at any desired location along the tank. For the bores and the solitary waves, a parabolic approximation was used, while for the dry bed surges the theory of Whitham (1955) was used.

4.2.7 Procedures

4.2.7.1 Solitary Waves

A schematic of the solitary wave experiment is shown in Figure 4.2.26. The origin of the coordinate system is located at the intersection of the still water surface and

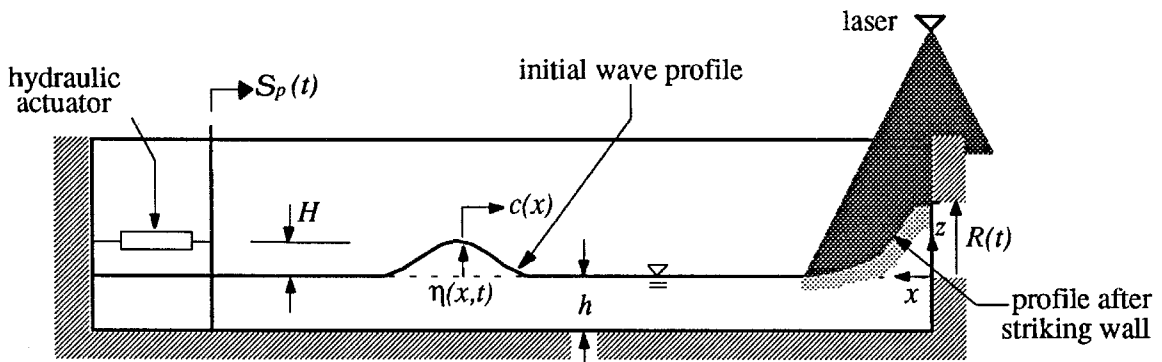


Figure 4.2.26 Definition sketch of the solitary wave experiments in the horizontal tank.

the instrumented wall on the centerline of the wave tank. As with the tilting tank study, the numerical model developed by Goring (1979) is used to produce the trajectories which controlled the wave generator.

Three personal computers were used during these experiments for wave generation and data acquisition. The first computer was used to control the wave generator. The LVDT signal from the wave plate motion, the wave gage records, and the celerity probe output were recorded with an analog to digital data acquisition card (Omega Model DAS-16), resident on the motherboard of a second personal computer. The signals collected on the second computer were sampled at 200 Hz for a total sampling duration of 36.25 sec. The forces and pressure were recorded with the RC card on the third computer at a sampling rate of 1 msec for a total sampling duration of 8.192 sec.

When the wave generator was started with the first computer, an electronic signal was used to trigger the second computer which began collecting the wave plate trajectory, the wave gage data, and the celerity gage output. When the water surface made contact with the last celerity probe at $x = 1.5$ m, an electronic signal was used to trigger the third computer as well as the clock in the video camera. The third computer was used to record the force and pressure time histories. Therefore, once the wave generator was started, the entire data acquisition system was automatically controlled through triggers producing data records and video images which were all properly referenced to each other in time.

For all the solitary wave experiments, the pressure cell was located 29.86 cm above the tank bottom in the top port of the wall. The still water depth for all the solitary wave experiments ranged from 17.86 cm to 17.46 cm. This location for the pressure cell was selected since the very thin runup tongues which occur during the reflection of very steep solitary waves are difficult to model numerically. Thus, the pressure records from this location, about 0.7 water depths above the still water level, should provide a good test for theoretical models. The initial position of the wave board was $x = 24.480$ m.

One wave gage was placed at $x = 19.000$ m, another wave gage was placed at $x = 2.200$ m, and the five celerity probes were located at $x = 1.500$ m, $x = 6.500$ m, $x = 11.500$ m, $x = 16.500$ m, and $x = 21.500$ m. All the wave gages and celerity probes were located on the centerline of the wave tank, where $y = 0.0$ cm. However, for three runs, the wave gage at $x = 19.000$ m was moved to $x = 24.0$ cm and $y = -5.0$ cm so the wave gage record could be compared with the wave profile measurements obtained with the LIF system which was located on the centerline of the wave tank.

Before any runs were performed, the response of the wall was checked with the device shown in Figure 4.1.12, and the pressure cell was calibrated as described in Section 4.2.3. The wall was also checked with a hydrostatic calibration as shown in Figure 4.2.6. Approximately 1 gram of Rhodamine 6-G dye (which comes from the manufacturer as a powder) was mixed with about 2 cc of methanol and this mixture was diluted with 1 liter of water. The dye was first mixed in methanol to facilitate dissolution since the dye tends to remain in clumps when mixed with water. The lucite calibration plate was placed in the center of the tank and recorded with the Magnavox video camera.

Before each of the first few runs (and as required for subsequent runs), about 30 cc to 50 cc of the dye solution was mixed into the first 1.5 meters of the tank in front of the instrumented wall. Between each run, the glass sidewall and the vertical wall at $x = 0$ cm were dried and wiped with a cloth. The cloth was moistened with a solution of water and wetting agent (Kodak Photo-Flo 200). This prevented the water which runs up on the wall from beading on the glass sidewall when rundown occurs. When the field of view is obstructed by beaded water on the glass sidewall, the image of the free surface is significantly distorted relative to the calibrated field of view, which could produce significant errors in the measurements of the wave profile. The use of the wetting agent minimized this problem by preventing beading on the sidewall.

4.2.7.2 Bores and Dry Bed Surges

A schematic of the bore experiment is shown in Figure 4.2.27. Results were obtained with the pressure transducer in three different ports located 1.79 cm, 17.00 cm

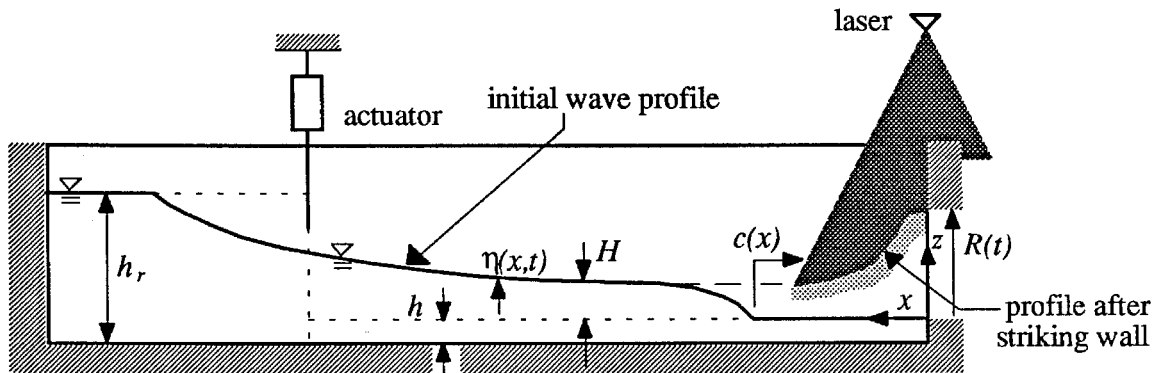


Figure 4.2.27 Definition sketch of the bore and dry-bed surge experiments in the horizontal tank using the dam-break method of wave generation.

and 29.86 cm above the bottom of the wave tank. The five celerity probes were located at $x = 1.500$ m, $x = 4.000$ m, $x = 6.500$ m, $x = 9.000$ m, and $x = 11.500$ m. All the celerity probes were located at $y = 0$. The reservoir side of the gate was at $x = 15.080$ m and the rest position of the wave board was at $x = 24.049$ m which gives a reservoir length of 8.969 m.

The forces and pressure time histories were recorded on separate computers with the RC card and the 100 KHz Omega card, respectively. The forces were recorded at a sampling rate of 0.12 msec for a total sampling duration of 9.83 sec. A program was written in assembler language to control the RC card and save the force data to the hard disk during the sampling interval. Sampling at a rate of 8.3 KHz should have resolved most of the dynamic response of the wall which had measured natural frequencies of 613

Hz and 909 Hz for two modes of oscillations. The 100 KHz Omega card was used to record the pressure cell response at a sampling frequency of 83.3 KHz for a sampling duration of 6.26 sec. The dynamic response of the pressure transducer, which had a natural frequency of 11.4 KHz, was fully resolved with this sampling rate. The 83.3 KHz sampling rate was sustained for the six seconds by continually monitoring the data buffer and saving the results on a virtual RAM drive. The sampling rates used on both computers were the maximum which could be obtained with the hardware used. The LVDT signal from the gate motion and the celerity probe output were recorded with the 50 KHz Omega card in a third computer at sampling rates ranging from 400 Hz to 800 Hz.

Before any runs were performed, the response of the wall was checked with the device shown in Figure 4.1.12 and the pressure cell was calibrated as described in Section 4.2.3. Approximately 5 grams of Rhodamine 6-G dye were mixed with about 50 cc of methanol and this mixture was diluted with 1 liter of water. The lucite calibration plate was placed in the center of the tank and recorded with the Magnavox video camera. The gate was placed on the bottom of the wave tank and the region behind the gate was filled with about 50 cm of water while gradually adding the entire liter of dye mixture. Once the tank was filled and the dye adequately dispersed, a sample of the fluid was collected, and its surface tension was measured with the device described in Appendix C.

When the gate movement was started with the air cylinder controller, an electronic signal was used to trigger the first computer which began sampling the gate trajectory and the celerity gage output. When the water surface made contact with the last celerity probe at $x = 1.5$ m, the second and third computers, as well as the clocks in both video cameras were triggered with electronic signals.

The second and third computers recorded the force and pressure time histories, respectively. Once the air cylinder on the gate was started, all the computers and the clocks in the video monitors were controlled automatically with the electronic triggering signals which allowed all the results to be properly referenced to the same time scale.

5. RESULTS AND DISCUSSION

This chapter presents the experimental results obtained in both wave tanks and comparisons of these results with the analytical and numerical models discussed in Chapter 3. The experimental results are presented in the chronological order in which they were conducted: the tilting tank results are presented in Section 5.1, the solitary wave results are presented in Section 5.2, the results from undular and turbulent bores are presented in Section 5.3, and the results from the dry bed surges are presented in Section 5.4. In Section 5.5, the results from Sections 5.1 through 5.4 are presented to indicate the differences, transitions, and/or similarities between the results for different wave types.

5.1 Tilting Wave Tank Study

Results from the tilting wave tank study are presented in this section. A solitary wave was produced in a sloping wave tank which produced a plunging breaking wave as shown in Figure 5.1.1. The breaking and shoaling of this wave resulted in the propagation of a turbulent bore toward the shoreline. The bore was reflected by a vertical wall that was instrumented with force transducers as described in Section 4.1.2. The origin of the coordinate system is at the shoreline, with the x -axis directed along the still-water surface toward the wave generator, and the z -axis directed upward as seen in Figure 5.1.1(b). The slope of the bottom, S , was 0.02 m/m, while the depth at the wall, h_w , was 5 mm for all runs. The location of the wall, x_w , was 25 cm as measured from the shoreline. The initial position of the wave generator piston was at $x = 24.02$ m.

5.1.1 Amplitude and Celerity Considerations

After the solitary wave broke, it continued to shoal and propagate as a turbulent bore with a celerity, $c(x)$, and a water surface profile, $\eta(x, t)$, as shown in Figure

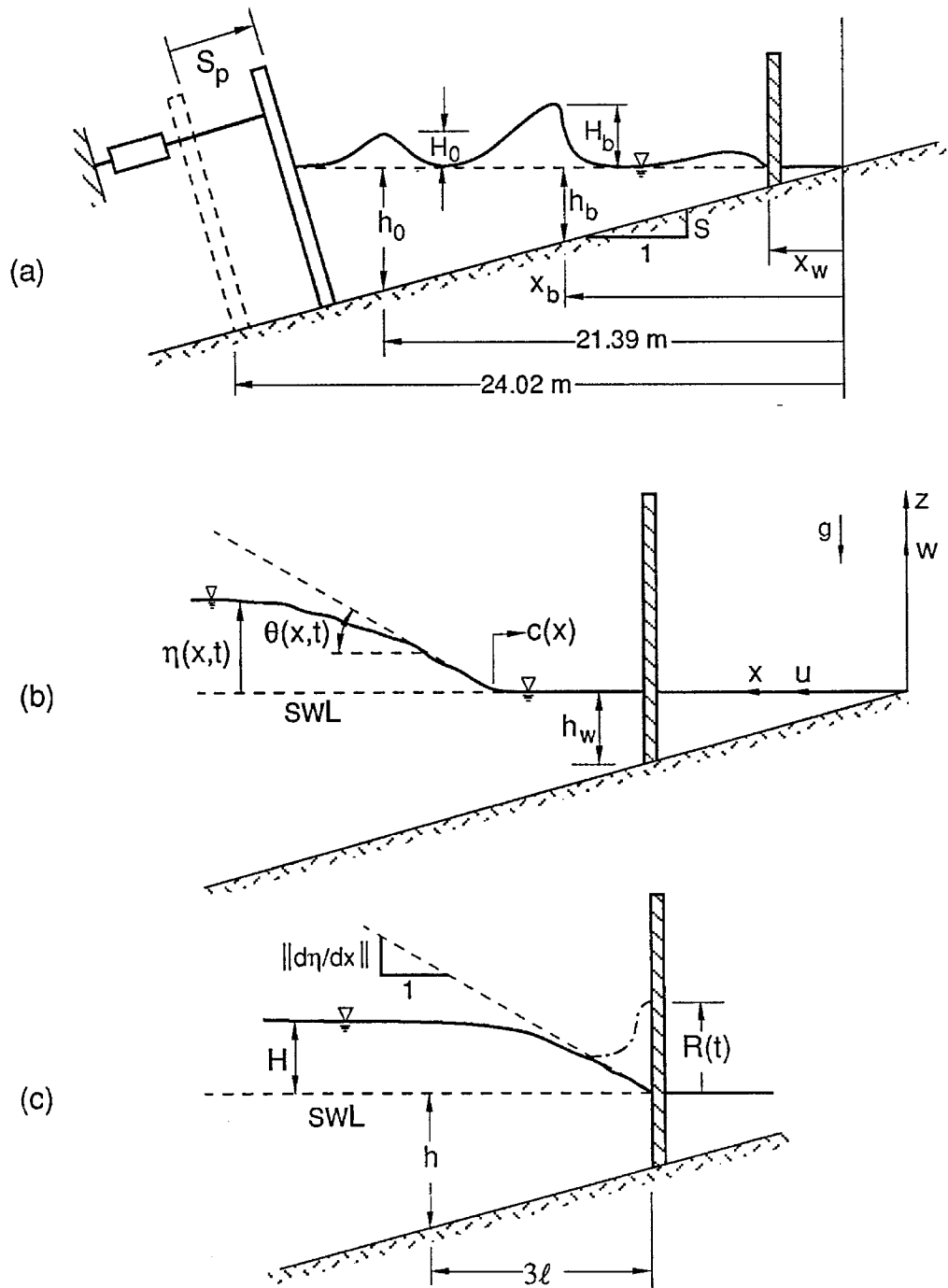


Figure 5.1.1 Schematic drawing of the tilting wave tank experiment where (a) a solitary wave was produced on a sloping beach, broke as a plunging breaker and arrived at the vertical wall as a turbulent bore; (b) and (c) show details near the wall.

5.1.1(b). The angle between the tangent to the surface of the bore and the horizontal direction is $\theta(x, t)$. The maximum height of the bore and the maximum slope on the front face of the bore before it strikes the wall are H and $\|d\eta/dx\|$, respectively, as shown in Figure 5.1.1(c). The operator $\| \|$ indicates the maximum value of the argument. The runup on the wall, R , above the still water level (swl) is also defined in Figure 5.1.1(c), as well as h , which is the effective depth three horizontal length scales, l , behind the tip of the bore.

In the case of complex non-periodic waves, such as undular bores, and solitary waves, there is no wave length analogous to that which can be defined for periodic waves. Hammack (1972) proposed the following length scale, l :

$$l = \frac{H}{\|d\eta/dx\|}, \quad (5.1.1)$$

which is a measure of the horizontal distance over which significant vertical accelerations of the fluid particles take place. As the horizontal length scale decreases for a given wave height, the vertical accelerations experienced by the fluid particle as they pass through the wave must increase. Along with larger vertical accelerations, there is also an increase in the frequency dispersion of the wave due to the difference in the pressure gradient from hydrostatic conditions. Peregrine (1966) presented an excellent physical description of the effects of vertical accelerations on waves. If the maximum wave slope on the front of a wave can be estimated along with the wave height immediately adjacent to this local region of maximum slope, Equation 5.1.1 can be used to determine the local length scale, l . As discussed by Hammack (1972), this measure of the length scale is only a local estimate since in a complex wave, l , may vary from one location to the next.

The effective depth, h , associated with the bore at the moment it strikes the wall is defined as the depth $3l$ behind the front of the tip of the bore as shown in Figure 5.1.1(c). The reason for selecting this definition of the effective depth will be discussed below. The runup on the wall $R(t)$ is also shown in Figure 5.1.1(c).

The measured incident relative wave height, H_o / h_o , varied from 0.044 to 0.288 which produced breaking wave heights, H_b , from 4.7 cm to 20.2 cm. These breaking waves reached the wall as turbulent bores with heights, H , and celerities, c , ranging from 2.2 cm to 4.6 cm and 75.2 cm/sec to 129.3 cm/sec, respectively. For a detailed summary of the experimental conditions see Appendix A.

The maximum bore height, H , and the maximum water surface slope, $\|d\eta / dx\|$, were obtained from the high-speed movies. Examples of the profiles obtained are shown in Figure 5.1.2(a) through 5.1.2(c). Figure 5.1.2(a) shows the profile of a bore just before it strikes the wall. For the tilting wave tank study, time, t , is zero when the clock was started, which is when the computer began recording the force time history on the wall. The time of the last movie frame before the bore begins interacting with the wall is $t - t_H$, where t_H is equal to the time of the last movie frame before the bore strikes the wall. Figure 5.1.2(b) shows a subsequent bore profile 0.120 sec after the last movie frame, before impact. If the assumption is made that the height of the bore is not changing rapidly, subsequent profiles can be used to determine the maximum bore height if the portion of the profile affected by the reflection from the wall is omitted. Only the portion of the bore profile unaffected by the wall is shown in Figure 5.1.2(b). To determine which portion of the profile was affected by the wall, the subsequent profile in Figure 5.1.2(b) was shifted in position, using the measured celerity. This profile is then compared to the profile at impact. It is readily apparent how far the reflected wave has extended back into the oncoming wave.

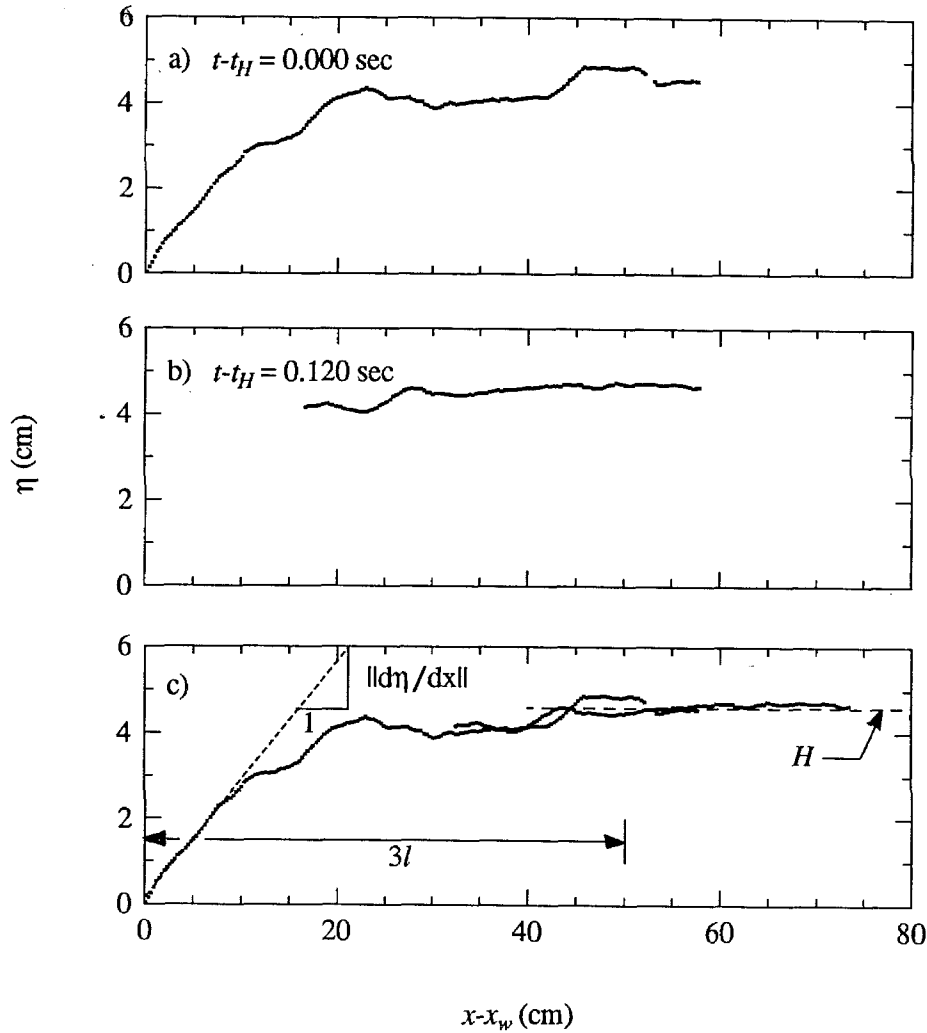


Figure 5.1.2 (a) Profile of a bore with a wave height of 4.59 cm which has just reached the vertical wall; (b) a subsequent bore profile during runup on the wall; (c) composite bore profile from the profiles shown in (a) and (b) (run no. TB109).

Both the profile just prior to impact and the shifted profile are shown in Figure 5.1.2(c). This method of augmenting the bore profile at impact with subsequent profiles was used due to the limited horizontal length of the field of view in the movie camera. In this way, a pseudo field of view is constructed essentially extending the spatial data available. For all cases except one, the mean bore height was computed from the bore profile for $x > 40$ cm. For the case corresponding to $H_o / h_o = 0.086$, the maximum measured point on the wave profile at the time of impact with the wall was used. No

subsequent profiles were used in this case, since the wave height was still increasing at the edge of the field of view seen in the movie. This indicates the field of view for this case may not have been quite long enough, which caused all subsequent profiles to look as though they were affected by the wall over their entire length. Therefore, the wave height for this case may be slightly smaller than the actual wave height.

The maximum slope on the front of the wave, $\|d\eta/dx\|$, was calculated using a linear least squares error analysis applied to all data points located within a horizontal "window." This window was centered on every point along the wave and the slope was calculated for that region. The maximum calculated slope, $\|d\eta/dx\|$, is shown in Figure 5.1.2(c). The window length used to calculate the slopes in this section were equivalent to those used in Section 5.3 for bores of similar strength where the ratio in wave heights was used to scale the window length to the smaller bores in this section. The window length used along with the computed slopes are presented in Appendix A.

The split frame technique used with the high-speed movie camera provided a 12 cm wide view (in the y -direction) of the advancing bore front. The average x position of the turbulent front was used to determine the celerity of the bore from several movie frames where the propagation distance of the bore was divided by the elapsed time. The film frames chosen for analysis to define the celerity, c , correspond to the time when the front is about 20 cm in front of the wall, where the depth as seen on the flume sidewall is h_w . Due to a slight imperfection in the tank bottom, the depth, h_w , occurred both here and in front of the instrumented wall at the center of the tank.

The horizontal distance, $3l$, behind the tip of the surge, where the effective water depth, h , was located, is shown in Figure 5.1.2(c). A distance equal to three times the horizontal length scale was selected since it tends to improve the agreement between the

experimental results obtained in the tilting and horizontal wave tanks (see Figure 5.5.1). In Figure 5.1.3 the relative bore celerity is plotted as a function of the relative wave height, where the results are normalized by the depth at the wall, h_w , and the effective depth, h , in Figures 5.1.3(a) and (b), respectively. The theoretical celerity for a moving hydraulic jump advancing into still water (Stoker(1957)) is shown with the dashed line which agrees well with the experimental results in Figure 5.1.3(b).

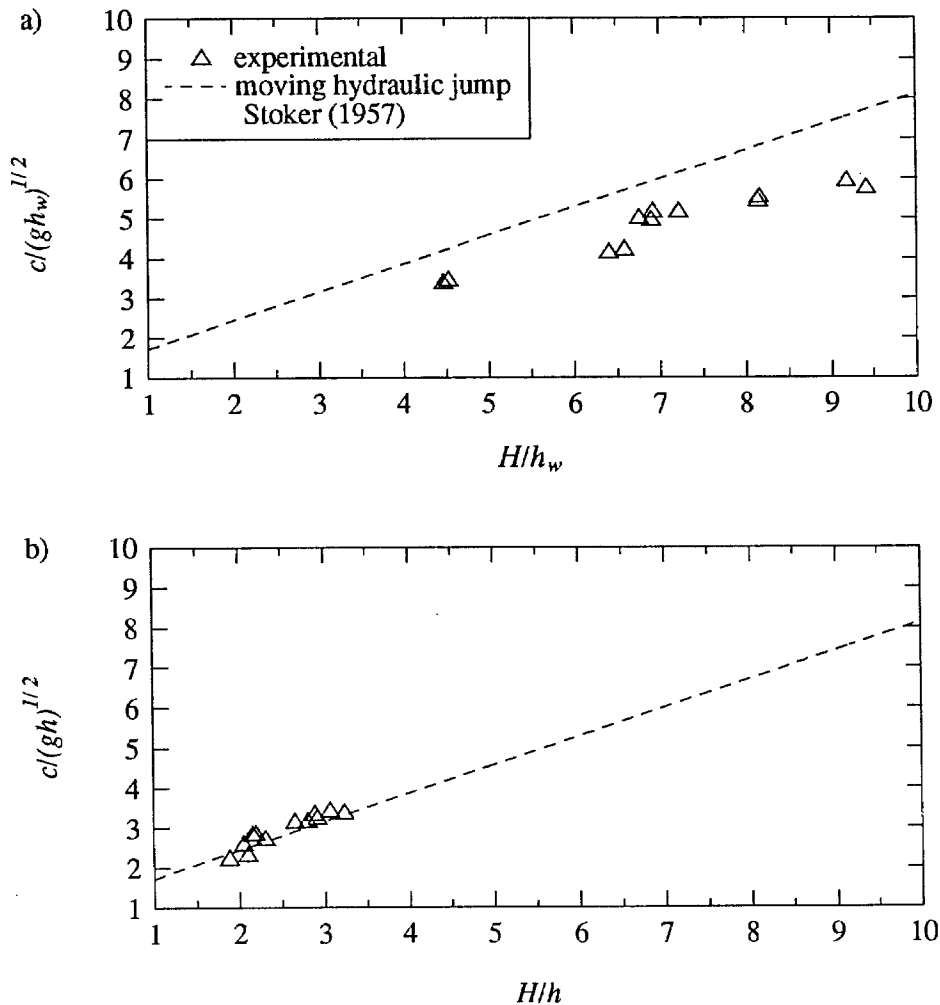


Figure 5.1.3 Relative celerity of the bores normalized using (a) the depth at the wall, h_w , (b) the effective depth, h , three horizontal length scales behind the tip of the bore (run no.'s TB108 through TB119).

Non-dimensional bore profiles measured at the instant the tip of the bore impacts the instrumented wall are shown in Figure 5.1.4. The ordinate is the relative amplitude, and the abscissa is the relative distance from the wall normalized by the horizontal length scale, l . Figures 5.1.4(a) through (f) show two measured profiles for each wave condition as solid lines; this provides some indication of the repeatability of the incident bores. The average of the two profiles is shown with dashed lines in Figures 5.1.4(a) through (f), and each of these averaged profiles are shown in Figure 5.1.4(g). The field of view used in Figures 5.1.4(e) and 5.1.4(f) were the same; however, as discussed earlier, the amplitude of the bore with $H_o/h_o = 0.086$ in Figure 5.1.4(e) was still increasing near the limit of the film frame. Therefore, the value of H used may be slightly smaller than the actual value for that case. Nevertheless, this profile seems to agree with the others in Figure 5.1.4(g). Not only do the profiles in Figure 5.1.4(g) tend to collapse, but all of them, except those corresponding to $H_o/h_o = 0.086$, reach a constant height about 3 horizontal length scales behind the tip of the bore. As mentioned earlier, this horizontal location also corresponds to the location used to determine the effective depth, h . It should be realized that since the bore was generated by a breaking solitary wave, the volume of the bore is finite, and the amplitude must tend to zero for large distances from the wall. Although the initial wave heights varied by over a factor of seven, the size of the bores at the wall only varied by a factor of two and the non-dimensional profiles are very similar.

The variation of the relative water particle velocity along the surface of the bore, $-u_\eta/c$, with relative distance from the wall at the moment of impact, $(x - x_w)/l$, is shown in Figure 5.1.5, where H_o/h_o is the initial relative solitary wave height 21.39 m from the shoreline. The velocity, u_η , was computed as the ratio of the distance traveled by the particles to the corresponding elapsed time, where five movie frames to either side of the one corresponding to the instant of impact were used. These data at the instant of

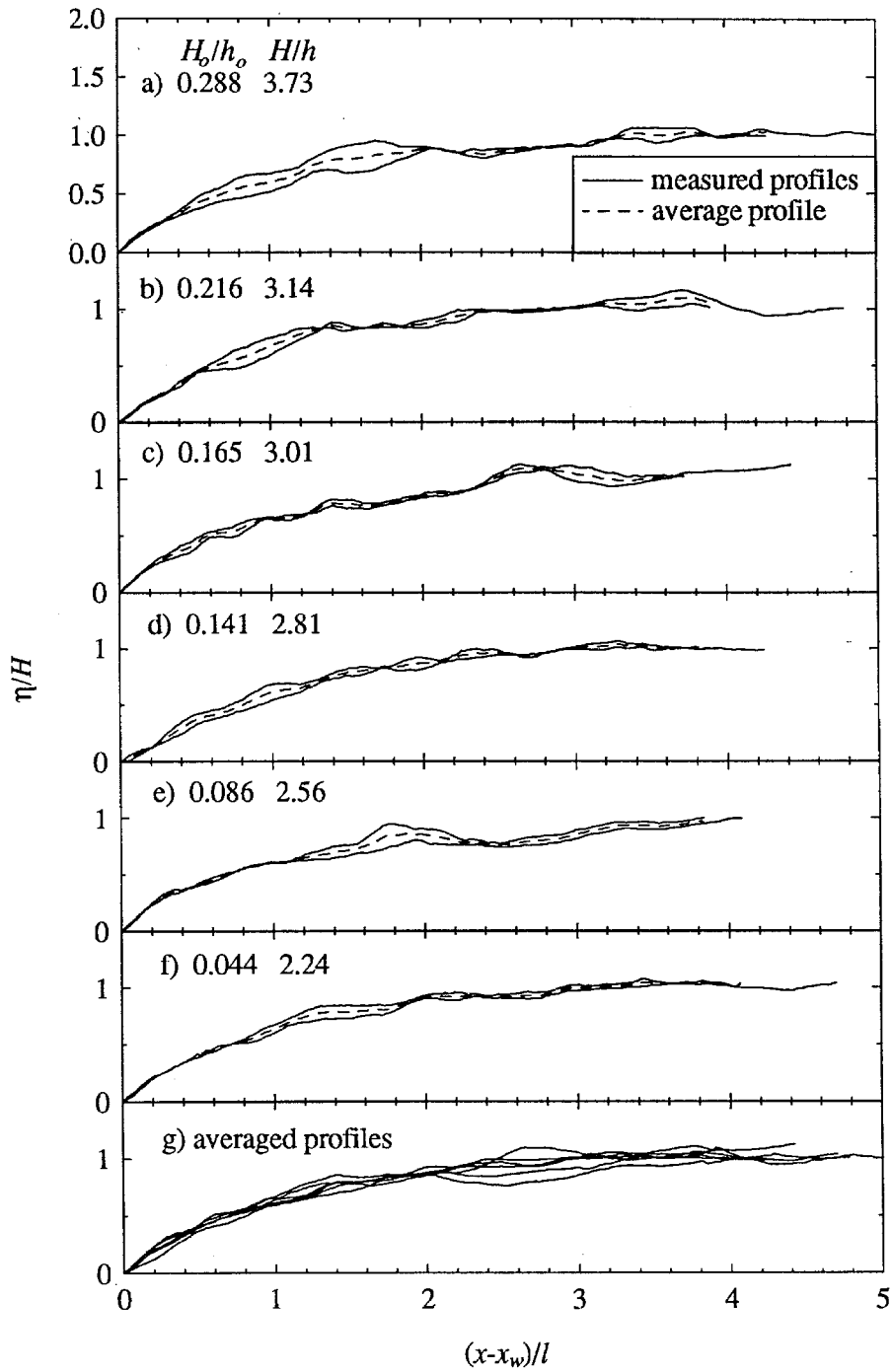


Figure 5.1.4 (a) through (f) measured and average bore profiles at the instant the bore tip meets the vertical wall; (g) averaged bore profiles from (a) through (f) (run no.'s TB108 through TB119).

impact are shown in Figure 5.1.5 with the hollow symbols. After impact, some disks traveled into the movie frame. Since these particles entering the field of view were on the constant depth region of the bore, it was assumed their velocity was relatively

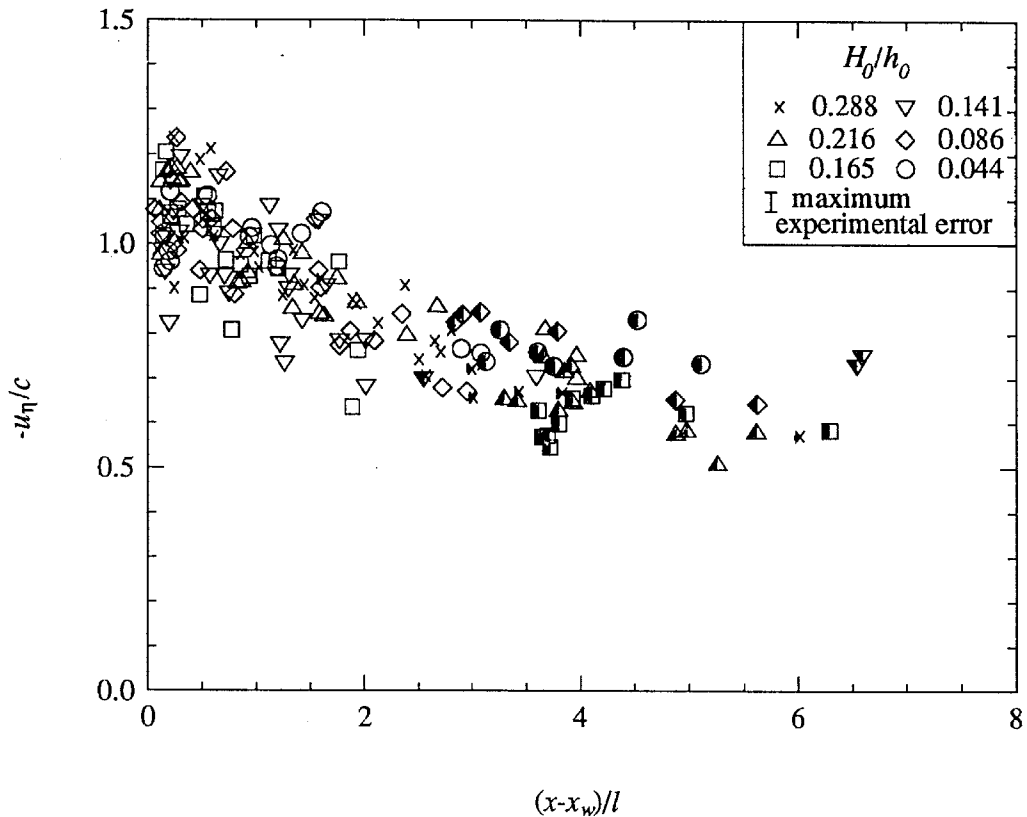


Figure 5.1.5 Relative horizontal water particle velocity along the bore surface at the moment the bore tip reaches the wall (run no.'s TB108 through TB119). The half filled symbols show measurements obtained after the bore reached the wall.

constant. From this assumption, one can estimate how far from the wall these disks were at the instant of bore impact. The data from these disks, whose location and velocity at the instant of impact were therefore estimated, are shown with the partially solid symbols in Figure 5.1.5. The scatter in the measurements shown in Figure 5.1.5 is much larger than the experimental errors ($\pm 0.022 c$) and is most likely due to the turbulent fluctuations in the flow. For each incident wave condition, results from two runs are shown. For each run about 10 to 15 data points were obtained.

Within the accuracy of the methods used, the results shown in Figure 5.1.5 indicate that the variation of the normalized velocity with the relative distance is approximately independent of the initial relative wave height. The particle speed near the tip of the bore varies from 80% to 125% of the bore celerity, while the relative velocity of the particles along the portion of the bore relatively far from the tip vary from about 50% to 75% of the celerity. On average, the particle speeds near the front of the bore are slightly larger than the celerity, although this difference is much smaller than the variability in the data at the front of the bore.

Photographs showing the impact and run-up of a bore generated by an incident wave with $H_o/h_o = 0.044$ are shown in Figure 5.1.6. The black particles, which might be seen in some frames, are the buoyant disks used to measure the horizontal velocity along the water surface. Although the bore tip has not quite reached the wall at the relative time, $t - t_i = 0$ sec, the force record indicated the impact started at this time. This discrepancy is most likely due to the slightly three-dimensional shape of the front of the bore, which makes it difficult to define precisely the time of impact. In Figure 5.1.6 time has been referenced to the time of impact, t_i . The movie frame for $t - t_i = 0.241$ sec corresponds to the time of maximum runup. However, for this case, the maximum force occurred at $t - t_i = 0.322$ sec; this difference is important and will be discussed in detail later. After the passage of this bore tip, it appears that the profile of the bore remains horizontal during the reflection process. As mentioned earlier, due to the method of bore production as time proceeds, the depth of the water in front of the wall must decrease, and eventually the shoreline recedes toward the wave generator.

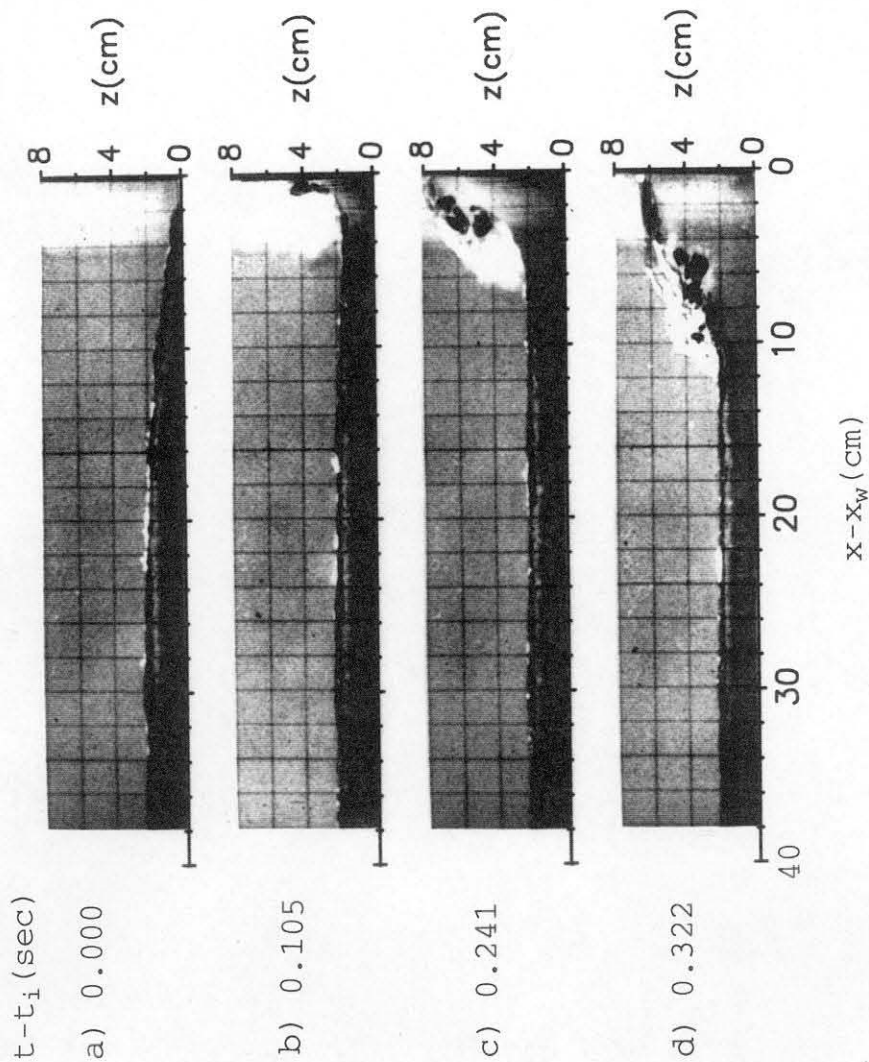


Figure 5.1.6 Impact of a bore on the vertical wall due to an incident solitary wave with $H_0/h_0 = 0.044$, as recorded with the movie camera; the maximum runoff and force occurred at $t - t_i = 0.241$ sec and 0.322 sec, respectively (run no. TB119).

5.1.2 Force Considerations

As mentioned earlier in Section 4.1.2, an experiment was conducted to investigate the effect of the width of the gap between the instrumented section of the wall and the tank bottom on the measured force. The same incident solitary wave, slope, and water depth were used with gap widths between the wall and the tank bottom of 0.13 mm, 0.24 mm, 0.76 mm, and 1.52 mm. The shoreline was located about 2 cm in front of the wall. The region between the edge of the water and the wall was wetted before each run. The force time histories shown in Figure 5.1.7 are essentially identical, indicating that there

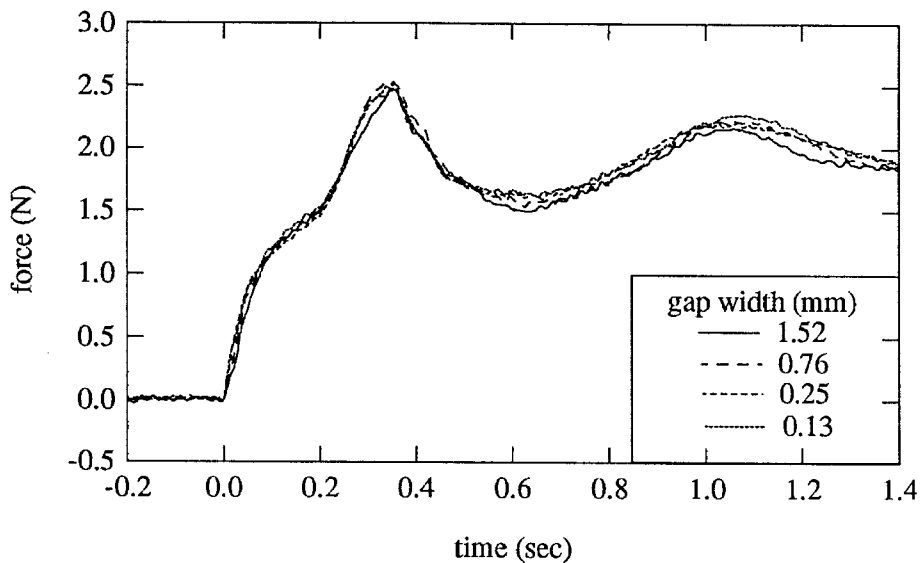


Figure 5.1.7 Effect of the gap width along the bottom of the instrumented wall on the measured force.

should be little error in isolating the instrumented wall in this way. Observations behind the wall showed that after bore impact, the water flowed under the wall and along the tank bottom shoreward of the wall from 7 cm to 70 cm depending on the gap width.

The water surface variation during the process of impact and reflection of a bore for a relative incident wave height of $H_o/h_o = 0.044$, 21.39 m from the shoreline, is

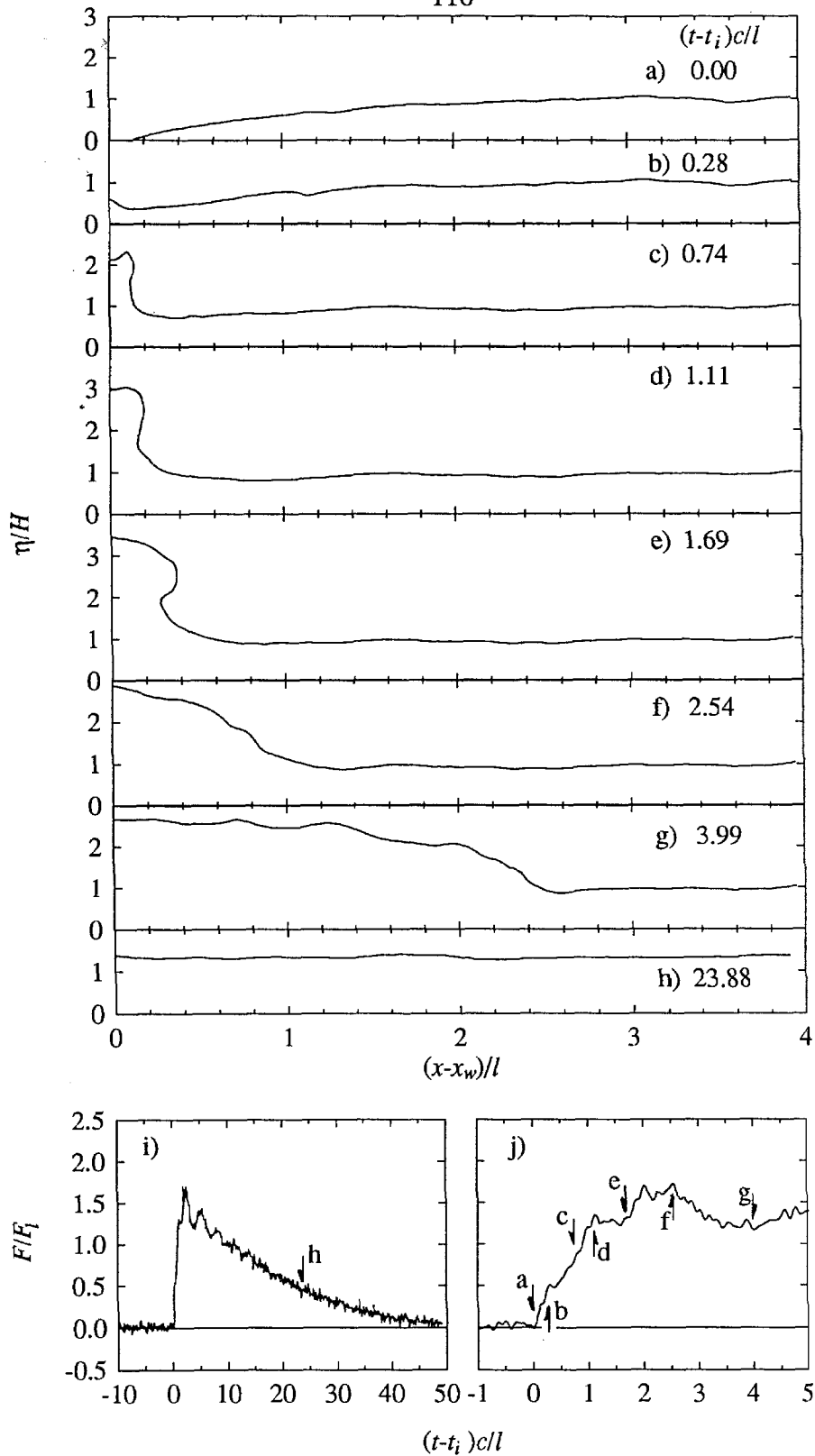


Figure 5.1.8 Relative force and water surface profiles at selected non-dimensional times for a 2.2 cm high bore generated from a solitary wave with $H_0/h_0 = 0.044$ (run no. TB119).

shown in Figures 5.1.8(a) through (h). These profiles were obtained from a frame-by-frame analysis of the movies. Figure 5.1.8(i) shows the corresponding time history of the measured force on the wall, normalized by the linear force scale, F_l , which is defined as:

$$\frac{F_l}{\frac{1}{2}\gamma b h_w^2} = \left(2\frac{H}{h_w} + 1\right)^2. \quad (5.1.2)$$

Equation 5.1.2 will be used frequently throughout Chapter 5 to normalize the experimental and theoretical forces. In Equation 5.1.2, γ is the unit weight of water at 20° Celsius; b is the width of the instrumented wall plus one-half the gap width on either side (4.97 cm); H is the maximum incident surge height; and h_w is the depth of water at the base of the vertical wall (5 mm). Equation 5.1.2 is equal to the force which would occur on the wall if the wave reflections at the wall were linear and the resulting pressure distribution on the wall was hydrostatic. A linear wave reflection at the wall would produce a runup equal to twice the incident wave height. Equation 5.1.2 is a reasonable approximation for the force produced on a wall due to the reflection of very small amplitude long waves. This is shown in Section 5.2 for small amplitude solitary waves. Figure 5.1.8(j) shows an expanded view of Figure 5.1.8(i), which includes the times of the maximum run-up and maximum force. Arrows identified by letters in the force plots correspond to the times of occurrence of the profiles given in Figures 5.1.8(a) through (g).

Figure 5.1.9 is similar to Figure 5.1.8, except that the bore was generated from a wave with an incident relative wave height of $H_o/h_o = 0.288$. Comparing the profiles

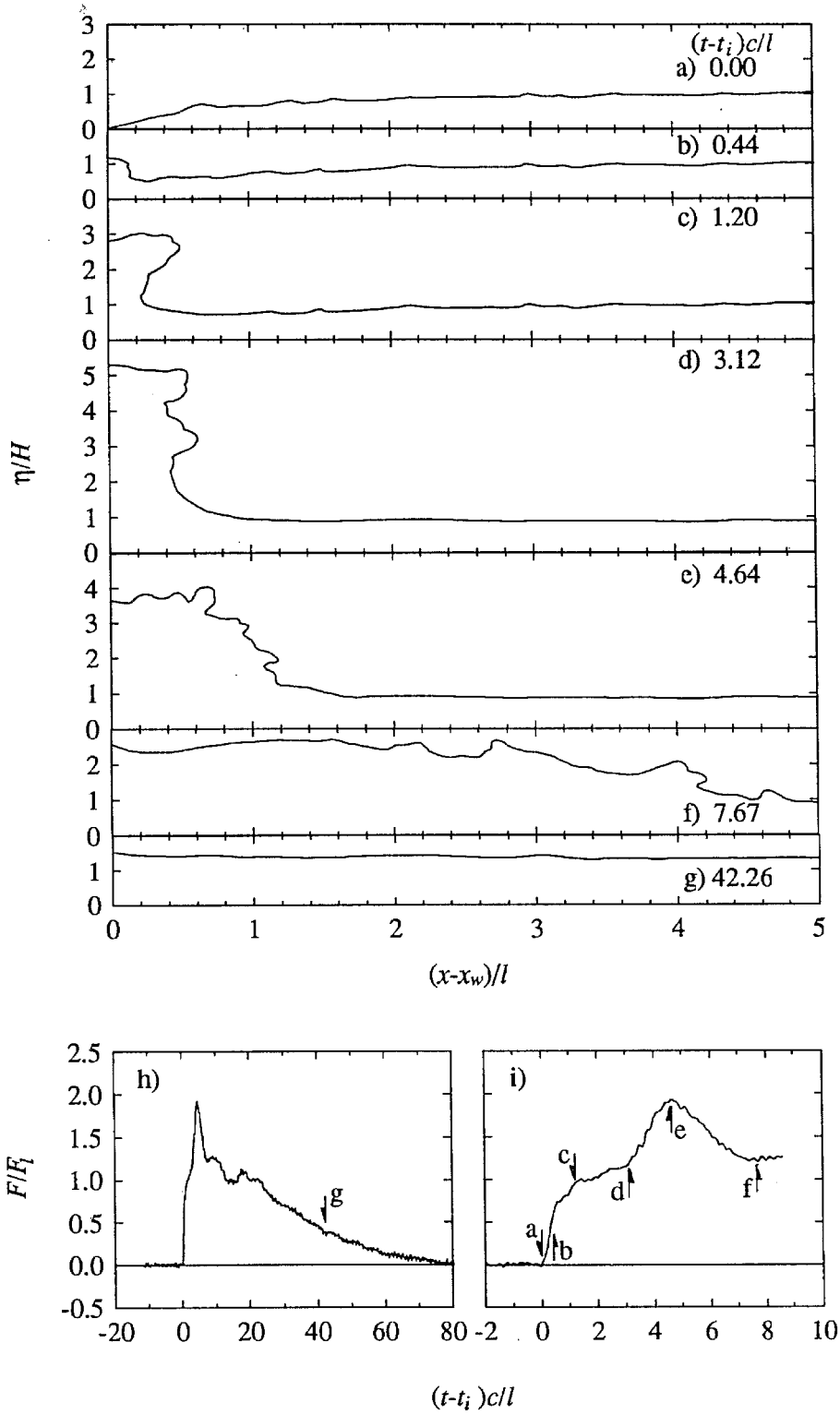


Figure 5.1.9 Relative force and water surface profiles at selected non-dimensional times for a 4.71 cm high bore generated from a solitary wave with $H_0/h_0 = 0.288$ (run no. TB108).

from the two wave conditions reveals a much more irregular surface profile for the larger bore. Figures 5.1.8(e) and 5.1.9(d) show the profile at the instant of maximum run-up, while Figures 5.1.8(f) and 5.1.9(e) show the profiles at the instant of maximum force. Again the maximum force occurs at a time after the maximum run-up. This was the case for all the incident wave conditions measured.

The variation of the measured force on the wall with time is shown in Figure 5.1.10 as solid lines. The data shown as the circles are the force, F_R , which is computed from the run-up height on the instrumented wall, assuming the pressure is distributed hydrostatically with depth as follows:

$$\frac{F_R}{\frac{1}{2}\gamma b h_w^2} = \left(\frac{R}{h_w} + 1 \right)^2, \quad (5.1.3)$$

where $R(t)$ is the runup history on the wall. Figure 5.1.10(b) shows the same force histories as Figure 5.1.10(a) with an expanded time scale. In Figure 5.1.10(c), the measured force is compared to the force calculated from:

$$\frac{F(t)}{\frac{1}{2}\gamma b h_w^2} = \left(\frac{\eta(t)}{h_w} + 1 \right)^2 + 2C_F \frac{\eta}{h_w} \frac{c^2}{g h_w} \quad (5.1.4)$$

which is shown as the dashed line. Equation 5.1.4 is equivalent to the expression proposed by Cross (1967) (Equation 2.3) except the ambient water depth at the wall, h_w , is added to the wave profile in the hydrostatic term. The measured wave profile was

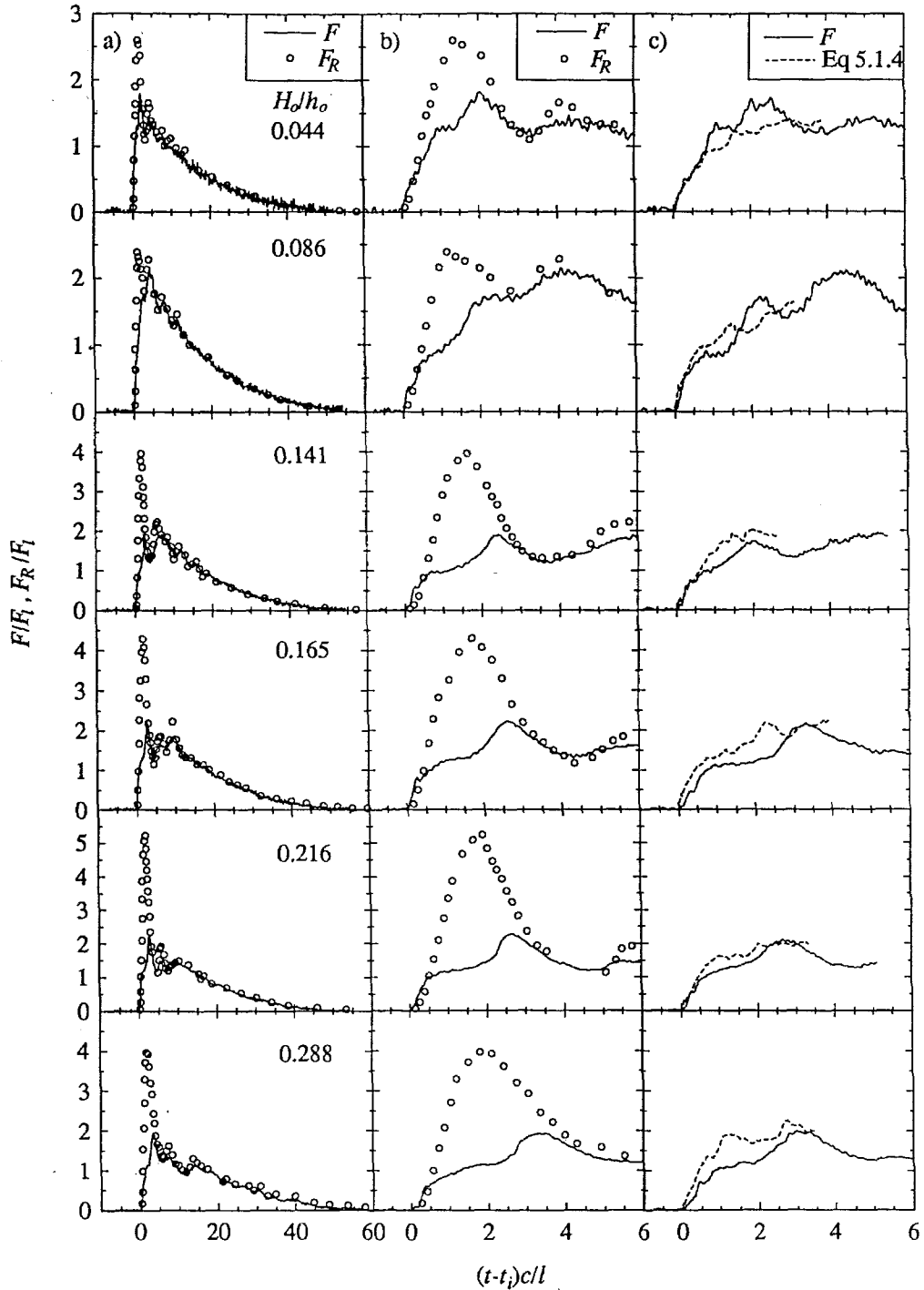


Figure 5.1.10 Non-dimensional plots comparing the measured force (F) to (a) the hydrostatic force (F_R) computed from the runup height on the vertical wall; (b) with expanded time scale (run no.'s TB94, TB96, TB98, TB100, TB102, and TB104); (c) normalized theoretical force from Equation 5.1.4 and 2.4 (run no.'s TB109, TB111, TB112, TB114, TB116, and TB119).

used to determine the slope of the wave, θ , which was used along with Equation 2.4 to calculate C_F . The measured incident bore celerity, c , and its profile, η , were used in Equation 5.1.4 to determine the force time history shown in Figure 5.1.10(c). The measured force shown in Figures 5.1.10(a) and (b) were obtained simultaneously with movies of the run-up on the instrumented wall. However, the measured force shown in Figure 5.1.10(c) was obtained at the same time as the movies of the bore profile; the latter is needed in the computation of the theoretical force (Equation 5.1.4). Since these two photographic records require different camera locations, the experimentally measured forces were somewhat different.

Most striking in all cases, is that the maximum force occurs after the maximum runup as shown in Figure 5.1.10(b). In addition, the measured force is significantly smaller than the hydrostatic force computed from the runup on the wall for non-dimensional times less than about three. For times greater than three, the measured force and the hydrostatic force agree reasonably well except for the bore generated from a wave with an initial relative height of $H_o / h_o = 0.288$, where the force on the wall does not become hydrostatic until a relative time of about four. This is probably due to a steeper water surface slope for this case relative to the others which contributed to a smaller time scale. The difference between the measured and hydrostatic forces, as well as the motion of the water surface along the wall, which appears to be in free fall, indicates the presence of vertical accelerations in the flow along the wall.

Consider the two-dimensional Euler equations applied in the z -direction along the wall between the free surface and the bottom:

$$\frac{\partial w}{\partial t} + u \frac{\partial w}{\partial x} + w \frac{\partial w}{\partial z} = -\frac{1}{\rho} \frac{\partial p}{\partial z} - g, \quad (5.1.5)$$

where the coordinate system (x, z) , velocity components (u and w), and gravity (g) are defined in Figure 5.1.1(b); and the fluid density and gage pressure are ρ and p , respectively. If the acceleration is zero, then one obtains the hydrostatic pressure condition. Since the wall is impermeable, u is zero everywhere along the wall. Thus, the second term in the left-hand side of Equation 5.1.5 vanishes and one obtains:

$$-\frac{1}{\gamma} \frac{\partial p}{\partial z} = \frac{1}{g} \left(\frac{\partial w}{\partial t} + w \frac{\partial w}{\partial z} \right) + 1. \quad (5.1.6)$$

Equation 5.1.6 shows that negative vertical accelerations in the flow decrease the pressure gradient and the force relative to those which would result if the pressure were distributed hydrostatically.

Although the variation of the vertical acceleration with z is unknown, it is possible to comment on $\partial w/\partial t$ and $w(\partial w/\partial z)$ at the water surface and at the bottom. If one assumes that the flow through the gap between the wall and the bottom is negligible, then this becomes a stagnation point where the velocity and acceleration are zero. The kinematic boundary condition at the water surface on the wall implies $\partial \eta/\partial t = w$. Thus, the local water particle acceleration, $\partial w/\partial t$, at the water surface can be evaluated from the measured runup. At the time of maximum runup, the vertical velocity on the free surface is zero, leaving only the local vertical acceleration. Therefore, the local acceleration varies from $\partial^2 \eta/\partial t^2$ at the surface, to zero at the bottom, while the convective acceleration varies in some fashion between zero at both the surface and the bottom at that time.

The variation of the relative measured run-up, $R/2H$, as a function of the non-dimensional time is shown in Figures 5.1.11(a) through (f) for various initial relative

wave heights. These data were obtained from a frame-by-frame analysis of the high-speed movies of the runup. (Since the runup tongue was not constant across the width of the instrumented wall, its average value was used.) The large negative curvature near the time of maximum runup for each case suggests strong temporal vertical accelerations in the water near the wall.

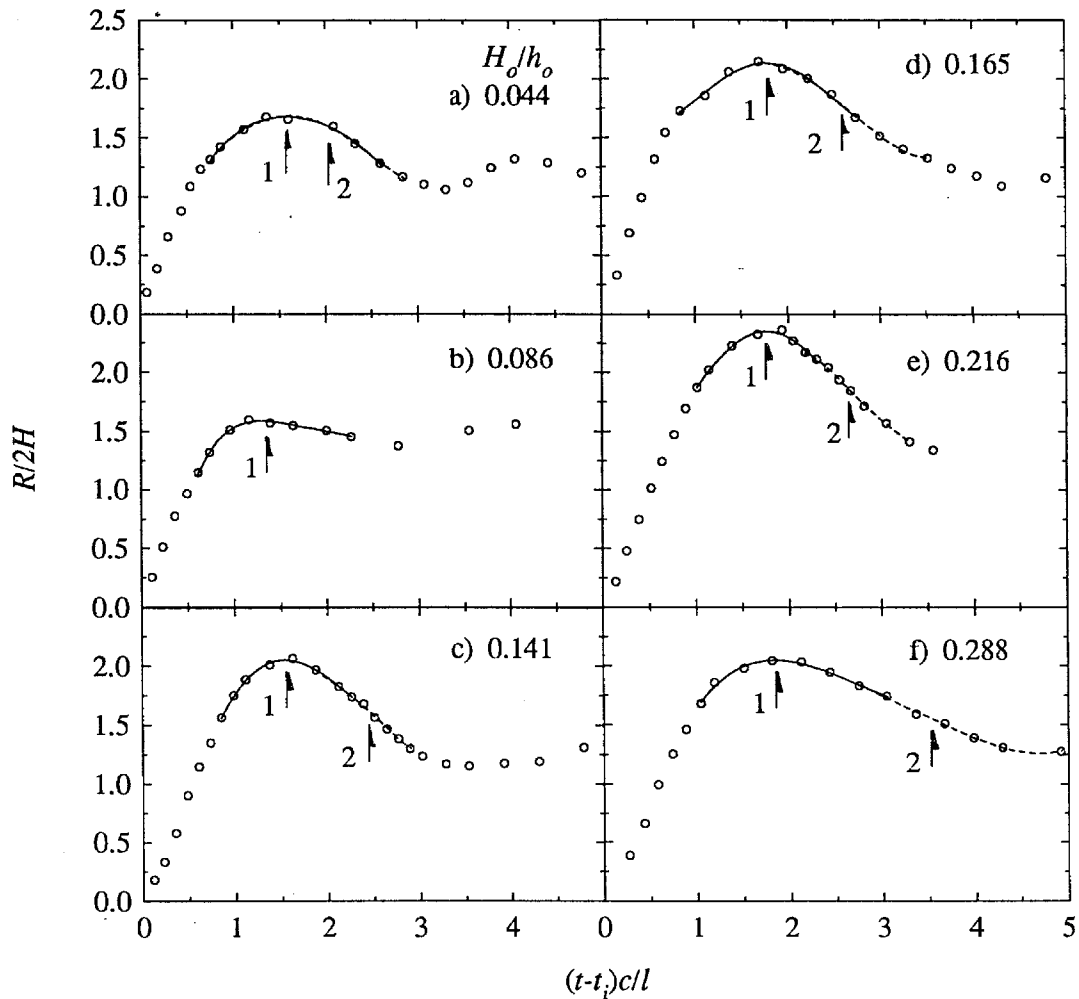


Figure 5.1.11 The (o) measured runup, R , and fourth order polynomial curves fitted to data points near (—) maximum runup and (----) maximum measured force (run no.'s TB94, TB96, TB98, TB100, TB102, and TB104).

To estimate the temporal acceleration at the water surface, the measured runup must be differentiated twice; however, the measurement errors in the runup prevent direct calculation from the raw data. Thus, the runup was approximated with fourth-order polynomial curves fitted through eight data points centered about the time of the maximum runup and the maximum force. The corresponding curves are shown as solid and dashed lines (for the section of the data in the vicinity of the times of the maximum runup and the maximum force, respectively); these appear essentially to be coincident. The vertical accelerations of the water surface computed from these curves corresponding to the time of maximum runup and the time of maximum force are normalized by gravity as shown in Table 5.1.1. In Figure 5.1.11(b), no vertical

| H_o/h_o | $-(\partial^2\eta/\partial t^2)/g$ | |
|-----------|------------------------------------|------------|
| | At $\ R\ $ | At $\ F\ $ |
| 0.044 | 0.20 | 0.18 |
| 0.086 | 0.28 | ---- |
| 0.141 | 0.69 | 0.20 |
| 0.165 | 0.61 | 0.09 |
| 0.216 | 0.91 | -0.07 |
| 0.288 | 0.67 | -0.02 |

Table 5.1.1 Variation of the relative acceleration of the water surface at the wall (computed from the polynomial curves shown in Figure 5.1.11) with the relative incident wave height, H_o/h_o .

acceleration is computed for the force, since there is no local maximum force immediately following the maximum runup as occurs for the condition corresponding to Figures 5.1.11(a) and 5.1.11(c) through (f). The accelerations shown in Table 5.1.1 tend to increase with increasing bore height at the time of maximum runup. This trend explains the difference between the measured force and force computed from the measured runup, assuming a hydrostatic pressure distribution. As was shown in Figures

5.1.10(a) and (b), the difference between the hydrostatic and measured forces increases as the bore height increases. The vertical acceleration computed at the time of the maximum measured force is considerably less than that computed at the time of the maximum runup. Thus, based on Equation 5.1.6, one would expect the hydrostatic force to approach the measured force at the time of the maximum force, which can be seen clearly in Figure 5.1.10(b).

In Figure 5.1.10(c), the agreement between the maximum measured force and the maximum force calculated from Equation 5.1.4 is within 22% of the maximum measured force. Equation 5.1.4 over-predicted the maximum measured force by 5%, 3%, and 14% for the bores generated from waves with initial relative heights of $H_o / h_o = 0.141$, 0.165, and 0.288, respectively. For a relative wave height of $H_o / h_o = 0.216$, Equation 5.1.4 under-predicted the measured maximum force by 3%. For the two smallest bores, Equation 5.1.4 over-predicted the maximum measured force by about 21%, which may indicate the growing importance of the water depth at the wall, relative to the bore height as the incident bore becomes very small or possibly scale effects (the smallest bores exhibited much less air entrainment relative to the largest bores). The different trends followed by Equation 5.1.4, compared to the measured force, indicates the inability of the theory to fully model the dynamics during the entire runup process. This is not surprising since the theory of Cumberbatch (1960) was intended for the impact on a horizontal surface of a wedge of water traveling in a vertical direction, with a uniform velocity and without gravitational effects. During this initial stage of impact, Equation 5.1.4 agrees very well with the measured force for relative times less than about 0.7. The agreement of the theory with the maximum measured force, for most of the largest bores, indicates a reasonable estimate of the maximum force can be obtained by using Equation 5.1.4, where the force coefficient is set to unity and the wave height is substituted in place of η . Following the development of Cross (1967), this indicates the maximum

force on the wall is proportional to the momentum flux for the four strongest bore conditions in this study.

Air entrainment can also reduce the force on the wall since it decreases the fluid density and the speed of sound in water. The high-speed movies taken in connection with these experiments showed more air entrained by the larger bores relative to the smaller ones. A decrease in fluid density will decrease the pressure gradient and the force on the wall since the pressure gradient is proportional to the density. Shock pressures that may be caused by water impacting a rigid surface are directly proportional to the speed of sound in water as shown by Von Karman and Wattendorf (1929). Gibson's (1970) experimental results show that air content of only 1% by volume will decrease the speed of sound in water to approximately 10% of its original value. This effect must be considered in coastal wave and surge impact problems when shock pressures are likely to occur, although the natural frequency of the walls used in this study most likely attenuated any response due to the high-frequency content of shock pressures.

The maximum measured water surface slope on the front of the wave, the runup, and the force are plotted as a function of the relative wave height, H/h , in Figure 5.1.12(a) through (e). In Figure 5.1.12(a) the maximum slope of the bore increases from about 0.2 to 0.3 as the relative wave height increases from 1.75 to 3.4. For all the incident wave conditions, the maximum runup normalized by twice the bore height, $2H$, ranged from 1.6 to 2.35 as seen in Figure 5.1.12(b). The runup normalized by twice the incident wave height seems to increase somewhat with the relative wave height, as does the maximum wave slope. Figure 5.1.12(c) indicates little or no trend in the maximum runup on the wall when normalized by the velocity head computed from the bore celerity. These values vary between 2.0 and 2.6 and are in agreement with the

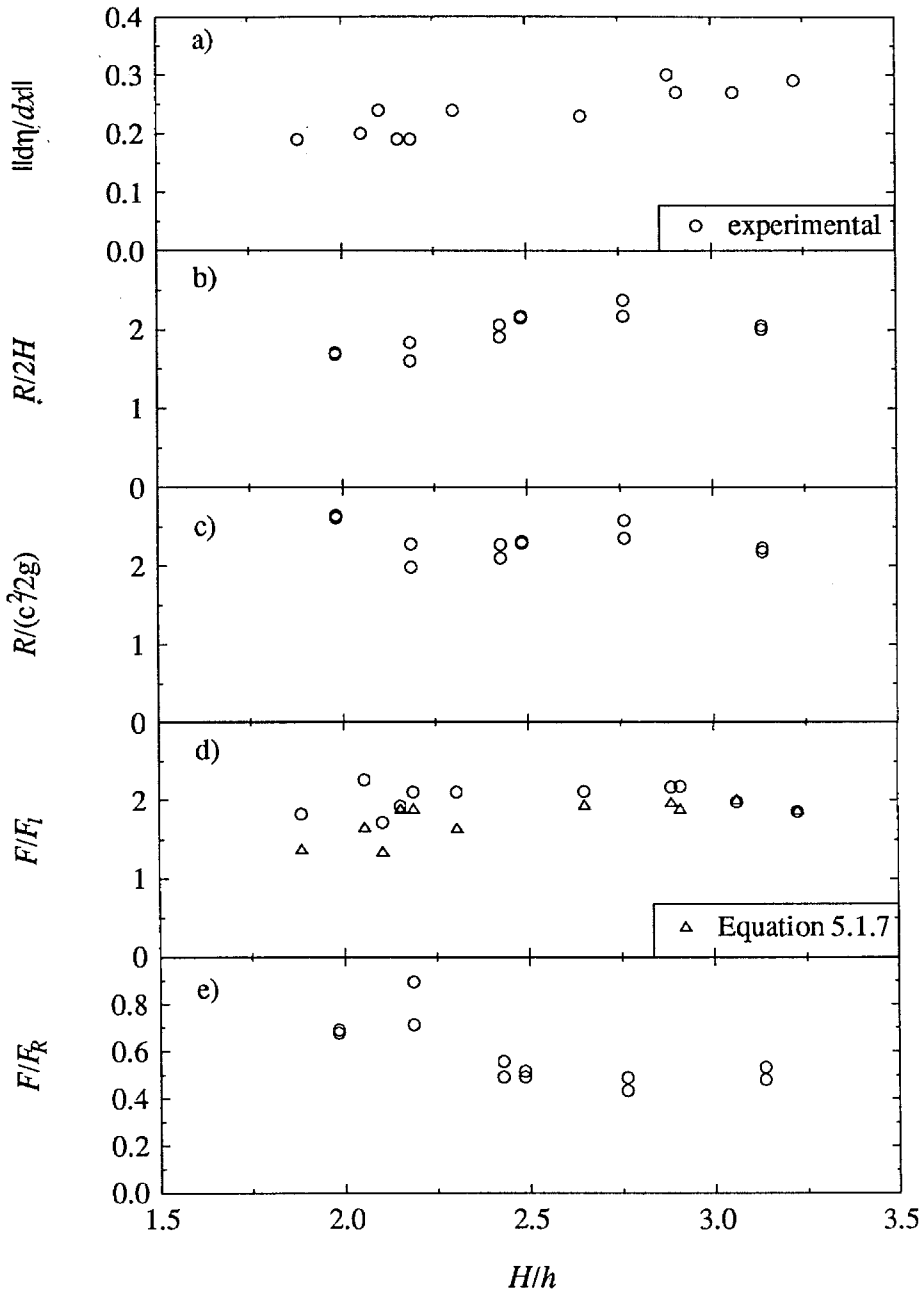


Figure 5.1.12 Variation with respect to the relative incident bore height of (a) the maximum measured wave slope; the maximum measured runup normalized by (b) twice the incident wave height and (c) the velocity head computed from the bore celerity; and the maximum measured force normalized by (d) the linear force scale, F_l ; (e) the hydrostatic force computed from the maximum runup on the wall, F_R .

experimental results of Cross (1966) which ranged from 2.0 to 2.3 times the velocity head for his "wet-bed" case ($h = 4.6$ mm). Fukui et al. (1963) reported maximum runup heights that were approximately three times the velocity head for his range of experimental bore conditions ($0.5 < H/h < 3$).

The maximum measured and theoretical forces normalized by the linear hydrostatic force, F_l , (Equation 5.1.2) are shown in Figure 5.1.12(d). The theoretical force shown in Figure 5.1.12(d) is obtained by substituting $C_F = 1$ and $\eta = H$ into Equation 5.1.4 which gives:

$$\frac{F(t)}{\frac{1}{2}\gamma b h_w^2} = \left(\frac{H}{h_w} + 1\right)^2 + 2\frac{H}{h_w} \frac{c^2}{g h_w}. \quad (5.1.7)$$

The measured results vary between 1.7 to 2.3, and agree quite well with the theory for the cases with the largest relative wave heights. As the relative wave height decreases, Equation 5.1.7 increasingly under-predicts the experimental force by up to 27% at a relative wave height of 2.05. This may indicate a growing importance of the still water depth relative to the incident wave height as the relative wave height decreases.

Figure 5.1.12(e) shows the maximum measured force normalized by the hydrostatic force, F_R , (Equation 5.1.3) computed from the maximum runup height on the wall. For the four strongest bores, the relative force lies between 0.43 and 0.56, and appears to be independent of the relative wave height. At $H/h = 2.18$ one of the points ($F/F_R = 0.9$) seems to lie outside the trend implied by the rest of the measurements. However, the measured force for both the points at $H/h = 2.18$ was the same, indicating

the runup height was smaller for the data point at $F / F_R = 0.9$. As Figure 5.1.12(e) shows, all the measured forces were less than the hydrostatic force due to the maximum runup height on the wall.

5.2 Solitary Waves

In this section, the experimental results for the solitary waves will be presented. The measurements include the celerity of the wave along the tank, the water surface profile at two locations using wave gages, the profile of the wave runup on the wall using the LIF method, and the force, moment, and pressure time histories. The results are compared with several theoretical and numerical models as well as both numerical models discussed in Chapter 3. See Figure 4.2.26 for a definition sketch of the experimental setup.

5.2.1 Amplitude and Celerity Considerations

A typical example of the experimental result obtained from the celerity probes is shown in Figure 5.2.1 for a wave with a relative wave height of $H / h = 0.504$ traveling on a water depth, h , of 17.74 cm. The ordinate is time measured from the beginning of the wave generator motion. The abscissa is the distance from the wave generator, $x_p - x$, where x_p is the location of the wave generator rest position. The coordinate system origin is located at the intersection of the still water surface and the vertical wall (Figure 4.1). The circles show the arrival time of the solitary wave at each of the five stations along the tank, and the solid line shows an approximation using a parabolic least squares fit. The resulting parabolic equation is differentiated, which then gives the velocity of the bore along the tank. This resulting approximation can be used to calculate the celerity of the wave at any desired location along the tank. For the case shown in Figure 5.2.1, the wave celerity at the wall (assuming the wall was not there to reflect the incident wave) was $c = 160.7$ cm/sec, which gives a relative wave celerity, c / \sqrt{gh} , of

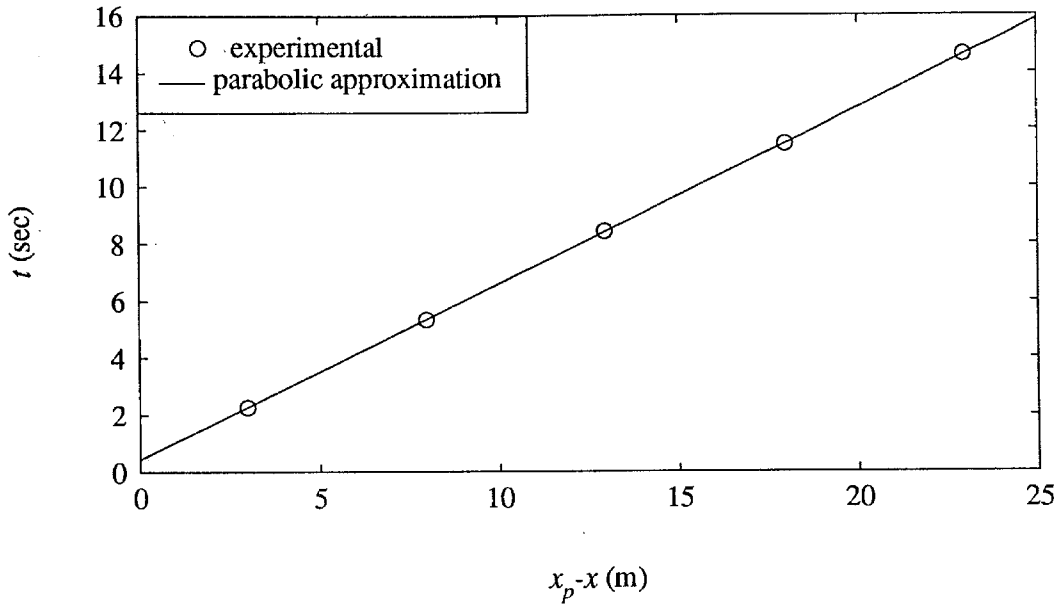


Figure 5.2.1 Times of solitary wave arrival at the celerity probes for a solitary wave of $H/h = 0.504$ which was propagating on a depth of $h = 17.74$ cm (run no. HW37).

1.22. The celerity probes were placed every five meters along the wave tank with the first probe located 1.500 meters (or $x/h = 8.45$) in front of the instrumented wall. For each experiment, the probes were all placed at the same elevation above the still water surface.

Figure 5.2.2 compares the measured relative wave celerity, c / \sqrt{gh} , as a function of the relative wave height, H / h , with theories due to Boussinesq (1872) (Equation 3.35) and Longuet-Higgins and Fenton (1974), where the squares and circles show the measured results 19.0 meters and 2.2 meters (or $x/h = 107.6, 12.5$) in front of the instrumented wall, respectively. Longuet -Higgins and Fenton (1974) computed a series solution for the mass, potential energy, and kinetic energy of a solitary wave in terms of the perturbation parameter, $\epsilon = 2(H / h) + 1 - (c^2 / gh)$. For a given value of ϵ , the solution for the mass and the potential energy can be used along with the known value of the perturbation parameter to calculate the wave speed and the wave height.

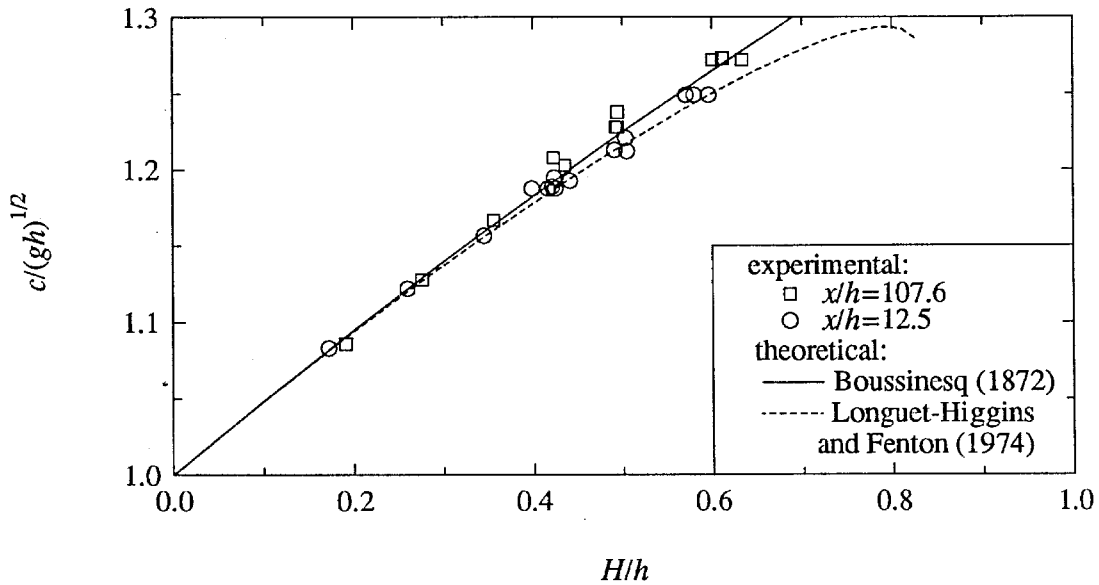


Figure 5.2.2 Relative celerity of solitary waves near the wave generator ($x/h = 107.6$) and near the vertical wall ($x/h = 12.5$).

The squares in Figure 5.2.2 show the experimental results 31.0 depths in front of the initial wave generator position, which tend to follow the Boussinesq solution over the full range of wave heights obtained. However, as the wave reaches the wave gage 12.4 depths in front of the instrumented wall (126.1 depths from the wave generator), the results shown with the circles tend to follow the numerical results of Longuet-Higgins and Fenton (1974). The difference between the experimental results and the analytical results using the Boussinesq theory near the wave generator, compared to the numerical results of Longuet-Higgins and Fenton at larger distances from the wave generator, may be due to the method of wave generation used in the experiments. The method developed by Goring (1979), which was used to produce the solitary waves, uses the Boussinesq (1872) wave speed and wave profile to calculate the appropriate trajectory for the wave generator. Thus, as the wave is generated, it should resemble the Boussinesq solution until it has a chance to deform due to the effects of both frequency

and amplitude dispersion. Figure 5.2.2 shows excellent agreement between both theories and the experimental results at both locations for relative wave heights smaller than approximately 0.4. As the relative wave height becomes large, the small wave height assumption in the Boussinesq theory is violated. Thus, a higher order theory such as that due to Longuet-Higgins and Fenton (1974) would be more accurate. This is evident in Figure 5.2.2 where it appears that the Boussinesq theory tends to over-predict the celerity computed by Longuet-Higgins and Fenton. As the relative wave height increases, the trajectory associated with the generation begins to deviate from the boundary conditions which would be required to produce a perfect solitary wave. This causes an initial wave profile which is not an exact solitary wave. As this wave propagates down the tank, a solitary wave and tail of oscillatory waves emerge from the initial wave as discussed by Hammack and Segur (1978). As a steep solitary wave emerges from this oscillatory tail, one would expect the full potential theory to be a more accurate model than the Boussinesq theory, where the small wave height assumption is violated. This phenomenon of the imperfect wave generation and the emergence of a solitary wave may be the reason the experimental results follow the Boussinesq theory near the wave generator, and the theory of Longuet-Higgins and Fenton, farther down the wave tank.

There are two additional factors which contribute to a gradual change in the wave as it propagates down the tank. Frictional effects due to the sidewalls and the tank bottom gradually decrease the energy in the solitary wave as shown by the analysis of Keulegan (1948) (see also French (1969) and Naheer (1976)). A second factor that may affect the volume of the wave is the apparent wetting of the sidewalls as the wave crest propagates down the tank. This causes fluid to be extracted from the wave, which is then continuously deposited behind the crest as it passes. Evidence of this phenomenon is readily observed in the laboratory as droplets remaining on the sidewall after the passage

of the wave. It is believed this effect is small, but it is difficult to determine its importance quantitatively.

Tanaka (1986) presents a method which iteratively solves for a solitary wave solution, satisfying the full potential theory (which is the Euler Equations coupled with the full nonlinear free surface boundary conditions). In Figure 5.2.3(a) and (b) the experimentally measured wave profiles are compared to the theoretical wave profiles

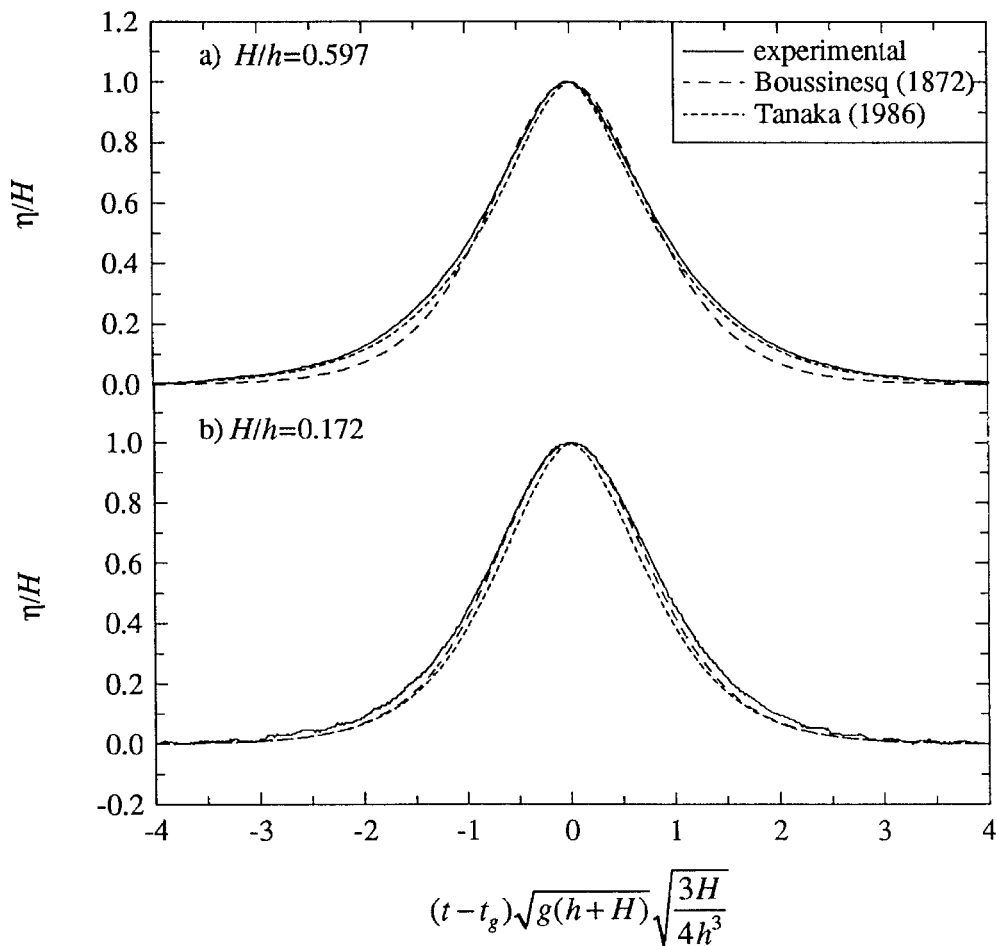


Figure 5.2.3 Comparison of theoretical and experimental solitary wave profiles for waves traveling on depths, h , of (a) 17.74 cm (run no. HW36) and (b) 17.71 cm (run no. HW42).

from Tanaka (1986) and the Boussinesq theory. The results for solitary waves with relative wave heights of 0.597 and 0.172 are shown in Figure 5.2.3(a) and (b), respectively. The primary discrepancy between the experimental and theoretical results is that the Boussinesq theory tends to under-predict the height of the steep wave near its tails (see Figure 5.2.3(b)). Tanaka's theory predicts the shape of the tail on the steep wave quite well, but gives a slightly narrower crest than both the experimental and Boussinesq profiles for the small wave shown in Figure 5.2.3(b).

Figure 5.2.4 shows a comparison between the water surface profile time histories obtained with the LIF method, and a wave gage 1.37 depths ($h = 17.46$ cm) in front of the instrumented wall. Figures 5.2.4(a) and (b) show the comparison for two identical experiments where $H/h = 0.42$. Figure 5.2.4(c) shows the two LIF time histories from Figures 5.2.4(a) and (b) plotted together. The agreement between the wave gage and the LIF method is within 3% of the maximum water surface elevation at this location, in both Figures 5.2.4(a) and (b), indicating the LIF method can accurately record the displacement of the free surface. The two LIF time series shown in Figure 5.2.4 agree to within 5% of the maximum wave height at this location. It is interesting that the water surface time history is not symmetric. This may be due to nonlinear interactions during the reflection (Su and Mirie (1980)).

The water surface profiles, η/H , measured with the laser induced fluorescence system are shown for five non-dimensional times, $(t - t_s)\sqrt{gh(1 + H/h)}\sqrt{3H/4h^3}$, during wave runup in Figure 5.2.5. The time, t_s , is when the crest of the solitary wave would be at the wall if the wall were not present. This time, t_s , is determined by adding the time it took the wave crest to arrive at the wave gage (12.4 depths ($h = 17.74$ cm) from the wall), to the time it would take the wave crest to propagate the rest of the distance to the

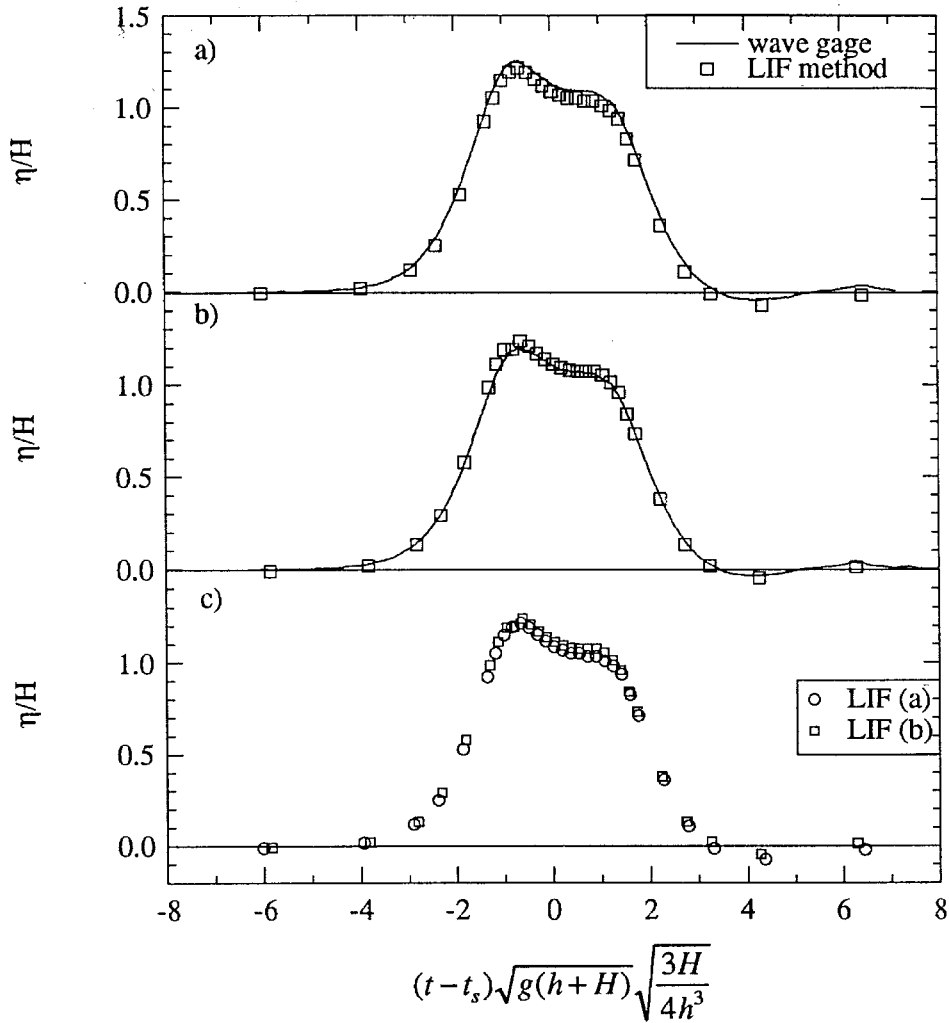


Figure 5.2.4 A comparison of water surface time histories at $x/h = 1.37$ using the LIF system and a wave gage for two identical experiments (a) (run no. HW45) and (b) (run no. HW46) with $H/h = 0.42$; both LIF time histories from (a) and (b) are shown in (c).

wall. The average celerity of the wave over the last 12.4 depths in front of the wall (computed from the parabolic approximation) is used to determine the propagation time. The abscissa in Figure 5.2.5 is the distance from the wall normalized by the horizontal length scale, $(l = H/(\|d\eta/dx\|))$. The slight curvature of the profiles at the wall is most pronounced at a relative time of -0.58. This is probably due to the meniscus along the instrumented wall.

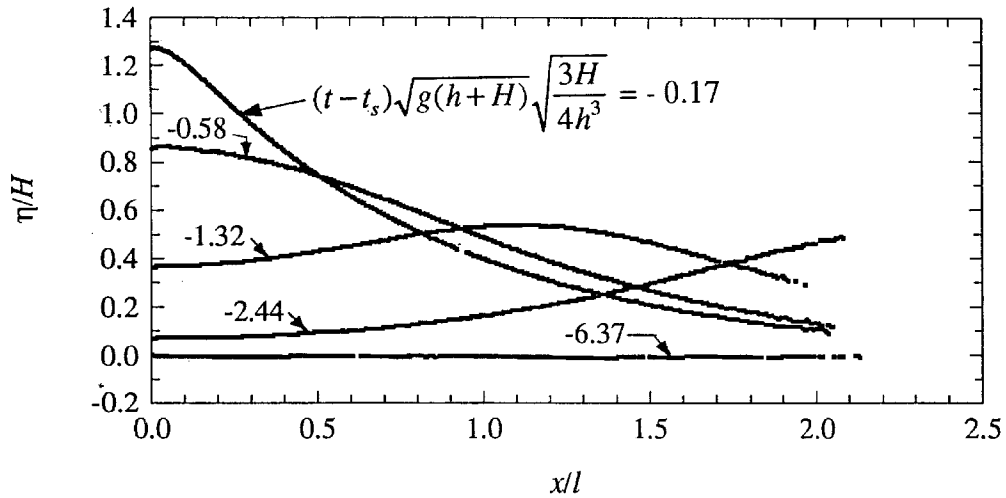


Figure 5.2.5 Profiles of a solitary wave with $H/h = 0.504$ running up the vertical wall as obtained from the laser induced fluorescence system (run no. HW37).

Profiles such as those shown in Figure 5.2.5 were used to experimentally define the runup history on the wall, which is shown in Figure 5.2.6 for five solitary waves with different relative wave heights, where the ordinate is the relative runup and the abscissa is non-dimensional time. Although the video camera only operates with a framing rate of 1/30 th of a second, this is apparently adequate to quantify the maximum runup height as can be seen by the small dots which show the actual data points along each curve. The runup has been non-dimensionalized by $2H$, which is the runup which would be caused by a linear reflection at the wall. One can see that the maximum relative runup height increases with increasing incident solitary wave height. This is due to the nonlinear interactions which occur during the reflection process, resulting in values of $R/2H$ greater than unity, which was shown by Su and Mirie (1980) in their third order (in H/h) analytical solitary wave collision theory. There is a lag in the time of the maximum runup, relative to the time the wave crest would be at the wall if the wall were not there. The lag in the runup and the magnitude of the negative runup, or rundown, after the reflection, increase as the incident wave height increases.

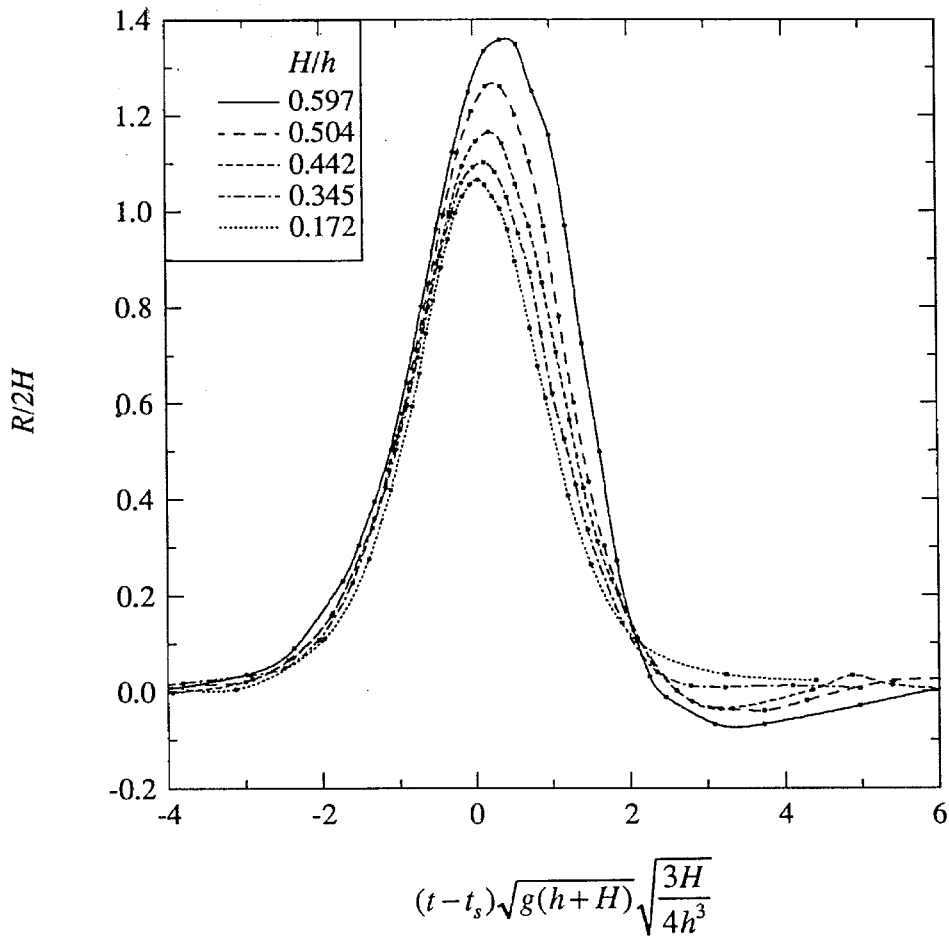


Figure 5.2.6 Plot of the measured runup time histories caused by solitary waves for various relative wave heights (run no.'s HW36, HW37, HW40, HW42, and HW44).

5.2.2 Pressure, Force, and Moment Considerations

Figures 5.2.7 and 5.2.8 show a comparison between experimentally measured results for a solitary wave with numerical models based on the boundary element method (BEM), (shown with the dashed line), and the finite difference model (SOLA-VOF), (shown with the dotted line) which were described in Chapter 3. The experimentally measured relative wave height 2.2 meters in front of the instrumented wall was $H/h = 0.504$ in a water depth, $h = 17.74$ cm. This wave height was used to determine the initial conditions for both numerical models. The "numerical wave tank" for both numerical simulations was 2.5 meters long. Initially, the BEM wave tank was longer,

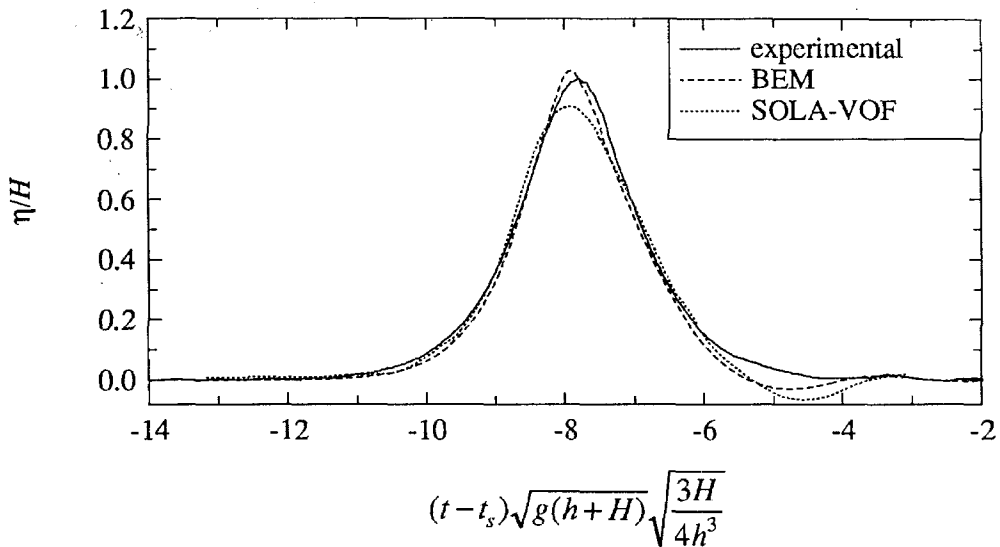


Figure 5.2.7 Comparison of experimental and theoretical water surface time histories 12.4 water depths in front of the vertical wall due to a solitary wave with $H/h = 0.504$ (run no. HW37).

but after the wave was generated, the resulting wave tank was about 250 cm long. The BEM model had 51 nodes along the free surface and the bottom, while 12 nodes were used along the lateral boundaries. The time step used was 0.086 sec, which was decreased by a factor of two during the runup on the wall, which improved the conservation of energy and mass during the numerical experiment. The SOLA-VOF model had 200 grids along the tank and 25 grids in the vertical direction, for a numerical tank depth of 50 cm. The automatic grid stretching mechanism of SOLA-VOF was used to obtain a horizontal grid spacing of 1 cm at the vertical wall, which increased to 2 cm at a location 50 cm in front of the wall. The remainder of the wave tank had horizontal grid lengths of 2 cm. The automatic time stepping option of SOLA-VOF was used to control the time step. For the boundary element method the numerical piston type wave generator was driven with a trajectory calculated by Goring's (1979) method. For the finite difference algorithm, the wave was produced by applying a time dependent velocity flux, determined as $u = c\eta / (h + \eta)$, through the right lateral boundary.

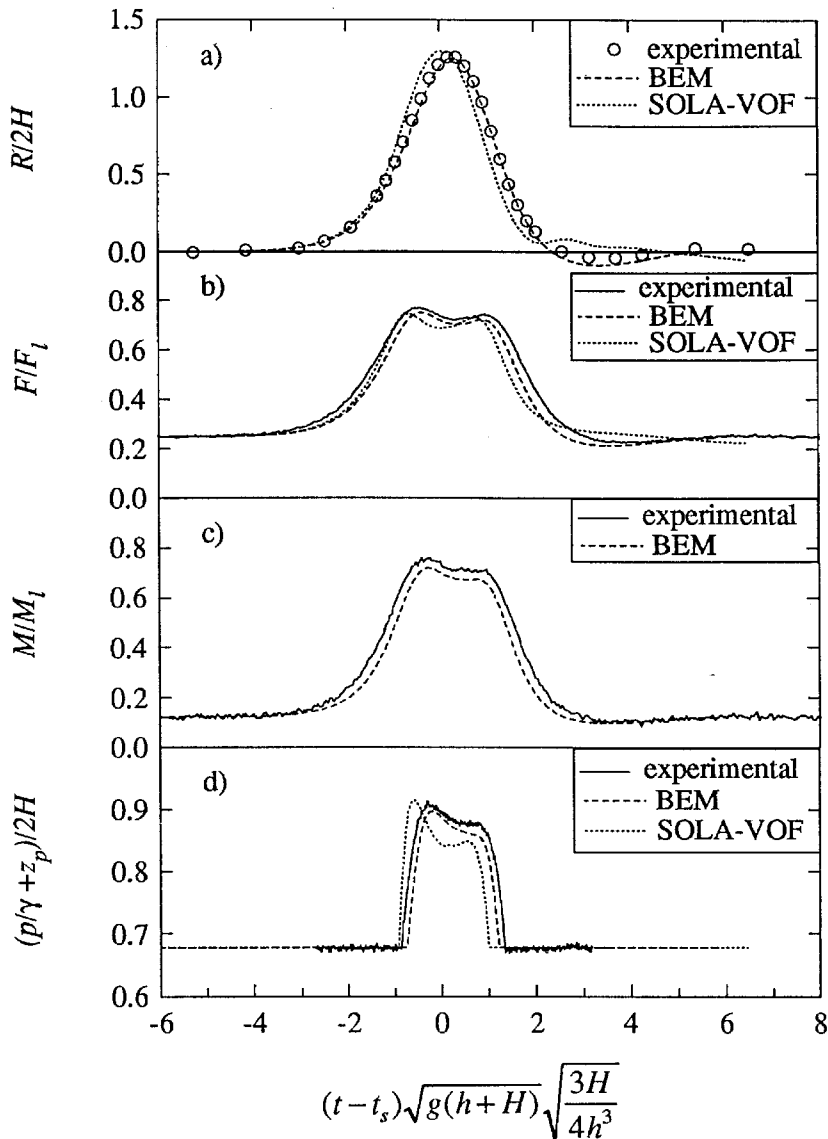


Figure 5.2.8 Comparison of experimental and theoretical time histories of the (a) runup; (b) force; (c) moment; and (d) pressure due to a solitary wave with $H/h = 0.504$ (run no. HW37).

A "numerical" wave gage 2.2 meters in front of the instrumented wall is used to determine the height of the incident wave in the numerical model. The times are determined when the water surface elevation equal to $H/2$ passes that location. The average of the two times so obtained, is taken as the time when the wave crest would pass the wave gage location (i.e., a symmetric wave is assumed). It is at this location, that the experimental and numerical model time scales are synchronized. The average

measured wave celerity between $x/h = 12.4$ and the instrumented wall $x = 0$ was used to compute the time it would take the wave crest to arrive at the location of the instrumented wall if the wall were not there. This is used as the time origin in the non-dimensional time scale for the solitary wave results presented in Figures 5.2.7, 5.2.8, and 5.2.10.

Let the time when the wave trajectory begins be defined as $t = 0$ and the time when the wave crest would be at the wall location, if the wall were not there, as t_i . The non-dimensional time, can then be expressed as $(t - t_i) \sqrt{g(H + h) \frac{3H}{4h^3}}$, where time has been normalized by the time scale in the Boussinesq (1872) solitary wave theory, where

$$c = \sqrt{g(H + h)}, \text{ and } l = \sqrt{\frac{4h^3}{3H}}.$$

The incident wave profiles measured experimentally, and determined numerically are compared in Figure 5.2.7 for the solitary wave with $H / h = 0.504$. In Figure 5.2.7, the ordinate is the water surface elevation above the still water level normalized by the wave height, and the abscissa is the relative time. For Figure 5.2.7, the measured relative wave height was used to normalize the resulting numerical wave profiles. The boundary element method shown with the dashed line, slightly over-predicted the measured wave height by 2.9%. However, as the BEM wave propagated down the tank, the wave height gradually decreased to a value well within 1% of the measured wave height. The SOLA-VOF model under-predicted the measured wave height by 8%, although as it propagated down the numerical wave tank, the wave height gradually increased. Both numerical models had a much more pronounced depression behind them, which is most likely due to the approximate theory used to generate the numerical waves. The discrepancy between the experimental and numerical wave profiles in Figure 5.2.7 are due to the

large difference in the distance from the wave generator. The numerical and experimental wave gages were 1.7 and 124.2 water depths from the wave generator, respectively. The errors in the boundary condition used to generate the wave produce oscillatory waves in addition to the solitary waves. Since the celerity of the solitary wave is larger than the oscillatory waves, the much larger distance in the experimental tank allowed the solitary wave to propagate beyond the leading edge of the oscillatory wave components. Thus, the experimental solitary wave has a symmetric shape, while the numerical wave, which includes the solitary and oscillatory waves, is somewhat asymmetric.

Both mass and energy should be conserved during the reflection of the solitary wave from the wall. The total energy and mass of the wave in the boundary integral element method remained within 0.12 % and 0.05 % of their original values, respectively. Although no calculation of the total energy is performed in the SOLA-VOF code, the conservation of mass is determined and remained within 0.08 % of its original value (once wave generation was complete) during the entire numerical experiment.

Figure 5.2.8 shows the relative runup, force, moment, and pressure as a function of the relative time for an incident solitary wave with $H/h = 0.504$. The abscissa in Figure 5.2.8 is relative time. The ordinates in Figures 5.2.8(a) through (d) are: the runup normalized by twice the incident wave height; the force normalized by F_l , which is the hydrostatic force due to a runup on the wall equal to twice the incident wave height ($1/2 \gamma b(2H + h)^2$, where b is the width of the wall); the moment normalized by M_l , which is the hydrostatic moment due to a runup on the wall equal to twice the incident wave height ($1/6 \gamma b(2H + h)^3$); and the measured pressure head, p/γ , added to the height of the pressure cell above the free surface, z_p , and normalized by twice the incident wave height. Figures 5.2.9(a) and (b) show reasonable agreement between the experimental

results and the boundary element method (BEM) solution as well as the finite difference method (SOLA-VOF), which were both described in Chapter 3. The measured wave celerity was used to compute the time, t_s , which was used to determine the abscissa for the experimental and the numerical models. The SOLA-VOF wave arrives slightly before the experimental wave, while the BEM wave agrees quite well with the experimental results.

Both numerical codes correctly predict the double maxima in the force record and the experimental fact that the first peak is the global maximum as seen in Figure 5.2.8(b). Note that the maximum force occurs before the maximum runup. This is due to the effect of negative accelerations along the wall, which reach their maximum near the time of maximum positive runup. These negative accelerations decrease the force compared to what would be expected if only the hydrostatic force were computed from the runup height on the wall. This has been shown to occur during surge impact on a vertical wall by Ramsden and Raichlen (1990) and was discussed in Section 5.1. For smaller wave heights this "double hump" is absent while it becomes more pronounced as the relative wave height increases. The theoretical moment on the wall from the BEM model, as seen in Figure 5.2.8(c), correctly predicted the shape of the experimental moment although it under-predicted the amplitude by 5 %. Some of the difference between experiment and theory may be reduced by using the method of Tanaka (1986) to define the incident solitary wave as the initial condition in the numerical models (Grilli and Svendsen (1991)). This would eliminate the oscillatory waves in the numerical simulations which caused the asymmetric wave profiles seen in figure 5.2.7. These oscillatory waves in the numerical simulations may have contributed to the discrepancy between the experimental and numerical results shown in Figure 5.2.8.

Figures 5.2.9(a) and (b) show the variation of the maximum measured force expressed non-dimensionally as F/F_l , and the maximum non-dimensional moment on the wall, M/M_l , as a function of the relative incident wave height, H/h . In Figure 5.2.9, F_l and M_l are the force and moment per unit width, calculated from a runup on the wall equal to twice the wave height assuming a hydrostatic pressure distribution. The solid triangles show the measured results, the circles denote the numerical Fourier series solution of Fenton and Rienecker (1982), the diamonds are the theoretical results of Grilli and Svendsen (1991) who used a boundary element method to solve the 2-D Euler equations, and the squares show the results of the boundary element method developed independently by the writer, using the approach described in Grilli, Skourup and Svendsen (1989) (denoted as BEM). The solid line is the result from the third-order analytical theory of Su and Mirie (1980). Grilli and Svendsen (1991) used the exact solitary wave solution of Tanaka (1986) as the initial condition in their numerical results shown here.

In Figure 5.2.9(a) and (b) all four models agree with the experimental results within 5% and 9%, respectively. Some of this discrepancy may be due to experimental errors in the wave height measurements. The errors in the wave height are squared in the force scale F_l and cubed in the moment scale M_l . It is interesting that as the relative wave height increases, the measured and theoretical forces decrease relative to the force which would be caused by a linear reflection at the wall, with a hydrostatic pressure distribution. This will be discussed with regard to Figure 5.2.10, below. Fenton and Rienecker (1982) showed no results for $H/h > 0.516$, since their algorithm was inaccurate for larger waves. The writer and Grilli and Svendsen (1991) found that the boundary element approach became unstable during rundown for relative wave heights larger than 0.5, although Grilli and Svendsen (1992) have indicated the origin of the errors which caused the solution to break down are due to inaccuracies in the way the

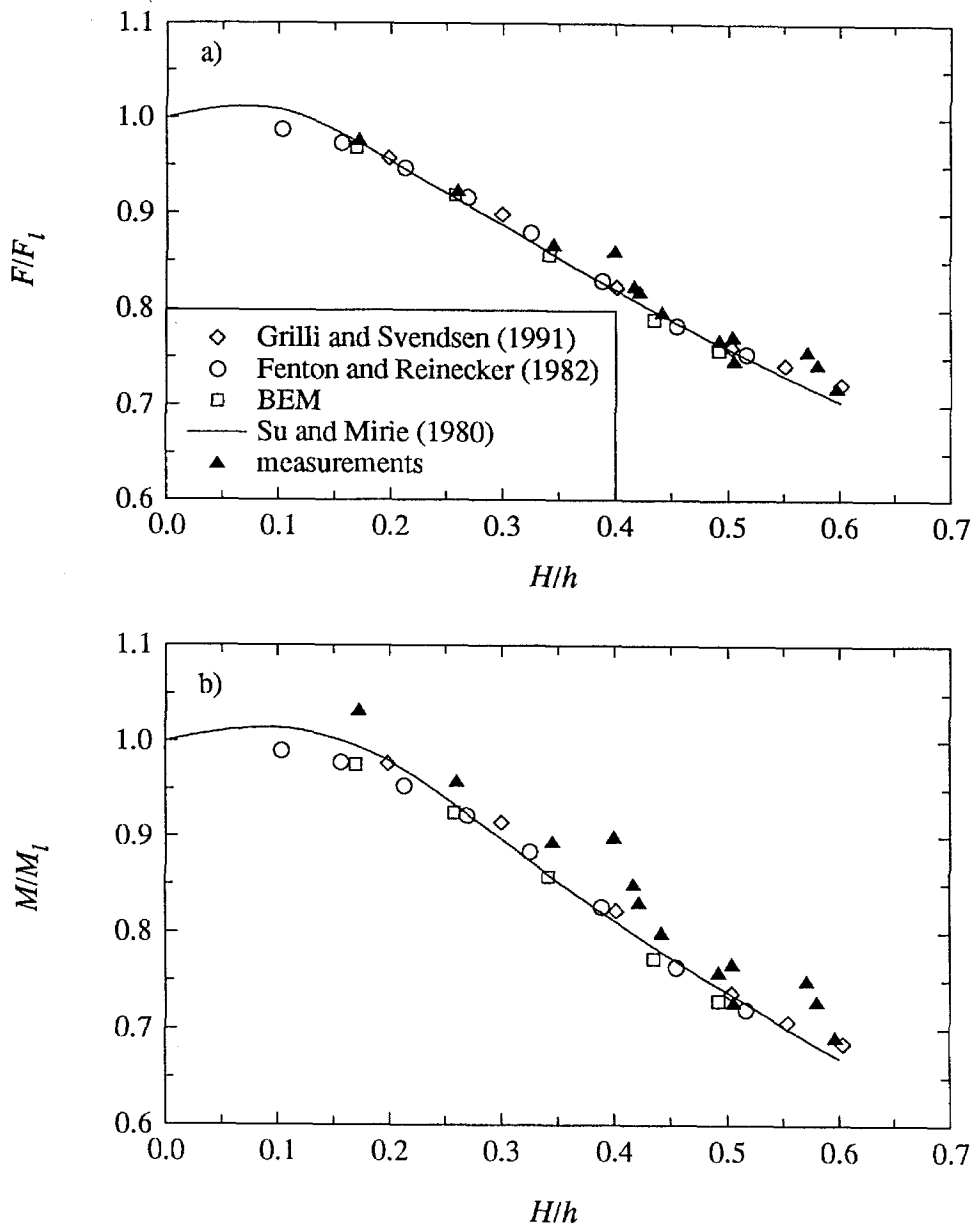


Figure 5.2.9 Comparison of the maximum experimental and theoretical (a) forces and (b) moments on a vertical wall due to the reflection of solitary waves.

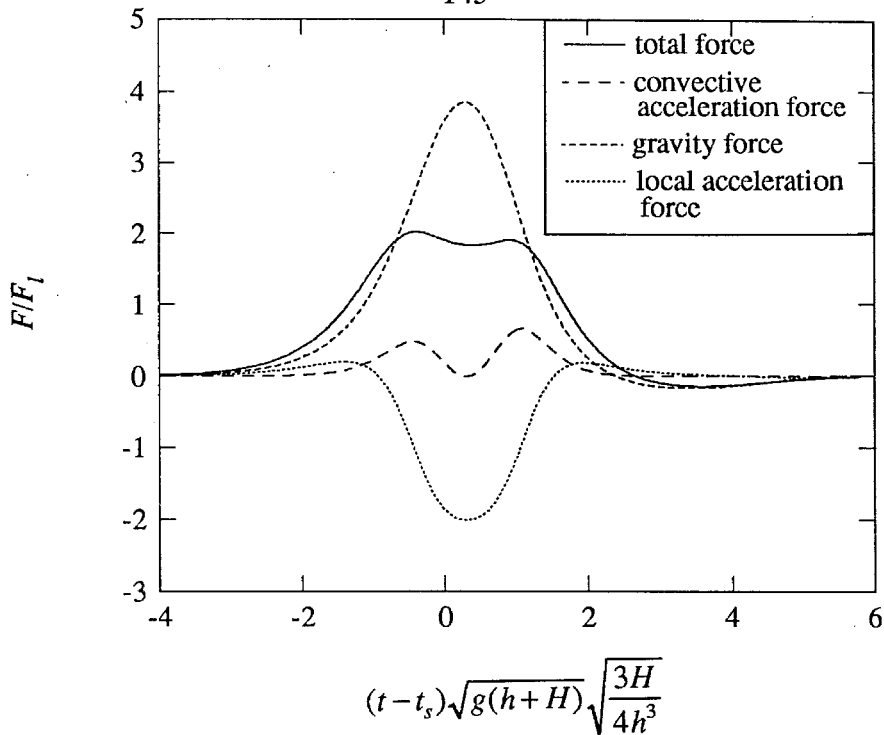


Figure 5.2.10 The forces on a vertical wall calculated using the BEM for a solitary wave with $H/h = 0.504$.

corner conditions are handled. For $H/h > 0.5$, it appears the model of Grilli and Svendsen (1991) and the data, are slightly greater than the force prediction of Su and Mirie (1980). This is not surprising, since large waves will cause contributions at higher orders of H/h , in which case a model based on the full Euler equations would be more accurate. However, the third-order theory of Su and Mirie (1980) agrees remarkably well with the numerical results and the measurements over the complete range of experimental conditions.

Figure 5.2.10 shows the contribution to the total force on the wall due to the forces resulting from the local acceleration, the convective acceleration, and the gravitational acceleration in the vertical equation of motion along the wall. The curves shown in Figure 5.2.10 were obtained with the BEM solution for a solitary wave with a relative incident wave height of 0.504, corresponding to the results shown in Figures

5.2.7 and 5.2.8. Although the convective terms play a role in the double humped structure of the force-time history, the two dominate terms are the body force and the local acceleration along the wall. The local acceleration force at the time of maximum runup is nearly half the value of the gravity force. These large local vertical accelerations along the wall are the primary reason the maximum force is much smaller than the hydrostatic force calculated from the maximum runup height on the wall. Ramsden and Raichlen (1990) calculated the magnitude of the temporal acceleration at the water surface during the maximum runup, due to the impact of bores and showed it can be nearly as large as the acceleration due to gravity.

5.3 Bores

Results from the undular and turbulent bores generated in the horizontal wave tank will be presented in this section. These cases extend from fairly steep undular bores, with relative wave heights of about $H/h \cong 0.55$, to very strong turbulent bores with relative wave heights on the order of 10. The undular bores are characterized by a smooth profile whose front face resembles that of a solitary wave and the presence of oscillatory waves trailing the bore front (or wave of elevation). The strong bores are characterized by a turbulent front with no oscillatory waves. There is a transition region between the strong bores and the undular bores, where the waves have both a turbulent breaking front and oscillatory waves. The experimental results are compared with the theory of Cross (1967) and the finite difference, "SOLA-VOF," model described in Chapter 3. This section is concluded with a comparison of the runup and force time histories caused by two bores with the same relative wave height propagating on a horizontal bottom and a 1/50 slope. Figure 4.2.27 shows a definition sketch of the experimental arrangement.

5.3.1 Amplitude and Celerity Considerations

Figure 5.3.1 shows the variation of the relative celerity at the wall, c / \sqrt{gh} , determined from the results of the celerity probe, with the relative wave height, H/h , for the bores generated in the horizontal tank. The turbulent bore and undular bore results are shown with the open squares and the solid diamonds, respectively. The solitary wave celerity calculated by Longuet-Higgins and Fenton (1974) is shown with the solid line,

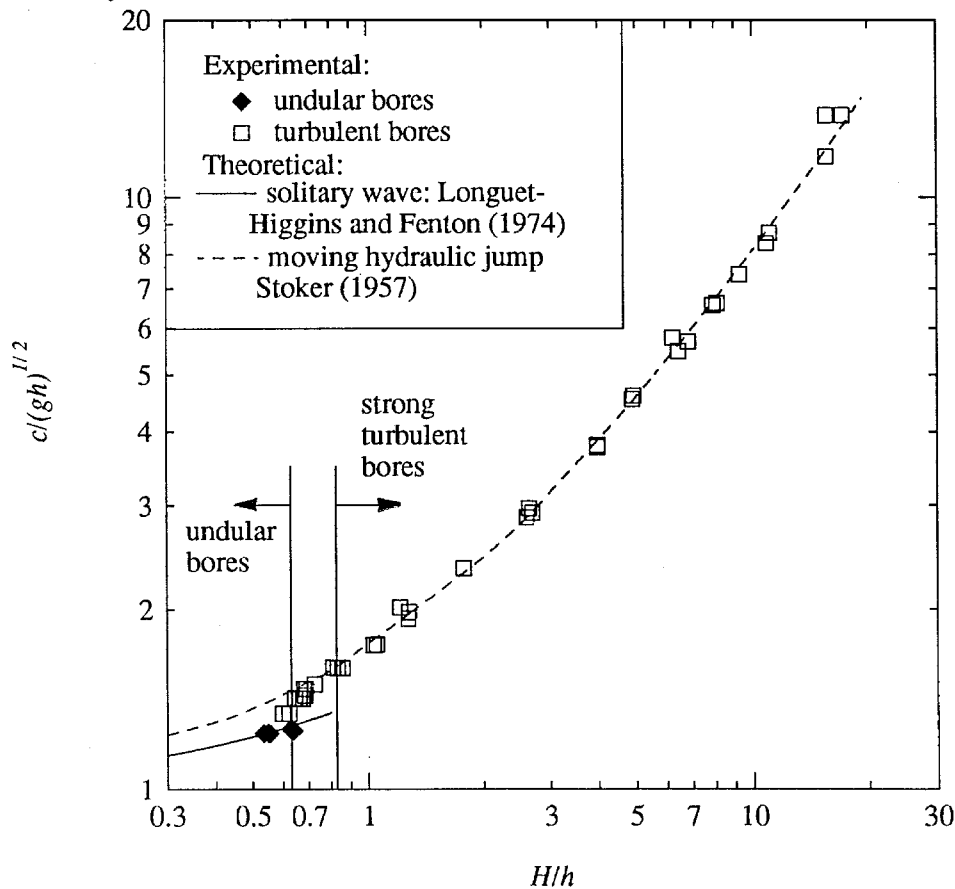


Figure 5.3.1 Experimental and theoretical celerity of the undular and turbulent bores as a function of the relative wave heights.

and the moving hydraulic jump theory (Stoker (1957)) is shown with the dashed line.

Equation 3.33 is the expression for the bore celerity given by Stoker (1957) if u_1 is replaced by c . The undular bore celerities agree with the solitary wave theory when

plotted against the relative wave height. Other investigators (Sandover and Zienkiewicz (1957), and Wilkinson and Banner (1977)) have shown that the celerity of undular bores agrees with the moving hydraulic jump theory if the mean level behind the front of the waves is used to compute the celerity. For relative wave heights greater than $H/h=0.83$, the experimental results agree well with the moving hydraulic jump theory. For relative wave heights less than 0.83, where oscillatory waves exist behind the front of the bore, the experimental results lie below the moving hydraulic jump theory because the theory is based on the mean water level behind the wave front, whereas the maximum wave height was used to plot the experimental values. Thus, for $H/h < 0.83$, where the maximum wave height is larger than the mean water level behind the bore, the theory is not expected to follow the experimental results. For relative wave heights greater than 0.83, there are no oscillatory waves behind the bore. Thus, the maximum measured wave height, used to plot the experimental results, is equal to the mean water level behind the bore on which the theory is based. When there cease to be any oscillatory waves behind the bore, the mean wave height behind the bore coincides with the maximum wave height. Thus, there is excellent agreement between the theory and the experimental results for $H/h > 0.83$, which has been shown by previous investigators including Bakhmeteff and Matzke (1936).

Figure 5.3.2 is a photo obtained from a television monitor which shows the still water level and the profile of a turbulent bore with a relative wave height of $H/h = 0.81$, which is propagating in a still water depth, $h = 10.26$ cm. The details of the wave are well defined, including the rapid variations in the water surface profile at the front of the turbulent region in the center of the photo. For this case, there is a region in front of the turbulent portion of the bore where the water surface is smooth but elevated, relative to the still water level, due to the advancing bore. Profiles similar to that shown in Figure

5.3.2 were used to obtain the wave heights and maximum water surface slopes reported in this study for the horizontal wave tank experiments with bores and dry bed surges.



Figure 5.3.2 Photo taken from the video image of a turbulent bore with a relative wave height of $H/h = 0.81$ and an ambient depth, h , of 10.26 cm (run no. HB66).

For the bore experiments, the maximum wave slope, $\|d\eta/dx\|$, and wave height, H , were determined from a composite wave profile which is described below. The video camera records an image every 1/30 th of a second, thus, several bore profiles are recorded before the water level at the instrumented wall begins to change. In the discussion that follows, the shape of the incident wave profile is assumed to change slowly in the region near the instrumented wall. This should be a reasonable approximation, since the celerity of the wave, which is a function of the wave height, was essentially constant in front of the wall. Figures 5.3.3(a) through (c) show several wave profiles obtained before the water level at the instrumented wall began rising for a bore with $H/h = 6.23$ advancing on a still water depth of $h = 1.43$ cm. In Figure 5.3.3,

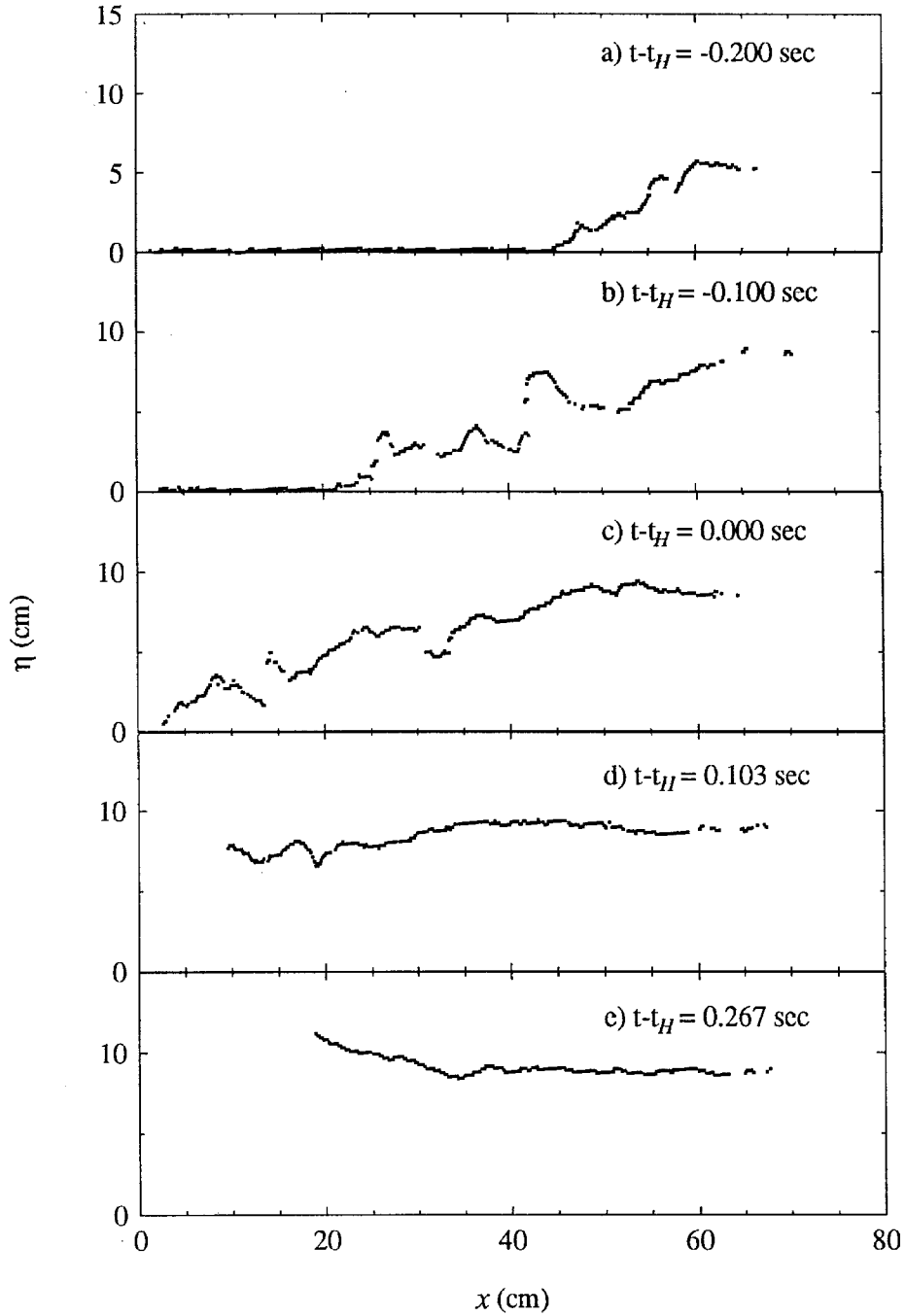


Figure 5.3.3 Experimental profiles of a bore ($H/h = 6.23$, $h = 1.43$ cm) at several times before and during reflection on the vertical wall (run no. HB64).

the ordinate is the water surface elevation, η , above the still water line, and the abscissa is the distance from the vertical wall. Figures 5.3.3(a) through (e) show the time scale, $t - t_H$, where t was set to zero when the gate began opening and t_H is the time at which the last profile was obtained before the water level at the wall began to rise due to the approaching bore. The wave profiles shown in Figures 5.3.3(a) and (b) were then superimposed on the profile shown in Figure 5.3.3(c) by shifting them in the x direction, a distance $\Delta x'$ which is determined by $\Delta x = c(t - t_H)$, where c is the experimentally determined bore celerity. The wave profiles shown in Figures 5.3.3(d) and (e) were obtained during the reflection from the wall. When the highly turbulent tongue of the bore runs up the wall, the profile near the runup tongue cannot be seen with the experimental arrangement used to measure the LIF profiles. Thus, the wave profiles shown in Figures 5.3.3(d) and (e) contain no data near the wall. However, a separate video camera is used to record the runup history on the wall as described in Section 4.2.5. The profiles shown in Figures 5.3.3(d) and (e) were shifted relative to the profile shown in Figure 5.3.3(c) and superimposed on it in the same way as the profiles shown in Figures 5.3.3(a) and (b). However, part of these subsequent wave profiles are affected by the reflection from the wall which can be seen for $x < 40$ cm in Figure 5.3.3(e). When superimposed on the wave profiles obtained before impact, the portion of the subsequent wave profile affected by the reflection could be identified easily and was omitted. In this way, fourteen of the available wave profile measurements from this individual experiment were combined to produce the composite profile shown in Figure 5.3.4(a). For this case, as well as for all the strong turbulent bores, the wave height was determined by averaging the composite wave profile results for $x > 80$ cm. This wave height, H , is shown in Figure 5.3.4(a) as well as the maximum wave slope, $\|d\eta/dx\|$, where the ordinate is the water surface profile above the still water level and the abscissa is the distance from the vertical wall.

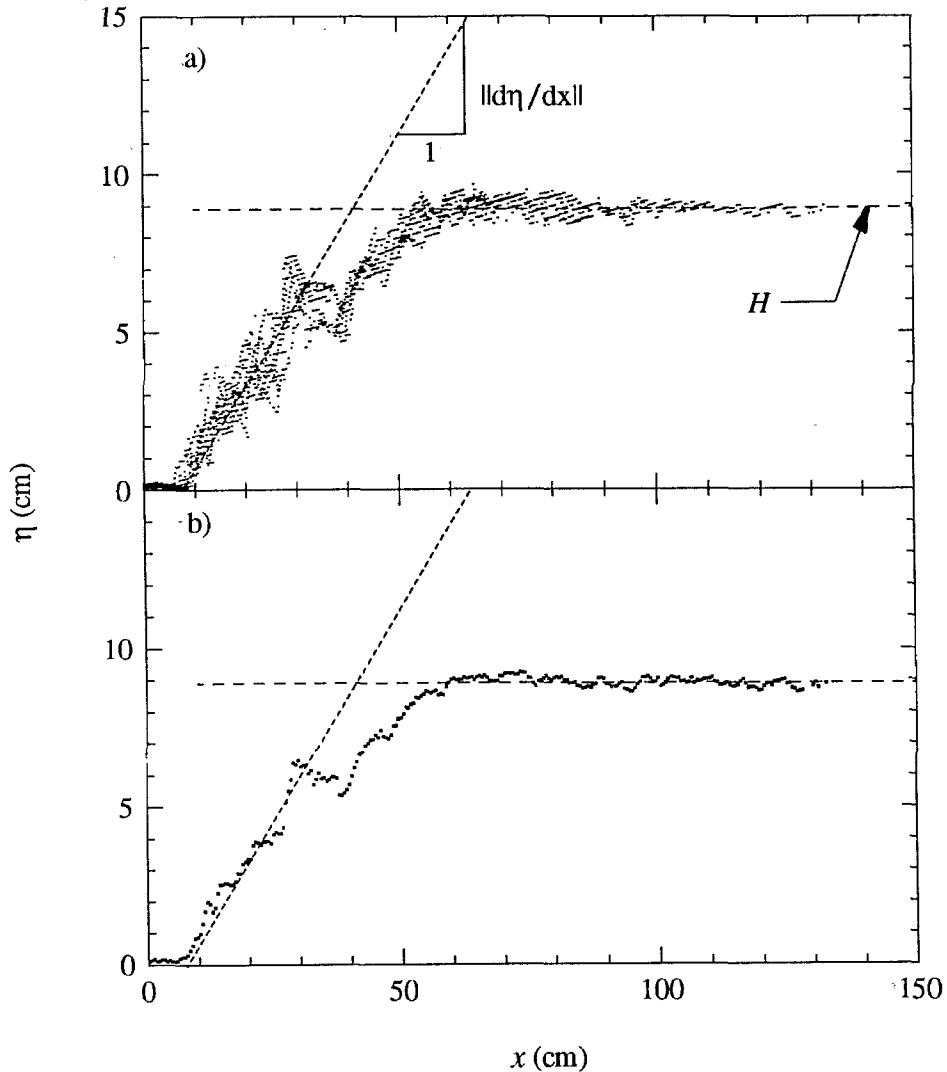


Figure 5.3.4 (a) Composite wave profile which includes the profiles shown in Figure 5.3.3; (b) the averaged profile.

The data from the composite wave profile in Figure 5.3.4(a) were averaged at each 0.5 cm horizontal station and the result is shown in Figure 5.3.4(b). This average profile was used to calculate the maximum water surface slope by computing a linear least squares fit to the profile over a window, which was placed at each 0.5 cm station along the wave profile. The window lengths used to calculate the wave slope are presented in Appendix A, and range from 3 cm for the steepest waves to 15 cm for the strong turbulent bores. Since the window length will affect the maximum slope

computed from the measured profiles, some limited experimentation was necessary to determine appropriate window lengths used in the slope calculation. This was accomplished by varying the window length and visually comparing the resulting maximum slope to the composite wave profile (as shown in Figure 5.3.4(a)). From these observations, the window lengths used in Appendix A were chosen. Although observation by eye was used and human judgment was involved, the four window lengths chosen were subsequently applied over specific ranges of the relative wave height. Therefore, each wave profile was assigned a window length based on its relative wave height. The "dip" in the mean wave profile of Figure 5.3.4(b) between $30 \text{ cm} < x < 40 \text{ cm}$ may be real, or may indicate that many more profiles may be needed to obtain an accurate estimate of the mean profile. However, two additional runs, with generation conditions identical to those used to produce the bore shown in Figure 5.3.4(b), exhibited no local features like the "dip" seen in Figure 5.3.4(b). This indicates the "dip" in the averaged record may be due to some local feature on the bore profile which was convected toward the wall along with the bore. Thus, it appears many repeated experiments would be required to obtain a statistically significant wave profile.

Several wave profiles are shown in Figure 5.3.5(a) through (e) where the ordinate is the wave profile, η , and the abscissa is the horizontal distance, $x - x_H$, which have been normalized by the wave height, H . In Figure 5.3.4, x_H is the distance between the location on the wave profile where $\eta = H/2$ and the vertical wall at the time, t_H . Thus, the composite profiles are lined up with $\eta = H/2$, located at $(x - x_H)/H = 0$. Both axes in Figure 5.3.4 were normalized by a common parameter to illustrate the change in wave slope as a function of the relative wave height. Figures 5.3.5(a) and (b) show the profile from two undular bores, where the wave slope is increasing with the relative wave height. This is analogous to the behavior found with the solitary waves in Section 5.2. Figure 5.3.5(c) shows a bore in the transition zone where the steepest waves were

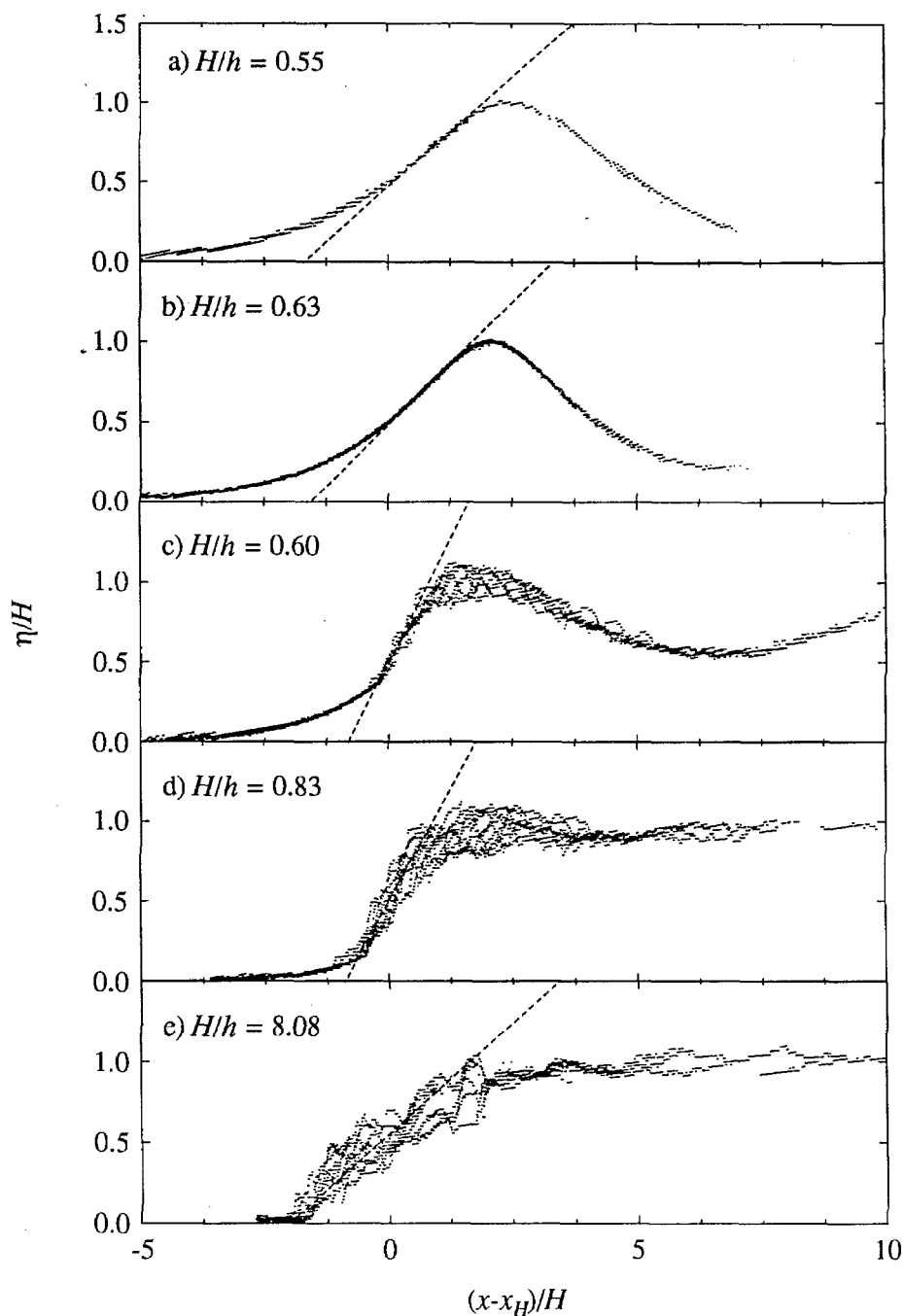


Figure 5.3.5 Several composite wave profiles showing the variation of the maximum wave slope as a function of the relative wave height (run no.'s HB68, HB84, HB83, HB79, and HB72).

obtained. The steepest waves obtained in this study were the smallest breaking bores, which in some cases, had relative wave heights slightly smaller ($H/h=0.60$) than the highest undular bores obtained ($H/h=0.64$). Figure 5.3.5(d) shows the wave profile from a turbulent bore at the limit between the transition zone, and the strong undular bores at $H/h=0.83$. Notice the lack of a well defined depression behind the wave front when compared with Figure 5.3.5(c). As the bore strength increases, there is a gradual transition from the wave profile shown in Figure 5.3.5(d) to the profile for a very strong turbulent bore shown in Figure 5.3.5(e). Of particular interest in Figure 5.3.5, is the fact that the maximum wave slopes occur for the turbulent bores with the smallest relative wave height. As the relative wave height of the turbulent bores increase, the turbulence extends farther down the front of the wave until at very large bore strengths (Figure 5.3.5(e)), there is no smooth region of wave elevation in front of the turbulent portion of the bore (Figures 5.3.5(c) and (d)). The LIF method allowed accurate measurements of the turbulent wave profiles as seen in Figures 5.3.4(c) through (e). However, as discussed in the preceding paragraph, many repeated experiments would be required to obtain a statistically significant estimate of the mean wave profile and its variability with respect to x .

5.3.2 Pressure and Force Considerations

The force time histories corresponding to the bores shown in Figure 5.3.5 are shown in Figure 5.3.6, where time has been referenced to $t_{H/2}$, and normalized by the time scale, l/c , where l is the horizontal length scale and c is the celerity of the bore. The time, $t_{H/2}$, is when the front of the wave corresponding to $\eta = H/2$, would have reached the wall if the wall were not there. The force has been normalized by F_l which is the hydrostatic force due to a runup on the wall, equal to twice the wave height, as defined in Equation 5.1.2. A dashed line has been placed at unity on the ordinate which indicates a force equal to the linear interaction force, F_l . Figure 5.3.6(a) shows a smooth force

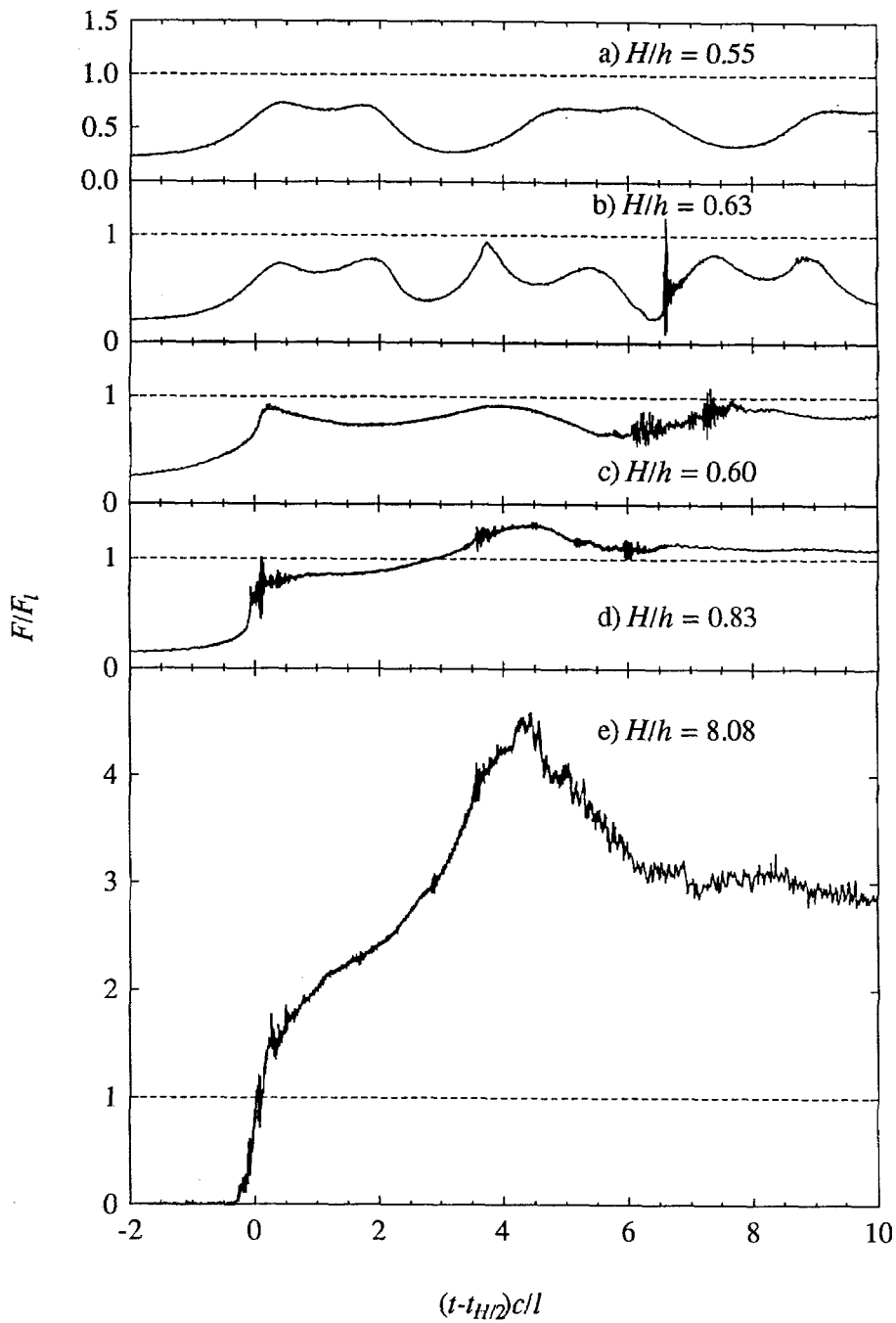


Figure 5.3.6 Experimental force time histories measured during the impact of the bores shown in Figure 5.3.5.

history similar to those shown for solitary waves with a relative wave height, $H/h > 0.5$. The initial wave crest is followed by each succeeding wave crest, where the maximum force due to subsequent peaks continues to decrease. The maximum force is also substantially less than the linear force, F_l , due to the large local vertical accelerations along the wall. This was shown to account for the same effect during the impact of steep solitary waves in Section 5.2 (Figure 5.2.10). Indeed, the shape of each maximum region is similar to that for a solitary wave.

The force history due to the impact of one of the steepest undular bores obtained in this study, is shown in Figure 5.3.6(b), which corresponds to the bore shown in Figure 5.3.5(b). Again, the force on the wall is substantially less than the linear force during the reflection of the first wave crest. However, the reflection of the first wave from the wall caused the second wave to crest and break on the wall resulting in the sharp peak in the force record, observed at: $(t - t_{H/2})c/l = 3.7$. This reflection and subsequent breaking also occurred during the impact of the third wave crest, which produced the oscillation in the force history seen at $(t - t_{H/2})c/l = 6.6$. The peak of this oscillation exceeds the rest of the force signal and reveals only the dynamic response of this particular structure to the hydrodynamic loading. Another structure will in general, have a different response to the same impulsive loading. The frequency of the oscillations in the force signal shown in Figure 5.3.6(b) are approximately 750 Hz. This is approximately equal to the estimated frequency of the first mode of the wall (i.e., all four force cells in phase with the wall undergoing heave in the x -direction) computed in Section 4.2.2. The wall is a dynamic system which will attenuate hydrodynamic loads of very short duration, relative to the natural periods associated with its modes of oscillation. Therefore, the measured force during wave impact in Figure 5.3.6(b) at $(t - t_{H/2})c/l = 6.6$, may not reflect the maximum hydrodynamic load imposed on the wall.

The time scale used to non-dimensionalize the abscissa of Figure 5.3.6 seems to line up the two peaks associated with the first wave crests shown in Figures 5.3.6(a) and (b). The subsequent wave crests in Figure 5.3.6(b) arrive at a much greater value of the abscissa than those in Figure 5.3.6(a). Thus, the time scale for subsequent wave peaks behind the lead wave of undular bores would probably be more reasonably estimated using the physical properties of the trailing waves themselves. Across the transition from undular bores to turbulent bores, the maximum wave slope increases dramatically as shown in Figures 5.3.5(b) and (c), while there is basically no change in the relative wave height which can be seen in Figure 5.3.1. This produces a much smaller time scale for the turbulent bores at the transition relative to the steepest undular bores. This change in time scale can be seen clearly when comparing the force profiles in Figures 5.3.6(a) and (b) to those in Figures 5.3.6(c) through (e). In Figures 5.3.6(a) and (b), the second local maximum in the force record due to the reflection of the first wave crest occurs at a relative time of about 1.9. This second local maximum coincides with the rundown and formation of the reflected wave. In Figures 5.3.6(c) through (e), the maximum in the force record corresponding to the rundown wave occurs at a relative time ranging from 3.9 to approximately 4.35 for relative wave heights of 0.6 and 8.08, respectively.

The second wave crest broke on the wall during the reflection of the turbulent bore with a relative wave height of $H/h = 0.60$, as seen in Figure 5.3.6(c) at $(t - t_{H/2})c/l = 6.1$. However, the amplitude of the oscillation is significantly less than that due to the undular bore shown in Figure 5.3.6(b). The local force maxima coinciding with the rise and fall of the runup tongue (corresponding to the first crest) in Figure 5.3.6(c) are within 10% of the value predicted by the linear force scale, F_l . This does not imply the interaction with the wall is nearly linear. Indeed, the maximum runup for this case is well over two times the linear value of twice the incident wave height. For

solitary waves, it was shown that the maximum force normalized by the linear force decreased as the wave height increased. Furthermore, it was shown that the reason for this was the existence of large vertical local accelerations along the wall near the time of the maximum runup. As the relative wave height increases beyond 0.6, the horizontal momentum flux associated with the incident bores continues to increase and causes maximum forces far in excess of the linear force as shown in Figure 5.3.6(e). However, the relatively large negative local vertical accelerations similar to those in steep solitary waves (Figure 5.2.10) are still present and contribute to the shape of the force history seen in Figure 5.3.6(c), which was discussed in detail in Section 5.1.

In Figure 5.3.7, the wave profile and the runup, pressure, and force-time histories on the wall are shown for a bore with a relative height of $H/h = 7.9$, where $h = 1.1$ cm. This bore produced the largest pressure measured during this study. Figure 5.3.7(a) shows the wave profile where the ordinate is the water surface elevation above the still water surface, which has been normalized by the wave height, and the abscissa is the distance from the wall normalized by the horizontal length scale, l , which for this case was 37.8 cm. In Figure 5.3.7(b), both the pressure head and the runup height are *normalized by twice the incident wave height and plotted as a function of time which has been normalized by the bore celerity (215.3 cm/sec) and the horizontal length scale.* Note that the elevation of the pressure cell above the still water surface, $z_p = 1.79$ cm, has been added to the measured pressure head. If a hydrostatic condition exists along the wall, the runup height will equal the sum of the measured pressure head and the pressure cell distance above the still water level. Figure 5.3.7(b) shows a very large short-duration pressure which occurs very soon after impact. This impact pressure is followed by a nearly constant value for the remainder of the reflection process. This maximum pressure head was 200 cm, which is equal to $23 H$ or $8.4 (c^2/2g)$ (see Appendix A).

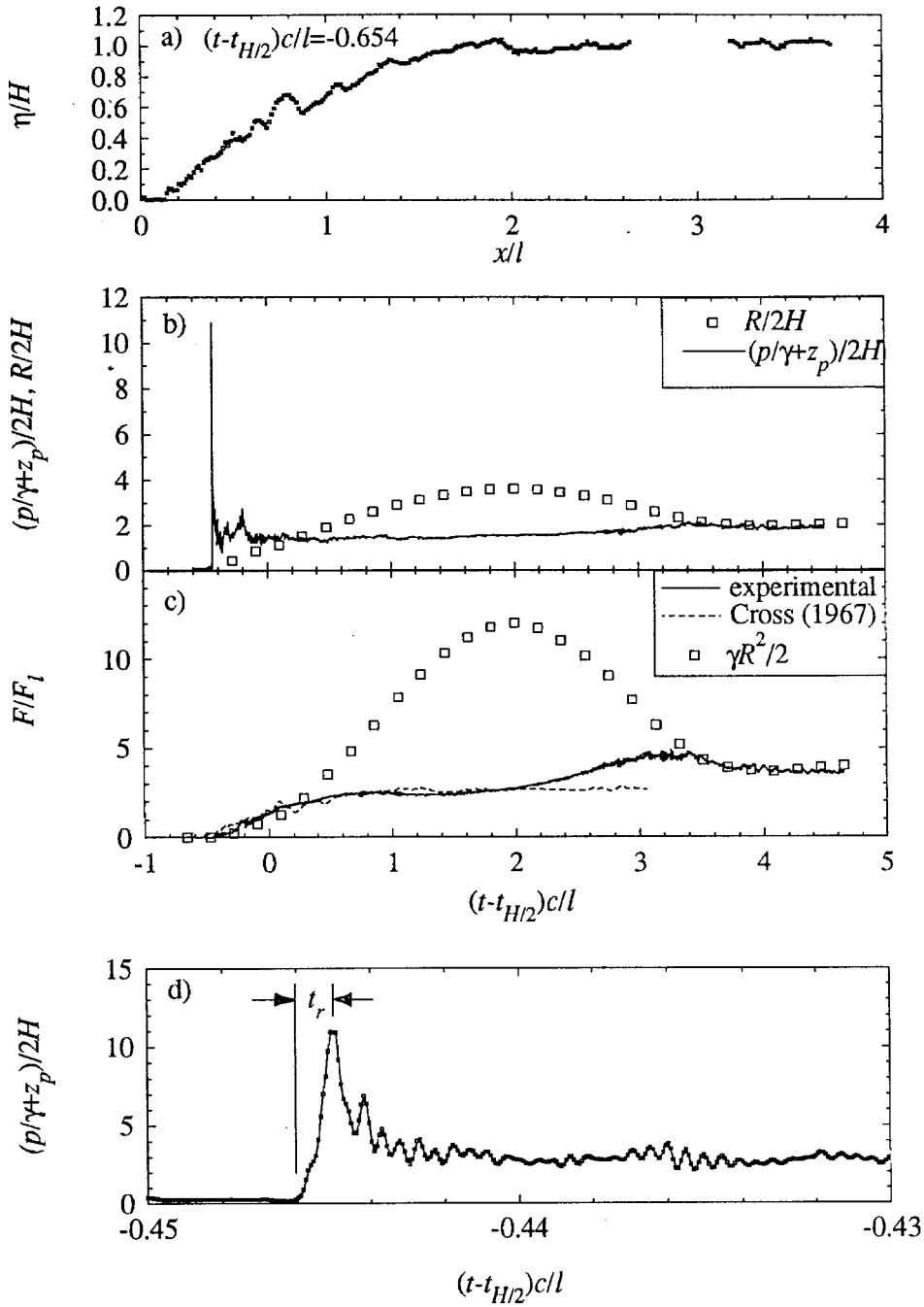


Figure 5.3.7 (a) Incident bore profile where $H/h = 7.9$ and $h = 1.1$ cm; (b) the pressure and runup time histories; (c) experimental and theoretical force time histories; (d) the pressure on an expanded time scale (run no. HB91).

This relative pressure is 55% greater than the largest relative pressure recorded by Fukui et al. (1963). The measured pressure head is significantly less than the measured maximum runup at a relative time of two, but becomes hydrostatic, as evident from the agreement with the runup height, for relative times greater than 3.5.

It is quite interesting that the measured force shown in Figure 5.3.7(c) shows essentially no response at all to the sharp pressure pulse at a relative time of -0.445 in Figure 5.3.7(b). This is due to the short duration of the pressure peak relative to the natural period of the wall as discussed below. It should be noted that this is the first study of bore impact on a wall where the force and pressure on the wall were measured simultaneously with the time history of the runup on the wall. The theory of Cross (1967) is compared with the measured force and agrees quite well for relative times less than two and under-predicts the maximum measured force by 48%. The hydrostatic force computed from the measured runup height on the wall indicates the measured force becomes hydrostatic for relative times greater than 3.5 in Figure 5.3.7(c), which agrees with the time a hydrostatic condition occurs in Figure 5.3.7(b).

Figure 5.3.7(d) shows the pressure time history which was presented in Figure 5.3.7(b), with the time scale expanded near the time of the impulsive pressure load. The rise time, denoted as t_r , is 0.001 relative time units, or 150 μ s. This rise time, t_r , is approximately 11% of the natural period of the wall corresponding to the fundamental mode discussed in Section 4.2.2. Thus, the wall most likely did not respond to the short duration high pressure pulse due to its inertia. The pressure pulse may not have simultaneously exposed a large region of the wall to a simultaneous pressure peak. This would also help to explain the lack of wall response to the pressure peak.

5.3.3 Comparison Between Theoretical and Experimental Results

The SOLA-VOF model is compared to experimental measurements of the incident wave profile and the force time history on the wall in Figures 5.3.8 and 5.3.9. For these numerical experiments, a 96 cm long tank was used which had a vertical dimension of 70 cm. The automatic time stepping option in SOLA-VOF was used, and the kinematic fluid viscosity was set to $0.01 \text{ cm}^2/\text{sec}$. For the case shown in Figure 5.3.8, 105 nodes and 70 nodes were used in the x and y directions, respectively. The automatic

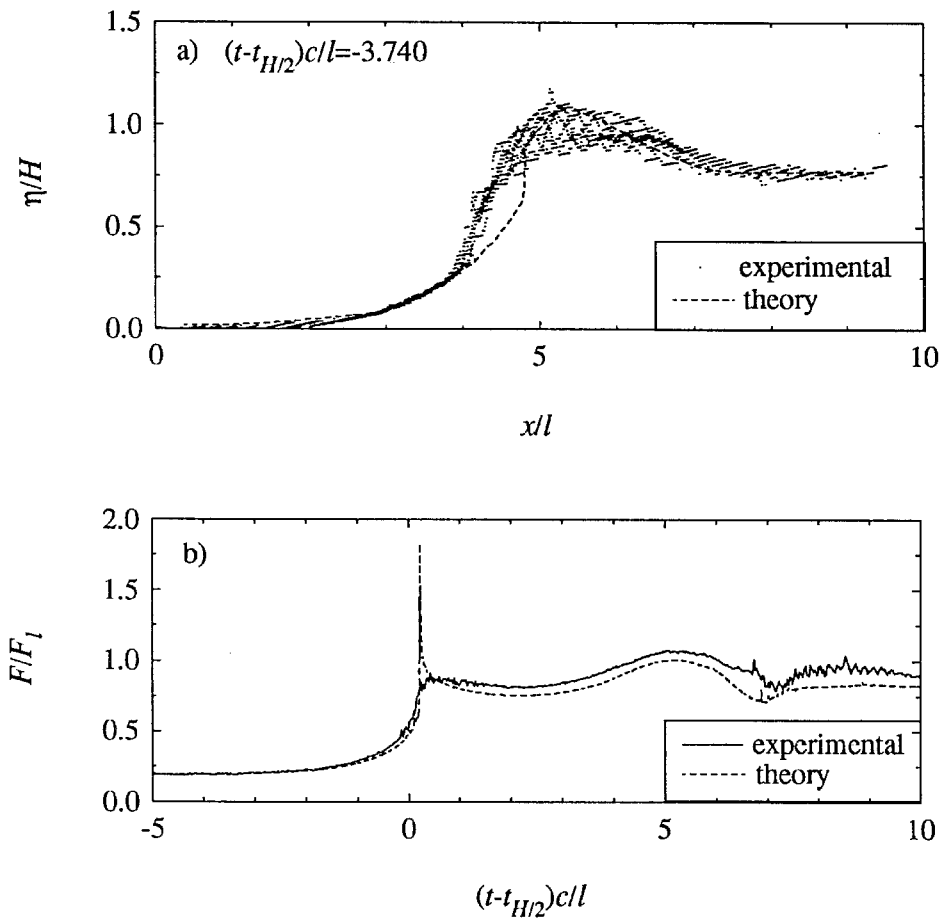


Figure 5.3.8 Comparison of experimental and theoretical (a) bore profiles and (b) force time histories for a bore with $H/h = 0.64$ and $h = 11.94 \text{ cm}$ (run no. HB67).

grid stretching option in the SOLA-VOF model was used to give a 0.5 cm spacing at the vertical wall in the x direction, which increased to 1.0 cm at a location 24 cm from the

wall. The remainder of the computational domain in the x direction had 1 cm spacing. In the y direction, the SOLA-VOF grid stretching option was used to cause a grid spacing of 0.5 cm at a distance of 19 cm above the bottom of the tank, near the crest of the wave. The grid spacing in the y direction increased to 1.5 cm at a location 70 cm above the bottom of the tank, to a dimension of 1.0 cm at the bottom of the tank. In Figure 5.3.8(a), the ordinate is the relative water surface profile, measured from the still water level ($h = 11.94$ cm), which has been normalized by the wave height, H (7.7 cm). The relative wave height, H/h , of the experimental bore shown in Figure 5.3.8, was 0.64. The abscissa in Figure 5.3.8(a) is the relative distance from the wall, normalized by the horizontal length scale, l (10.7 cm). The agreement between the measured and theoretical profiles are reasonable except near the front face of the bore, where the SOLA-VOF model over-predicts the steepness of the wave slope between $0.65 < \eta/H < 0.8$. The region in which the theory does not follow the experimental profile is where wave breaking is causing a spilling front on the experimental bore. Nichols et al. (1980) discuss the tendency of the Volume of Fluid (VOF) algorithm to cause free surfaces to steepen in the direction in which they are being convected. This may explain part of the disagreement between the theoretical and the experimental profiles. The theory most certainly cannot fully resolve the turbulence in the spilling breaker of the experimental bore, which may also contribute to the disagreement. One additional factor may be the relatively coarse grid spacing used, relative to the wave height. The numerical experiments shown in Figures 5.3.8 and 5.3.9 took several thousand time steps and 10 hours of computing time on a Sun IPC sparc station.

Figure 5.3.8(b) shows the measured and theoretical total forces normalized by the linear force per unit width (i.e. $1/2 \gamma(2H + h)^2$, which in this case is 366 N/m). The sharp peak in the theoretical force record, at $(t - t_{H/2})c/l = 0.2$, corresponds to the impact of the

very steep section of the theoretical profile at $x/l = 4.8$, in Figure 5.3.8(a). The maximum theoretical force is 112% larger than the measured force obtained at the same time. This dramatic over-prediction of the theoretical force may be due to several causes including: the theory produced an excessively steep wave front which contributed to the maximum theoretical force shown, the theory does not account for air-entrainment which may act to cushion the impact of broken waves on the wall, and the frequency response of the experimental wall will attenuate hydrodynamic forces of very short duration. For times greater than the time at which the maximum theoretical force occurred, the agreement between the theoretical and the experimental force time histories in Figure 5.3.8(b) is quite reasonable. The theory under-predicted the maximum measured force by only 6% at a relative time of five. This indicates the ability of the model to simulate wave propagation beyond the breaking process.

Figures 5.3.9(a) and (b) show a similar comparison to those shown in Figures 5.3.8(a) and (b) for an incident bore with a relative wave height, H/h , of 0.81 propagating on a still water depth, h , of 10.26 cm. In this case, 1 cm grid spacing over the entire 96 cm long by 70 cm high computational domain was used. The theory drastically over-predicts the steepness of the measured water surface profile as seen in Figure 5.3.9(a). Again, this steep front contributes to a sharp peak in the force record, which is not present in the measured force in Figure 5.3.9(b). The overall force records agree quite well except for the sharp peak in the force record at -0.1 relative time units. The SOLA-VOF model predicted the maximum measured force within 6% at a relative time of 3.1.

Although the SOLA-VOF model tended to over-predict the steepness of the measured wave profiles for the numerical experiments shown here, it agreed quite well with the measured force time histories for relative times greater than those corresponding

to the short duration peak in the theoretical record. This indicates the model's ability to compute violent splashing-type fluid motions while not breaking down computationally.

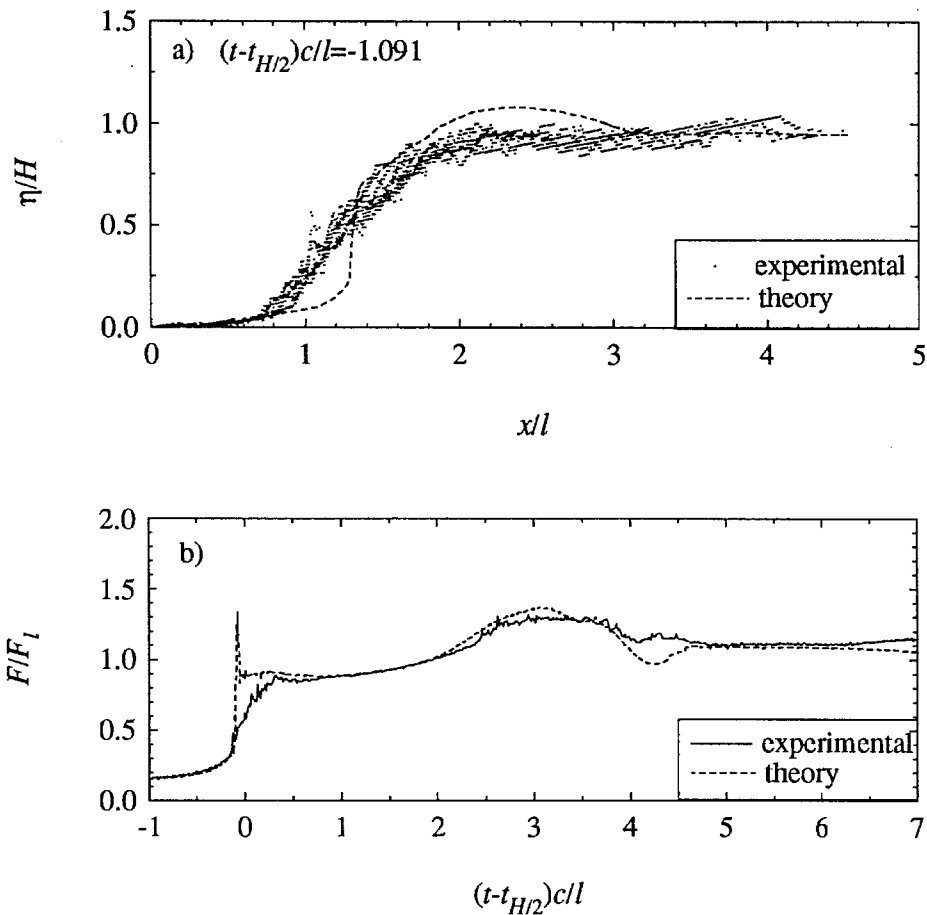


Figure 5.3.9 Comparison of experimental and theoretical (a) bore profiles and (b) force time histories for a bore with $H/h = 0.81$ and $h = 10.26$ cm (run no. HB66).

5.3.4 Comparison Between Bores on Different Slopes

Figure 5.3.10 shows the incident wave profiles and the runup and force-time histories on the wall due to turbulent bores with relative wave heights of 2.65 from both the horizontal and the tilting wave tank experiments. Figure 5.3.10(a) shows the incident wave profiles which agree with each other surprisingly well, considering the completely different means of wave generation used in each case, and the different bottom slopes. Figure 5.3.10(b) shows the runup history on the wall where the maximum runup for both

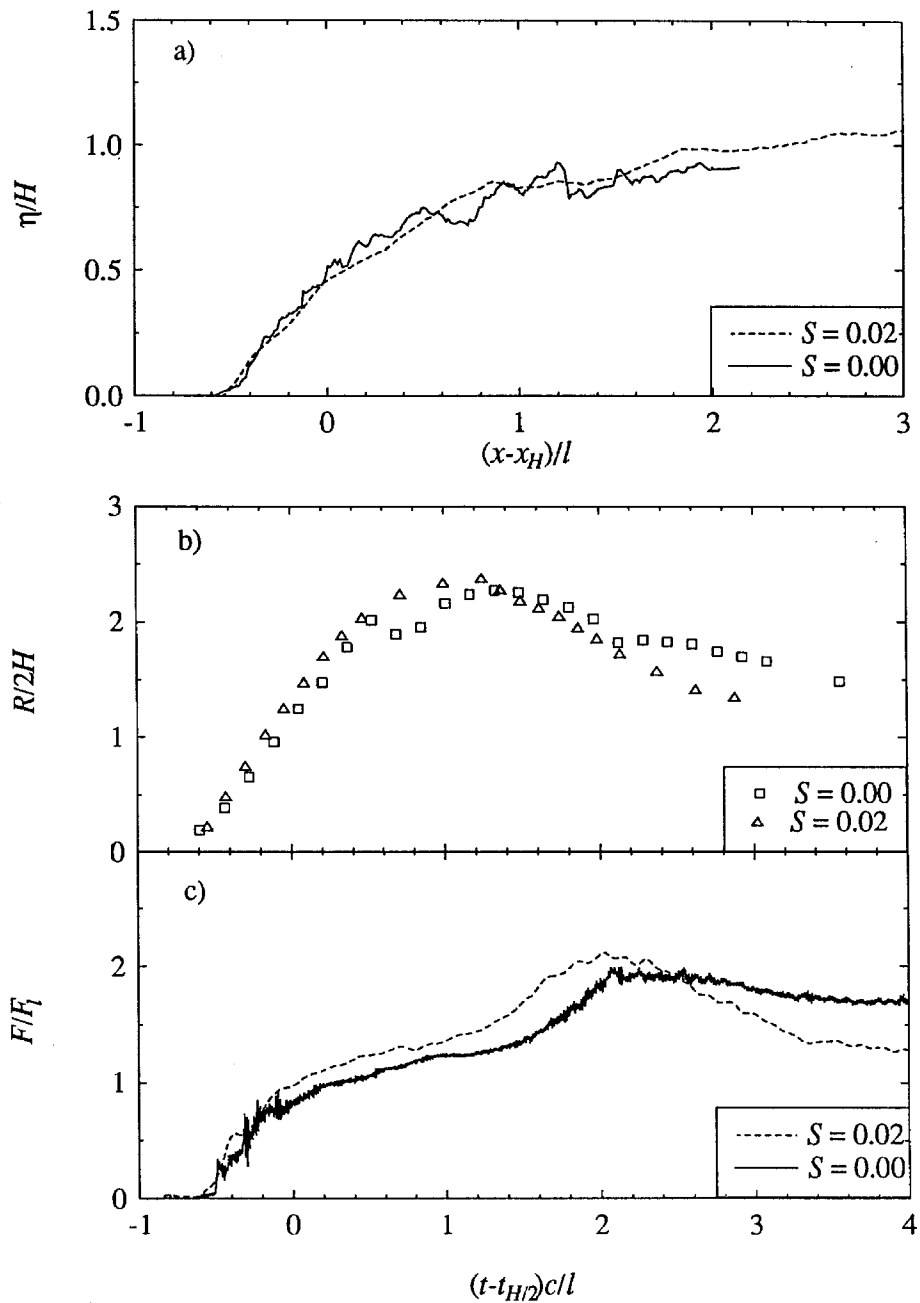


Figure 5.3.10 Comparison between bores with $H/h = 2.65$ in the horizontal tank (run no. HB63) and the tilting tank for (a) the incident bore profiles (run no. TB111); (b) the runup (run no. TB96); and (c) force time histories (run no. TB111).

cases are within about 5% of each other. The slight dip in the runup history from the horizontal wave tank at a relative time of 0.5 is due to the runup tongue separating from the wall. When the leading fluid in the runup tongue separates from the wall, the runup height then becomes identified with the next parcel of fluid located at the air-wall-water interface. Other than the slight discrepancy between the two runup histories near $(t - t_{H/2})c/l = 0.5$, the agreement is good for a relative time less than about 2.1. For relative times greater than 2.1, the runup on the wall in the horizontal wave tank is larger, which then affects the force time history, as well. It should be noted that the bore in the horizontal tank is essentially an infinite bore, whereas the bore on the slope which was created by a solitary wave has a finite volume. Figure 5.3.10(c) shows the maximum force from the tilting wave tank experiment is approximately 7% larger than that due to the bore in the horizontal wave tank experiment. The overall agreement between the two bores is particularly interesting in that it indicates broken waves traveling on mild slopes ($S < 1/50$) can be reasonably modeled by waves traveling on a horizontal slope. However, it should be pointed out that a broken wave may certainly reform into another breaking wave, given an appropriate wave climate and bottom bathymetry. It is not implied that once a wave breaks it will always reach the shoreline as a turbulent bore.

5.4 Surges on a Dry Bed

The results from the experiments with surges traveling over a dry bed are presented in this section. The propagation of the surge along the bed and the measured water surface profile are compared with the theory of Whitham (1955). The measured water surface profiles are also compared with an approach similar to that of Whitham (1955), where the shear stress coefficients, C_f , for a laminar boundary layer and a turbulent boundary layer on a smooth flat plate, from steady flow considerations (Daily and Harleman(1966)), are used to model the shear stress along the bed. The measured runup, pressure, and force time histories are shown. The measured force time histories

are also compared to the theory of Cross (1967). Finally, the water surface profile and the runup, pressure and force histories produced by a strong turbulent bore are compared to results from a dry bed surge where both waves had the same celerity at the wall.

5.4.1 Celerity Considerations

Figure 5.4.1 shows the progression of the surge along the tank between the pneumatic gate and the instrumented wall. The abscissa is the relative time, $t\sqrt{g/h_r}$, referenced to the moment the gate cleared a distance of one millimeter off the tank bottom, and h_r is the reservoir depth. This definition of the time scale was used, since a height of one millimeter was the smallest vertical distance which could be identified relative to the background noise in the displacement sensor record used to define the celerity of the dry bed surge. The ordinates on the left and right side of the figure are the relative distance of the surge, $(x_g - x)/h_r$, from the gate and the relative celerity, $c/\sqrt{gh_r}$, of the surge, where x_g is the location of the upstream edge of the pneumatic gate ($x_g = 15.08$ m and the wall is located at $x = 0.0$ m) as seen in the definition sketch of Figure 5.4.1(d). The open circles show the experimentally determined arrival times of the surge at 2.5 m intervals along the tank, and the solid line is the theory of Whitham (1955). In the model of Whitham, the friction force exerted on a horizontal element of fluid dx long is equal to $\frac{f}{8}\rho u^2 dx$, where the friction factor, f , is analogous to that used in the Moody diagram for head losses in open channel flow (Daily and Harleman (1966)). Note that $\frac{f}{8}$ is equivalent to the friction coefficient, K , used in the model of Whitham. To apply the model of Whitham, the friction coefficient must be specified. The friction factor was adjusted until the root mean square errors between the experimental data and the theory were minimized as shown in Figures 5.4.1(a) through (c). The friction factors which minimized the errors ranged from 0.024 to 0.023 and are shown in Figure 5.4.1 for each

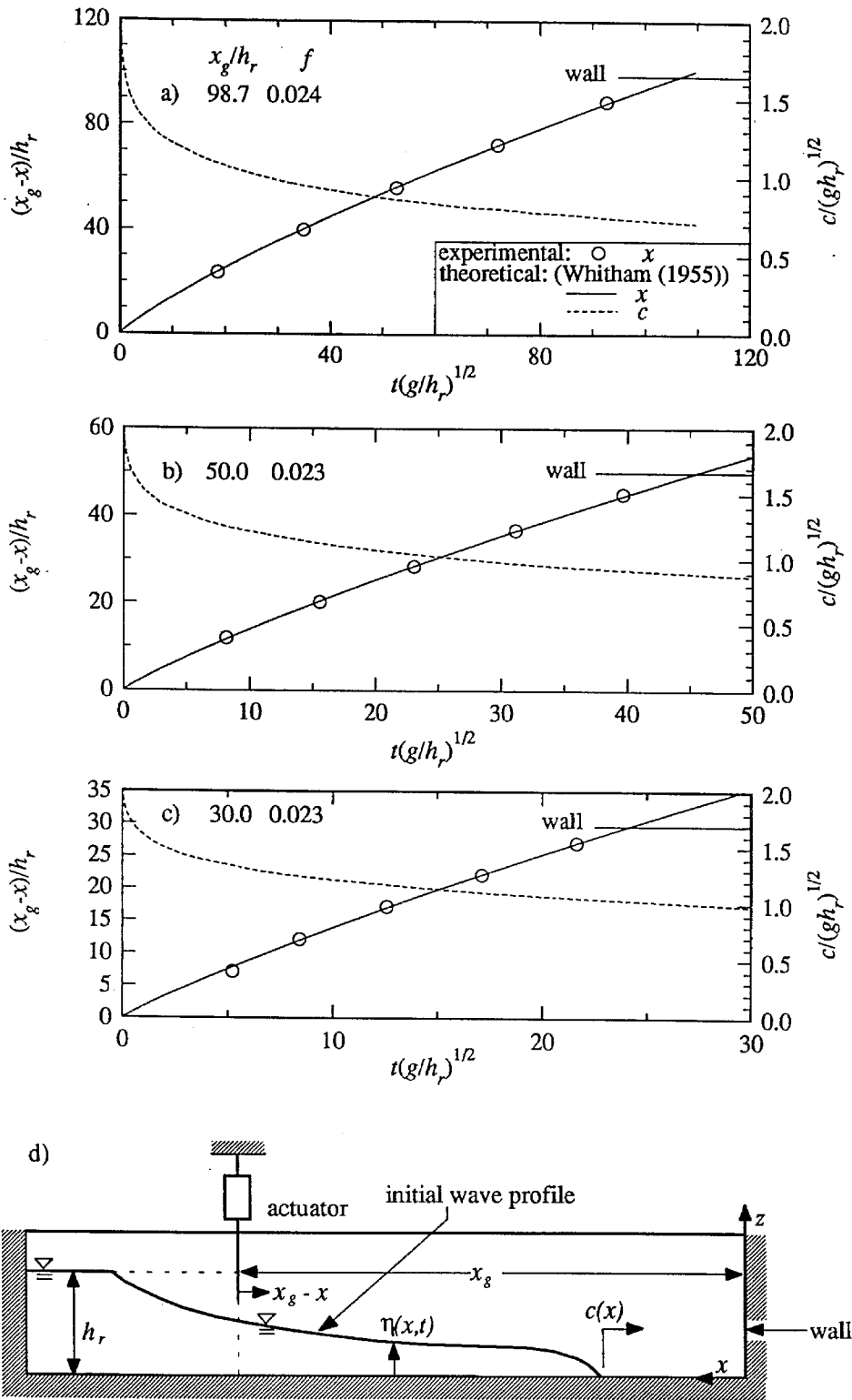


Figure 5.4.1 Comparison between experimental and theoretical propagation of a dry-bed surge for various reservoir depths, h_r ; (a) $h_r = 15.28$ cm; (b) $h_r = 30.17$ cm; (c) $h_r = 50.20$ cm; and (d) definition sketch (run no.'s HS86, HS102, and HS103).

case. The theory was constrained by requiring the surge front to begin from the origin of the $x-t$ diagram. Thus, one data point in the $x-t$ diagram is sufficient to determine the friction factor. The origin of the experimental time scale was set to the instant the dam-break gate had risen one mm off the tank bottom. The surges produced for reservoir depths of 15.28 cm and 30.17 cm are shown in Figures 5.4.1(a) and (b). There is excellent agreement between the theory and the experimental data. In Figure 5.4.1(c), where the reservoir depth was 50.20 cm, all the experimental points agree quite well with the theory, except the first. This may be a result of the finite time (0.185 sec) it takes the gate to clear the free surface for this case, where the reservoir depth was 50.20 cm. The dashed lines in Figure 5.4.1 show the celerity predicted from the model of Whitham. This approach was used to calculate the surge celerity at the instant the surge tip meets the wall. This computed celerity was 88 cm/sec, 155 cm/sec, and 229 cm/sec for the surges in Figures 5.4.1(a), (b), and (c), respectively.

5.4.2 Amplitude Considerations

The equations of shallow-water theory with a quadratic friction term can be written as (Dressler (1952) and Whitham (1955)):

$$\frac{\partial \eta}{\partial t} + \eta \frac{\partial u}{\partial x} + u \frac{\partial \eta}{\partial x} = 0 \quad (5.4.1)$$

and

$$\frac{\partial u}{\partial t} + u \frac{\partial u}{\partial x} + g \frac{\partial \eta}{\partial x} + \frac{(f/8)u^2}{\eta} = 0, \quad (5.4.2)$$

where subscripts denote partial differentiation, η is the water surface elevation above the dry bed, and f is the Darcy-Weisbach friction factor. In shallow-water theory, the vertical variations of the flow quantities are zero and the pressure is hydrostatic over the

depth at any location. Near the tip of the surge, η , becomes small and it has been experimentally shown (Wang and Ansari (1986), among others) that $\partial\eta/\partial x$ becomes large. Whitham reasoned that the shear and pressure gradient terms in the equation of motion must be approximately equal, since they both increase as the tip is approached (note the dependence of these terms in Equation 5.4.2 on η and $\partial\eta/\partial x$), while the local and convective accelerations are expected to remain finite. Assuming that the front of the surge is propagating with a constant shape at a constant celerity, and the horizontal fluid velocity throughout this tip region is equal to the celerity of the surge tip, Equation 5.4.1 is satisfied by any bore shape. With these assumptions Equation 5.4.2 reduces to:

$$g\eta \frac{\partial\eta}{\partial x} = (f/8)c^2 \quad (5.4.3)$$

which is the expression Whitham (1955) reasoned would govern the shape of the tip region very close to the front of the surge. This expression can be integrated with respect to distance, x , from the leading edge to a location behind the tip (i.e., $x=d$ as shown in Figure 5.4.2). This gives:

$$\frac{\eta}{d} = \frac{\sqrt{f}}{2} \left(\frac{c}{\sqrt{gd}} \right). \quad (5.4.4)$$

This expression is equivalent to the model proposed by Cross (1967) where the local acceleration term in his theory, is balanced by the body force on the fluid resulting from a finite bottom slope.

In the work of Fujima and Shuto (1990), they indicated the friction along the bed of a surge on a conveyor belt, was similar to the skin friction losses along a flat plate in a

uniform flow. An expression for the water surface profile can be obtained by equating the shear force along a flat plate to a hydrostatic pressure force some distance behind the tip of the plate. In Figure 5.4.2 the control volume has a constant shape and is propagating with the surge celerity. Since the horizontal water particle velocity is

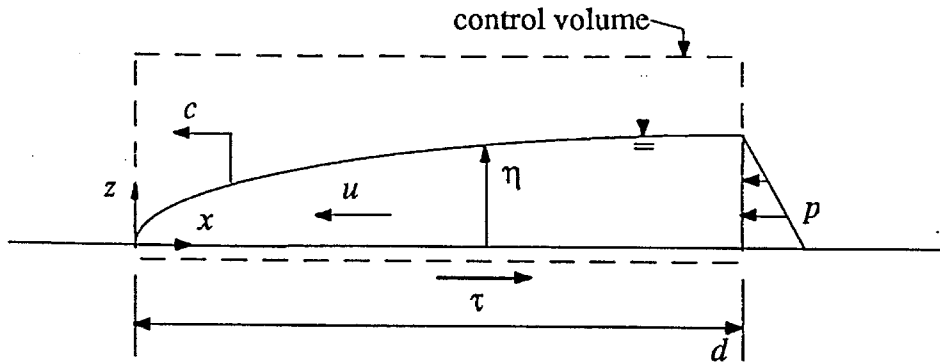


Figure 5.4.2 Definition sketch of the control volume for the tip of the surge.

assumed to be equal to the surge celerity, the momentum flux across the vertical control volume surface at $x=d$, is zero. Therefore, equating the skin-friction force per unit width along the bed to the hydrostatic force per unit width at $x=d$, one obtains:

$$\int_0^d \tau(x) dx = \frac{1}{2} \gamma \eta^2(d), \quad (5.4.5)$$

where τ is the shear stress along the bed and γ is the weight of water per unit volume. The shear stress coefficient, C_f , for the drag force per unit width along one side of a flat plate in a uniform flow can be defined as:

$$\int_0^d \tau(x) dx = C_f \rho \frac{u^2}{2} d, \quad (5.4.6)$$

where ρ is the density of the fluid per unit volume. Combining Equations 5.4.5 and 5.4.6 while substituting the celerity for the water particle velocity yields:

$$\frac{\eta}{d} = \sqrt{C_f} \left(\frac{u}{\sqrt{gd}} \right)^{1/2}. \quad (5.4.7)$$

Daily and Harleman (1966) present several experimental expressions for the behavior of C_f as a function of the Reynolds number of the flow, based on the length, d , behind the leading edge of the plate ($R = Ud/\nu$), where ν is the kinematic viscosity of the fluid. If the Reynolds number is smaller than $5(10)^5$, it is quite likely the boundary layer will be laminar (Schlichting (1979)) unless there is considerable turbulence in the incident flow or separation is triggered at the leading edge. Schlichting (1979) indicates the transition from a laminar to a turbulent boundary layer occurs in the range, $5(10)^5 < R < (10)^6$. The drag coefficient for a laminar boundary layer along a flat plate can be determined theoretically using Blasius' theory (Schlichting (1979)) which gives:

$$C_f = 1.328 / R^{1/2}. \quad (5.4.8)$$

Substituting this into Equation 5.4.7 and assuming the water particle velocity is equal to the surge speed gives the water surface profile explicitly in terms of the distance behind the tip:

$$\frac{\eta}{d} = \sqrt{1.328} \left(\frac{c}{\sqrt{gd}} \right) \left(\frac{cd}{v} \right)^{-1/4} \quad (5.4.9)$$

The shear stress coefficient for a turbulent boundary layer which begins at the leading edge of the plate can be expressed as (Daily and Harleman (1966)):

$$C_f = 0.074 / \mathbf{R}^{1/5} \quad (5.4.10)$$

Substituting Equation 5.4.10 into Equation 5.4.7 gives:

$$\frac{\eta}{d} = \sqrt{0.074} \left(\frac{c}{\sqrt{gd}} \right) \left(\frac{cd}{v} \right)^{-1/10} \quad (5.4.11)$$

Equations 5.4.4, 5.4.9, and 5.4.11 are compared with experimentally determined surge profiles in Figure 5.4.3. Each experimental profile shown in Figure 5.4.3 was obtained from a composite of superimposed profiles from a single run. This method, used to obtain averaged profiles, was discussed in Section 5.3 with regard to Figures 5.3.2 and 5.3.3. The ordinate and the abscissa are the water surface amplitude and the distance from the wall, respectively, where they have both been normalized by the reservoir depth. The surges shown in Figures 5.4.1(a) through (c) correspond to the position time histories shown in Figures 5.4.1(a) through (c). For all three reservoir depths, Equations 5.4.4 and 5.4.11 over-predict the surge height along the measured profile, except for the profile shown in Figure 5.4.3(a) where Equation 5.4.11 comes into agreement with the measured results about 4.5 reservoir depths behind the tip. As the reservoir depth increases, so does the incident surge celerity and the amount Equations 5.4.4 and 5.4.11 over-predict the measured profile. The laminar model also over-predicts the measured

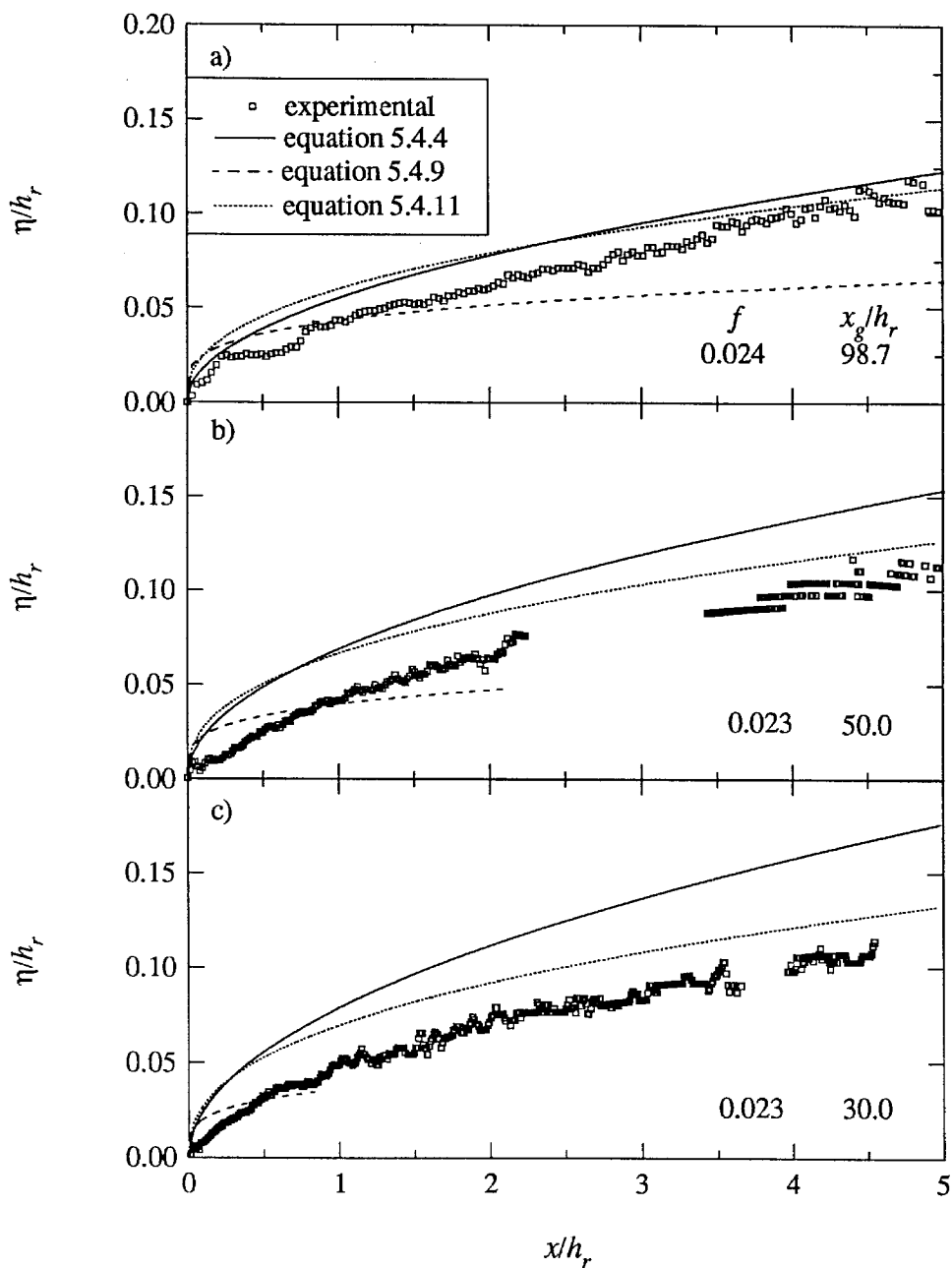


Figure 5.4.3 Theoretical and experimental surge profiles for various reservoir depths, h_r ; (a) $h_r = 15.28$ cm; (b) $h_r = 30.17$ cm; and (c) $h_r = 50.20$ cm (run no.'s HS86, HS102, and HS103).

profile near the tip, but then crosses the measured profile 0.5 to 1.0 reservoir depths behind the tip, depending on the surge celerity.

Although the model based on Whitham's argument (Equation 5.4.4) over-predicts the surge height, where the friction factor was determined from the position time history of the surge front propagation along the tank, the general shape of the predicted profiles qualitatively agree with the shape of the measured profiles in Figure 5.4.3. The friction factor used in Whitham's theory is independent of the fluid depth.

To quantitatively compare the parabolic profile predicted by Equation 5.4.4 with the measured profile, the friction factor was adjusted until the root mean square errors between the theoretical and measured profile were minimized. This caused a reduction in the friction factor from 0.024 to 0.0125, 0.023 to 0.0070, and 0.023 to 0.0056 for the surges shown in Figures 5.4.3(a) through (c), respectively. The measured profiles in Figures 5.4.3(a) through (c) are compared with Equation 5.4.4, in Figure 5.4.4(a), 5.4.5(a), and 5.4.6(a), where friction factors of 0.0125, 0.0070, and 0.0056 were used. The agreement is much closer, although there is a tendency for the theoretical profile to over-predict the surge slope near the tip and to under-predict the slope of the surge far beyond the tip region. Equation 5.4.4 is based on the assumption the friction losses along the bed behave as they do for uniform flow with a fully developed turbulent boundary layer. In Figures 5.4.4(b), 5.4.5(b), and 5.4.6(b), friction factors of 0.0125, 0.0070, and 0.0056 are used in Whitham's model for the propagation of the surge along the tank. Figure 5.4.6(b) indicates the sensitivity of the theory to the change in the friction factor required to predict the measured surge profile. With the smaller friction factor, the computed wave front arrival time at the last celerity probe was 20% smaller than measured, as seen in Figure 5.4.6(b), while this discrepancy decreased to essentially zero for the case shown in Figure 5.4.4(b).

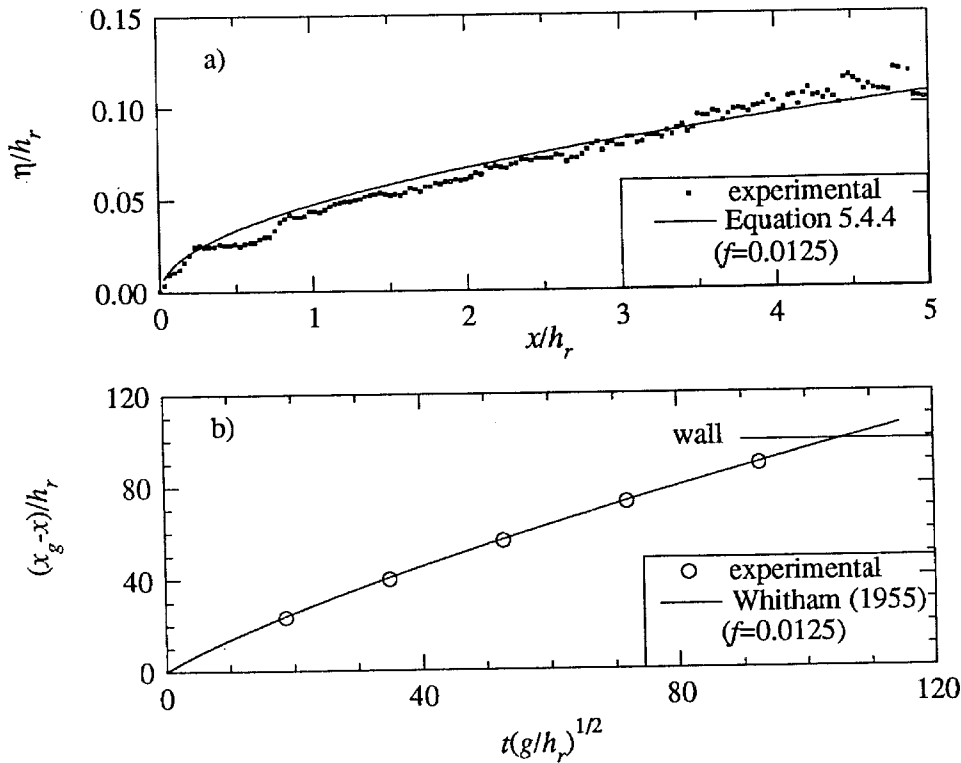


Figure 5.4.4 Experimental and theoretical (a) surge profile and (b) wave propagation down the tank where the friction term yielding the best fit to the experimental profile was used for a reservoir depth of $h_r = 15.28$ cm (run no. HS102).

The discrepancy between the measured and theoretical profiles near the tip of the surge may be caused by several factors including: the boundary layer approximation is violated near the leading edge of the tip since the gradient of the flow quantities in the x direction can no longer be neglected; a friction model based on uniform flow with a fully developed turbulent boundary layer may not accurately model the frictional losses near the tip region where the boundary layer may be laminar and large variations in the water surface profile occur; and the approximate equations may be inadequate to accurately model the physics of the flow in the tip region.

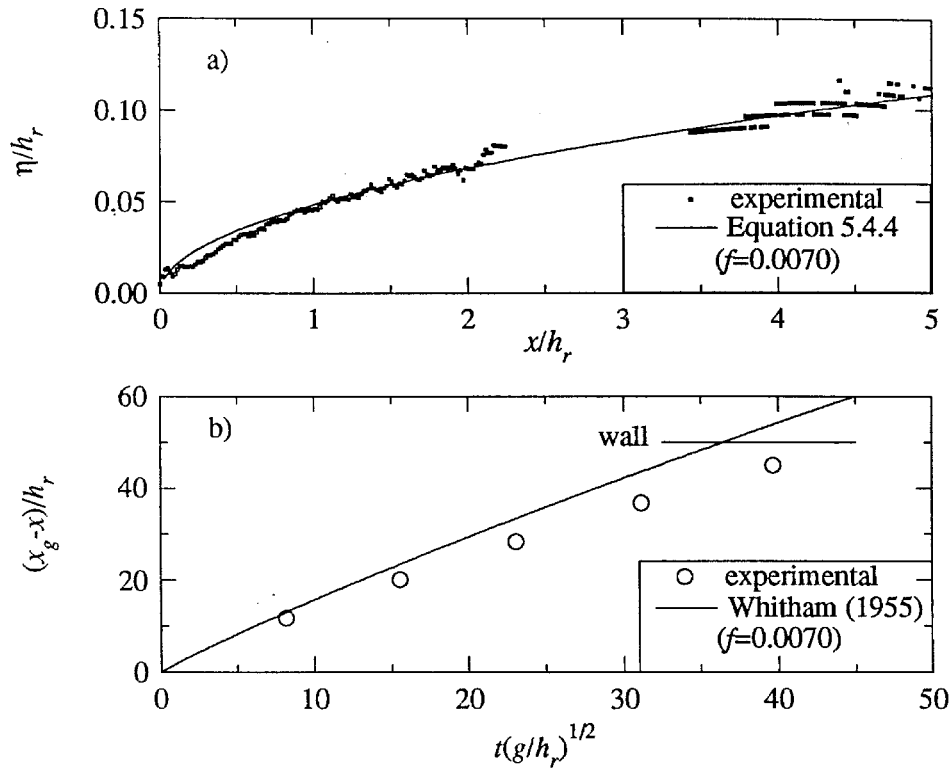


Figure 5.4.5 Experimental and theoretical (a) surge profile and (b) wave propagation down the tank where the friction term yielding the best fit to the experimental profile was used for a reservoir depth of $h_r = 30.17$ cm (run no. HS103).

The three measured surge profiles collapse when both the vertical and horizontal coordinates are normalized by the reservoir depth, as shown in Figure 5.4.7. The relative distance of the three surges from the gate vary by a factor of 3.3. The large relative distance of these surges from the wall, $x_g / h_r \geq 30$, indicates the tip profiles may tend to a shape which is independent of the distance from the wall for large propagation distances. The theories from Equation 5.4.4, where the friction factor was computed from the surge propagation along the tank (Figure 5.4.1), are also plotted for comparison. Due to the boundary layer along the bottom of the tank, it is expected there would be flow into the right side of the control volume in Figure 5.4.2 near the top, and flow out of the right side control volume near the bottom. This would contribute to spatial variations of the velocity field throughout the tip region. The model for the surge profile expressed in

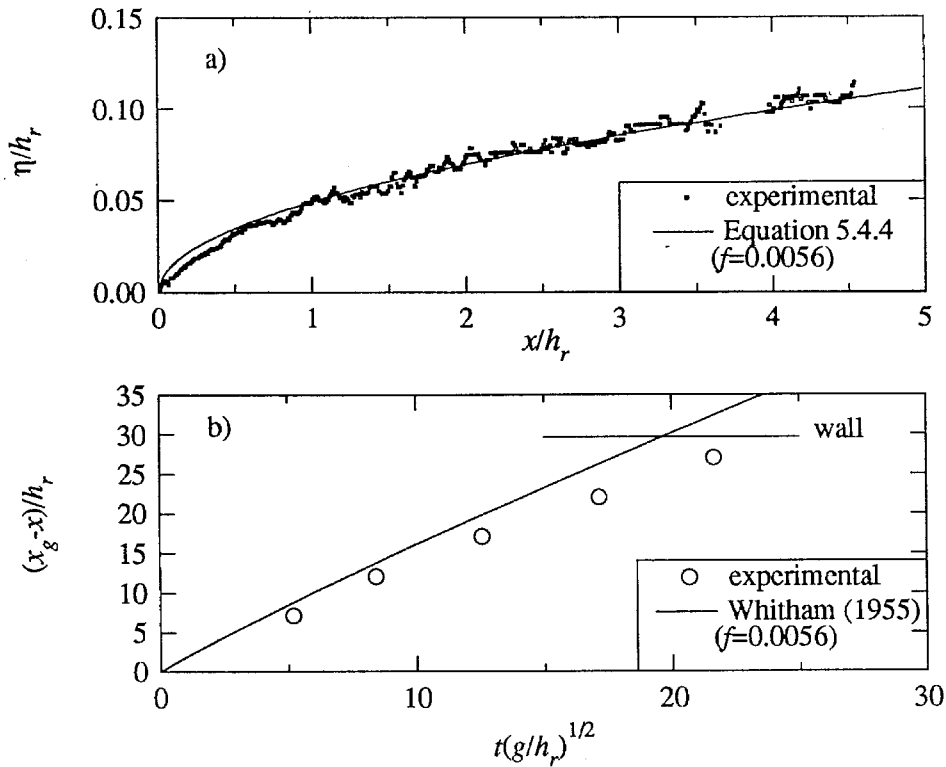


Figure 5.4.6 Experimental and theoretical (a) surge profile and (b) wave propagation down the tank where the friction term yielding the best fit to the experimental profile was used for a reservoir depth of $h_r = 50.20$ cm (run no. HS86).

The three measured surge profiles collapse when both the vertical and horizontal coordinates are normalized by the reservoir depth, as shown in Figure 5.4.7. The relative distance of the three surges from the gate vary by a factor of 3.3. The large relative distance of these surges from the wall, $x_g / h_r \geq 30$, indicates the tip profiles may tend to a shape which is independent of the distance from the wall for large propagation distances. The theories from Equation 5.4.4, where the friction factor was computed from the surge propagation along the tank (Figure 5.4.1), are also plotted for comparison. Due to the boundary layer along the bottom of the tank, it is expected there would be flow into the right side of the control volume in Figure 5.4.2 near the top, and flow out of the right side control volume near the bottom. This would contribute to spatial variations of the velocity field throughout the tip region. The model for the surge profile expressed in

Equation 5.4.4 clearly neglects any variation in the velocity distribution, which may explain the discrepancy between the theory and the experimental profiles shown in Figure 5.4.7. A more accurate theoretical approach may be to combine a hydrodynamics model for free surface fluid flows with a turbulence model, to simulate the shear along the bottom boundary. However, to simulate the impact of a surge on a vertical wall will require a hydrodynamics model which is able to simulate grossly deforming free surfaces and fluid reentry due to wave breaking.

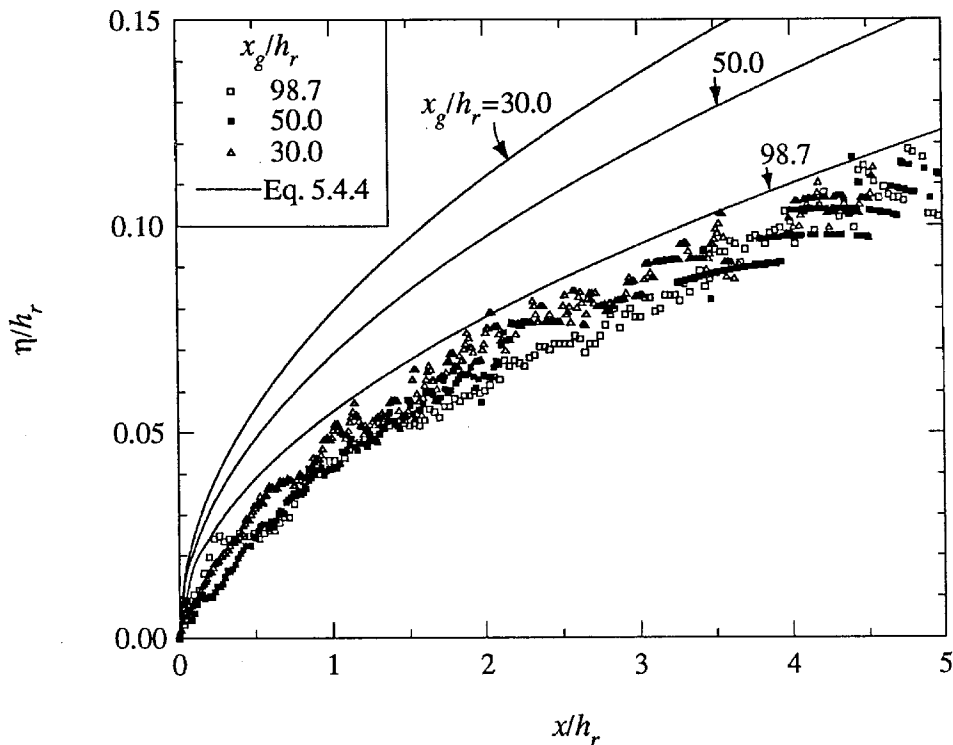


Figure 5.4.7 Experimental and theoretical surge profiles for reservoir depths of $h_r = 15.28$ cm, $h_r = 30.17$ cm, and $h_r = 50.20$ cm (run no.'s HS86, HS102, and HS103).

5.4.3 Runup, Force, and Pressure Considerations

Figures 5.4.8, 5.4.9, and 5.4.10 show the runup, pressure, and force histories on the wall due to the impact of the surges shown in Figures 5.4.3(a) through (c), respectively. In Figures 5.4.8(a) through 5.4.10(a) the runup and pressure on the wall

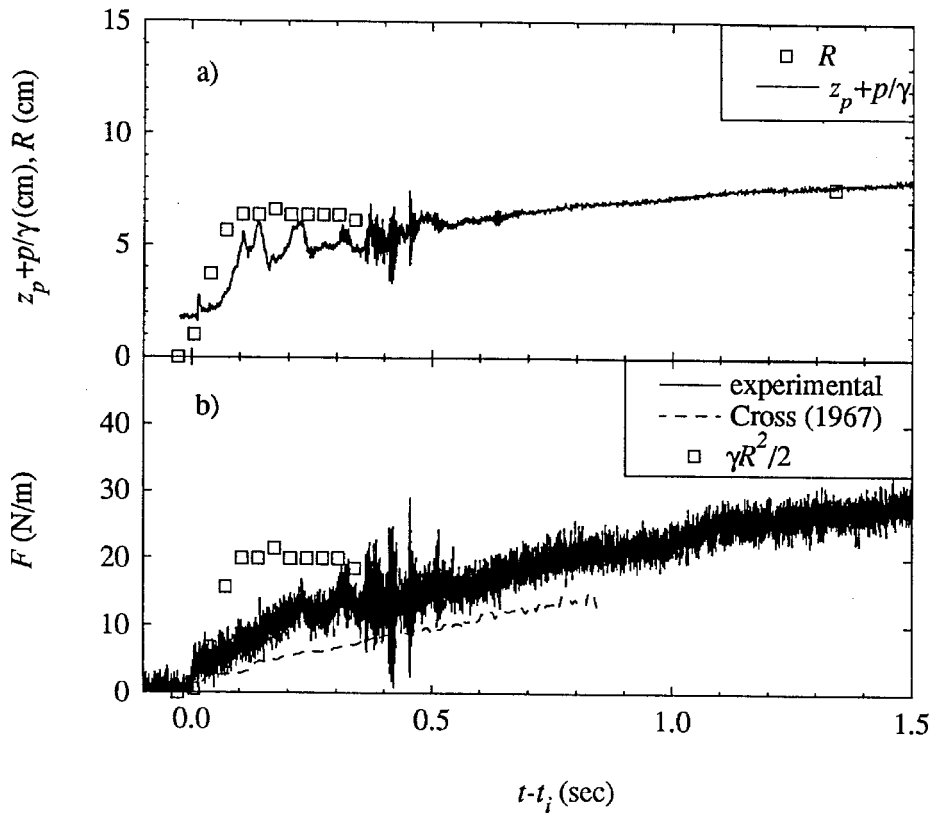


Figure 5.4.8 (a) Experimental pressure and runup time histories; (b) experimental and theoretical force time histories for a surge created with a 15.28 cm reservoir depth (run no. HS102).

1.79 cm above the tank bottom are shown. The height of the pressure transducer was added to the measured pressure head so it could be directly compared to the runup on the wall. Thus, the runup, R , should equal $z_p + p/\gamma$ when hydrostatic conditions exist at the wall. The abscissa is time which has been referenced to the time, t_i , when the surge tip reaches the wall. The time, t_i , was computed by extrapolating the model of Whitham (1955) from the time defined by the celerity probe closest to the wall. The runup height on the wall is only shown for the first 0.35 sec in Figure 5.4.8(a), since it rapidly approached a value of about 6 cm within 0.1 sec and then remained nearly constant with a very gradual rise which is indicated by the data point at 1.33 sec. The gradual rise in the runup on the wall for times greater than 0.5 sec is most likely due to the fact that the

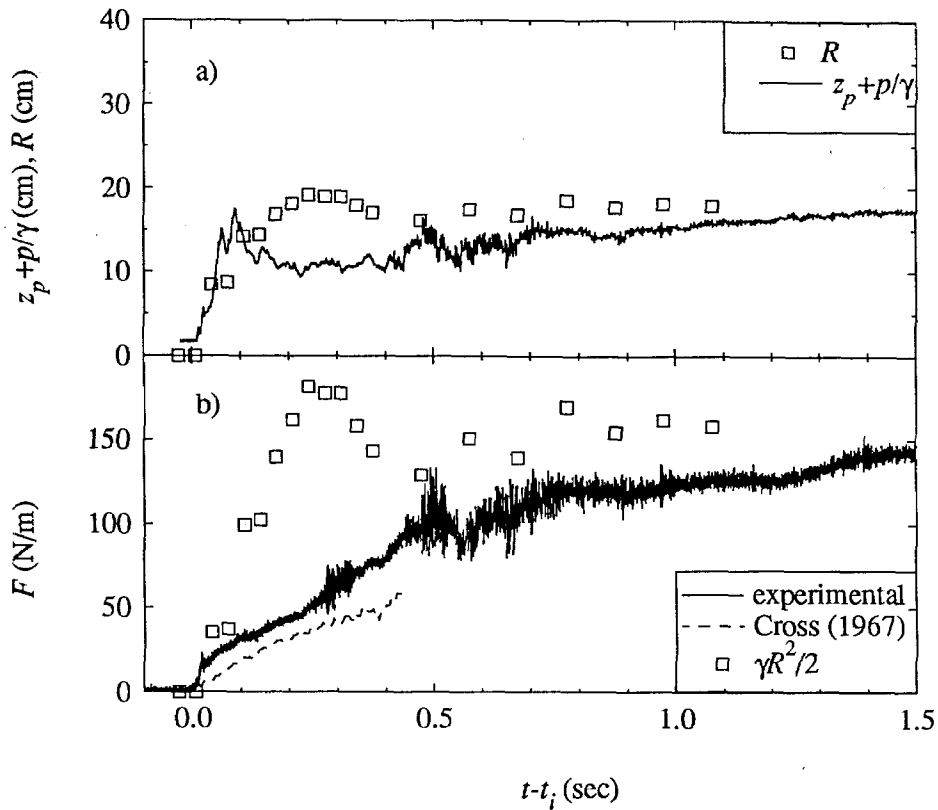


Figure 5.4.9 Experimental and theoretical force time histories for a surge created with a 30.17 cm reservoir depth (run no. HS103).

depth of the surge must continually increase behind the tip of the surge. This rise in the water surface provides the pressure gradient which overcomes the shear resistance along the tank. For this case, there is no runup tongue with large negative vertical fluid accelerations characteristic of the runup impact of strong bores.

Within the first 0.5 sec the pressure was less than hydrostatic and then gradually approaches a hydrostatic condition for times greater than 0.5 sec as seen in Figure 5.4.8(a). For times between 0.35 sec to 0.45 sec there were some rapid fluctuations in the pressure record which can also be seen in the force record shown in Figure 5.4.8(b). These oscillations in the force record may be due to relatively short duration pressure waves created by the formation of the reflected bore. However, the pressure record does not show any large pressures relative to the runup height on the wall. The hydrostatic

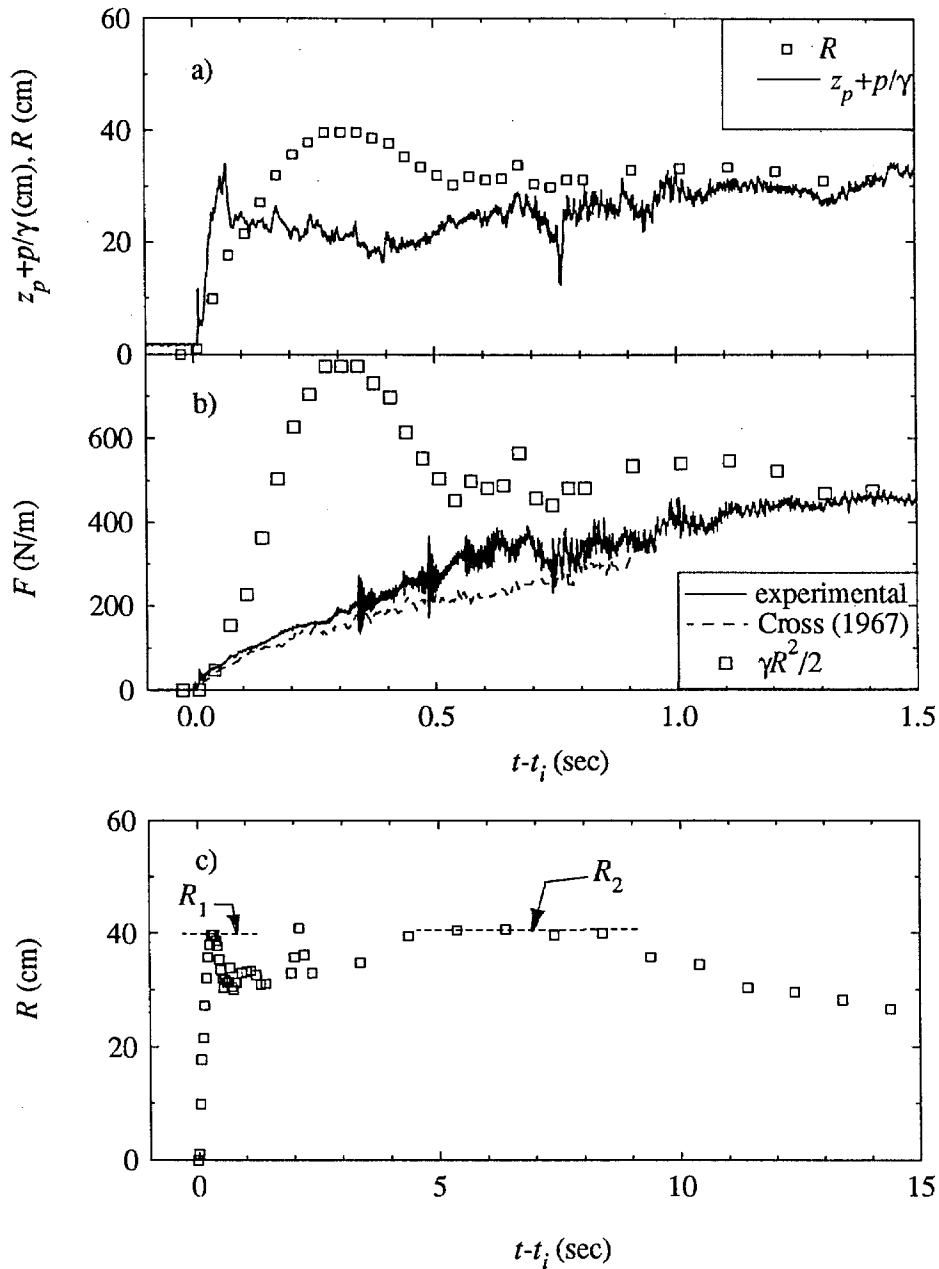


Figure 5.4.10 (a) Experimental pressure and runoff time histories; (b) experimental and theoretical force time histories; (c) experimental runoff time history on a reduced abscissa caused by a surge from a 50.20 cm deep reservoir (run no. HS86).

force computed from the runoff history on the wall is also shown in Figure 5.4.8(b).

Except for the rapid fluctuations in the force record between 0.35 sec to 0.45 sec, the increase in the force is quite gradual and progressively approaches a hydrostatic condition, 1.33 sec after impact. The runoff data point at $t-t_i = 1.33$ sec in Figure

5.4.8(a) has a corresponding hydrostatic force data point in Figure 5.4.8(b) at $t - t_i = 1.33$ sec, which is covered by the noise in the measured force signal. In Figure 5.4.8(b), the dashed line is the theory of Cross (1967) (Equation 2.3) which under-predicts the measured force from 30% to 50% over the first 0.85 sec. Since the model of Cross (1967) requires the incident surge shape, the theory can only be computed over a duration equal to the length of the known profile before impact, divided by the celerity. The large noise level in the measured force is due to the small incident surge which produced a very small force record relative to the background noise in the signal.

Figure 5.4.9 shows the case for a surge generated from a 30.17 cm reservoir depth. In this case, the runup height in Figure 5.4.9(a) exhibits a maximum about 0.3 sec after impact, although it is only slightly larger than the nearly constant runup left at the wall beyond 0.5 sec. The pressure head lies below the runup height over the entire first second after impact, even though the runup height at the wall is nearly constant for times greater than 0.5 sec. This effect, where the pressure head gradually approaches the runup height on the wall, can also be seen in Figure 5.4.10(a), where the pressure head finally agrees with the runup height, 1.4 seconds after impact. This lag, during which the pressure head lies below the runup height, may be due to both the vertical accelerations in the flow near the wall (similar to those described in Section 5.1) and the large amount of air which is entrained into the fluid next to the wall during the formation of the reflected bore. While these air bubbles are distributed over the vertical extent of the water column next to the wall, the density of the water-air mixture is significantly less than that due to pure water. This may contribute to the tendency of the measured pressure head to be less than the runup height on the wall even when the runup history indicates a constant water level near the wall. Since both the pressure and force are proportional to the fluid density, a void volume of 5% due to air entrainment would decrease the pressure and force by 5% assuming the density of gas in the bubbles is

negligible. The theory of Cross (1967) predicted the trend in the measured force in Figure 5.4.9(b), but it was up to 30% less than the experimental values.

The oscillations in the force record relative to the magnitude of the force on the wall in Figure 5.4.9(b) are much less than those shown in Figure 5.4.8(b). There also seems to be a sustained noise in the force signal beyond a time of 0.5 sec which is not present in the signal for earlier times. This may be caused by acoustic noise in the fluid produced from the turbulence generated at the shear layer near the tip of the reflected bore. The continuous production of noise at the shear layer would explain the tendency of the wall oscillations to be relatively continuous and free of the large amplitude damped oscillations, which are characteristic of the wall response to impact type loading apparent earlier in the force time history of Figure 5.4.9(b).

In Figure 5.4.10(a) the runup height on the wall has a more pronounced peak at 0.3 sec relative to the runup shown in Figures 5.4.8(a) and 5.4.9(a). The force history shows two damped oscillations at 0.35 sec and 0.50 sec in Figure 5.4.10(b), although in neither case can a corresponding peak in the pressure record be seen in Figure 5.4.10(a). Once again, the sustained noise in the force record can also be seen in the pressure record between about 0.7 sec and 1.1 sec. There is a large difference between the hydrostatic force computed from the runup on the wall and the measured force in Figure 5.4.10(b) between about 0.1 sec to 0.5 sec after impact. This is most likely due to large vertical accelerations in the fluid along the wall, like those described in Section 5.1.

The complete runup history on the wall ($h_r = 50.2\text{cm}$) is shown in Figure 5.4.10(c) where the abscissa extends to 15 sec after impact. The initial peak in the runup, which occurs just after impact, is identified as R_1 . A second peak, identified as R_2 , is associated with a hydrostatic condition along the wall at much longer times (on the order

of several seconds). The runup history near R_1 is governed by the celerity and shape of the surge tip, while the runup at R_2 is primarily dependent on the reservoir depth and length, the propagation distance between the gate and the wall, and the energy loss in the flow along the tank (i.e., the time for the negative wave generated at the gate to travel to the end of the reservoir where it is reflected, and to travel the complete distance of the wave tank to the instrumented wall). The ratio in runup heights, R_2/R_1 , varied from unity for reservoir depths of 50 cm to 2.0 for a reservoir depth of 15.28 cm. In Appendix A (Table A.2), the maximum forces and moments shown were obtained from the force and moment time-histories just after the maximum runup, R_1 , where a plateau in the force time-history occurs. Beyond this plateau, the force increases to the hydrostatic value associated with the maximum runup, R_2 . The plateau in the force record of Figure 5.4.10 occurs at about 1.5 sec after impact, which corresponds with a fairly constant value of the runup during this time as seen in Figure 5.4.10(c).

The force time histories shown in Figures 5.4.8(b), 5.4.9(b), and 5.4.10(b) gradually increase to a nearly hydrostatic value for times on the order of one second beyond the time of impact. The hydrostatic condition is indicated by the agreement of $1/2 \gamma R^2$ with the measured force in Figures 5.4.9(b) and 5.4.10(b) for $t - t_i < 1.3$. The runup histories shown in Figures 5.4.8(a), 5.4.9(a), and 5.4.10(a) initially rise to a maximum value which is equal to or slightly greater (up to 20%) than the relatively constant water level left at the wall for times greater than 0.5 sec. When normalized by the velocity head computed from the surge celerity, the initial maximum runup height on the wall for all the dry bed surge cases are in the range between 1.46 and 1.62. Thus, the maximum force (excluding the response to short duration impulsive loads) can be conservatively estimated as the hydrostatic force due to the runup, R_1 , where $R_1 = 1.62 (c^2/2g)$. If the maximum water surface slope of the surge is greater than approximately 0.06, then the runup height, R_1 , may be larger than 1.62 $(c^2/2g)$.

5.4.4 Comparison Between a Bore and a Dry Bed Surge

A comparison between the impact of a strong turbulent bore and a dry bed surge with nearly the same celerity is shown in Figure 5.4.11. Both these waves were produced in the horizontal wave tank using the dam break method. The dry bed surge was

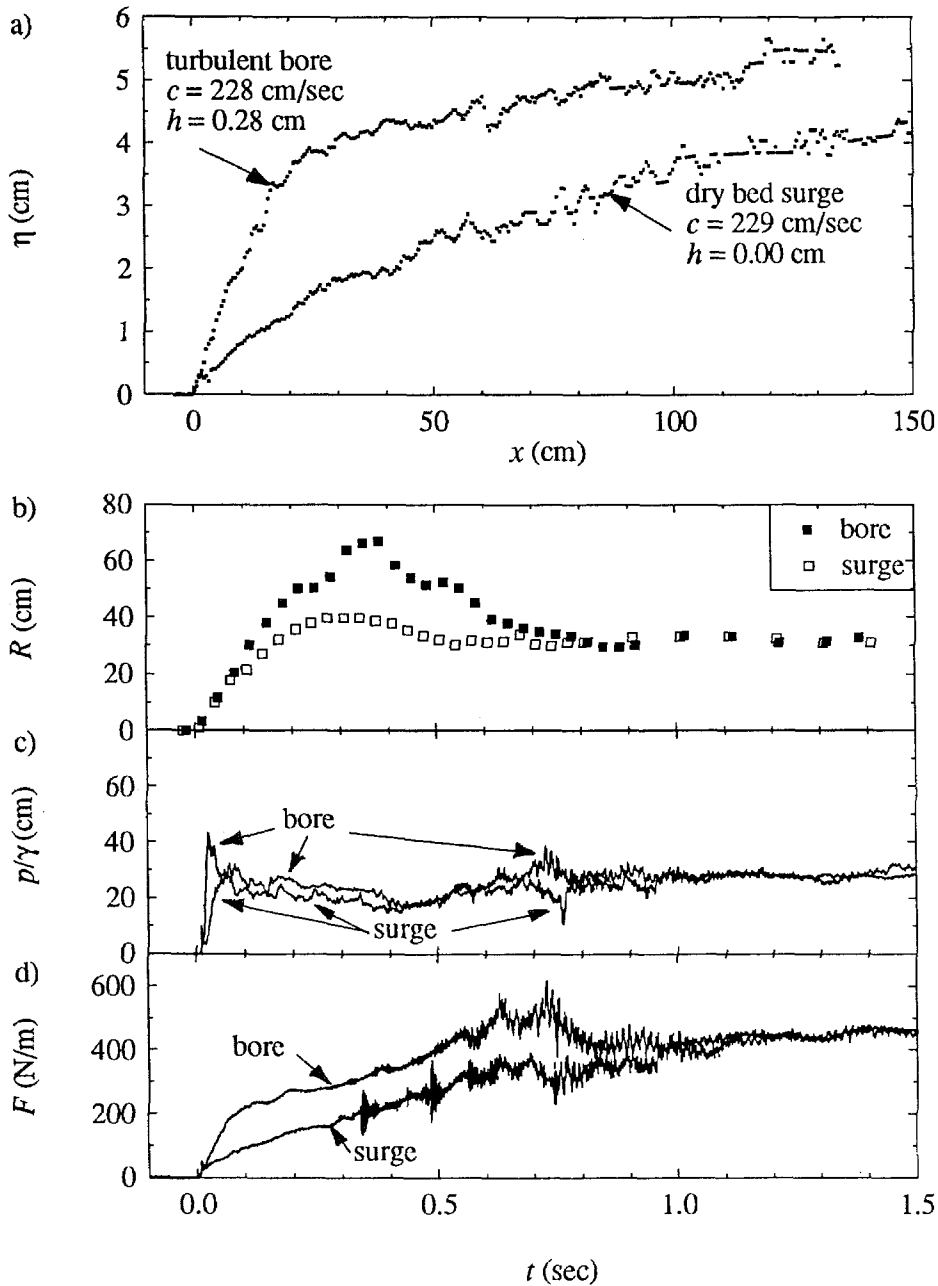


Figure 5.4.11 Comparison of the experimental (a) wave profile; (b) runup; (c) pressure head; and (d) force due to a strong turbulent bore and a dry bed surge with approximately the same celerity (run no.'s HS86 and HB87).

obtained by releasing a reservoir 50.20 cm in depth, while the bore was created by releasing a 48.01 cm reservoir into a still water depth of 0.28 cm. Although the reservoir depth for the bore was 4.4% less than the depth used for the dry bed surge, the celerity of the two waves just prior to impact at the wall were within 0.7% of each other. The slope of the front of the dry bed surge was 0.06 compared to 0.19 for the turbulent bore, as seen in Figure 5.4.11(a). Not only is the wave slope steeper for the bore, the wave height at any horizontal position behind the front of the bore dramatically exceeds the height of the dry bed surge. However, as the distance behind the tip of the bore increases, the slope of the two wave profiles tend to agree and the difference between the two wave profiles decrease.

The runup history on the wall is shown in Figure 5.4.11(b). The maximum runup due to the surge is approximately 20% larger than the relatively constant level left at the wall for times, $t - t_i > 0.8$ sec, as seen in Figure 5.4.11(b). The maximum runup height due to the bore is nearly 100% of the relatively constant water level left at the wall for times, $t - t_i > 0.8$ sec. The larger runup of the bore relative to the surge is most likely caused by the larger water surface slope of the bore which contributes to much more volume near the front of the tip.

The pressure histories 1.79 cm above the bottom of the tank are shown in Figure 5.4.11(c). The pressure due to the surge rapidly reaches a certain value and tends to maintain that value during the entire reflection process. The pressure head generated by the bore attains a maximum value about 50% greater than the relatively constant values for times greater than about 1.0 sec, although it is less than the elevation of the maximum runup above the pressure cell.

The force time histories are shown in Figure 5.4.11(d), where the force due to the surge gradually increases to the subsequent hydrostatic value for times greater than 1.3 sec, as was shown in Figure 5.4.10(b). The force time history due to the bore increases to a maximum value at a relative time of 0.72 sec, then decreases to a constant level which is hydrostatic for times greater than 1.3 sec after impact. Although there is some variability of the wave profiles in both space and time, there are no large surface fluctuations contributing to nearly vertical regions of the wave profile, such as that shown in Figure 5.3.2(b) about 42 cm in front of the wall, which may contribute to the generation of large pressures. The relatively smooth wave profiles may be the reason no large pressures were measured during the impact of very strong bores and dry bed surges. However, no pressure measurements were collected close to the bed where the surge fronts are the steepest and would most likely cause the largest pressures.

5.5 Summary

The objective of this section is to combine the results from Sections 5.1 through 5.4, where possible, to quantify the behavior of the measured results as a function of the relative incident wave height. The relative wave height can range from zero for very small solitary waves (Section 5.2) and mild undular bores (Section 5.3), to infinity for surges propagating over a dry surface (Section 5.4). For the experiments with the sloping bottom, the water depth h is defined at a distance of three horizontal length scales (3 l) from the tip of the bore as shown in Figure 5.1.1 (c).

The celerity of the incident wave is plotted as a function of the relative incident wave height in Figure 5.5.1, where the celerity has been normalized by the linear shallow water wave speed. The results from the solitary wave experiments, which were obtained in a water depth, h , of about 17.66 cm, are shown with the circles. These results agree quite well with the solid line, which is the numerical results of Longuet-Higgins and

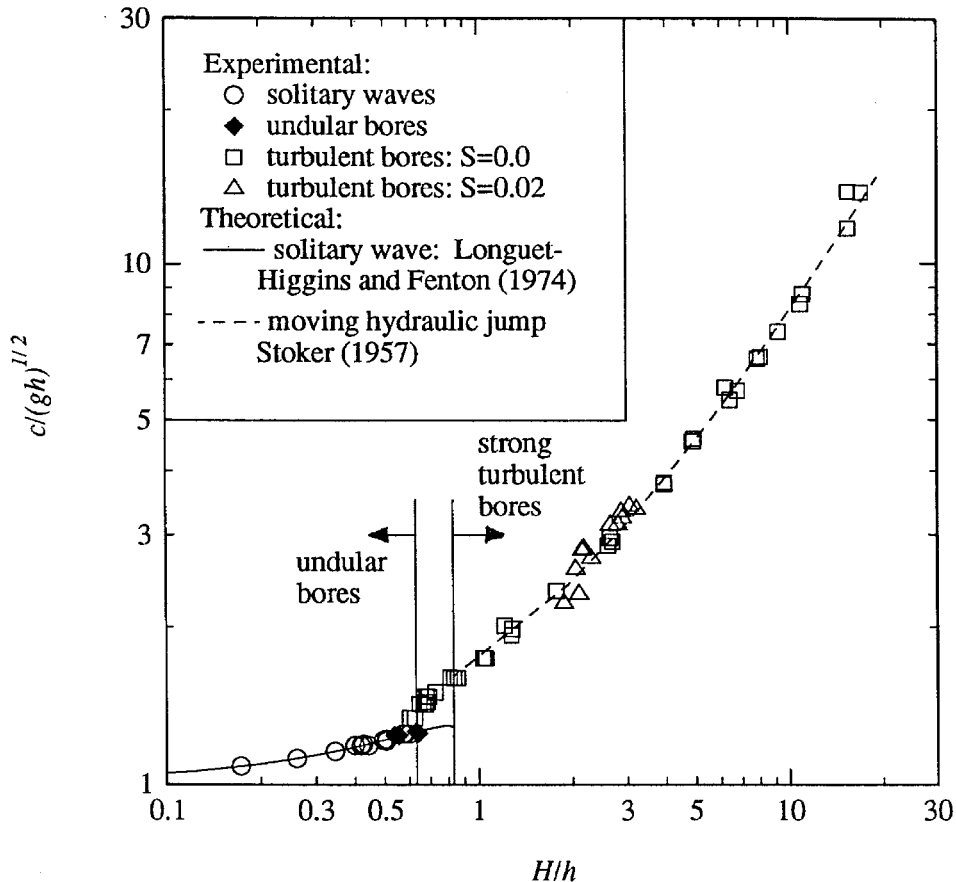


Figure 5.5.1 Experimental and theoretical wave celerities for all the experiments conducted during this study.

Fenton (1974). The celerity of the undular bores, which is shown with the solid diamonds, agrees quite well with the measured, empirical, and theoretical solitary wave celerity. The transition from undular bores (characterized by a smooth profile with no turbulence) to turbulent bores (which resemble a spilling breaking wave) occurs at a relative wave height of about 0.63. The largest undular bore and the smallest turbulent bore obtained in this study had relative wave heights of 0.64 and 0.62, respectively. The measured celerities for the turbulent bores generated in the horizontal tank and tilting tank are shown with the squares and triangles, respectively. The bore celerity predicted from the moving hydraulic jump solution of the nonlinear shallow water wave equations (Stoker (1957)) is shown with the long dashed line. It must be noted that the celerity

from the hydraulic jump theory is calculated with the mean water level behind the jump. For the undular bores and the slightly turbulent bores, the mean water level behind the jump could not be measured accurately with the experimental arrangement used. In Section 5.3, it was shown that the mean water level behind the bore and the maximum wave height are the same for strong turbulent bores (i.e., $H/h \geq 0.83$). Therefore, the moving hydraulic jump theory is only plotted over the range of relative wave heights corresponding to the strong turbulent bores. There is excellent agreement between the experimental results for the bore from both wave tanks and the moving hydraulic jump solution over the full range of strong turbulent bores. The transition region from undular bores to strong turbulent bores, as defined in Section 5.3, is shown in Figure 5.5.1 which lies between $H/h \cong 0.63$ and $H/h \cong 0.83$. The asymptotic approach of the experimental and empirical solitary wave celerity to $c/\sqrt{gh} = 1$ as $H/h \rightarrow 0$, can be seen in Figure 5.5.1 indicating the celerity of very small solitary waves can be predicted with linear shallow water wave theory.

The agreement between the celerity predicted from the solitary wave theory and experimental results, has been well documented in earlier works (Daily and Stephan (1952), French (1969), Longuet-Higgins and Fenton (1974), and Naheer (1976), among others). The celerity predicted from the moving hydraulic jump solution of the turbulent bore also has been well documented (Bakhmeteff and Matzke (1936), Rouse (1950)). Sandover and Zienkiewicz (1957) and Wilkinson and Banner (1977), have shown excellent agreement between the celerity predicted from the moving hydraulic jump theory (Stoker (1957)) and experimental results for undular bores and bores in the transition zone, where the mean water level behind the bore front was measured and used to compare the experimental results with the theory. Although the moving hydraulic jump theory predicts the celerity of the wave quite well for a given ratio of the depths across the bore, a more elaborate theory based on rapidly varied flow analysis (Sobey

and Dingemans (1992)) is needed to predict the maximum wave height for undular bores and slightly turbulent bores.

The measured maximum wave slope, $\|d\eta/dx\|$, and runup, R , are plotted as a function of the relative wave height in Figure 5.5.2. The maximum runup height has been normalized by $2H$, and twice the velocity head computed from the wave celerity in Figures 5.5.2(b) and 5.5.2(c), respectively. The measured wave slopes from the solitary waves and the undular bores agree with the slope computed from the solitary wave theory of Tanaka (1986). In the transition zone between undular bores and strong turbulent bores, there is a jump in the maximum measured wave slope from approximately 0.3 to values ranging from 0.6 to 1.0. In addition, there appears to be a rapid decrease in the maximum slope across the transition zone to slopes varying from 0.3 to 0.5. In the region of the graph corresponding to strong turbulent bores, the wave slopes decrease gradually to approximately 0.2 at relative wave heights of about 15.

Although the maximum slope is not well defined for the dry bed surges, an attempt was made to obtain an estimate of the wave slope near the front of the surge as described in Section 5.4. Since by definition the dry bed surges have no ambient depth, the relative wave height for these cases is infinity. Thus, the range of slopes calculated from the dry bed surge profiles are shown with the appended scale at the right side of Figure 5.5.2(a). For all the dry bed surges, except for the smallest case, the maximum slope of the front face of the bores varied from 0.053 to 0.064. This is about a factor of three less than the slopes obtained from the strongest bores traveling on a constant depth of water. It is interesting that the celerities of the strongest bore and the strongest dry bed surge were within 0.5% of each other, yet a depth of only 2.8 mm increased the slope of the front of the turbulent bore by a factor of three (Figure 5.4.11). As shown in Figure 5.5.2(a), the maximum measured slope from the front face of the bores in the tilting tank

agree with those from the horizontal tank. It appears the steepest waves of permanent form are those in the transition region which are spilling breakers. As the relative incident wave height increases beyond the transition zone for turbulent bores, the region of turbulence on the front of the wave begins to increase in extent, and extends farther along the front face of the wave. This elongation of the turbulent zone, discussed in Section 5.3 (see Figure 5.3.5), corresponds to a decrease in wave slope as the relative wave height increases.

It seems reasonable that the maximum slope of the wave will affect the runup on the wall during the reflection. This is clearly shown in Figure 5.5.2(b) where the maximum measured runup, normalized by $2H$, increases by about a factor of about two at the same relative wave height, where the maximum wave slope increases by a factor of two to three. It should be noted from Figure 5.5.1 that within the transition from undular to turbulent bores, the relative wave celerity increases by only a few percent, while the relative wave height actually decreased slightly. The solid line shows the third-order solitary wave interaction theory of Su and Mirie (1980). The solitary wave theory predicts the maximum runup for both the experimental solitary waves and the undular bores, well for relative wave heights less than about 0.5. As the relative wave height becomes greater than about 0.5 the results of the third-order solitary wave theory is less than the measured maximum runup on the wall.

For the experimental and theoretical solitary wave results, the relative runup approaches unity as the relative wave height tends to zero, indicating a linear interaction with the wall. As the relative wave height increases, so do the nonlinear effects. This is indicated by the increase in the maximum relative runup beyond a value of one in Figure 5.5.2(b).

For the largest undular bore, the maximum runup is quite large and does not follow the trend evident in the rest of the undular bore and solitary wave runup measurements. This is explained by the fact that during the reflection of the largest undular bore, as discussed in Section 5.3, the reflection of the first or second wave from the wall caused the second or third wave to peak and break on the wall. The maximum runup height corresponding to the first wave crest for the highest undular bore case, which is not shown in Figures 5.5.2(b), and (c), is $R/2H = 1.46$ and $Rg/c^2 = 1.17$, for a relative wave height, $H/h = 0.64$, which agree with the trend of the experimental solitary wave results.

For all the transitional bores, except for one, and the strong turbulent bores, the maximum runup is approximately proportional to the velocity head as shown in Figure 5.5.2(c). The plateau in Rg/c^2 with respect to the wave height in Figure 5.5.2(c) ranges from $Rg/c^2 \cong 1.5$ for the transitional bores, to $Rg/c^2 \cong 1.25$, for the strongest bore. Although there is some experimental variability in both the runup of Figure 5.5.2(c) and the wave slope of Figure 5.5.2(a), both appear to follow a linear trend on the log plot with a slightly negative slope in the strong turbulent bore regime. The range of results from the dry-bed cases are shown on the right side of Figure 5.5.2(c), with the appended scale. The apparent correlation between the runup and the wave slope for the strong bores also holds for the dry-bed surges. Although the dry-bed surge results cannot be plotted on the abscissa, it will be noted that as the wave slope decreases by a factor of three between the strongest bores and the strongest dry bed surges, a simultaneous decrease in the relative runup from $Rg/c^2 \cong 1.25$ for the strongest bores, to $Rg/c^2 \cong 0.8$, for the dry bed surges occurs as seen in Figures 5.5.2(a) and (c). Cross (1967) reported values which ranged from $0.65 < Rg/c^2 < 1.1$ for dry bed surges and very strong bores on a slightly wetted bed, while Fukui et al. (1963) concluded the relative

For the largest undular bore, the maximum runup is quite large and does not follow the trend evident in the rest of the undular bore and solitary wave runup measurements. This is explained by the fact that during the reflection of the largest undular bore, as discussed in Section 5.3, the reflection of the first or second wave from the wall caused the second or third wave to peak and break on the wall. The maximum runup height corresponding to the first wave crest for the highest undular bore case, which is not shown in Figures 5.5.2(b), and (c), is $R/2H = 1.46$ and $Rg/c^2 = 1.17$, for a relative wave height, $H/h = 0.64$, which agree with the trend of the experimental solitary wave results.

For all the transitional bores, except for one, and the strong turbulent bores, the maximum runup is approximately proportional to the velocity head as shown in Figure 5.5.2(c). The plateau in Rg/c^2 with respect to the wave height in Figure 5.5.2(c) ranges from $Rg/c^2 \cong 1.5$ for the transitional bores, to $Rg/c^2 \cong 1.25$, for the strongest bore. Although there is some experimental variability in both the runup of Figure 5.5.2(c) and the wave slope of Figure 5.5.2(a), both appear to follow a linear trend on the log plot with a slightly negative slope in the strong turbulent bore regime. The range of results from the dry-bed cases are shown on the right side of Figure 5.5.2(c), with the appended scale. The apparent correlation between the runup and the wave slope for the strong bores also holds for the dry-bed surges. Although the dry-bed surge results cannot be plotted on the abscissa, it will be noted that as the wave slope decreases by a factor of three between the strongest bores and the strongest dry bed surges, a simultaneous decrease in the relative runup from $Rg/c^2 \cong 1.25$ for the strongest bores, to $Rg/c^2 \cong 0.8$, for the dry bed surges occurs as seen in Figures 5.5.2(a) and (c). Cross (1967) reported values which ranged from $0.65 < Rg/c^2 < 1.1$ for dry bed surges and very strong bores on a slightly wetted bed, while Fukui et al. (1963) concluded the relative

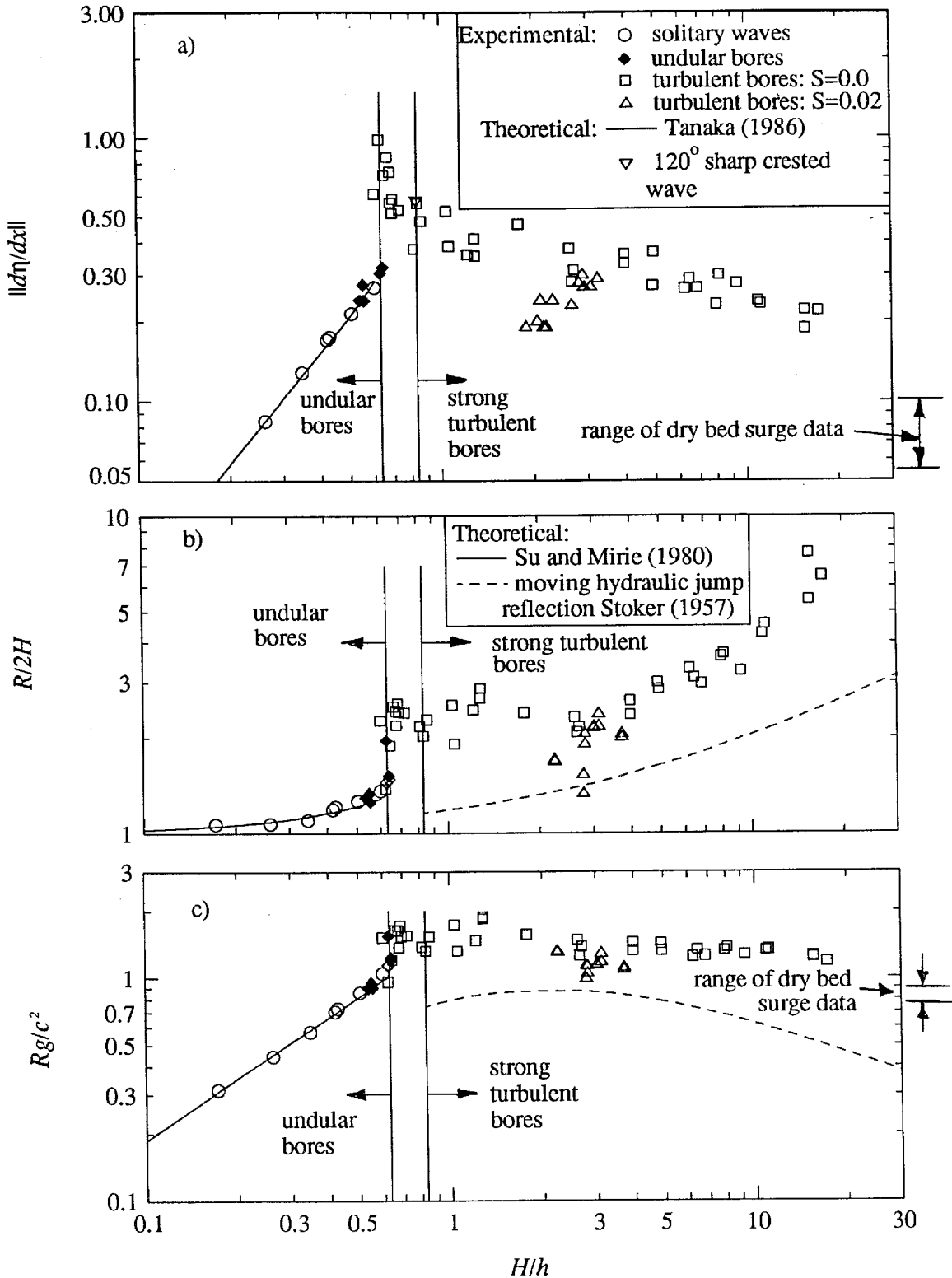


Figure 5.5.2 Experimental and theoretical (a) maximum water surface slopes; (b) runup normalized by twice the incident wave height; and (c) runup normalized by twice the velocity head due to the wave celerity.

runup height was $Rg/c^2 = 1.65$ for all their experiments with bores impacting a vertical wall.

Figures 5.5.2(b) and (c) show the maximum measured runup heights from the tilting wave tank study agree with the experimental results obtained in the horizontal wave tank. An exception are the data which correspond to the two smallest incident waves used in the tilting wave tank experiments. The runup heights corresponding to these two smallest incident waves tend to lie below the corresponding results from the horizontal wave tank. However, all the runup heights measured in the tilting wave tank were within 60% to 100% of the runup heights obtained in the horizontal wave tank experiments for equivalent relative incident wave heights. There are several possibilities which may contribute to the differences between the runup in the tilting and horizontal wave tank experiments. These include the effect of the $1/50$ slope used in the tilting wave tank experiment, the smaller scale of the tilting tank experiments which decreased the observed air entrainment for the smallest bores relative to the largest, the two different methods used to observe the runup history on the wall, and the different methods used to measure the celerity of the wave and the wave height. Taking into account all the differences between the tilting and horizontal tank experiments, where the bores were generated by completely different means, the overall agreement is surprisingly good. The results in Figures 5.5.2(b) and (c) indicate the maximum runup height of bores traveling over mild slopes with $S \leq 1/50$ can be conservatively estimated from the runup height of bores traveling over horizontal slopes.

The moving hydraulic jump theory of Stoker (1957) is shown with the dashed lines in Figures 5.5.2(b) and (c). This theory predicts the ambient water level left at the wall after the reflection of the bore is completed. This theory does not account for the dynamics which take place during the reflection process and thus, it is not expected to be

an accurate estimate of the maximum runup height. However, the theory was included in Figures 5.5.2(b) and (c), since it is this fluid depth which would produce sustained overtopping in the event the wall was less than this height. If the wall were greater than the theoretical runup height (Stoker (1957)), but less than the maximum experimental runup, then a very limited amount of overtopping may occur.

The theoretical curve (Stoker (1957)) in Figures 5.5.2(b) and (c) tends to under-predict the maximum measured runup. In some cases the theoretical value was only 55% of the measured runup. Although air entrainment in the flow may contribute to larger runup heights than would be obtained with pure water, due to the reduced fluid density, this effect is probably small. If air entrainment alone were the primary reason the experimental runup height in Figures 5.5.2(b) and (c) exceeded the theory of Stoker (1957), air content of 50% by volume would be required if the runup height were assumed to be proportional to the density of the air-water mixture.

The temporal maximum of the measured pressure from each experiment in the horizontal tank is plotted as the abscissa of Figure 5.5.3; data for many different relative wave heights are included and indicated by the different symbols for ranges of H/h . The ordinate of Figure 5.5.3 is $(1 + z_p / h)$, where z_p is the distance of the pressure cell above the still water level, and h is the still water depth in front of the wall. Thus, ordinates of zero and unity correspond to the pressure cell located at the bottom of the wave tank and the still water surface, respectively. The pressure has been non-dimensionalized by the hydrostatic pressure, at the vertical location of the pressure transducer, computed from the maximum measured runup height on the wall. The results in Figure 5.5.3 should not be considered as an instantaneous pressure distribution along the wall, since the maximum pressure at different vertical locations on the wall may occur at different times during the reflection process. Table 5.5.1 shows that all the

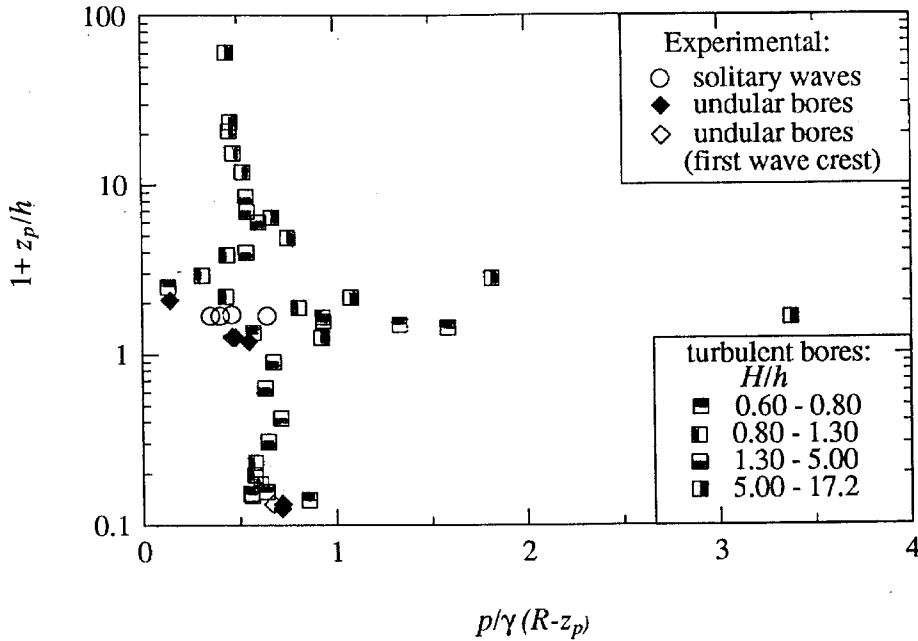


Figure 5.5.3 Maximum experimental pressures as a function of the relative vertical position on the wall for various relative wave heights.

maximum measured pressures which were greater than the hydrostatic pressure, due to the maximum runup on the wall, are confined to a region which lies between 0.08 and 0.71 wave heights above the still water surface. Table 5.5.1 provides a summary of the five largest relative pressures shown in Figure 5.5.3, which indicates that the two highest measured pressures occurred within $0.16 H$ of the still water surface during the impact of strong turbulent bores. In Table 5.5.1, the pressures are non-dimensionalized with the same scale used in Figure 5.5.3, as well as pressure scales based on the hydrostatic

| Run No. | h (cm) | H/h | c / \sqrt{gh} | z_p / H | $\frac{p}{\gamma(R-z_p)}$ | $p/\gamma H$ | $\frac{p}{\gamma(c^2/2g)}$ |
|---------|-------------|-------|-----------------|-----------|---------------------------|--------------|----------------------------|
| HB081 | 11.40 | 0.69 | 1.47 | 0.71 | 1.34 | 5.48 | 3.50 |
| HB082 | 11.94 | 0.66 | 1.42 | 0.64 | 1.59 | 6.96 | 4.57 |
| HB089 | 0.64 | 11.09 | 8.70 | 0.16 | 1.82 | 16.36 | 4.80 |
| HB090 | 0.83 | 9.24 | 7.38 | 0.13 | 1.08 | 7.99 | 2.71 |
| HB091 | 1.10 | 7.91 | 6.56 | 0.08 | 3.27 | 23.00 | 8.45 |

Table 5.5.1 Maximum measured pressure heads obtained during this study which were greater than the runup height on the wall.

pressure due to the incident wave height and the velocity head associated with the incident bore. The last two columns in Table 5.5.1 are provided, since these pressure scales have been used to non-dimensionalize results in many previous works including Chan and Melville (1986) and Cooker and Peregrine (1990), among others. The maximum measured pressure heads, obtained during the dry bed surge experiments, were all less than the maximum measured runup on the wall, when added to the location of the pressure cell above the bottom of the tank, z_p .

Due to the limited amount of pressure measurements obtained during this study, it is difficult to determine whether large pressures can be developed over the full range of types of turbulent bores. Fukui et al. (1963) reported maximum measured pressures due to turbulent bores ranging up to $p / (\rho c^2 / 2) \cong 5.4$. The maximum measured pressure obtained during run HB091 (see Table 5.5.1) appears to be the highest relative pressure measured on a laboratory scale during the impact of a turbulent bore (relative to all previously published values). However, it should be noted that impact pressures can vary considerably from one run to the next, especially when associated with an aerated flow which may also trap air during impact (Chan and Melville (1986)). Therefore, there is no reason to believe that the maximum measured pressure during run HB091 represents in any way the maximum possible pressure which could be expected during the impact of a turbulent bore. To obtain statistics on the maximum measured pressures, one needs to repeat the same experiment many times with enough pressure transducers distributed vertically along the structure to resolve the location and the magnitude of the maximum pressure when it occurs. Results from an experimental program using this approach, were reported by Chan and Melville (1988) to resolve the vertical distribution and occurrence of the maximum pressure due to the impact of a deep water plunging breaking wave. However, due to the number of repeated experiments required to

develop the necessary statistics, only one wave condition was reported in Chan and Melville (1988). In this study it was considered important to cover a wide range of incident wave conditions. Therefore, only a limited number of experiments were conducted for each wave condition.

Chan and Melville (1986) found that the typical range of impact pressures for deep water plunging breaking waves was $6 \leq p / (\rho c^2 / 2) \leq 20$, while the highest maximum measured pressure was 42 times the stagnation pressure computed from the incident wave celerity. Earlier investigators such as Bagnold (1939), and Weggel and Maxwell (1970) reported maximum measured pressures of $p / (\rho c^2 / 2)$ equal to 180 and 80, respectively, while the typical maximum measured pressures ranged from $22 \leq p / (\rho c^2 / 2) \leq 80$ and $16 \leq p / (\rho c^2 / 2) \leq 40$, respectively. In the studies of Bagnold (1939) and Weggel and Maxwell (1970), a sloping beach was used to cause the wave to break directly on a vertical wall. The maximum measured pressure obtained in this study ($p / (\rho c^2 / 2) = 8.45$) is considerable less than the maximum values measured in the studies mentioned.

Cooker and Peregrine (1988) reported a maximum theoretical pressure of $p / \gamma h = 60$ during their numerical study of the impact of a breaking shallow water wave on a vertical wall. They used a boundary element model to solve the potential flow problem with the full nonlinear free surface boundary conditions. They used a relative incident wave height, $H/h = 1.5$. If their maximum calculated pressure is normalized by the wave height, then the resulting value is $p / \gamma H = 40$. The value of $p / \gamma H = 23$, measured in this study is of the same order of magnitude, even though the maximum pressures obtained in this study are smaller than the maximum pressures reported from the breaking wave impact studies of others.

The maximum measured force on the wall as a function of the relative incident wave height is shown in Figure 5.5.4. In Figure 5.5.4(a), the maximum measured force is normalized by the linear force, F_l , (defined in Equation 5.1.2) which is equal to the hydrostatic force due to a runup height on the wall equal to twice the wave height. The solitary wave results indicate the maximum measured force approaches the value corresponding to the linear force, F_l , for small relative incident wave heights while it becomes less than unity as the relative wave height increases. The decrease in the relative force as the solitary wave height increases, is due to a corresponding increase in the vertical accelerations along the wall near the time of maximum runup (see Figure 5.2.10). The solitary wave measurements in Figure 5.5.4(a) agree quite well with the *third-order solitary wave collision theory of Su and Mirie (1980)*.

There is a sudden increase in the relative measured forces of Figure 5.5.4(a) at a relative wave height corresponding to the transition from undular to slightly turbulent bores. The relative force increases from about 0.7 to slightly more than 1.0. Across the bore transition zone, the maximum measured forces increase slowly, and then follow the trend predicted from the moving hydraulic jump reflection theory of Stoker (1957). This curve is calculated from the reflection of a moving hydraulic jump at a vertical wall, where the force is taken to be equal to the hydrostatic force on the wall after the reflection takes place. This theory is based on the nonlinear shallow water wave equations. The moving hydraulic jump reflection theory tends to under-predict the maximum measured forces by about 30% for bores with relative wave heights of the order of unity, and by about 40% for bores with relative wave heights equal to about 10. The results for $H/h > 10$ in Figure 5.5.4(a), correspond to the two strongest bores where the water surface elevation immediately behind the front of the bore continued to increase. In the dam-break problem, if there is an insufficient downstream depth, there

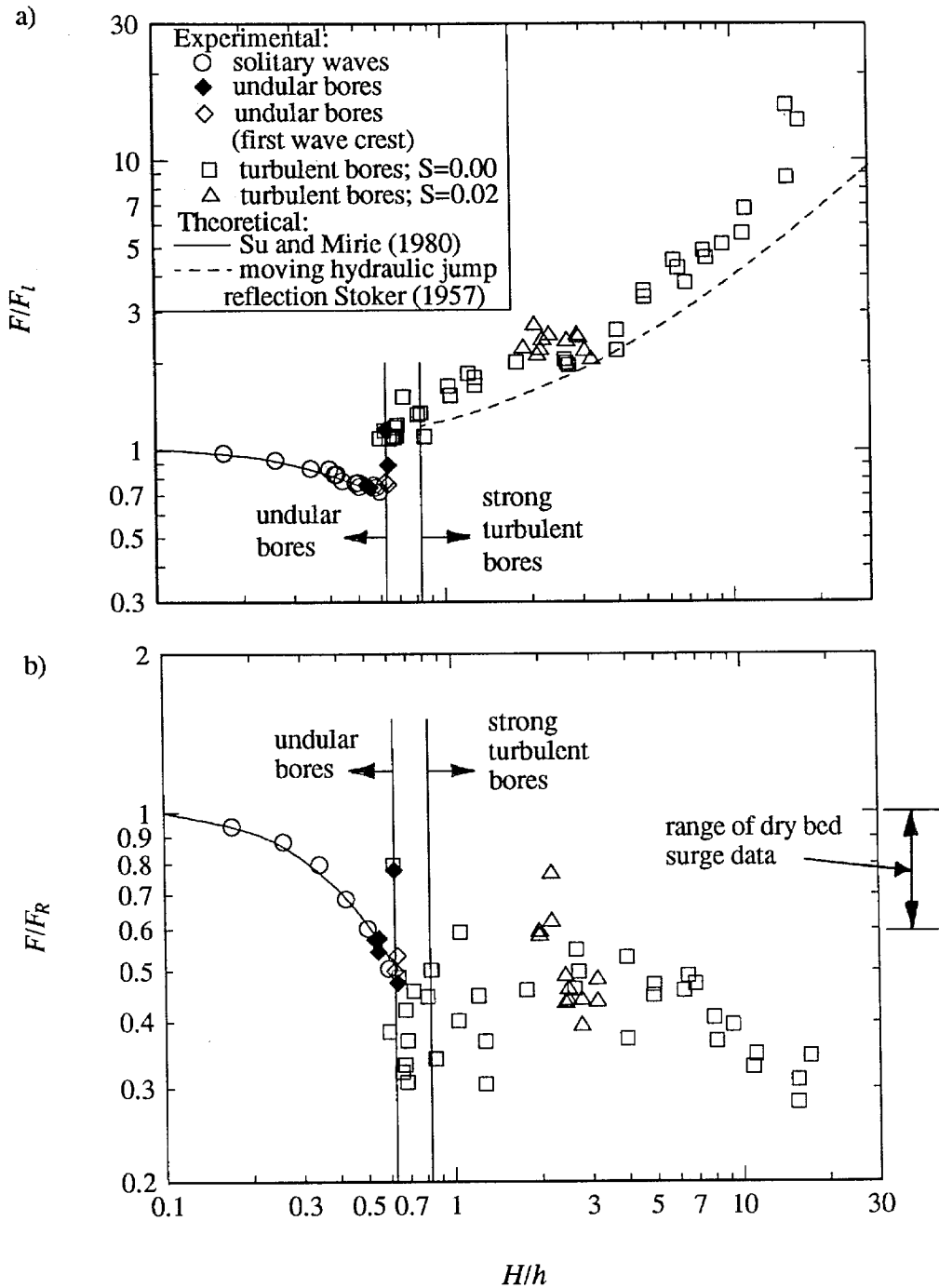


Figure 5.5.4 Experimental and theoretical maximum force on the wall normalized by (a) the hydrostatic force due to a runup equal to twice the incident wave height; (b) the hydrostatic force due to the maximum runup.

will be no constant depth region behind the bore front. This can be seen in the solution of the nonlinear shallow water wave equations, where the characteristics of the expansion wave generated by the gate will cover the entire region in the $x-t$ diagram between the negative wave traveling up the reservoir and the shock wave traveling down the tank (Stoker (1957)). Thus, the linear force used to normalize the measured force for these two cases is small compared with the rest of the bores, where the wave height represents the maximum height of the incoming bore. This effect of the wave height on the normalized forces can also be seen for the normalized runup in Figure 5.5.2(b), where the results, for the two strongest bore cases tend to lie above the general trend indicated by the rest of the results from the case of the strong turbulent bore.

Of particular interest is the agreement between the maximum forces due to the turbulent bores in the horizontal and tilting wave tanks in Figure 5.5.4(a). For the strongest bores generated in the tilting wave tank, the maximum forces agree quite well with the results from the bores produced by the dam-break method in the horizontal tank. The results corresponding to the smallest bores in the tilting tank are slightly above the horizontal wave tank results. Since the smallest bores in the tilting wave tank entrained much less air than the stronger bores, this may have resulted in larger effective fluid density for those experiments. This would naturally contribute to a larger force on the wall and may explain the tendency of the smallest bore force data to lie above the corresponding results from the horizontal tank, where all the wave heights were large enough to entrain significant amounts of air. The smallest waves in the tilting wave tank were about 2.2 cm high, while the bores in the horizontal wave tank at the same relative wave heights were about 12 cm high. Even though the range in wave heights is nearly an order of magnitude, the results all collapse in Figure 5.5.4(a). This indicates scale effects on the maximum measured force are probably small, although some limited large scale

tests would be useful to determine if scale effects for wave height heights larger than 10 cm exist.

The maximum measured force was normalized by the hydrostatic force computed from the maximum measured runup height on the wall, and plotted in Figure 5.5.4(b). This figure is intended to show that no maximum forces were measured which exceed the hydrostatic force computed using the maximum runup height on the wall. For all the turbulent bore cases, except for a few to be discussed below, the maximum measured force was limited to less than about 60% of the hydrostatic force, due to the maximum measured runup on the wall. The solid diamond corresponding to the largest undular bore obtained in this study caused a relative force of 0.8 due to the impact of the third wave crest (see Figure 5.2.5(b)) which broke on the structure. The open square corresponding to the same relative force was caused by a wave with an unusually small runup height as did the smallest bores in the tilting wave tank study. This is most likely the reason why these data lie above the rest in Figure 5.5.4(b).

Figures 5.5.5(a) and (b) show the maximum measured moment on the wall as a function of the relative incident wave height. The overall comments made about the forces shown in Figures 5.5.4(a) and (b) also apply to the moments shown in Figure 5.5.5. The moving hydraulic jump reflection theory tends to under-predict the envelope formed by the maximum measured moments by about 50% for bores with relative wave heights of the order of unity, and by about 60% for bores with relative wave heights equal to about 10. As with the forces shown in Figure 5.5.4(b), the maximum measured moment never exceeded the hydrostatic moment calculated from the maximum measured runup height on the wall. The solitary wave results agree with the third order theory of Su and Mirie (1980), reported by Grilli and Svendsen (1991), up to the largest solitary wave obtained in this study.

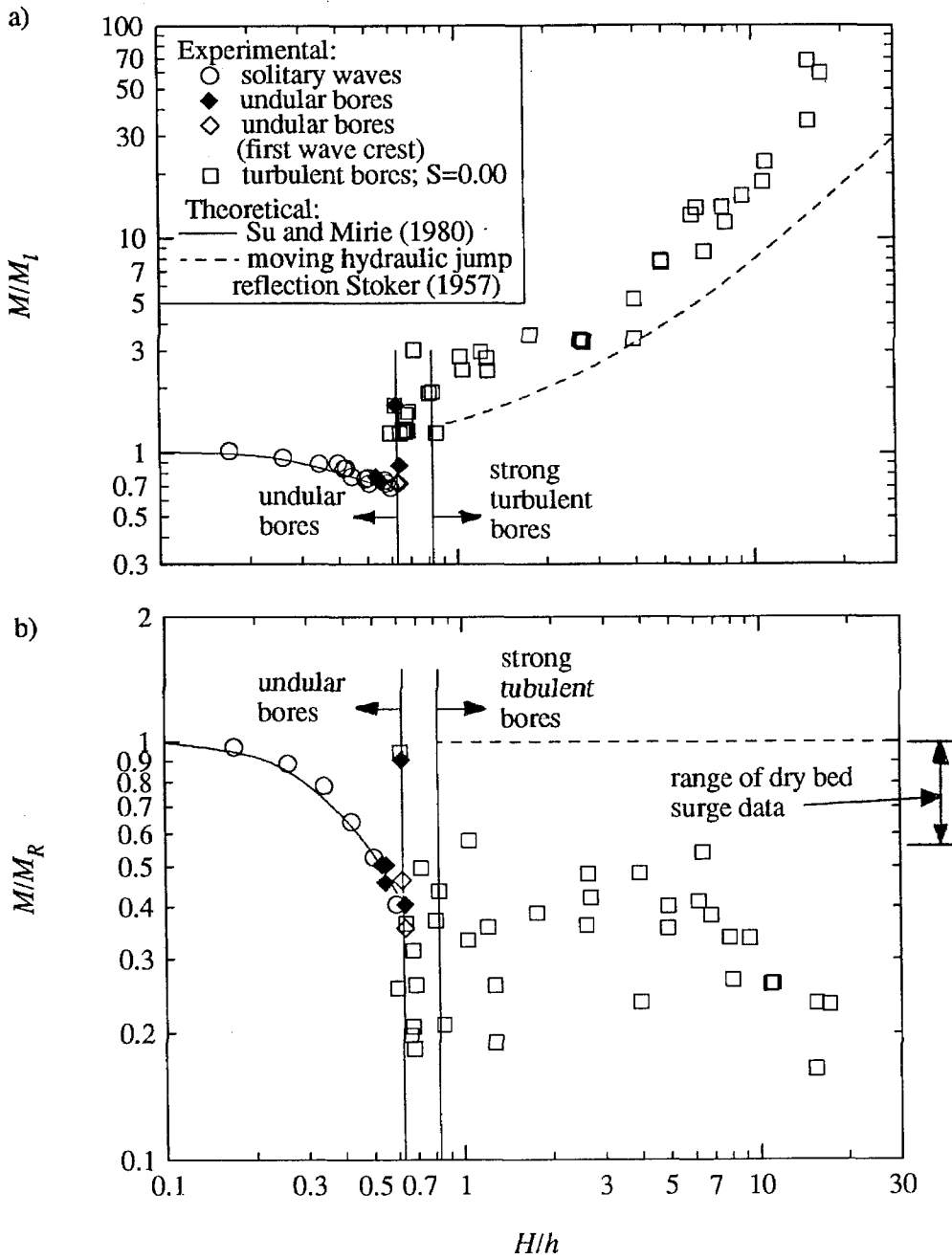


Figure 5.5.5 Experimental and theoretical maximum moment on the wall normalized by (a) the hydrostatic moment due to a runup equal to twice the incident wave height; (b) the hydrostatic moment due to the maximum runup.

The maximum measured force in general, did not always occur at the same time as the maximum measured moment. This is especially true near the transition from steep undular bores to turbulent bores. For steep undular bores and solitary waves, the maximum force and moment occurs before the maximum runup on the wall. For turbulent bores, the maximum force and moment occurred after the maximum runup. In the transition between these two wave types, there are cases where the maximum force and moment occur before and after the maximum runup. However, the error in calculating the moment arm as the maximum moment divided by the maximum force is very small in most cases. This error may be quite small for the cases where the maximum force and moment occur before and after the maximum runup. When this occurs, the force before and after the maximum runup is nearly equal, as is the moment.

5.6 Application to the 1960 Chilean Tsunami at Hilo, Hawaii

In this section, the results of this study are applied to the tsunami bore which developed in Hilo Bay, Hawaii early on the morning of Monday, May 23, 1960. Eaton, Richter, and Ault (1961) describe eye-witness accounts of the bore by a team of observers from the U. S. Geological Survey Volcano Observatory. This team was stationed just north of the Wailuku River on the western edge of Hilo Bay. They were able to record the rise and fall of the water surface against a bridge pier marked with reference points. Their vantage point provided a clear view of the entire bay from the terminus of the breakwater at the mouth of the bay, to the town of Hilo on the southern edge of the bay.

Just after midnight, the USGS group noted the arrival of the tsunami as a rise in the water level of 1.2 m, followed by a trough of -0.9 m. The second wave crested at 2.7 m approximately 33 minutes after the first wave, and this was followed by a trough which resulted in a -2.1 m water elevation. The third wave formed a bore which had a

wave height of 6.1 m at the bridge pier on the north side of the Wailuku River. It took the bore approximately two and one half to three minutes to travel the 2100 m from the tip of the breakwater to the shoreline along the town of Hilo (Eaton et al. (1961)). This gives an average velocity for the bore of about 12.7 m/sec.

The bathymetry of Hilo Bay is very mild and depths relative to mean lower low water extend to about 18 m near the mouth of the bay. From Figure 6 in Eaton et al. (1961), the 20 ft. (6 m) depth contour parallels the shoreline and is located about 400 m offshore along the town of Hilo between the mouths of the Wailuku and Wailoa Rivers. This gives an estimate of the beach slope of about 0.015 m/m which is slightly less than the slope of 0.02 m/m used in the tilting wave tank study.

Suppose for the purposes of this example, the vertical wall shown in Figure 5.6.1 was located on a beach slope of 0.015 m/m and has a depth of 3 m corresponding to

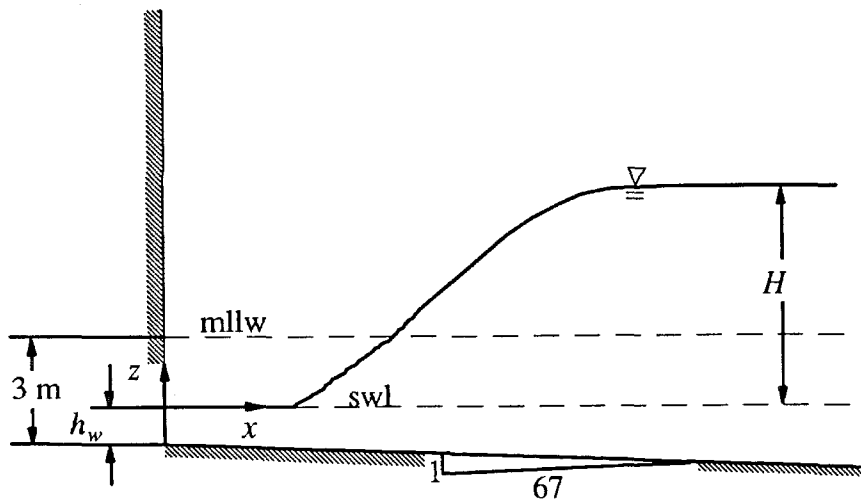


Figure 5.6.1 Schematic drawing for the impact of the 1960 Chilean Tsunami on a vertical wall at Hilo, Hawaii.

mean lower low water (mllw). Due to the trough of the second tsunami wave (-2.1m) reported by Eaton et al. (1961), the depth at the wall, h_w , corresponding to the still water

level (swl) shown in Figure 5.6.1 would be 0.9 m. Assume the 6.1 m bore reported by Eaton et al. (1961) is about to impinge on the wall.

The comparison between the bore results in the tilting and horizontal wave tanks indicate a reasonable definition of the effective water depths for a bore on a mild beach is the depth three horizontal length scales, l , behind the tip of the bore. In this example, it is assumed the wave height and the water depth at the wall are known and that the beach slope is uniform in front of the wall. To calculate the effective depth, an initial guess of the maximum water surface slope, $\|d\eta/dx\|$, must be made, which in this case will be taken as 0.3. This gives a length scale of $l = H/\|d\eta/dx\| = 20.3$ m for the 6.1 m high bore. The effective depth, $3l$ behind the tip of the bore as it strikes the wall would be:

$$h = h_w + 3lS \quad (5.6.1)$$

which is 1.8 m with a beach slope of $S = 0.015$ m/m. Thus, the first estimate of the relative wave height, H/h , is 3.4. At this point, the accuracy of the guess for the wave slope should be checked against the experimental measurement shown in Figure 5.5.2(a). A wave slope of 0.3 for a relative wave height of 3.4 agrees with the results from the bores in both the horizontal and tilting wave tanks in Figure 5.5.2(a). For other relative heights, it is recommended the wave slopes from the horizontal wave tank be used for making these calculations.

With the relative wave height, H/h , based on the effective water depth, h , Figures 5.5.2(b), 5.5.4(a), and 5.5.5(a) can be used to obtain the maximum runup, force, and overturning moment about the base of the wall due to the wave reflection. To dimensionalize the results, the linear force and moment scales, F_l and M_l , should be computed using the water depth, h_w , at the wall. Using the top of the envelope formed

by the experimental data, the relative runup, $R/2H$, from Figure 5.5.2(a), with $H/h = 3.4$, is 2.6. This corresponds to a dimensional runup of 32 m. The maximum relative force on the wall, F/F_l , can be obtained from the top of the envelope formed by the data in Figure 5.5.4(a) which is 3.1 for a relative wave height of 3.4. The linear force scale corresponding to a wave height of 6.1 m and a depth of 0.9 m at the wall is 840 KN/m. Thus, the maximum force on the wall would be 3.1 times this value, which is 2.6 MN/m. To put this load into perspective, a force of 2.6 MN/m is about two and a half times the weight of a 100 metric ton locomotive. The maximum relative overturning moment on the wall can be obtained from Figure 5.5.5(a), from the envelope through the top of the data, which gives $M/M_l = 6.3$. The linear moment scale for this case is 3.7 MNm/m. Therefore, the maximum overturning moment about the base of the wall would be 23.1 MNm/m.

Suppose the effective height 3 l behind the tip of the bore were not used in the computation of the force and moment. The depth would then be taken as the depth at the wall, $h_w = 0.9$ m. With a wave height, H , equal to 6.1 m, the relative wave height, H/h , is 6.8, which gives force, F_l , and moment, M_l , scales of 0.84 MN/m and 3.7 MNm/m, respectively. From Figures 5.5.2(c), 5.5.4(a), and 5.5.5(a) with $H/h = 6.8$, the relative runup (Rg/c^2), force (F/F_l), and moment (M/M_l) are 3.6, 4.9, and 15.4, respectively. This gives a dimensional runup, force, and moment of 43 m, 4.1 MN/m, and 57 MNm/m, which are 34%, 58%, and 146% greater than the values obtained using the effective depth, respectively. Therefore, the effective depth should be used for bores on mild slopes when estimating the force using these laboratory results.

Froude scaling can be used to calculate the time duration over which the maximum force would be applied to the prototype structure. The non-dimensional duration of the maximum force for $H_o/h_o = 0.288$ in Figure 5.1.10(c) (i.e., run TB109)

is about unity. From Appendix A, the time scale for run TB109 can be determined and is 0.14 sec. Thus, the maximum force occurs for about 0.14 sec. Scaling this time to the prototype scale using Froude scaling (with model and prototype wave heights of 0.046 m and 6.1 m, respectively) gives a duration of 1.6 sec. A typical structure would have to resist this load statically (i.e., the dynamics of the structure are relatively unimportant and the loading could not be resisted with the inertia of the structure itself).

There are several points which should be discussed regarding this example. If the width of the wall is of the order of the wave height, then three-dimensional effects would become important. Three-dimensional effects would decrease the pressures and the runup height near the lateral edges of the wall, relative to a pure two-dimensional problem. If the wall is sufficiently narrow, these three-dimensional effects can extend to the center of the wall. If the width of the wall is much smaller than the wave height, then the wave will pass the wall without generating a reflected wave, and the loading imposed on the structure would be similar to a hydrodynamic drag force. If the height of the wall is less than the maximum runup height, some over-topping can be expected. However, significant over-topping will only occur if the height of the wall is less than the hydrostatic water level left at the wall once the reflection is completed. Using the theory of Stoker (1957) to calculate the resulting hydrostatic level for this case gives a total depth in front of the wall of 19.2 m. If the height of the wall is less than the maximum runup height, not only would overtopping occur, but the resulting force on the wall would also be less. With the relative wave height based on the effective depth, the celerity of the surge can be calculated from the expression for a moving hydraulic jump (Stoker (1957)) when the wave height and effective water depth are used, which gives $c = 14.4$ m/s. This is slightly higher than the average celerity, 12.7 m/s, computed from the time it took the wave to travel from the breakwater to the town of Hilo (Eaton et al. (1961)).

6. CONCLUSIONS

The objective of this study has been to investigate the interaction of tsunamis with a vertical wall. The study has been primarily experimental, and included several types of waves in a horizontal tank including solitary waves, bores, and surges propagating on a dry bed, as well as bores in a tilting tank with a 0.02 m/m slope. Various measurements were made, including the incident wave celerity, the wave profile using a high-speed motion picture camera in the tilting tank, and a laser-induced fluorescence system in the horizontal tank, as well as the runup and force time histories in both wave tanks. The overturning moment and the pressure at one vertical station were also measured during the horizontal wave tank experiments. The laser-induced fluorescence system was developed to allow high speed turbulent wave profiles to be measured in a two-dimensional plane. Such measurements are unreliable when using intrusive devices such as wave gages or conventional flow visualization methods with a video or high-speed motion picture cameras. The results of this study were compared with several analytical and numerical models.

Several features of this study are unique with respect to previous research involving tsunami wave impact on a vertical wall. The wave profiles were measured at a two-dimensional plane in the center of the tank with an optical system. The runup history on the wall was measured simultaneously with the force, the overturning moment, and the pressure. In earlier works authors have reported pressure measurements or force measurements, *but no runup time histories*. A wide range of wave conditions were included which essentially cover the full range of relative wave heights for quasi-steady waves. This is the first study to show a comparison of the interaction of bores on a horizontal and a mild slope with a vertical wall. The reason why the maximum force due to bores and steep solitary waves is less than hydrostatic and occurs at a time different

from that of the maximum runup, is explained with both experimental and theoretical results.

The forces and overturning moments presented in this research were obtained by measuring the displacements of a multiple degree of freedom wall through the use of strain gage instrumented force transducers. Thus, the force measurements are not accurate estimates of short duration hydrodynamic loading with time scales of the order, or smaller than, the natural periods of the vibration modes of the wall. The lowest natural frequency of the wall in the horizontal wave tank experiments was 609 Hz which is approximately two orders of magnitude larger than the frequency scales (c/l) associated with the incident wave forms. The force measurements presented here should accurately reflect the hydrodynamic loading with frequency content below approximately 150 Hz. For the higher frequency content, the wall attenuates the force and may not define the true amplitude or duration of the hydrodynamic load. However, for very short duration impact loads, large prototype structures resist failure through their inertia, as does this experimental wall. The maximum measured pressure obtained in this study had very little effect on the displacement of the laboratory wall. Short duration high pressure loads may be more important in brittle failures of individual structural members such as concrete slabs or windows as opposed to catastrophic failures such as sliding or overturning of large structures. Scaling the natural frequency of the laboratory wall in the horizontal tank (613 Hz, with waves heights on the order of 10 cm) to a prototype structure subjected to a tsunami wave (6.1 m wave height for the Hilo tsunami discussed in section 5.6) using Froude scaling, gives a prototype structure having a natural period of 78 Hz. This is probably large relative to the natural periods of most buildings and other large structures. Thus, this laboratory wall in many cases may be at least as stiff as the prototype structure when the laboratory results are scaled to limited prototype conditions.

The following major conclusions may be drawn from this study:

- 1) The boundary integral element model (BIEM) agreed with the experimental measurements for solitary waves with $H/h \leq 0.6$.
- 2) Both the BIEM and the SOLA-VOF models agreed with the measured runup and force time histories on the wall during the reflection of a steep solitary wave ($H/h = 0.504$). Although the SOLA-VOF model over-predicted the water surface slope on the front of turbulent bores, the predicted force time history agreed well with the measured force history except for a short duration large amplitude force which was not *present in the measured force signal*. This large amplitude theoretical force coincided with the arrival of the steepest part of the theoretical wave profile at the wall. Therefore, this peak in theoretical force time history may be much larger than would be obtained if the theoretical and measured wave profiles agreed.
- 3) During the reflection of bores, dry-bed surges, and steep solitary waves at a vertical wall, large vertical accelerations of the fluid occur and reduce the force relative to what it would be if a hydrostatic condition prevailed.
- 4) For all the experimental conditions of this study, the force computed from the maximum measured runup height on the wall, assuming a hydrostatic condition, exceeded the maximum measured force. The same was found for the maximum measured overturning moments.

5) The maximum force occurred either before or after the maximum runup, depending on the relative wave height, due to the vertical accelerations of the fluid along the wall for incident bores, dry-bed surges, and steep solitary waves.

6) The maximum measured relative runup height was 3.8 times the velocity head computed from the wave celerity, and occurred for a bore with a relative wave height of 1.23. For larger and smaller relative wave heights, the relative runup was less than this. The maximum runup on the wall during the tilting tank experiments ranged from 2.0 to 2.6 times the velocity head computed from the incident bore celerity. For the dry bed surges, the maximum measured runup was within 1.46 to 1.62 times the velocity head computed from the incident surge celerity. Assuming a hydrostatic pressure distribution, the maximum measured runup height can be used to calculate conservative estimates of the force and overturning moment on the wall.

7) The maximum water surface slope along the front of the wave exhibited a discontinuity where the slope increased by a factor of 2.5 to 3 across the transition from undular bores to turbulent bores. This discontinuity in the surface slope corresponded to a rapid increase in the maximum measured runup, force, and moment across the transition from undular to turbulent bores. Across this transition, there is very little change in either the celerity or the relative wave height. Therefore, the observed increase in the runup, force, and overturning moment in this transition region, is most likely due to the increase in wave steepness.

8) The forces imposed on a wall due to the impact of bores propagating on a 0.02 m/m sloping beach were equivalent to those produced by bores in a horizontal tank. The maximum measured relative force, F/F_l , obtained from the bores on different beach slopes agree when plotted as a function of H/h , where h is the effective depth three

horizontal length scales ($3 D$) behind the tip of the bore. For bores on any slope, the linear force scale, F_b , must be computed using the ambient depth at the wall which is different from the depth, h , for bores on a sloping beach. This result indicates the forces on vertical walls due to the impact of bores on a mild slope, can be estimated from the impact of bores on slopes less than 0.02 m/m.

9) In the tilting wave tank experiments, all the bores were generated from a breaking solitary wave and the bore profiles at the moment of impact were similar for all cases investigated. The measured water surface velocities near the tip of the bore in the tilting wave tank experiments were slightly larger than the celerity of the bore. This may be caused by the turbulent flow near the tip of the bore which has commonly been referred to as a roller in the open literature.

10) The theory of Whitham (1955) predicted the propagation of the dry bed surges along the tank quite well when the friction coefficient was adjusted to obtain the most favorable agreement in each case.

11) Extending the theory of Whitham (1955) for the surge shape in the tip region over much larger distances behind the tip as was proposed by Whitham, gives reasonable agreement with the measured profiles if the friction coefficient is adjusted to obtain the most favorable agreement in each case. The fact that the adjusted friction factor was different from that used for the propagation speed, indicates the theory does not fully model the physics of the flow for large distances behind the tip.

12) The first wave crest of an undular bore produced runup heights and maximum forces equivalent to those produced by a solitary wave with the same relative

wave height. For very steep undular bores subsequent wave crests may break directly on the wall causing larger impact-type loads.

13) The laser-induced fluorescence method permits accurate wave profiles of high-speed turbulent flows and runup to be obtained with an optical system, eliminating side-wall effects and several difficulties encountered with conventional lighting techniques and intrusive devices such as wave gages.

14) The model of Cross (1967) under-predicted the measured forces due to strong bores and surges on a dry bed by about 30% to 50% of the measured value, while it predicted the maximum measured force due to the bores in the tilting tank experiments within $\pm 22\%$.

Recommendations for future research:

1) All the maximum measured pressures, except for a few runs, were less than the hydrostatic pressure computed from the maximum measured runup height on the wall. All the pressures larger than this hydrostatic value were recorded within one wave height above the still water level. The largest measured pressure head was equal to 23 times the wave height and 8.4 times the velocity head computed from the bore celerity. This appears to be the largest relative pressure reported in the literature, obtained during the impact of bores on a vertical wall. Due to the limited number of experiments, and since only one pressure cell was used, the possibility of significantly larger pressures occurring during the impact of bores is possible and may be an avenue for further study.

2) By observation, there is a significant amount of air entrainment near the tip of the turbulent bores and during the reflection of the dry bed surges at the vertical wall. In

this study the air content was not measured. The amount of air in the flow can decrease both the density and the acoustic velocity of the air-water mixture relative to the values for pure water. A change in the air entrainment will affect the force on the wall since the pressure gradient term in the equation of motion is proportional to the density of the fluid. Since shock pressures are proportional to the speed of sound in the fluid (Von Karman and Wattendorf (1929)), the amount of air entrainment in the flow can affect the amplitude of these pressures if they are produced. Gibson (1970) showed that air content of only one percent by volume can reduce the acoustic velocity by an order of magnitude. Both small scale and large scale laboratory tests are needed with measurements of the air entrainment to determine whether scale effects exist in small scale laboratory model studies.

3) It appears further research using a model, similar to the SOLA-VOF model, to simulate dry bed surges and strong turbulent bores could lead to promising results. An approach where a turbulence model is combined with the SOLA-VOF algorithm may provide a more accurate model of the physics of the flow in the tip region of dry bed surges.

REFERENCES

- Abramowitz, M., and Stegun, I. A. (1970). Handbook of Mathematical Functions with Formulas, Graphs, and Mathematical Tables. Dover Publications, Inc., New York.
- Adam, N. K. (1930). The Physics and Chemistry of Surfaces. Clarendon Press, Oxford, U. K.
- Bagnold, R. A. (1939). "Interim Report on Wave Pressure Research." *J. of the Institution of Civil Engineers*, London, Vol. 12.
- Bakhmeteff, B. A., and Matzke, A. E. (1936). "The Hydraulic Jump in Terms of Dynamic Similarity." *ASCE Trans.* (101),630-653.
- Battjes, J. A. (1988). "Surf-Zone Dynamics." *Ann. Rev. Fluid Mech.*, 20: 257-93.
- Blackmore, P. A., and Hewson, P. J. (1984). "Experiments on Full-Scale Wave Impact Pressures." *Coastal Engineering*, 8: 331 - 346.
- Boussinesq, M. J. (1872). "Theorie des ondes et des remous qui se propagent le long d'un canal rectangulaire horizontal, en communiquant au liquide contenu dans ce canal des vitesses sensiblement pareilles de la surface au fond." *J. Math. Pures Appl.* (2) 17: 55 - 108; transl. A. C. J. Vastano, J. C. H. Mungall, Texas A & M Univ., Ref. 76-2-T (March 1976).
- Brebbia, C. A. (1978). The Boundary Element Method for Engineers. John Wiley and Sons, U.K.

- Bruch, E., Grilli, S, and Lejeune, A. (1986). "Computation of the Fluid Flow in Zoned Anisotropic Porous Media and Determination of the Free Surface Seepage." *In Proc. 8th Intl. Conf. of Boundary Elements*, Tokyo, Japan, (ed. M. Tanaka and C. A. Brebbia), Springer-Verlag, Berlin, 889 - 903.
- Camfield, F. E. (1980). "Tsunami Engineering." *Special Report SR-6*, Dept. of the Army, Coastal Engineering Research Center, Fort Belvoir, Va.
- Chan, E. S., and Melville, W. K. (1988). "Deep-Water Plunging Wave Pressures on a Vertical Plane Wall." *Proc. Roy. Soc. London, A* 417, 95-131.
- Chan, R. K. C., and Street, R. L. (1970). "A Computer Study of Finite Amplitude Water Waves." *J. Comp. Phys.*, 6, 68-94.
- Cooker, M. J., and Peregrine, D. H. (1990). "Violent Water Motion at Breaking-Wave Impact." *Proc. 22nd ICCE*, 12: 164-176.
- Cross, R. H. (1966). "Water Surge Forces on Coastal Structures." *Tech. Report No. HEL-9-10*, College of Engineering, Univ. of California, Berkeley, Calif.
- Cross, R. H. (1967). "Tsunami Surge Forces." *J. Wtrwys. and Harb. Div.*, ASCE, 93(4), 201-231.
- Cumberbatch, E. (1960). "The Impact of a Water Wedge on a Wall." *J. Fluid Mech.*, 7(3), 353-373.

Daily, J. W., and Harleman, D. R. F. (1966). Fluid Dynamics. Addison-Wesley Publishing Company, Inc., Reading, Mass.

Daily, J. W., and Stephan, S. C. (1952). "The Solitary Wave: Its Celerity, Profile, Internal Velocities and Amplitude Attenuation in a Horizontal Smooth Channel." *Proc. 3rd Conf. Coastal Eng.*, 13-30.

Dean, R. G., and Ursell, F. (1959). "Interaction of a Fixed, Semi-Immersed Circular Cylinder with a Train of Surface Waves." *Technical Report No. 37*, Massachusetts Institute of Technology, Hydrodynamics Laboratory, Department of Civil and Sanitary Engineering.

De Boor (1978). A Practical Guide to Splines. Springer-Verlag, New York, 392.

Dold, J. W., and Peregrine, D. H. (1984). "Steep Unsteady Water Waves: An Efficient Computational Scheme." *In Proc. 19th Intl. Conf. on Coastal Engineering*, Houston, USA, 955-967.

Dressler, R. F. (1952). "Hydraulic Resistance Effect Upon the Dam-Break Functions." *J. Research Nat. Bur. Standards*, 49 (3), 217-225.

Eaton, J. P., Richter, D. H., and Ault, W. U. (1961). "The Tsunami of May 23, 1960 on the Island of Hawaii." *Bull. Seism. Soc. Am.*, 51(2), 135-157.

Fenton, J. D., and Reinecker, M. M. (1982). "A Fourier Method for Solving Nonlinear Water-Wave Problems: Application to Solitary-Wave Interactions." *J. Fluid Mech.*, 118: 411 - 443.

- French, J. A., (1969). "Wave Uplift Pressures on Horizontal Platforms." *Ph.D. Thesis*, Environmental Engineering Laboratory, California Institute of Technology, Pasadena, California.
- Fujima, K., and Shuto, N. (1990). "Formulation of Friction Laws for Long Waves on a Smooth Dry Bed." *Coastal Engineering*, 33 (1), 25-47.
- Fukui, Y., Nakamura, M., Shiraishi, H., and Sasaki, Y. (1963). "Hydraulic Study on Tsunami." *Coastal Engineering. Japan*, 6, 67-82.
- Gibson, F. W. (1970). "Measurement of the Effect of Air Bubbles on the Speed of Sound in Water." *J. Acoustic Soc. Am.*, 48(5), 1195-1197.
- Goring, D. G. (1979). "Tsunamis - The Propagation of Long Waves onto a Shelf." *Report No. KH-R-38*, W. M. Keck Laboratory of Hydraulics and Water Resources, California Institute of Technology, Pasadena, California.
- Green, F. J. (1990). The Sigma-Aldrich Handbook of Stains, Dyes, and Indicators. Aldrich Chemical Co., Milwaukee, WI.
- Grilli, S. and I. A. Svendsen (1991). "The Runup and Reflection of Solitary Waves on Steep Slopes." *Report No. CACR091-03*, Center for Applied Coastal Research, University of Delaware, Newark, Delaware.
- Grilli and Svendsen (1992). Personal communication.

Grilli, S. T., Skourup, J., and Svendsen, L. A. (1989). "An Efficient Boundary Element Method for Nonlinear Water Waves." *Engineering Analysis*, 6(2), 92-107.

Hammack, J. L. (1972). "Tsunamis - A Model of their Generation and Propagation." *Ph.D. Thesis*, W. M. Keck Laboratory of Hydraulics and Water Resources, California Institute of Technology, Pasadena, California.

Hammack, J. L., and Segur, H. (1978). "Modeling Criteria for Long Water Waves." *J. Fluid Mech.*, 84 (2), 359-373.

Harlow, F. H., and Welsh, J. E. (1965). "Numerical Calculation of Time-Dependent Viscous Incompressible Flow of Fluid with Free Surface." *Phys. Fluids*, 8: 2182

Heinrich, P. (1992). "Nonlinear Water Waves Generated by Submarine and Aerial Landslides." *J. Waterway, Port, Coastal, and Ocean Engineering*, 118 (3): 249 -266.

Hildebrand, F. B. (1974). Introduction to Numerical Analysis. Second Edition, Dover Publications, Inc., New York.

Ho, D. V., and Meyer, R. E. (1962). "Climb of a Bore on a Beach. Part I. Uniform Beach Slope." *J. Fluid Mech.*, 14: 305 - 318.

Horikawa, K. (1978). Coastal Engineering: An Introduction to Ocean Engineering. Halsted Press, John Wiley and Sons, New York.

Keller, H. B., Levine, D. A., and Whitham, G. B. (1960). "Motion of a Bore over a Sloping Beach." *J. Fluid Mech.*, 7(2), 302-316.

Keulegan, G. H. (1948). "Gradual Damping of Solitary Waves." *J. Res. Natl. Bur. Stand.*, 40: 487 - 498.

Keulegan, C. H. (1950). "Wave Motion." *Engineering Hydraulics*, H. Rouse, ed., John Wiley, New York, NY, 711-768.

Korteweg, D. J., and De Vries, G. (1895). "On the Change of Form of Long Waves Advancing in a Rectangular Canal, and on a New Type of Long Stationary Wave," *London, Edinburgh, and Dublin Philosophical Magazine*, 5(39): 422 - 443.

Liggett, J. A., and Liu, P. L.-F. (1984). "Application of Boundary Element Methods in Fluid Mechanics." *Topics in Boundary Element Research*, Springer-Verlag, Berlin, 1(4).

Longuet-Higgins, M. S., and Fenton, J. D. (1974). "On the Mass, Momentum, Energy, and Circulation of a Solitary Wave." *Proc. Roy. Soc. London A.*, 340, 471-493.

Longuet-Higgins, M. S., and Cokelet, E. D. (1976). "The Deformation of Steep Surface Waves on Water - I. A Numerical Method of Computation." *Roy. Soc. Lond. A*, 350, 1-26.

Madsen, P. A., and Svendsen, I. A. (1983). "Turbulent Bores and Hydraulic Jumps." *J. Fluid Mech.*, 129, 1-25.

Matlock, H., Reese, L., and Matlock, R. (1962). "Analysis of Structural Damage from the 1960 Tsunami at Hilo, Hawaii." *Report DASA-1268*, Struct. Mech. Res. Lab., Univ. of Texas, Austin, Tex.

- Miles, J. W. (1980). "Solitary Waves." *Ann. Rev. Fluid Mech.*, 12: 11-43.
- Naheer, E. (1976). "Stability of Bottom Armoring Under the Attack of Solitary Waves." W. M. Keck Laboratory of Hydraulics and Water Resources, *Report No. KH-R-34*, California Institute of Technology, Pasadena, California.
- Nakamura, S., and Tsuchiya, Y. (1973). "On Shock Pressure of Surge on a Wall." *Bull. Disaster Prevention Res. Inst.*, Kyoto Univ., 23, Parts 3-4, No. 12, 47-58.
- Nichols, B. D., Hirt, C. W., and Hotchkiss, R. S. (1980). "SOLA-VOF: A Solution Algorithm for Transient Fluid Flow with Multiple Free Boundaries." *Report LA-8355*, Los Alamos Scientific Laboratory, University of California, Los Alamos, New Mexico.
- Partenscky, H. W. (1988). "Dynamic Forces Due to Waves Breaking at Vertical Coastal Structures." *21st ICCE*, 186: 2504-2518.
- Peregrine, D. H. (1966). "Calculations of the Development of an Undular Bore." *J. Fluid Mech.*, 25: 321-330.
- Peregrine, D. H. (1967). "Long Waves on a Beach." *J. Fluid Mech.*, 27: 815-827.
- Peregrine, D. H. (1983). "Breaking Waves on Beaches." *Ann. Rev. Fluid Mech.*, 15: 149-178.
- Peregrine, D. H., and Svendsen, I. A. (1978). "Spilling Breakers, Bores, and Hydraulic Jumps." *16th ICCE*, 30: 540-550.

Raichlen, F. (1965). "Wave-Induced Oscillations of Small Moored Vessels." *Report No. KH-R-10*, W. M. Keck Laboratory of Hydraulics and Water Resources, California Institute of Technology, Pasadena, California.

Ramsden, J. D., and Raichlen, F. (1990). "Forces on Vertical Wall Caused by Incident Bores." *J. Waterway, Port, Coastal, Ocean Engr.*, 116 (5), 592-613.

Rienecker, M. M., and Fenton, J. D. (1981). "A Fourier Approximation Method for Steady Water Waves." *J. Fluid Mech.* 104: 119-137.

Ritter, A. (1892) "Die fortpflanzung der wasserwellen." *Zeitschrift des Vereines Deutscher Ingenieure*, 36 (24): 947 - 954.

Rouse, H. (1950). "Engineering Hydraulics." *Proc. 4th Hydr. Conf.*, Iowa Institute of Hydraulic Research, John Wiley and Sons, Inc., New York.

Sandover, J. A., and Zienkiewicz, O. C. (1957). "Experiments on Surge Waves." *Water Power*, November 1957, 418-424.

Schlichting, H. (1979). Boundary-Layer Theory. McGraw Hill Book Co, New York.

Shen, M. C., and Meyer, R. E. (1963). "Climb of a Bore on a Beach. Part 3: Run-up." *J. Fluid Mech.*, 16(1), 113-125.

Silvester (1974). "Effect of Waves on Structures." *Coastal Engr.*, American Eseevier Publ. Co., 8, 371-435.

Skjelbreia, J. E., (1987). "Observations of Breaking Waves on Sloping Bottoms by use of Laser Doppler Velocimetry." *Report No. KH-R-48*, W. M. Keck Laboratory of Hydraulics and Water Resources, California Institute of Technology, Pasadena, California.

Sobey, R. J., and Dingemans, M. W. (1992). "Rapidly Varied Flow Analysis of Undular Bore." *J. Waterway, Port, Coastal, Ocean Engr.*, 118 (4), 417-436.

Stoker, J. J. (1957). Water Waves; the Mathematical Theory With Applications. Interscience, New York.

Stroud, A. H., and Secrest, D. (1966). Gaussian Quadrature Formulas. Prentice-Hall International Inc., London.

Su, C. H., and Mirie, R. M. (1980). "On Head-on Collisions Between Two Solitary Waves." *J. Fluid Mech.*, 98 (3), 509-525.

Svendsen, I. A., and Madsen, P. A. (1984). "A Turbulent Bore on a Beach." *J. Fluid Mech.*, 148, 73-96.

Tanaka, M. (1986). "The Stability of Solitary Waves." *Phys. Fluids*, 29 (3), 650-655.

Ting, F. C. K. (1989). "Interaction of Water Waves with a Density-Stratified Fluid in a Rectangular Trench." *Ph. D. Thesis*, W. M. Keck Laboratory of Hydraulics and Water Resources, California Institute of Technology, Pasadena, California.

- Togashi, H. (1986). "Wave Force of Tsunami Bore on a Vertical Wall." *Report of The Faculty of Engineering, Nagasaki University*, 16 (26), 73-80.
- Torrey, M. D., Cloutman, L. D., Mjoisness, R. C., and Hirt, C. W. (1985). "NASA-VOF2D: A Computer Program for Incompressible Flows with Free Surfaces." *Report LA-10612-MS*, Los Alamos National Laboratory, Los Alamos, New Mexico.
- U. S. Army Corps of Engineers (1984). Shore Protection Manual, Coastal Engineering Research Center, Waterways Experiment Station, Vicksburg, Mississippi, Chapter 7.
- Vinje, T., and Brevig, P. (1981). "Numerical Simulation of Breaking Waves." *Adv. Water Resources*, 4, 77-82.
- Von Karman, T., and Wattendorf, F. L. (1929). "The Impact on Seaplane Floats during Landing." *Tech. Note No. 321*, Nat. Advisory Committee for Aeronautics, Washington, DC., 309-313.
- Wang, J. D., and Ansari, H. R. (1986). "Dynamics of Surge Run-up on Dry Bed." *Internal Report*, Division of Applied Marine Physics, Rosentiel School of Marine and Atmospheric Science, University of Miami.
- Weast, R. C. (1985). CRC Handbook of Chemistry and Physics. CRC Press, Boca Raton, Florida.
- Weggel, J. R., and Maxwell, W. H. C. (1970). "Numerical Model for Wave Pressure Distributions." Preprint Volume of the Offshore Technology Conf., *Paper No. OTC 1244*.

- Whitham, G. B. (1955). "The Effects of Hydraulic Resistance on the Dam-Break Problem." *Proc. of the Royal Society, Ser. A*, 227: 399 - 407.
- Whitham, G. B. (1958). "On the Propagation of Shock Waves through Regions of Non-uniform Area or Flow." *J. Fluid Mech.*, 4(4), 337-360.
- Wiegel, R. L. (1955). "Parallel Wire Resistance Wave Meter." *Proc. First Conference on Coastal Engineering Instruments*, Berkeley, California, 39-43.
- Wiegel (1964). "Wave Forces on Vertical Walls." *Oceanograph. Engr.*, Prentice-Hall, 11: 277-298.
- Wiegel, R. L. (1970). "Tsunamis." *Earthquake Engineering*, R. L. Wiegel, ed., Prentice-Hall, Englewood Cliffs, NJ., 253-306.
- Wilkinson, D. L., and Banner, M. L. (1977). "Undular Bores." *6th Australasian Hyd. and Fluid Mech. Conf.*, Adelaide, Australia, 369-373.
- Wilson, B. W., and Torum, A. (1972). "Effects of the Tsunamis: An Engineering Study." *The Great Alaska Earthquake of 1964, Pub. 1605*, Oceanography and Coastal Engrg., Nat. Academy of Sci., Washington DC.
- Yeh, H. H., Ghazali, A., and Marton, I. (1989). "Experimental Study of Bore Runup." *J. Fluid Mech.*, 206, Sep., 563-578.
- Yeung, R. W. (1982). "Numerical Methods in Free Surface Flows." *Ann. Rev. Fluid Mech.*, 14, 395-442.

Zelt, J. A. (1991). "The Run-up of Non Breaking and Breaking Solitary Waves." *Coastal Engineering*, 15: 205-246.

APPENDIX A:

Data tables

Table A.1 shows the initial water depth, h ; the relative wave height, H/h ; the celerity, c ; the maximum water surface slope on the front face of the wave, $\|dn/dx\|$; the maximum runup height with respect to the still water level, $\|R\|$; the height of the pressure transducer above the still water level, z_p ; the maximum measured pressure head, $\|p/\gamma\|$; the maximum measured force per unit width, $\|F/b\|$; and the maximum measured moment per unit width, $\|M/b\|$, for the solitary wave experiments in the horizontal wave tank. The run number designation, H and W in Table A.1, denote the horizontal wave tank and a solitary wave. In Table A.2, S denotes a dry bed surge. In Tables A.3 through A.6, B denotes a bore, and in Table A.6, T denotes the tilting wave tank. The definition of the symbols given for Table A.1 are the same throughout the rest of the tables (A.2 through A.6) unless indicated otherwise.

Table A.1. Solitary wave data (horizontal tank)

| run No. | h (cm) | H/h (cm) | c (cm/sec) | $\ dn/dx\ $ | $\ R\ $ (cm) | z_p (cm) | $\ p/\gamma\ $ (cm) | $\ F/b\ $ (N/m) | $\ M/b\ $ (Nm/m) |
|---------|-------------|---------------|-----------------|-------------|-----------------|---------------|------------------------|--------------------|---------------------|
| HW33 | 17.86 | 0.571 | 164.8 | .250 | ----- | 29.86 | 6.09 | 541.8 | 68.4 |
| HW35 | 17.74 | 0.580 | 164.3 | .264 | ----- | 29.86 | 5.91 | 534.1 | 66.7 |
| HW36 | 17.74 | 0.597 | 164.3 | .269 | 28.74 | 29.86 | 5.89 | 532.6 | 66.5 |
| HW37 | 17.74 | 0.504 | 160.7 | .214 | 22.57 | 29.86 | 4.22 | 479.4 | 56.4 |
| HW38 | 17.74 | 0.492 | 159.6 | .202 | ----- | 29.86 | ----- | 465.8 | 53.9 |
| HW39 | 17.74 | 0.505 | 159.5 | .212 | ----- | 29.86 | 3.83 | 164.8 | 53.8 |
| HW40 | 17.71 | 0.345 | 152.1 | .128 | 13.48 | 29.86 | 0.86 | 380.2 | 39.0 |
| HW41 | 17.71 | 0.260 | 147.5 | .084 | 9.85 | 29.86 | ----- | 327.4 | 30.4 |
| HW42 | 17.71 | 0.172 | 142.5 | .045 | 6.51 | 29.86 | ----- | 270.8 | 22.6 |
| HW43 | 17.53 | 0.416 | 155.4 | .160 | ----- | 29.86 | 2.40 | 417.2 | 46.0 |
| HW43a | 17.53 | 0.424 | 156.3 | .162 | ----- | 29.86 | ----- | ----- | ----- |
| HW43b | 17.53 | 0.399 | 155.4 | .149 | ----- | 29.86 | 2.44 | 418.2 | 45.8 |
| HW44 | 17.53 | 0.442 | 155.5 | .165 | ----- | 29.86 | 2.42 | 418.7 | 45.7 |
| HW45 | 17.46 | 0.424 | 155.8 | .174 | 18.00 | 29.86 | 2.60 | 422.1 | 46.9 |
| HW46 | 17.46 | 0.417 | 155.1 | .170 | 17.28 | 29.86 | ----- | ----- | ----- |

In Table A.2, h_r is the reservoir depth, $\|R_1\|$ is the initial maximum runup height on the wall which occurred within the first second after impact, $\|R_2\|$ is the absolute maximum runup which occurred on the order of about 5 seconds after impact and for the dry bed surges, z_p is measured from the bottom of the wave tank. The runup heights, R_1 and R_2 were discussed in Section 5.4 and defined in Figure 5.4.10(c). The window length, l_w , over which the maximum water surface slope, $\|dn/dx\|$, was calculated, is given in Tables A.2 through A.6.

Table A.2. Dry bed surge data (horizontal tank - measurements during initial impact with the wall)

| run No. | h_r (cm) | c (cm/se c) | l_w (cm) | $\ dn/dx\ $ | $\ R_1\ $ (cm) | $\ R_2\ $ (cm) | z_p (cm) | $\ p/\gamma\ $ (cm) | $\ F/b\ $ (N/m) | $\ M/b\ $ (Nm/ m) |
|---------|---------------|---------------------|---------------|-------------|-------------------|-------------------|---------------|------------------------|--------------------|-------------------------|
| HS60 | 50.92 | 227.7 | 20.0 | .057 | 42.13 | 43.1 | 29.86 | 13.19 | ----- | ----- |
| HS69 | 50.92 | 230.0 | 20.0 | .062 | 43.35 | 43.0 | 17.00 | 13.87 | ----- | ----- |
| HS86 | 50.20 | 229.5 | 20.0 | .064 | 39.70 | 40.9 | 1.79 | 32.45 | 465.4 | 58.4 |
| HS99 | 40.10 | 193.2 | 14.0 | .057 | 28.82 | 33.9 | 1.79 | 26.48 | 342.4 | 32.4 |
| HS100 | 40.07 | 193.1 | 14.0 | .055 | 27.84 | 32.6 | 1.79 | 21.68 | 287.9 | 27.5 |
| HS101 | 15.28 | 87.8 | 3.0 | .086 | 5.91 | 11.3 | 1.79 | 7.38 | ----- | ----- |
| HS102 | 15.28 | 87.8 | 3.0 | .097 | 6.63 | 11.5 | 1.79 | 5.70 | ----- | ----- |
| HS103 | 30.17 | 154.7 | 9.0 | .053 | 19.25 | 24.2 | 1.79 | 15.82 | 135.8 | 11.6 |

Table A.3. Undular bore data (horizontal tank: maximum values during first wave crest)

| run No. | h_r (cm) | h (cm) | H/h (cm) | c (cm/se c) | l_w (cm) | $\ dn/dx\ $ | $\ R\ $ (cm) | z_p (cm) | $\ p/\gamma\ $ (cm) | $\ F/b\ $ (N/m) | $\ M/b\ $ (Nm/ m) |
|---------|---------------|-------------|---------------|---------------------|---------------|-------------|-----------------|---------------|------------------------|--------------------|-------------------------|
| HB68 | 22.96 | 14.28 | 0.548 | 146.8 | 5.0 | .28 | 20.86 | 29.86 | 0.75 | 328.1 | 32.5 |
| HB84 | 64.64 | 13.45 | 0.626 | 144.7 | 3.0 | .31 | 24.36 | 17.00 | 9.72 | 349.2 | 33.1 |
| HB85 | 22.96 | 14.28 | 0.553 | 146.7 | 5.0 | .24 | 19.84 | 17.00 | 9.43 | 328.5 | 32.7 |
| HB109 | 24.64 | 13.45 | 0.639 | 143.8 | 3.0 | .32 | 25.37 | 1.79 | 24.89 | 349.7 | 34.1 |
| HB110 | 22.88 | 14.25 | 0.534 | 146.5 | 5.0 | .24 | 19.69 | 1.79 | 23.04 | 322.8 | 32.3 |

Table A.4. Undular bore data (horizontal tank: absolute maximum values during the entire interaction with the wall)

| run No. | $\ R\ $ (cm) | z_p (cm) | $\ p/\gamma\ $ (cm) | $\ F/b\ $ (N/m) | $\ M/b\ $ (Nm/m) |
|--------------------|-----------------|---------------|------------------------|--------------------|---------------------|
| HB84 ² | 33.01 | 17.00 | 14.14 | ----- | ----- |
| HB84 ³ | 23.73 | 17.00 | ----- | 526.3 | 76.2 |
| HB109 ² | 26.08 | 1.79 | 27.14 | 408.4 | 41.0 |

2.3 The superscript on the run number denotes which wave crest of the undular bore caused the maximum value indicated.

Table A.5. Turbulent bore data (horizontal tank)

| run No. | h_r (cm) | h (cm) | H/h (cm) | c (cm/sec) | l_w (cm) | $\ dn/dx\ $ | $\ R\ $ (cm) | z_p (cm) | $\ p/\gamma\ $ (cm) | $\ F/b\ $ (N/m) | $\ M/b\ $ (Nm/m) |
|---------|---------------|-------------|---------------|-----------------|---------------|-------------|-----------------|---------------|------------------------|--------------------|---------------------|
| HB63 | 41.24 | 4.26 | 2.65 | 191.2 | 15.0 | .28 | 47.01 | 29.86 | 11.68 | 703.7 | 105.7 |
| HB64 | 45.52 | 1.43 | 6.23 | 216.0 | 15.0 | .27 | 59.07 | 29.86 | 13.93 | 820.0 | 149.4 |
| HB65 | 35.95 | 7.73 | 1.21 | 174.9 | 15.0 | .36 | 45.95 | 29.86 | 10.52 | 630.7 | 90.6 |
| HB66 | 30.80 | 10.26 | 0.811 | 160.3 | 10.0 | .38 | 36.15 | 29.86 | 5.14 | 469.2 | 60.7 |
| HB67 | 27.46 | 11.94 | 0.645 | 153.8 | 3.0 | .72 | 29.06 | 29.86 | 1.52 | 399.6 | 41.1 |
| HB70 | 48.01 | .28 | 17.2 | 227.7 | 15.0 | .22 | 62.43 | 17.00 | 20.31 | 662.2 | 94.1 |
| HB71 | 46.51 | .72 | 10.9 | 221.8 | 15.0 | .24 | 66.84 | 17.00 | 23.37 | 733.6 | 131.6 |
| HB72 | 45.40 | 1.10 | 8.08 | 217.0 | 15.0 | .30 | 65.72 | 17.00 | 23.73 | 802.0 | 130.4 |
| HB73 | 45.52 | 1.43 | 6.45 | 204.7 | 15.0 | .29 | 57.17 | 17.00 | 21.83 | 821.0 | 178.0 |
| HB74 | 44.08 | 1.99 | 4.90 | 200.4 | 15.0 | .27 | 58.43 | 17.00 | 23.52 | 799.9 | 128.1 |
| HB75 | 43.99 | 2.83 | 3.97 | 198.0 | 15.0 | .36 | 53.12 | 17.00 | 23.63 | 810.3 | 137.9 |
| HB76 | 41.24 | 4.26 | 2.61 | 184.8 | 15.0 | .38 | 51.68 | 17.00 | 21.08 | 705.9 | 103.3 |
| HB77 | 35.95 | 7.73 | 1.28 | 172.1 | 15.0 | .35 | 56.75 | 17.00 | 20.74 | 620.8 | 83.2 |
| HB78 | 33.77 | 9.07 | 1.05 | 164.3 | 10.0 | .39 | 36.50 | 17.00 | 23.21 | 601.0 | 89.5 |
| HB79 | 30.80 | 10.26 | 0.833 | 159.9 | 10.0 | .56 | 34.58 | 17.00 | 26.06 | 493.1 | 64.3 |
| HB80 | 29.61 | 10.82 | 0.724 | 154.2 | 5.0 | .53 | 37.65 | 17.00 | 29.52 | 525.7 | 92.3 |
| HB81 | 28.56 | 11.40 | 0.691 | 155.4 | 5.0 | .58 | 37.94 | 17.00 | 43.21 | 438.8 | 51.0 |
| HB82 | 27.46 | 11.94 | 0.661 | 153.5 | 3.0 | .85 | 39.65 | 17.00 | 55.00 | 418.9 | 44.3 |
| HB83 | 25.99 | 12.69 | 0.599 | 149.1 | 3.0 | .61 | 34.49 | 17.00 | 17.38 | 417.6 | 43.9 |
| HB87 | 48.01 | .28 | 15.5 | 228.0 | 15.0 | .19 | 66.67 | 1.79 | 43.86 | 616.9 | 80.4 |
| HB88 | 46.72 | .37 | 15.5 | 222.7 | 15.0 | .22 | 62.70 | 1.79 | 46.31 | 604.0 | 96.4 |
| HB89 | 45.64 | .64 | 11.1 | 217.8 | 15.0 | .23 | 65.01 | 1.79 | 116.15 | 732.6 | 121.5 |
| HB90 | 44.55 | .83 | 9.24 | 210.4 | 15.0 | .28 | 57.53 | 1.79 | 61.29 | 657.1 | 109.1 |
| HB91 | 45.40 | 1.10 | 7.90 | 215.3 | 15.0 | .23 | 62.98 | 1.79 | 200.00 | 817.8 | 145.3 |
| HB92 | 45.52 | 1.43 | 6.83 | 212.6 | 15.0 | .27 | 57.98 | 1.79 | 53.60 | 813.2 | 130.7 |
| HB93 | 44.08 | 1.99 | 4.92 | 203.1 | 15.0 | .37 | 55.92 | 1.79 | 38.18 | 769.8 | 127.3 |
| HB94 | 43.99 | 2.83 | 3.97 | 199.5 | 15.0 | .33 | 57.78 | 1.79 | 38.04 | 690.1 | 90.4 |
| HB95 | 42.24 | 4.26 | 2.70 | 188.0 | 15.0 | .31 | 49.85 | 1.79 | 37.40 | 712.5 | 108.9 |
| HB96 | 38.63 | 5.82 | 1.78 | 176.7 | 15.0 | .47 | 49.82 | 1.79 | 34.94 | 695.3 | 109.0 |
| HB97 | 35.95 | 7.73 | 1.28 | 167.6 | 15.0 | .41 | 52.71 | 1.79 | 34.17 | 357.0 | 93.7 |
| HB98 | 33.77 | 9.07 | 1.04 | 164.2 | 10.0 | .53 | 47.63 | 1.79 | 31.86 | 631.1 | 99.5 |
| HB104 | 30.80 | 10.26 | 0.857 | 160.0 | 15.0 | .48 | 40.10 | 1.79 | 29.52 | 422.4 | 43.8 |
| HB105 | 29.61 | 11.68 | 0.686 | 153.5 | 5.0 | .52 | 41.20 | 1.79 | 28.41 | 420.9 | 44.4 |
| HB106 | 28.56 | 11.40 | 0.679 | 155.7 | 5.0 | .57 | 33.93 | 1.79 | 27.85 | 422.9 | 47.8 |
| HB107 | 27.46 | 11.94 | 0.675 | 153.4 | 3.0 | .374 | 39.22 | 1.79 | 27.74 | 425.1 | 45.4 |
| HB108 | 25.99 | 12.69 | 0.623 | 149.2 | 3.0 | .99 | 21.80 | 1.79 | 28.12 | 463.4 | 63.3 |

In Table A.6, H_0/h_0 is the relative solitary wave height 21.39 m from the shoreline and h is the effective depth (between the bottom of the wave tank and the still water level) three horizontal length scales behind the tip of the bore at the instant it strikes the wall. Note that for Runs TB94 through TB105 the relative wave height, H/h ; the celerity, c ; and the maximum water surface slopes $\|d\eta/dx\|$ are the average values from the two corresponding runs (i.e. with the same H_0/h_0) between TB108 and TB119. This is because the movie camera was located to record the runup on the wall and not the incident wave profile (which is needed to obtain H , c , and $\|d\eta/dx\|$) for Runs TB94 through TB105.

Table A.6. Turbulent bore data (tilting tank)

| run No. | H_0/h_0 (cm) | h (cm) | H/h (cm) | c (cm/sec) | l_w (cm) | $\ d\eta/dx\ $ | $\ R\ $ (cm) | $\ F/b\ $ (N/m) |
|---------|-------------------|-------------|---------------|-----------------|---------------|----------------|-----------------|--------------------|
| TB94 | 0.288 | 1.48 | 3.13 | 129.3 | ----- | .33 | 19.04 | 89.8 |
| TB95 | 0.288 | 1.48 | 3.13 | 129.3 | ----- | .33 | 18.61 | 94.8 |
| TB96 | 0.216 | 1.47 | 2.76 | 121.2 | ----- | .25 | 19.31 | 83.1 |
| TB97 | 0.216 | 1.47 | 2.76 | 121.2 | ----- | .25 | 17.66 | 78.7 |
| TB98 | 0.165 | 1.42 | 2.49 | 114.1 | ----- | .24 | 15.18 | 62.1 |
| TB99 | 0.165 | 1.42 | 2.49 | 114.1 | ----- | .24 | 15.33 | 60.1 |
| TB100 | 0.141 | 1.40 | 2.43 | 110.0 | ----- | .24 | 14.00 | 50.3 |
| TB101 | 0.141 | 1.40 | 2.43 | 110.0 | ----- | .24 | 12.95 | 49.1 |
| TB102 | 0.086 | 1.24 | 2.18 | 92.5 | ----- | .22 | 8.66 | 36.7 |
| TB103 | 0.086 | 1.24 | 2.18 | 92.5 | ----- | .22 | 9.95 | 37.9 |
| TB104 | 0.044 | 1.13 | 1.98 | 75.2 | ----- | .22 | 7.54 | 21.7 |
| TB105 | 0.044 | 1.13 | 1.98 | 75.2 | ----- | .22 | 7.63 | 21.8 |
| TB108 | 0.288 | 1.46 | 3.23 | 127.5 | 7.0 | .29 | ----- | 89.4 |
| TB109 | 0.288 | 1.50 | 3.06 | 131.2 | 7.0 | .27 | ----- | 90.8 |
| TB110 | 0.216 | 1.40 | 2.91 | 120.2 | 7.0 | .27 | ----- | 79.4 |
| TB111 | 0.216 | 1.54 | 2.65 | 122.1 | 7.0 | .23 | ----- | 77.5 |
| TB112 | 0.165 | 1.20 | 2.88 | 114.3 | 6.0 | .30 | ----- | 58.4 |
| TB113 | 0.165 | 1.65 | 2.19 | 113.9 | 6.0 | .19 | ----- | 61.2 |
| TB114 | 0.141 | 1.57 | 2.15 | 110.5 | 5.0 | .19 | ----- | 49.6 |
| TB115 | 0.141 | 1.23 | 2.80 | 109.5 | 5.0 | .28 | ----- | ----- |
| TB116 | 0.086 | 1.21 | 2.30 | 93.4 | 5.0 | .24 | ----- | 37.9 |
| TB117 | 0.086 | 1.28 | 2.05 | 91.5 | 5.0 | .20 | ----- | 36.6 |
| TB118 | 0.044 | 1.20 | 1.88 | 76.2 | 3.0 | .19 | ----- | 22.4 |
| TB119 | 0.044 | 1.06 | 2.10 | 74.6 | 3.0 | .24 | ----- | 20.6 |

APPENDIX B:**Calibration of the laser induced fluorescence system**

In this appendix, the calibration method for the laser induced fluorescence system is described. A lucite plate with a 4 cm square grid of control points was placed in the center of the wave tank and recorded with the video camera. The known locations of these control points were used in a least squares analysis to determine the unknown coefficients in two-dimensional polynomial equations. These polynomial equations were used to relate positions in the video image to corresponding locations on a vertical plane in the center of the wave tank.

The video camera records the intensity of light at each location in a two-dimensional array of pixels (i.e., each location in the two-dimensional array is a unique pixel location). Thus, the ordinate and the abscissa in the video image range from unity to 480 for a total of 230,400 pixel locations. For the purposes of this discussion, pixel space will refer to the two-dimensional plane in the video camera where the image is recorded, while physical space will refer to the two-dimensional plane in the wave tank where the image is located. Figure B.1 shows the locations of a 4 x 4 cm grid of control points (on a vertical plane in the center of the wave tank) as recorded with the video camera. In Figure B.1, the abscissa and the ordinate are the horizontal and vertical pixel locations (x_p, z_p) in the video image. The distortion is quite pronounced and increases toward the bottom left corner in Figure B.1, while the intersection of the tank bottom and the vertical wall is located near the lower right corner.

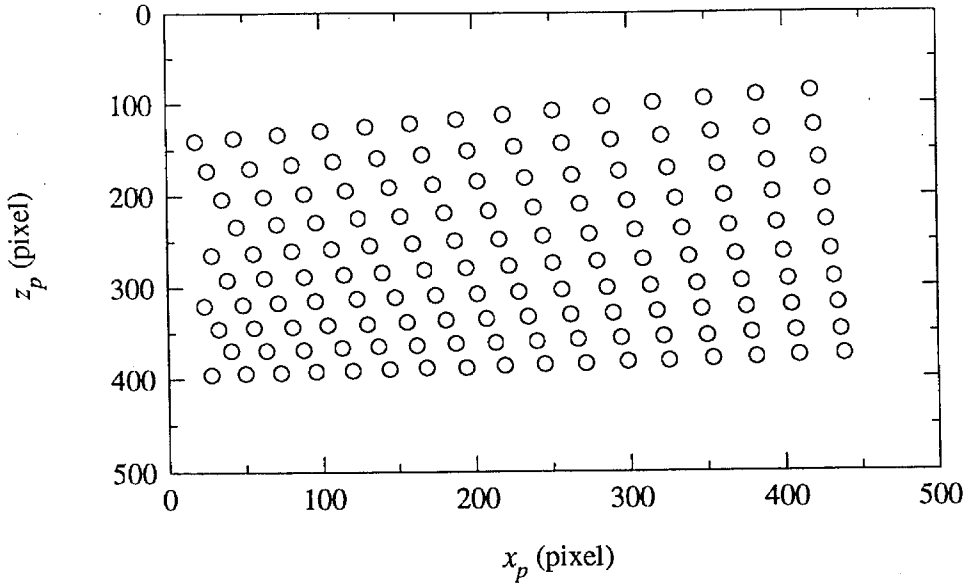


Figure B.1 Distorted view of the control points in the wave tank as seen with the video camera.

The following derivation shows that, neglecting optical distortion due to the camera, the location and orientation of the camera can be modeled as several linear transformations and one nonlinear transformation between the pixel locations, (x_p, z_p) , and the physical locations, (x, z) . Figure B.2 is a schematic drawing which shows the two dimensional plane, (x_v, z_v) , in the video camera and the physical plane in the wave tank, (x, z) , where the air-water interface is located. The coordinates, (x_p, z_p) , in units of pixels, can be related to the coordinates, (x_v, z_v) , in units of length as:

$$\begin{Bmatrix} x_v \\ z_v \end{Bmatrix} = \begin{bmatrix} A_x & 0 \\ 0 & A_z \end{bmatrix} \begin{Bmatrix} x_p \\ z_p \end{Bmatrix} = \mathbf{A} \mathbf{x}_p \quad (\text{B.1})$$

where A_x and A_z are scale factors in units of length/pixel.

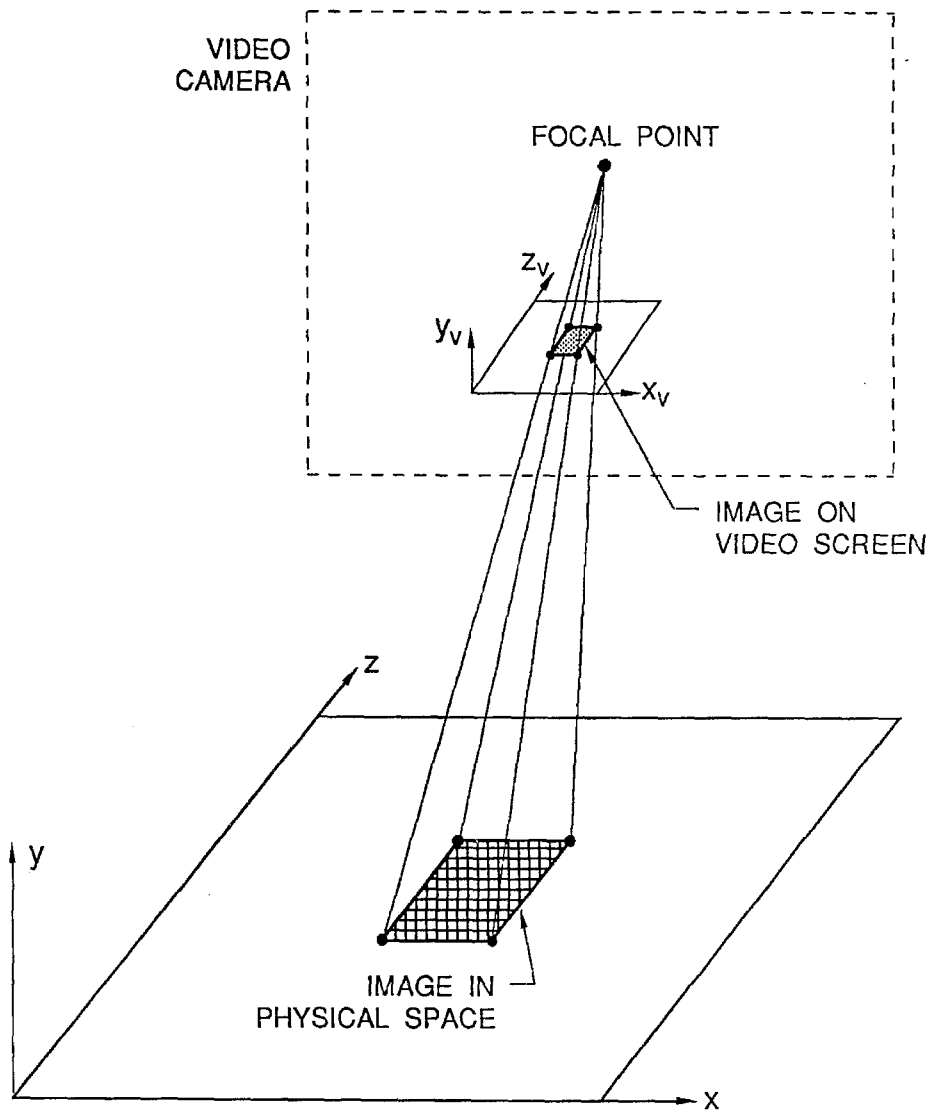


Figure B.2 Definition sketch of the image plane in the video camera and the plane in the center of the wave tank where the air-water surface is located.

In Section 4.2.5, the optimal orientation of the video camera was discussed and shown in Figure 4.2.25. The camera orientation shown in Figure 4.2.25 requires a rotation of the video camera about the x axis of the physical coordinate system. The

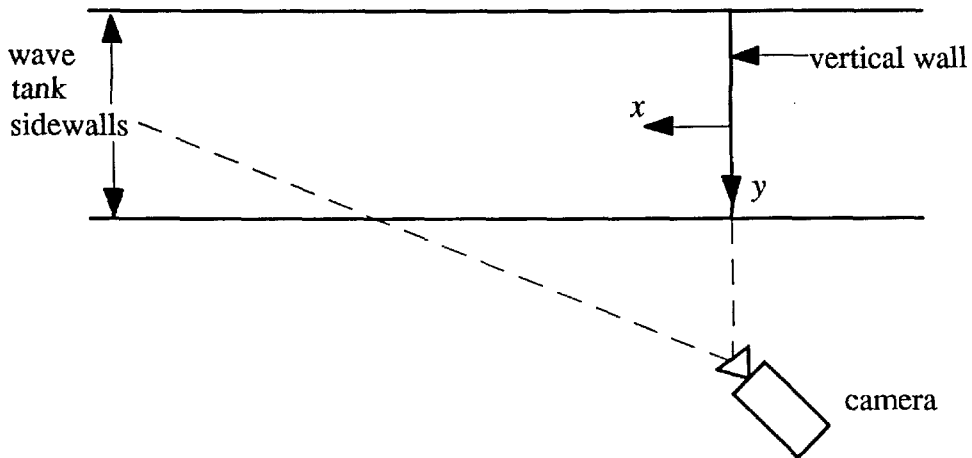


Figure B.3 Schematic of the camera orientation as seen from above the wave tank.

camera was also rotated about the z axis which produced the field of view shown in Figure B.3. The two camera rotations about the z and x axes are equivalent to a rotation of the camera about the z' axis of a new coordinate system. The y' axis in the new coordinate system (x', z', y') is parallel to the y axis in the (x, z, y) coordinate system. However, the new coordinate system is rotated about the y axis through an angle θ so the camera rotations about the z and x axes (shown in Figures 4.4.25 and B.3) are equivalent to a single rotation of the camera about the z' axis. The resulting geometry for a camera rotation through an angle, α , about the z' axis is shown in Figure B.4, where a relation between the distance, x_{v1} , on the video plane, and x'_1 in the physical plane must be determined. In Figure B.4, the angle γ is

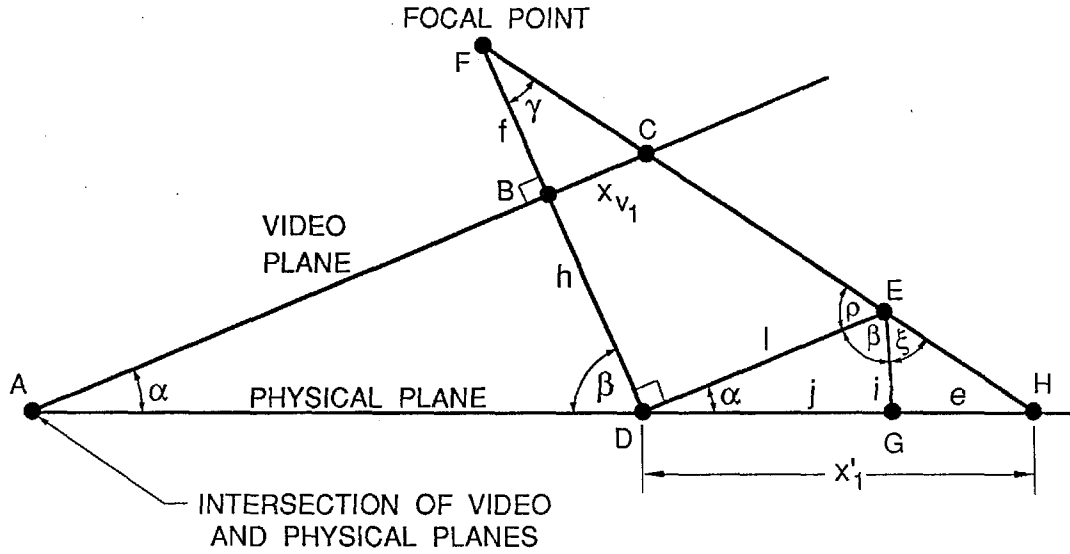


Figure B.4 Definition sketch showing the relationship between distances in the video image and the plane in the wave tank for an oblique camera orientation.

$$\gamma = \tan^{-1}\left(\frac{x_{v1}}{f}\right), \quad (\text{B.2})$$

the distance, l , between points D and E is

$$l = x_{v1}\left(\frac{h+f}{f}\right), \quad (\text{B.3})$$

and the distance, i , between points E and G is

$$i = l \sin \alpha. \quad (\text{B.4})$$

Since $\beta = \pi/2 - \alpha$ and $\rho = \pi/2 - \gamma$, the angle, ξ , can be expressed as:

$$\xi = \pi - \rho - \beta = \alpha + \gamma, \quad (\text{B.5})$$

and the distances e , j , and x'_1 can be expressed as:

$$e = i \tan \xi, \quad j = l \cos \alpha, \quad \text{and } x'_1 = j + e. \quad (\text{B.6})$$

After substituting Equations B.2 through B.5 into Equation B.6 and simplifying, the following relationship between x'_1 and x_{v1} can be obtained:

$$x'_1 = x_{v1} \left(\frac{h+f}{f} \right) \left(\cos \alpha + \sin \alpha \tan \left(\alpha + \tan^{-1} \left(\frac{x_{v1}}{f} \right) \right) \right). \quad (\text{B.7})$$

Using the trigonometric identity for the tangent of a sum while letting $((h+f)/f) \cos \alpha = a$ and $(\tan \alpha)/f = b$, gives:

$$x'_1 = ax_{v1} + af^2b^2 \left(\frac{x_{v1}}{1-bx_{v1}} \right) + ab \left(\frac{x_{v1}^2}{1-bx_{v1}} \right). \quad (\text{B.8})$$

In Equation B.8, the two terms in parentheses become singular for $bx_{v1} = 1$ (i.e., $\tan \alpha = f/x_{v1}$). However, f/x_{v1} is equal to the tangent of $\angle BCF$ in Figure B.4. Figure B.4 shows that if $\angle BCF$ is equal to α , then the point H will be located at infinity in the x' direction. When looking through the video camera, infinity in the x' direction is the horizon. When $-1 < -bx_{v1} < 1$, the two terms in parentheses in Equation B.8 can be expanded as power series in x_{v1} and combined, which after some simplification gives:

$$x'_1 = a_1 x_{v1} + a_2 \left(\frac{x_{v1}^2}{1 - b x_{v1}} \right) \quad (\text{B.9})$$

where all the constant parameters including f , a , and b were absorbed into the new coefficients a_1 and a_2 . In Equation B.9, the second term on the right hand side can be approximated as the first few terms of the power series expansion, provided the term $|b x_{v1}| \ll 1$.

The relationship between a position on the video image in the z_v direction and the corresponding location z' in the physical plane depends on both the z_v and x_v coordinates. The relationship between z' and the location in the video plane is much more complicated than the relationship for x' shown in Equation B.9. Using similar triangles, the relationship between z'_1 and z_{v1} can be shown to be:

$$z'_1 = z_{v1} \left(\frac{(f+h)^2 + a_1^2 x_{v1}^2 + a_2^2 x_{v1}^4 / (1 - b x_{v1})}{f^2 + x_{v1}^2} \right), \quad (\text{B.10})$$

where f and h were defined in Figure B.4 and the coefficients a_1 , a_2 , and b were defined in connection with Equation B.9. The terms in the relationship for z'_1 in Equation B.10 can be expanded in a power series in terms of x_{v1} . Since the equations governing the relationship between the locations in the video plane and the physical plane (Equations B.9 and B.10) can be expanded in power series, the distortion caused by the oblique video image was modeled with two-dimensional polynomial equations.

The rotated coordinates, (x', z') , can be related to the physical plane coordinates, (x, z) , with a rotation and an offset relative to the (x, z) plane as follows:

$$\mathbf{x} = \begin{Bmatrix} \delta_x \\ \delta_z \end{Bmatrix} + \begin{bmatrix} \cos\theta & -\sin\theta \\ \sin\theta & \cos\theta \end{bmatrix} \mathbf{T}_N \mathbf{A} \mathbf{x}_p = \mathbf{D} + \mathbf{T}_\theta \mathbf{T}_N \mathbf{A} \mathbf{x}_p, \quad (\text{B.11})$$

where $\mathbf{x}' = \mathbf{T}_N \mathbf{A} \mathbf{x}_p$, \mathbf{T}_N is the nonlinear transformation given by Equations B.9 and B.10, \mathbf{T}_θ is the transformation for the rotation of the (x',z') plane relative to the (x,z) plane, and \mathbf{D} is the transformation due to an offset of the (x',z') plane relative to the (x,z) plane by distances δ_x and δ_z in the x and z directions, respectively. The effect of the rotation and the offset in Equation B.11 is to multiply the nonlinear transform results by a constant and to add a constant, respectively. Therefore, a linear polynomial approximation will accurately model the last two transforms in Equation B.11.

The equations used to calibrate the LIF system were obtained by multiplying polynomial equations in each direction (i.e., $(1+x_p)$ and $(1+z_p)$ for a linear approximation) to obtain two-dimensional polynomial equations. For the linear approximation, the following equations were obtained:

$$\begin{aligned} x &= a(1) + a(2)x_p + a(3)z_p + a(4)x_p z_p \\ z &= b(1) + b(2)x_p + b(3)z_p + b(4)x_p z_p, \end{aligned} \quad (\text{B.12})$$

where the coefficients a and b are determined by the least squares error analysis (Hildebrand(1974)). The equations used for the parabolic approximation have nine terms, while the equations for a cubic approximation have 16 terms. As can be seen in Figure B.1, a typical image of the lucite calibration plate may have over 150 control points, depending on the field of view. For a two-dimensional cubic approximation, this provides over 130 degrees of freedom which will indicate whether the approximation used adequately models the distortion in the video image. If the model is not an accurate

representation of the distortion, there will be large RMS errors between the known control point locations and those calculated from the video image.

Figure B.5 shows the control point locations in the wave tank, along with the control point locations computed from the video image using the cubic polynomial approximation. The control point locations shown in Figure B.5 are those shown in Figure B.1 as seen with the video camera. The errors between the actual and computed control point locations were within the expected errors, based on the digital resolution of the video image of about 2.0 mm/pixel. This corresponds to an uncertainty of ± 1.0 mm. The fact that the RMS errors were on the order of the digital resolution of the video image indicates a cubic model is an adequate approximation for the distortion shown in Figure B.1.

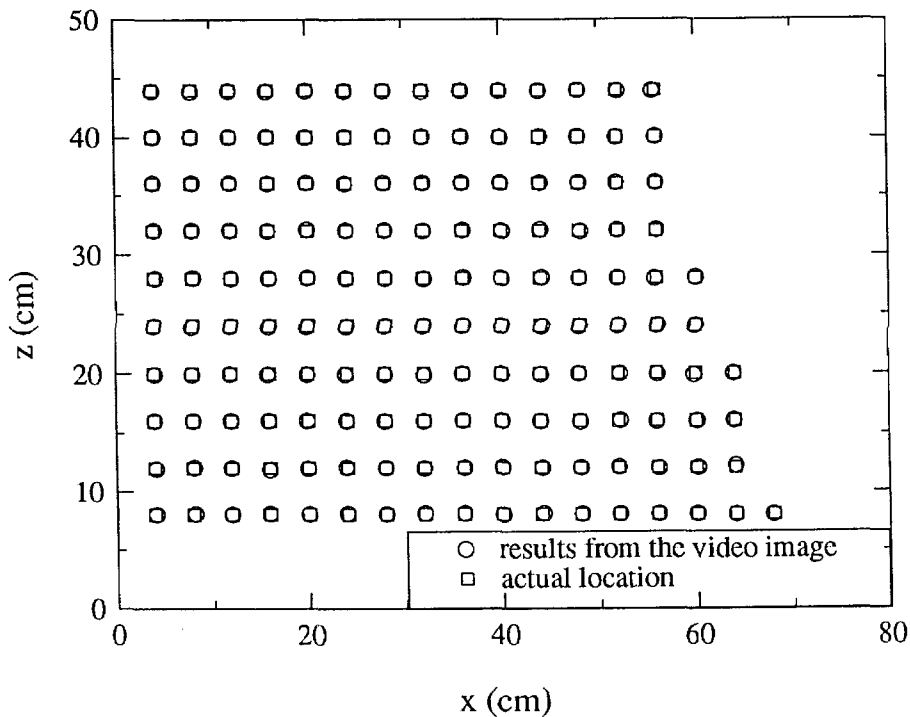


Figure B.5 Comparison of control point locations in the wave tank with locations computed from the video image (as seen in Figure B.1) using a cubic calibration model.

The still water surface was recorded with the video camera and converted to physical coordinates using a linear, parabolic, and a cubic least squares approximation as shown in Figure B.6, where the ordinate is the water surface profile, η , relative to the still water level. The ambient water depth was 14.28 cm. The abscissa is the horizontal distance, x , measured from the instrumented wall. The vertical scale has been

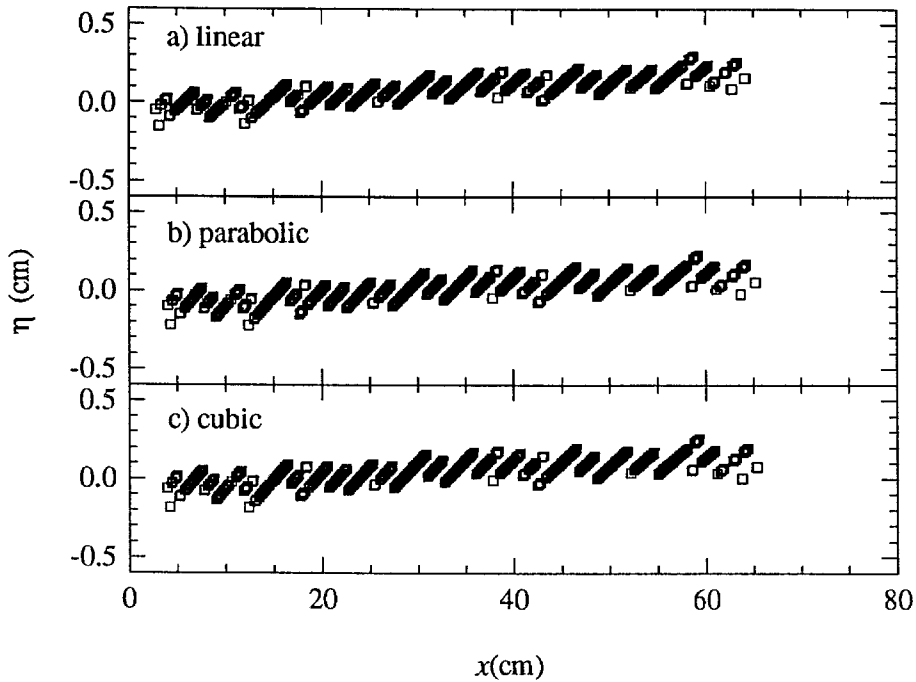


Figure B.6 Image of the still water surface computed from the video image using a (a) linear, (b) parabolic, and (c) cubic two-dimensional polynomial approximation.

exaggerated to magnify the error in the results obtained from the video image. Although the errors in Figures B.6 (a) through (c) are about the same, the linear approximation had large RMS errors relative to the parabolic and cubic approximations. The errors in Figure B.6 (c) are within ± 3 mm, which includes a small but consistent linear trend in the data. This linear trend accounts for about ± 1 mm of the error, which is probably due to a slight rotation of the laser sheet from the plane formed by the lucite calibration plate. Therefore, for each run, the linear trend in the still water surface was eliminated from all subsequent images obtained during a given run. For all the horizontal wave tank

experiments, a parabolic approximation was used to calibrate the video camera for the solitary waves, while a cubic approximation was used for all the bores and dry bed surges. An additional check of the LIF method was made by comparing the results with a water surface time history, which was measured with a wave gage. This comparison is shown in Figure 5.2.4 and discussed in Section 5.2.

APPENDIX C:**Air-water surface tension measurements**

Surface tension at the air-water interface can influence the rate of air-entrainment at the tip of a turbulent bore if the scale of the problem is small enough so the surface tension effects dominate. At very small scales surface tension can cause the fluid surface to act like a stretched membrane which prevents the entrainment of air at the tip of a turbulent bore. This effect was qualitatively observed from the high-speed movies of the bores in the tilting wave tank. For the smallest bores, which had a wave height of 2.2 cm, there were very few bubbles relative to the tremendously bubbly flows observed in the 5 cm high bores. During the horizontal wave tank experiments a methyl alcohol-dye mixture was added to the water which allowed the laser induced fluorescence method to be used. Methyl alcohol has a surface tension of 22.6 dynes/cm at 20° Celsius (Weast (1985)) while water has a surface tension of 73.0 dynes/cm at 18° Celsius (Weast (1985)), therefore, the surface tension of the resulting mixture in the wave tank was measured. Since the volumetric ratio of alcohol to water used was only approximately 1/300,000 (i.e. 10 cc/ 3 m³), no effect on the surface tension of the fluid was expected. However, the surface tension was measured to ensure it did not vary from one set of experiments to the next which, in some cases, were conducted up to eight months apart.

A sample of fluid was taken from the horizontal tank before each set of experiments where a new supply of water and alcohol-dye mixture were to be used. These samples, along with a sample from the supply for the tilting tank, were tested to determine the surface tension between the air-water interface.

A variation on the maximum bubble pressure method, which is described in Adam (1930), was used to measure the surface tension at the air-water interface. This approach was followed since it is accurate to within 0.3% (Adam (1930)) and the required apparatus is easy to construct and use. The method is based on the pressure difference produced across the gas-fluid interface of a bubble created at the tip of an open-ended tube which is submerged in the fluid sample. The pressure difference across the interface will be a function of the bubble radius and the surface tension. Two tubes of different diameters were used where the end of both tubes are located at the same elevation. The surface tension can be related to the pressure difference generated across each tube as:

$$\sigma = a[(P_a - P_b) + r_b \rho_s g(0.69)] \quad \text{C.1}$$

where σ is the surface tension; P_a and P_b are the pressures generated across the tubes with radii r_a (0.1 mm) and r_b (2.01 mm), respectively; ρ_s is the density of the fluid sample, g is the acceleration due to gravity, and A is the constant of proportionality to be determined experimentally.

The device shown in Figure C.1 was built to measure the surface tension. The fluid sample is placed in the Pyrex jar and a Teflon lid, which was machined to accommodate the necessary plumbing, is screwed onto the jar forming an air-tight seal. Figure C.2 shows a schematic of the additional equipment needed to complete the measurement system which includes an air pump and a manometer. The large and small radius tubes are shown where both must terminate at equal elevations approximately 2 cm below the fluid surface. By opening the appropriate valves, the manometer can be

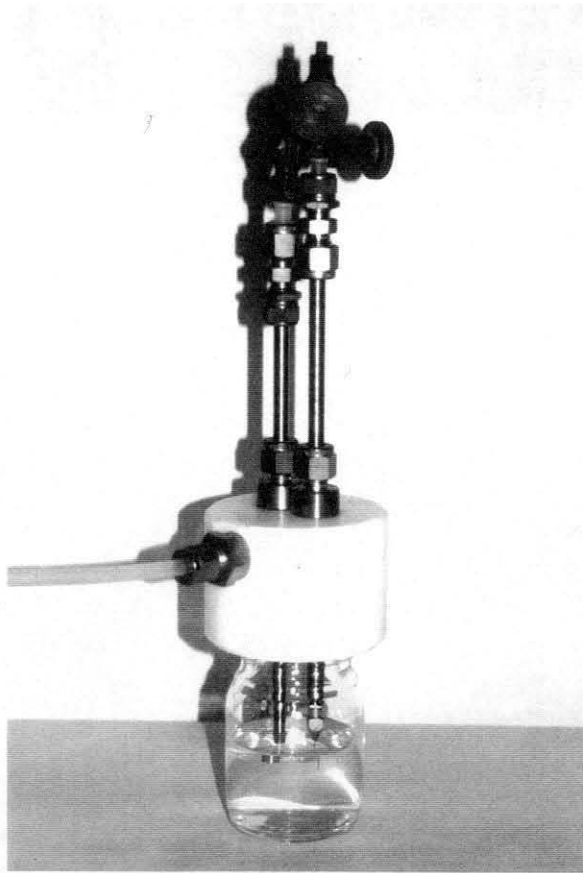


Figure C.1 Photo of the device used to measure the air-water surface tension.

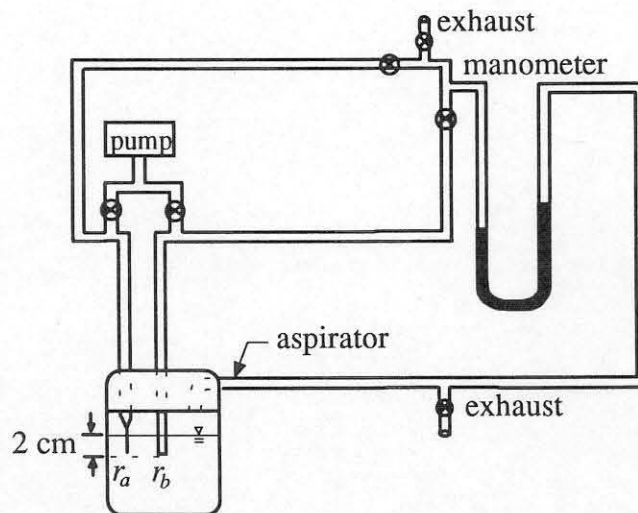


Figure C.2 Schematic of the surface tension meter

placed between the aspirator and one of the tubes which is supplied by the pump. The air pump was used to increase the head difference between the tube and the air space in the jar which produced bubbles at the tip of the tube. When the bubble formation rate was stabilized (which was determined by visual observation) at about 2 Hz, the pressure difference across the manometer was recorded. After adjusting the valves, the procedure can be repeated to obtain the pressure difference across the other tube.

The system must first be calibrated to determine the constant a . Toluene was used to calibrate the system. Using the known (Adam (1930)) air-fluid surface tension and density of toluene, the coefficient a for this system was calculated to be 0.05734 mm. The calibration was checked by using the calibration constant a and comparing the value for distilled water 73.0 dynes/cm with the experimentally determined value obtained with this system which was 73.2 dynes/cm which is within 0.3% of the published value. This provided some confidence in the system and the procedure.

For all the samples tested, the measured surface tensions are given in Table C.1 where the run numbers corresponding to a given fluid sample are indicated for the horizontal wave tank experiments. All the surface tension measurements shown in Table C.1 are between 0.1% to 1.7% larger than the published value and lie within 1.3% of the experimentally determined value for distilled water. Therefore, it appears the air-water surface tension can be considered constant for the experiments conducted in the horizontal wave tank. It must be noted that the water sample collected from the tilting wave tank supply was obtained three years after the experiments were performed. Thus, no surface tension measurements from the fluid used during those experiments was obtained.

| Wave tank | Run Numbers | σ (dynes/cm) |
|------------|---------------|---------------------|
| Tilting | TB94 - TB119 | 73.6 |
| Horizontal | HS60 | 73.1 |
| | HB63 - HB68 | 73.1 |
| | HS69 | 74.2 |
| | HB70 - HB85 | 74.2 |
| | HS86 | 73.3 |
| | HS99 - HS103 | 73.3 |
| | HB87 - HB98 | 73.3 |
| | HB104 - HB110 | 73.3 |

Table C.1 Measured air-water surface tension for the water used in this study.